Functional Anatomy and Biophysical Mechanisms of Fluid Transport in Vascular Plants: Implications for Structural Optimisation in Fossil and Extant Plants

Dissertation
zur Erlangung des Grades eines Doktors der Naturwissenschaften

der Geowissenschaftlichen Fakultät
der Eberhard-Karls-Universität Tübingen

vorgelegt von
Wilfried Konrad
aus Karlsruhe

2007

Tag der mündlichen Prüfung:	9. November 2007
Dekan:	Prof. Dr. Michal Kučera
1. Berichterstatter:	Priv.-Doz. Anita Roth-Nebelsick
2. Berichterstatter:	Prof. Dr. Thomas Speck
3. Berichterstatter:	Prof. Dr. John A. Raven

Zusammenfassung

Pflanzen transportieren Wasser- und Kohlendioxidmoleküle: Von den Wurzeln zu den Blättern strömt flüssiges Wasser. Zwischen Blättern und Atmosphäre werden Wasserdampf und gasförmiges Kohlendioxid ausgetauscht.

Angetrieben wird der Wassertransport zwischen Wurzeln und Blättern durch die Transpiration, welche in den teils luftgefüllten Interzellularen der Blätter erfolgt. Am Gewebe, das diese Hohlräume ausbildet, heftet sich das obere Ende eines Netzwerks aus Wassermolekülen fest. Zusammengehalten wird dieses Netzwerk von den kurzreichweitigen elektromagnetischen van der Waals Kräften, die benachbarte Moleküle aneinander binden. Aufgrund des Gewichts des Molekülnetzwerks stehen die zwischenmolekularen Bindungen unter Zugspannung, was sich makroskopisch in einem negativen Wasserdruck äussert. Ein derartiges System ist thermodynamisch metastabil und hat die Tendenz in einen stabilen Zustand zu kollabieren, sei es aufgrund statistischer Fluktuationen oder als Folge äusserer Einflüsse wie z.B. Winddruck oder Aktivitäten von Tieren. Es bilden sich dann Gasblasen, die Wasserdampf und eventuell auch Luft enthalten und zur Unterbrechung des Wasserstromes, zur Embolie, führen können. Die Gefässpflanzen haben verschiedene Strategien entwickelt, um die Folgen solcher Embolien zu begrenzen: Sie legen eine Vielzahl paralleler Gefässe an, welche wiederum in Segmente unterteilt sind, die untereinander durch ventilartige Durchlässe (sogennante Tüpfel) verbunden sind. Tritt Embolie ein, wird das betroffene Segment hydraulisch isoliert und der Wasserstrom darumherum geführt. Ausserdem verfügen die Gefässpflanzen über einen Reparaturmechanismus, der die Gasblase aus dem embolierten Segment entfernt, dieses wieder auffüllt und schliesslich in den Wasserstrom reintegriert.

Der Gasaustausch zwischen Blättern und Atmosphäre beruht auf Diffusion: An den Orten der Transpiration, innerhalb der Blätter, herrscht Wasserdampfsättigung, in der Atmosphäre in der Regel jedoch nicht. Deshalb diffundieren die Wassermoleküle aus dem Blatt hinaus. Kohlendioxid wird von der Pflanze assimiliert, etwa dort, wo die Transpiration stattfindet. Diese Kohlendioxidverarmung bewirkt einen in das Blatt hinein gerichteten Diffusionsstrom von Kohlendioxidmolekülen. Da beide Molekülströme dieselben Blattöffnungen (die Stomata) benutzen, befinden sich die Pflanzen in folgendem Dilemma: Einerseits sollte die Assimilationsrate hoch sein, denn die Assimilationsprodukten dienen den Pflanzen als Nahrung und Baustoff. Andererseits sollte die Transpirationsrate niedrig sein, denn in den meisten Habitaten ist Wasser nicht im Überfluss vorhanden. Kurzfristig verhalten sich die Pflanzen nun so, dass sie den Öffnungsgrad ihrer Stomata den Tagesgängen von Sonneneinstrahlung, Temperatur und Luftfeuchte aktiv anpassen. Langfristig passen sie auch die Anzahl der Stomata (pro Blattfläche) dem sich ändernden Kohlendioxidgehalt der Atmosphäre an. Wie diese Regelkreise physiologisch realisiert sind, ist unklar. Vorhersagen lässt sich das pflanzliche Verhalten dennoch: Ausgehend von den physikalischen und biochemischen Grundlagen von Diffusion und Assimilation lässt sich ein entsprechendes Optimierungsprinzip mathematisch formulieren.

Da dieses Optimierungsprinzip die Stomatadichten fossiler Blätter mit der Kohlendioxidkonzentration der Paläoatmosphäre verknüpft, wird es möglich, letztere aus physikalischen Prinzipien anstatt aus empirisch gewonnenen Transferfunktionen zu bestimmen.

Summary

In plants, water and carbon dioxide molecules are transported either in liquid or gaseous state: From the roots to the leaves water flows as a liquid. Between leaves and atmosphere water and carbon dioxide are exchanged as gases. Accordingly, the driving forces and mechanisms of transport are also different.

The driving force of the water transport between roots and leaves is transpiration which takes place in the gas-filled intercellulars of the leaves. Attached to this tissue is a network of water molecules which extends down to the ground water. This network is held together by short-ranged electro-magnetic forces ("van der Waals forces") between adjacent water molecules. Due to the weight of the molecular network the intermolecular forces are tensile which is — macroscopically speaking — equivalent to a negative water pressure. Such a system is thermodynamically metastable and has the tendency to collapse into a stable state, caused either by statistical fluctuations or by disturbances originating from the environment (e.g. by wind or animal action). In any case, gas bubbles containing water vapour and/or air develop within the water column and may lead to embolism, i.e. the breakdown of the water flow. Vascular plants have developed various strategies to cope with such incidents: they employ a multitude of parallel conduits which are segmented and (both laterally and longitudinally) connected by valve-like openings ("pits"). Thus, if embolism occurs, the affected segment becomes hydraulically isolated and the water flow is re-routed around this segment. There exists, moreover, a repair mechanism which is able to remove the gas bubble from the affected segment, to refill it completely with water and to put it into operation once again.

The exchange of water vapour and gaseous carbon dioxide between leaves and atmosphere is governed by diffusion: Within the leaves, where transpiration takes place, humidity is at its saturation value, the atmosphere, however, is usually not saturated with water vapour. Hence, water vapour diffuses *out of* the leaves. Carbon dioxide molecules are consumed by the plants' assimilation machinery, close to the sites where transpiration takes place. This depletion establishes the flow of carbon dioxide molecules *into* the leaves. Because both sorts of molecules navigate through the same leaf openings ("stomata") which connect gas-filled intercellulars and atmosphere plants are faced with a dilemma: On the one hand, assimilation rates should be high, because plants have to assimilate carbohydrates in order to feed themselves properly. On the other hand, transpiration rates should be kept low because in most habitats water is not in plentiful supply. In the short term, plants compromise between these contradicting requirements by actively adjusting stomatal openings to the diurnal changes of insolation (which is a necessary prerequisite for assimilation), temperature and atmospheric humidity. Additionally, plants vary the number of stomata per leaf area along with the long-term variations of atmospheric carbon dioxide concentration. It is not known how plants realise these control circuits in terms of physiology. Plant behaviour can, however, be predicted from a mathematically formulated optimisation principle which is based on first principles of physics and biochemistry regarding diffusion and assimilation, respectively.

This optimisation principle can also be used to reconstruct palaeoatmospheric carbon dioxide concentrations from stomatal densities of fossil leaves without recourse to experimentally obtained transfer functions.

Weißt Du, warum so beständig der Hahn
Seine Stimme erhebt bei des Morgens Nahn?
Er kräht, daß schon wieder die Nacht entschwindet
Und der kommende Tag Dich nicht klüger findet.

Omar Châjjam (⋆1048 – †1131, [11])

Ich versichere, daß ich bei der Anfertigung der vorliegenden Arbeit lediglich die angegebenen Hilfsmittel benutzt habe.

Tübingen, den 8. April 2007

Für Wilhelm Konrad (⋆1921 – †2004),
der jetzt im Nirwana sitzt
und sich bestimmt über diese Arbeit freut.

Wilhelmovi Konradovi (⋆1921 – †2004),
ktorý teraz v Nirwane sedí
a ktorého táto práca urcite tesí.

Contents

1 Introduction

The fossil record is notorious for being incomplete: after death, most plants and animals disintegrate. The remains of the organisms are often reduced to an imprint or consist of material which has been altered or replaced during diagenesis. Usually, little more than parts of the anatomical structure is preserved. This is problematic, not only if one wants to reconstruct a complete organism, but also if one wants to gain insight into its physiology or even the biocenose and habitat to which it once belonged: The greatest obstacle for the reconstruction of an ecosystem of extinct species is that direct evidence of the species' physiology and behaviour is most often gone.

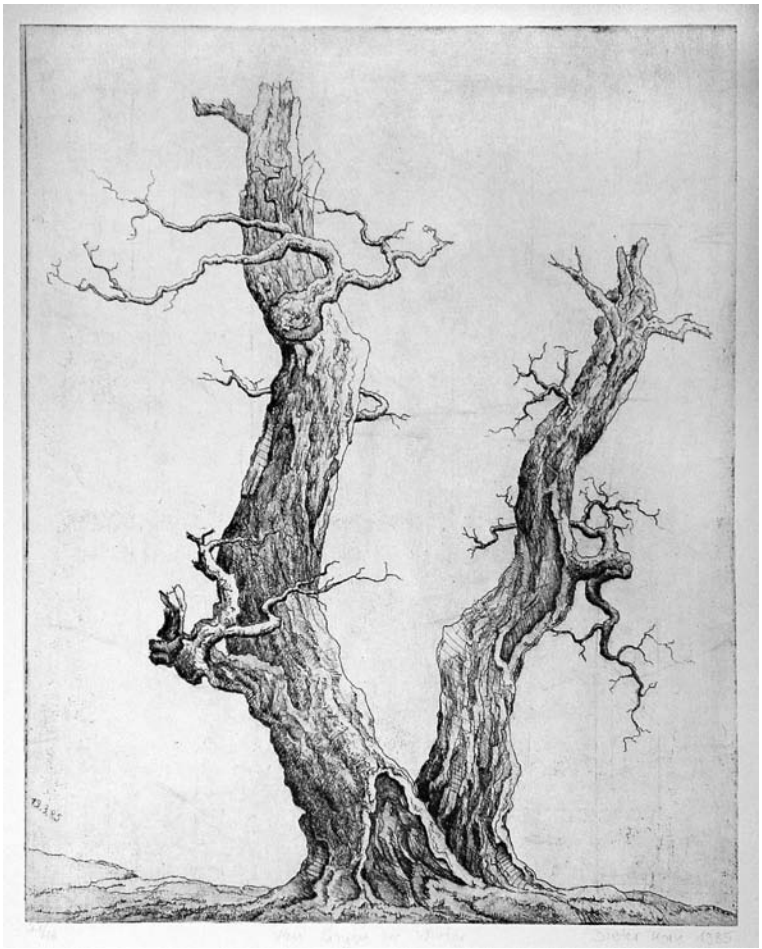

Figure 1.1: Oak trees, quite dead. (Etching by Dieter Korn, Humboldt-Museum, Berlin.)

The application of Functional Morphology can be used to compensate for these difficulties: In order to interprete the function of a fossil plant or animal from its morphology, anatomical evidence is combined with the principles of physics and chemistry which govern

the physiology of the living organisms. Physics and chemistry are universal in time and space and therefore provide information which generally escapes preservation in the fossil record. Using this supplementary information it often becomes feasible to draw conclusions regarding a species' physiology, its ecology and habitat. Often, however, more detailed information is needed.

In such cases an Optimisation Principle can be applied. The reconstruction of a species' physiology and ecology may proceed in the following manner:

(i) Sampling of preserved anatomic evidence,

(ii) application of Functional Morphology,

(iii) application of an Optimisation Principle.

This sequence is characterised by a shift in the relative proportions of direct evidence and theoretical concepts: the amount of theoretical concepts which supply information independent of fossilised evidence increases from (i) to (iii).

Figure 1.2: Lower Devonian Landscape near Rhynie (Scotland). (Painting by Birgit Binder, Tübingen.)

An illustration of this approach is given by the reconstruction of the extinct plant *Rhynia gwynne-vaughanii* from the Rhynie Cherts near Aberdeen (Scotland):

(i) The fossil record provides excellent information concerning its anatomy (with a resolution of a few micrometers).

(ii) Functional Morphology consists in this case of applying the laws of gas diffusion to the network of *Rhynia's* former, meanwhile chert-filled, intercellular voids which connects the transpiration sites inside the plant with the atmosphere. Thus, *Rhynia's*

transpiration rate can be calculated as an explicit function of the atmospheric humidity. Furthermore, the assimilation rate of *Rhynia* can be calculated as an explicit function of the atmospheric CO_2-concentration. This calculation relies on a few plausible assumptions concerning the biochemistry of photosynthesis and the parameters which characterise the assimilation process. Since there is reason to believe that the biochemistry of C_3-plants has not changed since the first land plants appeared the assimilation parameters can be borrowed from extant plants. From these results other ecophysiological quantities, such as the Water Use Efficiency can be derived.

(iii) Going a step further, we may replace several of the *ad hoc* assumptions which formed the basis for the calculations in (ii) by applying an Optimisation Principle. It relates a plant's assimilation and transpiration behaviour to the plant's water supply: In many habitats ground and rain water supply is limited during the growth season and is often also subject to more or less periodic fluctuations. Hence, in order to avoid dehydration, a plant should *not* simply maximise its assimilation, irrespective of the consequences of high water loss by transpiration. Usually, a plant is much better off if it maximises assimilation *on the condition* that not more than a fixed amount of water per water supply cycle is used for transpiration.

The term "optimisation" can be used in two different meanings:

- The Theory of Evolution postulates that those individuals which are best adapted to their ecosystem have the best prospects of reproduction ("survival of the fittest"). This statement can be viewed as an Optimisation Principle. Actually, since the Theory of Evolution deals only with *real* individuals, the only means with which the fittest individual can be singled out is by comparison with its competitors. Hence, the fittest individual is merely required to be *fitter* than all its competitors.

- This contrasts with mathematical Optimisation Principles which would seek out the fittest individual by comparing the fitness of a group of *fictitious* individuals. Thus, in a mathematical Optimisation Principle the fittest individual would occupy the maximum of a function describing the individual's performance in relation to its environment. In the Theory of Evolution, however, the fittest individual would merely be located closer to the maximum of that function than its competitors.

This thesis contains papers concerning the water transport system of vascular plants. These papers address various aspects centered around the following topics:

- The transport of liquid water between roots and leaves: how the water transport system works; why it often fails; under what conditions a repair process may set in; on what principles the repair mechanism relies.

- The transport of vapourised water and of CO_2 between leaves and atmosphere: transpiration as the ultimate cause for plant water transport; derivation of transpiration and assimilation rates and consequences for the ecophysiology of extinct plants; application of the underlying biological Optimisation Principle for the reconstruction of palaeoatmospheric CO_2 concentrations from stomatal densities.

2 Water transport between roots and leaves

Plants evolved in and were for the longest part of their history restricted to aquatic habitats. Hence, when they started to adapt to a terrestrial life style they were forced to develop an effective water transport system.

Figure 2.1: Robert Kidston and David Thomas Gwynne-Vaughan share a pipe over fossils from the Rhynie cherts (ca. 1920). (Photograph: University of Aberdeen.)

Plants need a reliable water supply because (i) the process of photosynthesis uses water as a raw material, and — more important — because (ii) water is inevitably lost from the plant tissue by transpiration. The problem of water supply became acute when plants began to grow higher than a few centimeters, since water had now to be elevated against gravity which is not the strongest but the most persistent force of nature. Moreover, with increasing height above ground, atmospheric humidity decreases from the saturation value near the soil surface. Hence, the taller a plant grows, the greater becomes the difference between the atmospheric humidity which prevails close to its leaves and saturated atmospheric humidity near the soil surface. Since this difference is the "driving force" of transpiration, a taller plant transpires more water than a short plant, demanding a more elaborate water transport system.

Eventually, the problem of water transport was solved by the vascular plants. *Rhynia gwynne-vaughanii* from the Lower Devonian (Pragian, 410 Ma) of Scotland is not the earliest land plant, but the earliest land plant which is generally recognised to have been a vascular plant.

Whether *Cooksonia caledonica* (Upper Silurian, 420 Ma, originally described from Wales) or *Baragwanathia longifolia* (?Upper Silurian to Lower Devonian, 420 Ma – 410 Ma from Australia) should be regarded as vascular plants and which one of the two is the earlier is still

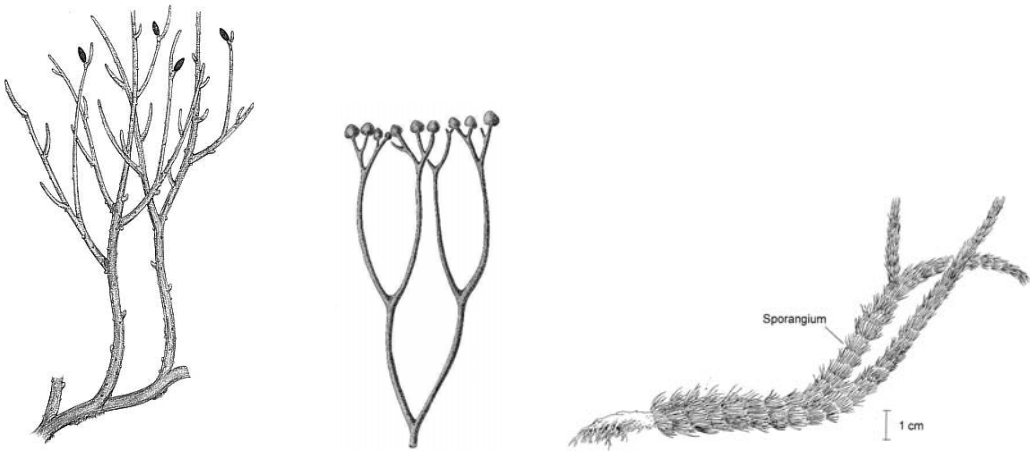

(a) *Rhynia* (b) *Cooksonia* (c) *Baragwanathia*

Figure 2.2: Reconstructions of early land plants. (a) *Rhynia gwynne-vaughanii* (Lower Devonian, 410 Ma) from the Rhynie cherts near Aberdeen (Scotland). Height: about 20 cm (b) *Cooksonia caledonica* (Upper Silurian, 420 Ma), originally described from Wales. Height: about 7 cm (c) *Baragwanathia longifolia* (?Upper Silurian to Lower Devonian, 420 Ma – 410 Ma) from Australia. (Illustrations: (a) University of Münster, (b) `www.palaeos.com/Plants/Rhyniophytes`, (c) [70].)

(a) *Wattieza* (b) *Archaeopteris* (c) *Lepidodendron*

Figure 2.3: Tree-like vascular plants from the Palaeozoic.
(a) *Wattieza*, Middle Devonian, height $\geq$ 8 m
(b) *Archaeopteris*, Upper Devonian, height $\sim$ 20 m
(c) *Lepidodendron*, Upper Devonian and Carboniferous, height $\leq$ 35 m
(Illustrations: (a): [61]. (b) and (c): `http://biodidac.bio.uottawa.ca`.)

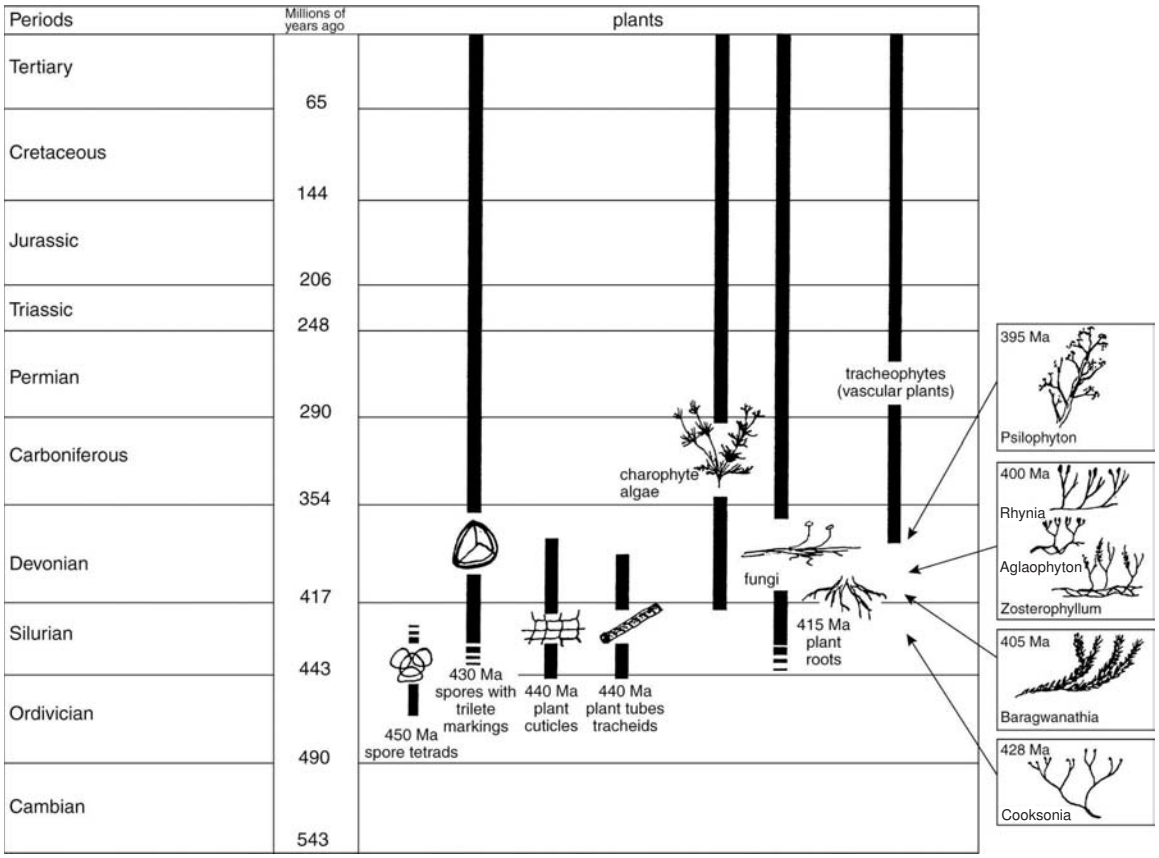

Figure 2.4: First appearance in the plant fossil record of innovations leading to the colonisation of land by plants. (Illustration from [70].)

a matter of debate (see Figure 2.2 and [62], [70]). The solution proved to be quite a success: already in the Middle Devonian — the tiny Lower Devonian *Rhynia gwynne-vaughanii* (with a moderate height of about 15 cm to 20 cm) had meanwhile become extinct — *Wattieza*, a more than 8 m tall tree, had appeared. During the Upper Devonian trees became even taller: *Archaeopteris* (which colonized all known Devonian land masses and formed the first forests) grew about 20 m high and *Lepidodendron* reached even 35 m.

2.1 Short history of the cohesion-tension theory

Although vascular plants have been using their water transport system for more than 400 million years humans realised the mechanism behind it only about 100 years ago. We give here a very short account of the history of the cohesion-tension theory. More information can be found e.g. in [66].

Modern attempts to understand water transport in plants date back to about 400 years ago when William Harvey (1628) and Marcello Malpighi (1661) drew analogies with blood circulation in animals. In 1727, Stephen Hales could show that water flow in trees is only upwards, from the soil to the leaves.

An important step towards the Cohesion-Tension-Theory was Heinrich Cotta's identifica-

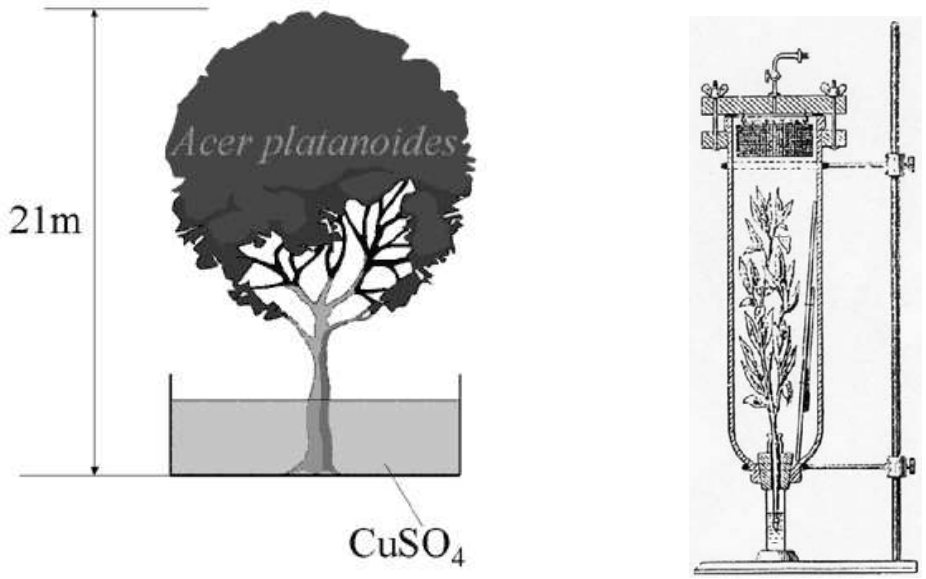

(a) (b)

Figure 2.5: (a) Strasburger proved (ca. 1890) that water uptake and transpiration of a tree work for weeks even if the living cells have been killed by copper sulfate mixed into the uptaken water. (b) With this experiment Joly and Dixon showed (ca. 1895) that water is lifted against gravity even if the leaves are under higher pressure than the reservoir watering the lower end of the twig. (Illustrations from [66].)

tion of sapwood as the transporting plant tissue, the result of a prize competition organised by the Imperial Academy of Scientists in Erlangen in the year 1798.

The question for the driving force of water movement became the subject of heated debates between "vitalists" and "physicists". The first group contended the idea that living cells should play a major role in the transport mechanism although they were neither able to identify these cells nor to suggest a detailed transport mechanism. The "physicists" view that only dead cells are involved, hence, the mechanism of water transport must rely directly on physical effects, was confirmed by an experiment conducted by Eduard Strasburger (1891) (see Figure 2.5(a)). He immersed the roots of a tree into a concentrated solution of copper sulfate ($CuSO_4$). Although the $CuSO_4$ killed all living cells in its way almost instantly it moved upwards into the leaves (which became evident when they were killed, too). Moreover, the uptake of the solution and the process of transpiration from the dead leaves went on for several weeks.

J. Joly and H. H. Dixon of the Trinity College in Dublin showed (see 2.5(b)) about 1895 that water is lifted against gravity even if the leaves of a detached twig put into a pressure vessel and kept there under three bars overpressure while the lower end of the twig is put into a water reservoir and kept under atmospheric pressure.

That water can — apparently contradicting everyday experience — withstand high tensional forces (but is very weak against shear forces, which explains the common misperception) has been known since the experiments of Berthelot (1850) and Jäger (1892).

The last missing element of the cohesion-tension theory was provided more or less independently by Joly and Dixon and by Eugen Askenasy of Heidelberg University in 1894

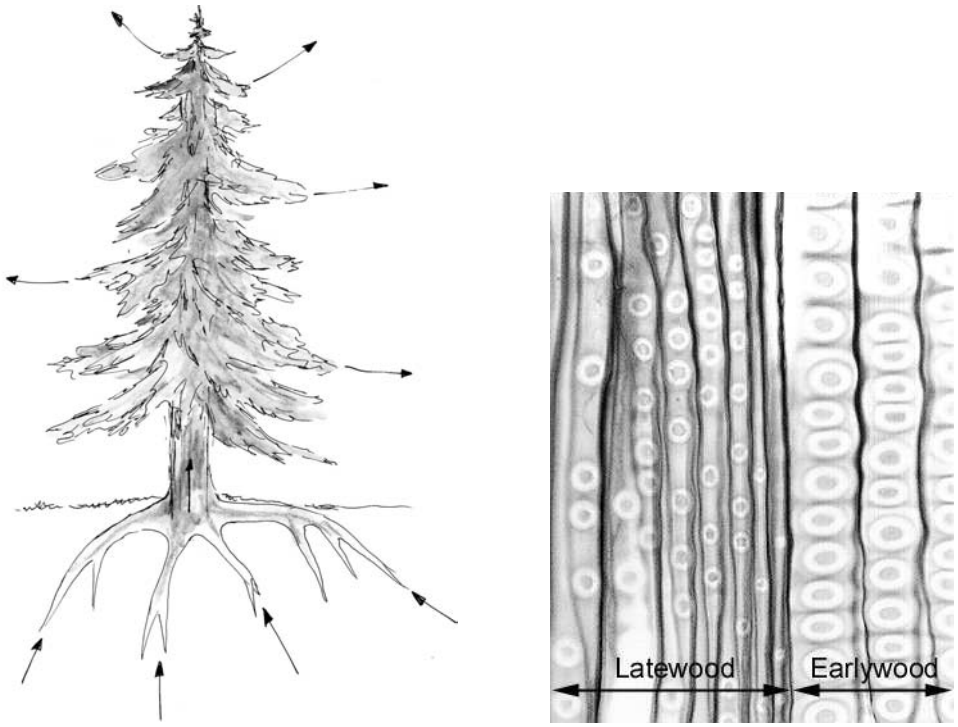

(a) (b)

Figure 2.6: (a) Schematical pathway of water through a schematical conifer. (b) Radial section of pine wood showing tracheids with circular bordered pits. (Illustrations: (a) Birgit Binder, Tübingen, (b) James D. Mauseth, `http://www.sbs.utexas.edu/mauseth/weblab`.)

(afterwards they quarrelled about priority): They found that in the leaf parenchyma where transpiration takes place strongly curved water/air interfaces develop, providing the surface tensions which counteract the weight of the water column and pull it up against gravity. With Dixon's book from 1914 ("Transpiration and the Ascent of Sap in Plants") the cohesion-tension theory found its final form.

2.2 Outline of the cohesion-tension theory

Plant water transport in vascular plants relies on two basic principles:

- The driving force which allows water flow to overcome gravity is provided by transpiration which takes place in the leaves.
- The cohesion of water.

Imagine a long chain (or rather a threedimensional network) of water molecules whose upper end is fastened to the parenchyma tissue of a plant leaf where transpiration, the transformation of liquid water into water vapour, takes place. From there it hangs down through twigs, trunks, stem and roots into the ground water.

Each chain link adheres to its neighbours by electromagnetic forces (van-der-Waals forces) which are due to the highly inhomogeneous and different distributions of positive and

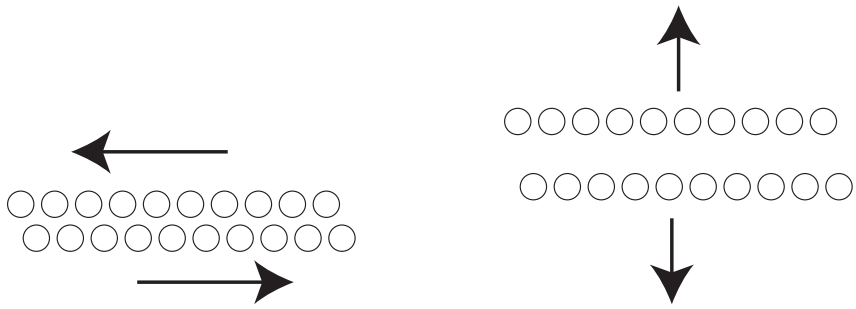

(a) Shear stress (b) Tensional stress

Figure 2.7: (a) Two layers of water molecules move *along* a common plane due to shear stress. (b) Two layers of water molecules move *away* from a common plane due to tensional stress. In order to realise case (b) a much higher stress must be applied than in case (a).

negative electric charges within the water molecule (see Figure 2.8). (Another example of the biological fruitfulness of the physical “anomaly" of water, as compared to other liquids.)

Every layer of water molecules which evaporates in the leaves draws up the whole chain for about one molecular diameter (the required energy is provided by transpiration i.e. ultimately by the sun). Like in a traditional metal chain, the higher up in the chain a link (= water molecule) is, the higher the load it has to carry, because the latter consists of the weight of all molecules below (this is why a chain which is hanging down can be expected to break at its uppermost link). Thus, the tension in the water chain increases towards the crown of the tree. When the chain is drawn up by evaporation, friction between the water molecules and the vessel walls adds to the tensile forces within the water molecules forming the chain.

The following calculation gives a rough estimate of the stresses acting upon the water in a plant conduit. A water column of cross section A hanging down a distance h exerts a force

$$G = \rho A h g \tag{2.1}$$

onto its attachment (with $\rho = 10^3\,\mathrm{kg/m^3}$ = density of water, $g = 10\,\mathrm{m/s^2}$ = acceleration of gravity at surface of earth). This force corresponds to a stress

$$p = \frac{G}{A} = \rho g h = 10^4\,\frac{\mathrm{kg}}{\mathrm{m^2\,s^2}}\,h = 10^4\,\frac{\mathrm{Pa}}{\mathrm{m}}\,h \tag{2.2}$$

Keeping in mind that trees are not taller than about $h_{max} \approx 120\,\mathrm{m}$ we obtain

$$p_{max} = 10^4\,\frac{\mathrm{Pa}}{\mathrm{m}}\,120\,\mathrm{m} = 1.2\,\mathrm{MPa} \tag{2.3}$$

for the stress which the uppermost molecular layers of the water column within the conduit of a tree must be able to resist. This is a crude approximation because it accounts only for the weight of the water column. It neglects additional resistances due to friction, e.g.. Therefore, realistic stresses may be higher by an order of magnitude (see [43], [66], [34]).

Given how easily a spoonful of tea or coffee can be separated from the bulk of the respective liquid within a cup, it may come as a surprise that liquid water can resist astonishingly high tensions before it breaks. But everyday experience is misleading in this case: here, the crucial quantity is shear stress, against which the resistance of water is indeed very low: it is very

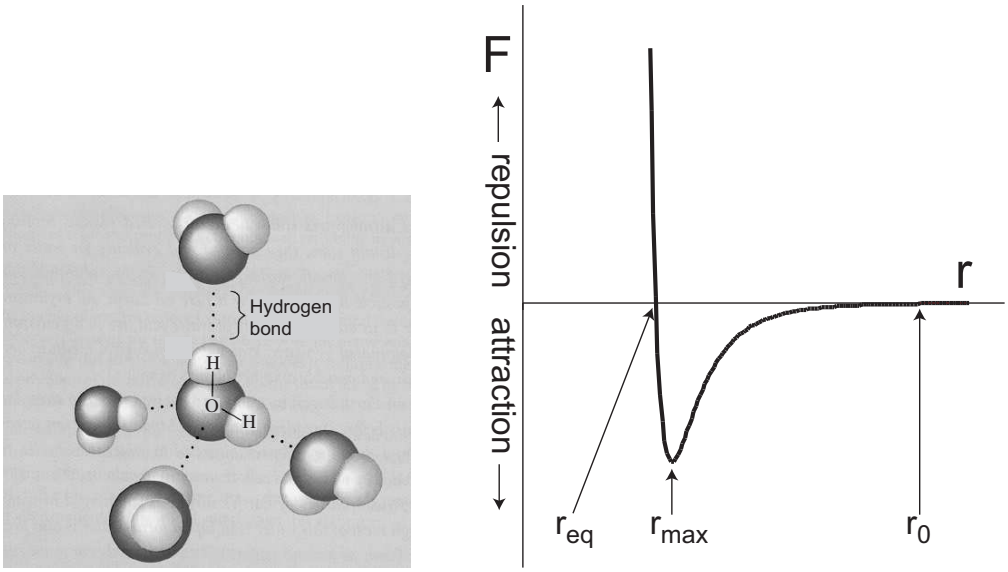

(a) (b)

Figure 2.8: (a) Semi-classical picture of five water molecules and the hydrogen bond (van der Waals force) between two of them. (b) Lennard-Jones-potential, describing molecule-molecule interaction similar to that between two water molecules. (For explanantion see text.)

easy to move two layers of water molecules relative to each other *along* a common plane by applying shear stress. In order to *separate* the two layers from each other much higher tensional stress must be applied, however (see Figure 2.7).

Experimentally, it is difficult to distinguish resistance against shear stress from resistance against tension stress because it is not easy to apply only one of the two stress varieties to liquid water. Hence, measurements of the breaking strength of water against tension stress should be treated *cum grano salis*: Instead of reporting the true value of breaking strength they may rather tell something about the quality of the experimental setup. Nonetheless, such experiments provide reliable lower limits of the effect. From the literature values of the breaking strength of water between 50 MPa and 100 MPa seem to be (i) reliable and (ii) in accordance with theoretical considerations ([67]).

Hence, even if realistic stresses are much higher than the 1.2 MPa estimated above for the water in a tree conduit they are well below the lower limit of the breaking strength of water.

Things are, however, not so simple. Chiefly, because the values of breaking strength just given apply only to very pure water which contains at most insignificant quantities of molecular species other than water (for example no air bubbles). The reason for this restriction is found in the radial characteristics of the intermolecular force between water molecules (see Figure 2.8): For distances r smaller than an equilibrium separation r_{eq} two water molecules exchange a repulsive force (whose great strength accounts for the small compressibility of water). For separations greater than r_{eq} the molecules attract each other. The attractive force has a maximum at a separation r_{max}. If the separation is increased further the attraction decreases (asymptotically), beyond a distance r_0 it becomes effectively zero.

If water is “polluted” by other molecular species, some water molecules become farther separated from one another than they were before (in pure water) because molecules of

the polluting species have entered the space between them. If this effect shifts the mean separation between adjacent water molecules to values much beyond r_{max} the attractive force between these water molecules decreases. So becomes the effective breaking strength of the whole network of water molecules. If the breaking strength is reduced far enough this effect becomes disastrous. It should be noted, however, that solitary molecules which are completely surrounded by water molecules (macroscopically speaking, they are dissolved in the water) do usually not represent a threat for the integrity of the network of water molecules. Soil particles or air bubbles, however, may become dangerous if their diameter is large enough. In order to minimise this threat the roots of (vascular) plants have developed into excellent filter systems which are able to keep these out of the flowpath (see, e.g. [63]).

2.3 Hazards to water transport

Even perfect root filters would be no guarantee against a suddden loss of conductivity of the plant water transport system. There are two other potentially hazardous effects: spontaneous cavitation and air seeding.

2.3.1 Spontaneous cavitation

Spontaneous cavitation is basically due to statistical fluctuations (caused, for instance, by Brownian movement) of the energy of a group of neighbouring water molecules in liquid state: if they acquire enough kinetic energy to "cut" the network of intermolecular binding forces defining the liquid state and to become a cluster of gaseous molecules, then an embryonic bubble filled with water vapour forms within the liquid. Whether this embryonic bubble disappears soon afterwards because its constituents are being "resorbed" into the liquid surrounding the bubble or whether it grows because more water molecules vapourize into it depends (i) on its initial radius R_0 and (ii) on the tension $p_s < 0$ (= negative water pressure) existing in the water column.

The reversible free energy associated with the spontaneous formation of an embryonic bubble with radius R is given by (see [22], [60])

$$W(R) = 4\,\pi\gamma\,R^2 - \frac{4\pi}{3}\,(p_w - p_s)\,R^3 \tag{2.4}$$

(γ: surface tension of air/water interface, p_w: pressure of water vapour within the bubble, p_s: water pressure). The further development of the gas bubble is essentially controlled by the following forces:

- Contracting forces: surface force exerted by liquid/gas-interface at bubble surface and xylem water pressure (if positive)
- Expanding forces: gas pressure of water vapour and air molecules and xylem water pressure (if negative)

They are obtained from (2.4) by differentiation:

$$\begin{aligned}\frac{\partial W}{\partial R} &= [\text{contracting forces}] - \{\text{expanding forces}\} \\ &= [8\,\pi\gamma\,R] - \left\{4\pi\,(p_w - p_s)\,R^2\right\}\end{aligned} \tag{2.5}$$

A bubble of radius R which does neither expand nor contract because the respective forces are at equilibrium is characterised by $\partial W/\partial R = 0$. In molecular terms, at equilibrium, the number of water vapour molecules vapourising into the bubble equals the number of molecules condensating into the surrounding liquid. In the case $\partial W/\partial R > 0$ condensation dominates vapourisation and the bubble disappears. For $\partial W/\partial R < 0$ vapourisation is the dominating effect and the bubble expands further. In order to locate the extrema of $W(R)$ given in expression (2.4) we solve expression (2.5) for its zeros. We obtain $R = 0$ (representing an artefact) and

$$R = \frac{2\gamma}{p_w - p_s} =: R_{vap} \tag{2.6}$$

The second derivative of $W(R)$, evaluated at R_{vap}, amounts to

$$\frac{\partial^2 W}{\partial R^2} = 8\,\pi\gamma - 8\pi\,(p_w - p_s)\,R\Big|_{R=R_{vap}} = -8\,\pi\gamma < 0 \tag{2.7}$$

Hence, $R = R_{vap}$ represents a maximum of $W(R)$ corresponding to an unstable equilibrium of forces (whereas a positive value would indicate a minimum of $W(R)$ and stable equilibrium). In other words: if the radius R of a spontaneously emerging vapour bubble obeys the relation $R > R_{vap}$ the bubble expands (in principle infinitely), for $R < R_{vap}$, however, it vanishes.

R_{vap} depends approximately reciprocal on the water pressure (or, rather, tension) p_s: Thus, the more negative the water pressure is, the smaller is the bubble radius which divides the regimes of bubble collapse and expansion. For example, under a water pressure of $p_s = -0.01\,\text{MPa}$, all bubbles with a radius smaller than $R_{vap} \approx 10.94\,\mu\text{m}$ will collapse immediately. For the more negative pressure $p_s = -1\,\text{MPa}$ this radius amounts to the much smaller value $R_{vap} \approx 0.143\,\mu\text{m}$ (see Figure 2.9 and the discussion in [51]). Put differently, a bubble of initial radius $R \approx 5\,\mu\text{m}$ collapses (without doing harm) under a water pressure of $p_s = -0.01\,\text{MPa}$ but expands until embolism under $p_s = -1\,\text{MPa}$.

The threshold energy related to the equilibrium at R_{vap} follows from insertion of (2.6) into (2.4):

$$W_{crit} = \frac{16\pi\gamma^3}{3}\,\frac{1}{(p_w - p_s)^2} \tag{2.8}$$

Hence, if the energy associated with the embryonic bubble is smaller than the threshold value W_{crit}, the bubble disappears, if it is greater than W_{crit}, the bubble grows.

This result suggests that a water column under tension constitutes a metastable system in the following sense: if the water column is "disturbed" by the introduction of an embryonic bubble carrying an energy $W < W_{crit}$ the bubble dissolves. But if the bubble carries an energy $W > W_{crit}$ the bubble inflates until the water column collapses into a stable state characterised by a positive water pressure $p_s > 0$.

Based on arguments from statistical physics and thermodynamics it has been shown ([46], [51], [55]) that for the negative pressures to be expected in plant conduits spontaneous cavitation plays only a minor role in causing embolism (as compared to the air seeding process, see below) because the tension values occurring in the xylem are not high enough to permit a significant formation rate of expanding bubbles.

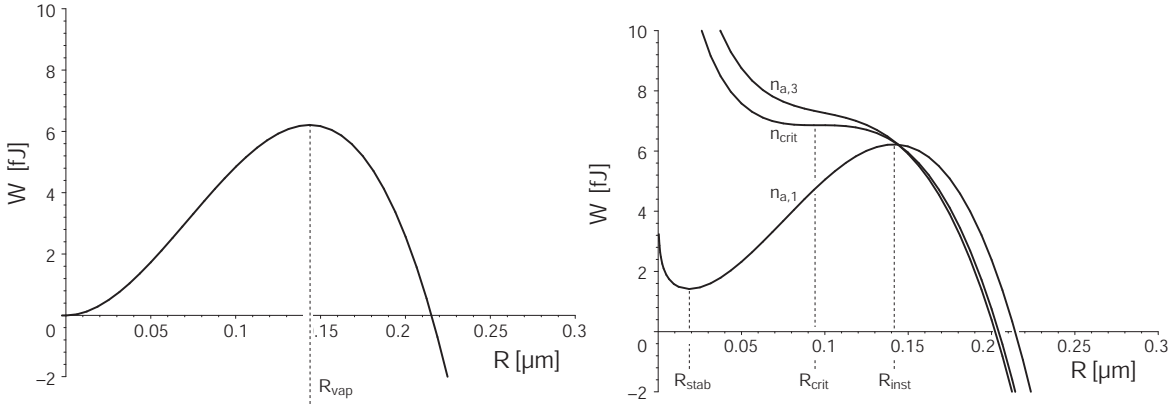

(a) Only water vapour (b) Water vapour and air

Figure 2.9: Energy of bubble formation W plotted against bubble radius R. Water pressure in the conduit amounts to $p_s = -1$ MPa. Equilibrium between expanding and contracting forces is realised only at bubble radii R representing extrema of $W(R)$. Maxima indicate unstable, minima stable equilibrium. (a) Bubble filled only with water vapour. (b) Bubble filled with water vapour and air. Curves are plotted for the following numbers of air molecules: $n_{a,1} = 7.5 \times 10^{-20}$ mol, $n_{crit} = 7.5 \times 10^{-19}$ mol and $n_{a,3} = 9 \times 10^{-19}$ mol.

2.3.2 Air seeding

Air seeding may occur if a group of "air" molecules finds its way into a tree water conduit. Suitable cracks and openings in the wood may be produced by the wind bending twigs of the tree as a whole, or by animals like woodpeckers or beetles in search of food. If such a passage remains open, at least one segment (see below) of the embolised conduit is permanently lost for water transport. If it closes, however, after a limited number of "air molecules" has entered the conduit these form one or several embryonic air bubbles which may — but need not necessarily — cause the rupture of the water column.

In order to describe this mixture of water vapour and air we extend expression (2.4) by a term representing n_a air molecules

$$W = 4\,\pi\gamma\,R^2 - \frac{4\pi}{3}\,(p_w - p_s)\,R^3 + 3\,\mathcal{R}\,T\,n_a\,\log\left(\frac{R_{max}}{R}\right) \tag{2.9}$$

where two arbitrary constants have been chosen such that (i) in the absence of air molecules (i.e. $n_a = 0$, that is, in the case of a water vapour bubble) the formation energy W vanishes for $R = 0$, and, (ii) the contribution of the air molecules to the formation energy W (the last term in expression (2.9)) vanishes for $R = R_{max}$.

$$R_{max} := \frac{2\,\gamma}{-p_s} \tag{2.10}$$

denotes the maximum equilibrium radius which a gas bubble immersed in water of negative pressure $p_s < 0$ can attain (see [38]).

In what follows, the compressing and expanding forces acting upon a bubble will be analysed based upon equation (2.9). For these calculations the following two assumptions are made:

- $p_w \approx p_w^{sat}$ (p_w^{sat}: saturation pressure of water vapour) The exchange of water molecules between bubble and surrounding liquid is a very intensive one. Therefore, the water vapour partial pressure in the bubble readjusts to the water vapour saturation pressure almost immediately.

- $n_a \approx$ const.: This simplifying assumption is only valid on the very short time scale of bubble formation considered here. The assumption is based on the low solubility of air in water, implying that only a small fraction of the air molecules in the bubble's interior are lost to the surrounding liquid within the considered time scale.

Proceeding similarly as above, the bubble radii where equilibrium of forces prevails are found from the zeros of

$$\begin{aligned} \frac{\partial W}{\partial R} &= [\text{contracting forces}] - \{\text{expanding forces}\} \\ &= [8\,\pi\gamma\,R] - \left\{4\pi\,(p_w - p_s)\,R^2 + \frac{3\,\mathcal{R}\,T\,n_a}{R}\right\} \end{aligned} \tag{2.11}$$

and their stability is assessed by evaluating $\partial^2 W/\partial R^2$ at the equilibrium point(s). The zeroes of (2.11) depend on the values of the quantities n_a, p_s and p_w. They are located at the radii

$$\begin{aligned} R_{stab} &= \frac{R_{vap}}{3}\left(1 - 2\,\cos\left[\frac{1}{3}\,\arccos\left(1 - \frac{2\,n_a}{n_{crit}}\right) + \frac{\pi}{3}\right]\right) \\ R_{inst} &= \frac{R_{vap}}{3}\left(1 + 2\,\cos\left[\frac{1}{3}\,\arccos\left(1 - \frac{2\,n_a}{n_{crit}}\right)\right]\right) \end{aligned} \tag{2.12}$$

where

$$n_{crit} := \frac{128\,\pi\gamma^3}{81\,\mathcal{R}\,T}\,\frac{1}{(p_w - p_s)^2} \qquad \text{and} \qquad R_{vap} = \frac{2\,\gamma}{p_w - p_s} \tag{2.13}$$

Air-water vapour bubbles show a more complex behaviour than pure water vapour bubbles because their behaviour depends also on the number n_a of air molecules in the bubble:

- Evaluating $\partial^2 W/\partial R^2$, we find that a bubble at radius R_{stab} is in stable, at radius R_{inst}, however, in unstable equilibrium.

- For $n_a \to 0$ we find $R_{stab} \to 0$ and $R_{inst} \to R_{vap}$.

- For $n_a \to n_{crit}$ both R_{stab} and R_{inst} approach the quantity

$$R_{crit} := \frac{4\,\gamma}{3\,(p_w - p_s)} = \frac{2}{3}\,R_{vap} \tag{2.14}$$

- For $n_a > n_{crit}$ both R_{stab} and R_{inst} become undefined, meaning that the bubble expands without limits (see Figure 2.9(b)).

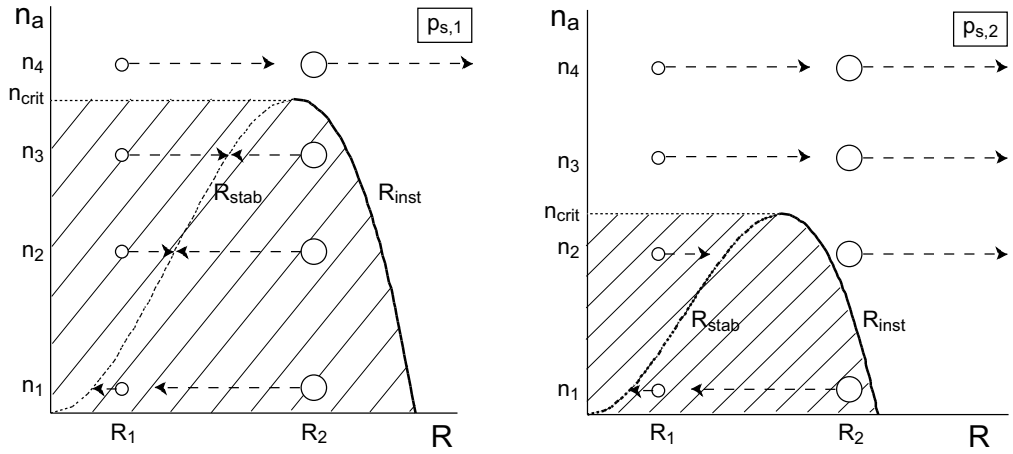

Figure 2.10: Regions of stability and instability of bubbles of radius R, filled with water vapour and n_a air molecules. (a): Stability diagram for a given water pressure $p_{s,1}$. (b): Stability diagram for a water pressure $p_{s,2}$ with $p_{s,2} < p_{s,1}$ (i.e. $p_{s,2}$ is more negative than $p_{s,1}$).
Only bubbles lying *on* the curves R_{stab} (broken line) and R_{inst} (solid line) are in stable resp. unstable equilibrium. Bubbles represented by other (n_a, R)-values either contract or expand (indicated by broken arrows). Bubbles belonging to the hatched region (left and below the solid curve R_{inst}) are contracting or expanding towards the stable radius R_{stab} lying on the dotted curve. Bubbles characterised by (n_a, R)-values outside the stability region expand. If p_s decreases, the region of stability shrinks. Hence, bubbles which are in equlibrium under water pressure $p_{s,1}$ (like those inhabited by n_3 air molecules in part (a) of the figure) fall outside of the equilibrium region if p_s drops to $p_{s,2} < p_{s,1}$ (see part (b) of the figure).

The bubble behaviour is illustrated by Figure 2.9(b). A bubble which contains $n_{a,3} > n_{crit}$ air molecules fulfills for all $R > 0$ the condition $\partial^2 W/\partial R^2 < 0$. Equation (2.11) implies then that the bubble can only expand. If the bubble contains $n_{a,1} < n_{crit}$ air molecules its future depends also on its initial radius R: in the case $R > R_{inst}$ it expands, in the case $0 < R < R_{inst}$ the bubbles expands or contracts towards R_{stab}.

Figure 2.10 illustrates the interdependance of initial radius and air content in a stability diagram in the (n_a, R)-plane. It allows to discuss several aspects of the embolism potential of an embryonic bubble:

- The ability of an air-water vapour bubble to seed embolism increases with its air content (with the water pressure being constant) (see Figure 2.10): A bubble of initial radius R_2 containing n_1 air molecules contracts towards the stable radius R_{stab}, a bubble of the same initial radius containing n_4 air molecules (with $n_4 > n_1$), however, bursts.

- Because of $p_w \ll |p_s|$ (the water vapour pressure p_w is usually much smaller than the absolute value of the water pressure p_s) the quantities n_{crit}, R_{inst}, R_{stab} and R_{vap} are approximately proportional to the reciprocal of p_s (see equations (2.12) and (2.13)). Thus, if p_s decreases (i.e. becomes more negative) the stability region which represents all bubbles (of radius R and containing n_a air molecules) drifting to stable equilibrium shrinks (In Figure 2.10 the stability regions are the hatched areas left and below the

solid curves R_{inst}). Hence, bubbles which were within the stability region at a given water pressure may become unstable because the borderline between stability and instability has wandered across their (fixed) location in the (n_a, R)-plane, due to the drop in p_s.

- Immediate collapse of an air-water vapour bubble is impossible. This is because — different to the water vapour molecules in the bubble — the air molecules cannot condensate to the liquid state (at least not under temperatures and pressures compatible with living plants). Hence, a stable air-water vapour bubble can only disappear by dissolution via diffusion of the air content into the surrounding water. Whether or not this will happen depends on the concentration C_{air} of air molecules already dissolved in the surrounding water.

It is worthwhile to pursue the last line of thought a little further: First, we use Henry's Law

$$p_{air} = \frac{C_{air}}{k_H} \tag{2.15}$$

to facilitate notation by defining a (fictitious) pressure p_{air} which is equivalent to C_{air}. Now, if p_{air} is smaller than p_a (the partial pressure of air molecules within the bubble) given by the gas equation by

$$p_a = \frac{3\mathcal{R}T\,n_a}{4\pi R^3} \tag{2.16}$$

air molecules from the bubble dissolve at the gas/liquid interface in the xylem water and diffuse away from the bubble (see Figure 2.11). For $p_{air} > p_a$ the reverse process takes place, dissolved air molecules diffuse towards and enter the bubble. For $p_{air} = p_a$ the (net) exchange of air molecules between bubble and surrounding xylem water ceases (this "diffusional equilibrium" should not be confused with the equilibrium between expansive and contractive forces at R_{inst}, R_{stab} and R_{crit}!).

The Young-Laplace-Equation

$$p = p_s + \frac{2\gamma}{R} \tag{2.17}$$

connects the gas pressure p within an equilibrated(!) bubble with the surface tension γ, the bubble radius R and the pressure p_s of the liquid surrounding the bubble. Splitting the gas pressure into the partial pressures of water vapour and air according to $p = p_w + p_a$ we find for bubbles in stable equilibrium

$$p_a = p_s - p_w + \frac{2\gamma}{R_{stab}} \tag{2.18}$$

The relation $R_{stab} < R_{crit}$ (see Figure 2.10) implies that the air pressure p_a in any stable bubble is necessarily greater than

$$p_a^{min} := p_s - p_w + \frac{2\gamma}{R_{crit}} \tag{2.19}$$

(a) $p_a < p_{air}$ (b) $p_a > p_{air}$

Figure 2.11: Diffusional fluxes of air molecules between bubble and xylem water. p_a designates the partial pressure of air molecules in the bubble. The fictitious pressure p_{air} represents the concentration C_{air} of air molecules dissolved in the xylem water (close to the bubble). It is defined via Henry's Law $C_{air} = k_H\, p_{air}$.
(a) $p_a < p_{air}$ causes a diffusional flux into the bubble.
(b) For $p_a > p_{air}$, air molecules leave the bubble and dissolve in the xylem water.

Hence, the condition $p_{air} < p_a^{min} < p_a$ for the dissolution of stable bubbles transforms upon insertion of relations (2.19) and (2.14) into the relation

$$p_s < -2\, p_{air} + p_w \tag{2.20}$$

It encompasses all bubbles which are stable at a given water pressure p_s, irrespective of their individual radii.

Since groundwater in the soil is in contact with air of atmospheric pressure the value of p_{air} can be expected to approximate atmospheric pressure, too. Therefore, the condition for the water pressure reads $p_s \lessapprox -2 \times 10^5$ Pa. The term $p_w \approx 3167$ Pa (at 25 °C) on the right hand side of equation (2.20) can be neglected, in comparison with the first term. Hence, if condition (2.20) is fulfilled embryonic bubbles appearing in the stability region depicted in Figure 2.10 dissolve after a while in the surrounding water.

2.4 Safety measures before and repair mechanism after embolism

In plant water conduits exist several safety measures concerned with embolism. Their purpose is to avoid embolism altogether, to minimise its consequences by isolating embolised conduit segments and to reestablish conduit functionality.

2.4.1 Dissolution of embryonic bubbles

A safeguard which relies solely on the properties of water under tension has just been explained: If condition (2.20) is fulfilled (which is usually the case) equations (2.13) and (2.14) imply that embryonic air bubbles which are initially smaller than R_{crit} and contain less than n_{crit} air molecules dissolve without doing any harm. Since completely impermeable

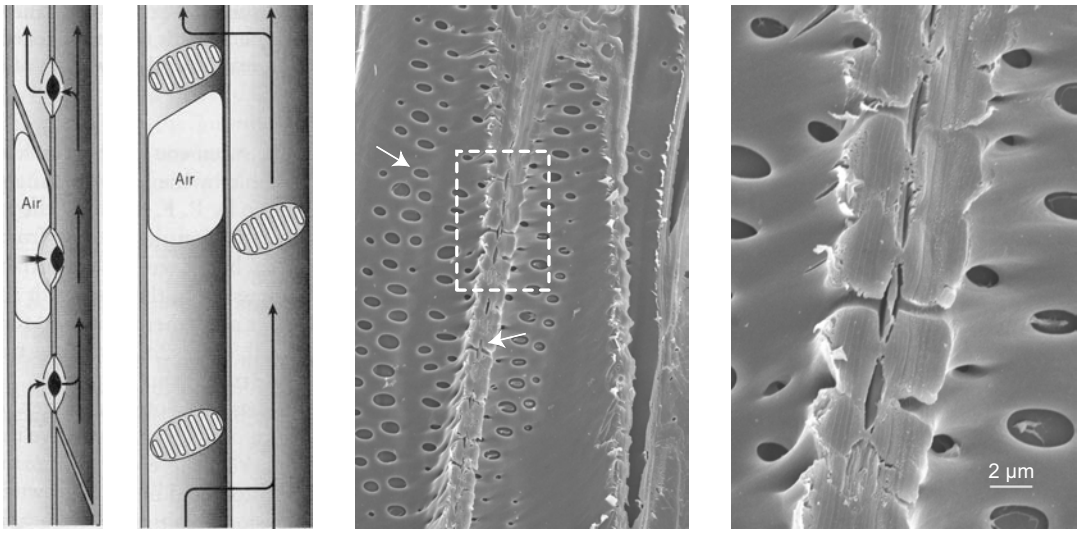

(a) (b) (c) (d)

Figure 2.12: (a) Re-routing of water flow in a conduit with torus-margo-pits (typical for gymnosperms) and with (b) membrane pits (typical for angiosperms). In torus-margo-pits, a pressure difference in adjacent conduits caused by embolism pushes the torus against the pit opening, the pit closes. Membrane pits possess sieve-like membranes with tiny openings. In case of embolism, highly curved gas/water-interfaces develop in these openings, effectively closing the pit. (c) Adjacent conduits of *Laurus nobilis*. The conduits are cut open along their longitudinal axes. The pits can be seen in cross section (left arrow) and top view (right arrow). (d) Detail of (c). (Illustrations: (a) and (b) from [65], (c) and (d) by A. Roth-Nebelsick, Tübingen.)

material exists neither as biological nor artificial tissue, tiny leaks will always and everywhere arise. Hence, the value of this safeguard should not be underestimated. Table 2.1 gives a few values for $R_{crit}(p_s)$ and $n_{crit}(p_s)$.

Table 2.1: Values of R_{crit} and n_{crit} calculated from equations (2.13) and (2.14) for the conduit water pressures p_s given in the first row.

p_s	-10^6 Pa	-10^5 Pa	-10^4 Pa
R_{crit}	0.096 µm	0.93 µm	7.29 µm
n_{crit}	7.4×10^{-19} mol	7.0×10^{-17} mol	4.3×10^{-15} mol

2.4.2 Anatomic features limiting spreading of embolism

Plants have also developed anatomical features to limit the damage caused by embolism.

2.4.2.1 Segmentation of conduits

These include a segmentation of the water conduits into compartments which are connected by pits, openings between adjacent conduits which may hydraulically isolate a conduit

segment befallen by embolism (see Figure 2.12). Since the pits connect not only successive segments of one conduit but also segments being part of adjacent conduits, a re-routing of the water flow avoiding the dysfunctional segment can be established. Thus, a conduit plagued by a dysfunctional segment is not completely lost for water transport, its transport capacity is merely lowered.

When an embryonic bubble with $R > R_{crit}$ and/or $n > n_{crit}$ expands the mean distances between the (liquid) water molecules decrease, the water pressure increases (see Figure 2.8). Hence, water molecules are pushed through the pit openings into conduit elements which are still intact, that is, under "operating pressure". From now on, the two pit types proceed on different routes to achieve hydraulic isolation of the dysfunctional conduit segment:

- If a **torus-margo pit** operates in "normal mode" the flow velocity is rather low (gymnosperms have maximum flow velocities of $1\,\mathrm{m/h} \ldots 2\,\mathrm{m/h}$, see [43]) and the flow rate Q through a pit opening (see Figure 2.13) attains moderate values below a critical flow rate Q_{crit}. The two forces acting on the torus — one originates from the flowing water pushing the (impermeable) torus, the other one is exerted by the elastic (and permeable) margo — are in stable equilibrium (see [16]) and the torus occupies a somewhat (depending on the flow rate Q) deflected but stable position within the pit.

  In "embolism mode" the water rushes much quicker through the pit opening. Then it is to be expected that $Q > Q_{crit}$ is realised. Equilibrium between the two forces becomes impossible (see [16]), hence a stable position for the torus does not exist any more. The torus is pushed against the pit border, the pit closes and remains closed due to the water pressure difference between dysfunctional and intact conduit element.

- **Membrane pits** (see Figure 2.13) possess sieve-like membranes with numerous tiny pores (typically with a radius of $r_p \approx 0.005\,\mu\mathrm{m} \ldots 0.02\,\mu\mathrm{m}$) through which the conduit water flows in "normal mode" (see [17]). During embolism, the embryonic gas bubble inflates — perhaps also releasing daughter bubbles — until it touches eventually the pit membrane. In the small membrane pores develop strongly curved gas/water interfaces ("menisci") whose radii of curvature have probably similar values as the membrane pore radii. Hence, according to the Young-Laplace-Equation, the menisci can be expected to withstand pressure differences (related to the r_p values just given) of about

$$\Delta p = \frac{2\gamma}{r_p} \approx 7\,\mathrm{MPa} \ldots 28\,\mathrm{MPa} \tag{2.21}$$

  This should be sufficient to isolate an embolized conduit segment from its intact neighbours.

2.4.2.2 Narrow vs. wide conduits

The water transport relies on a network of interconnected conduit elements. The more primitive gymnosperm groups (the Ginkgophyta [Early Permian, 280 Ma], Cycadophyta [Early Permian, 280 Ma] and Pinophyta [Upper Carboniferous, 310 Ma], see [47] and [70]) employ just one conduit type, the tracheids, with typical radii of $5\,\mu\mathrm{m} \ldots 25\,\mu\mathrm{m}$.

Evolutionary younger are the fourth gymnosperm division (the Gnetophyta [Early Cretaceous, 140 Ma]) and the angiosperms [Early Cretaceous, 140 Ma]. Both of them — and

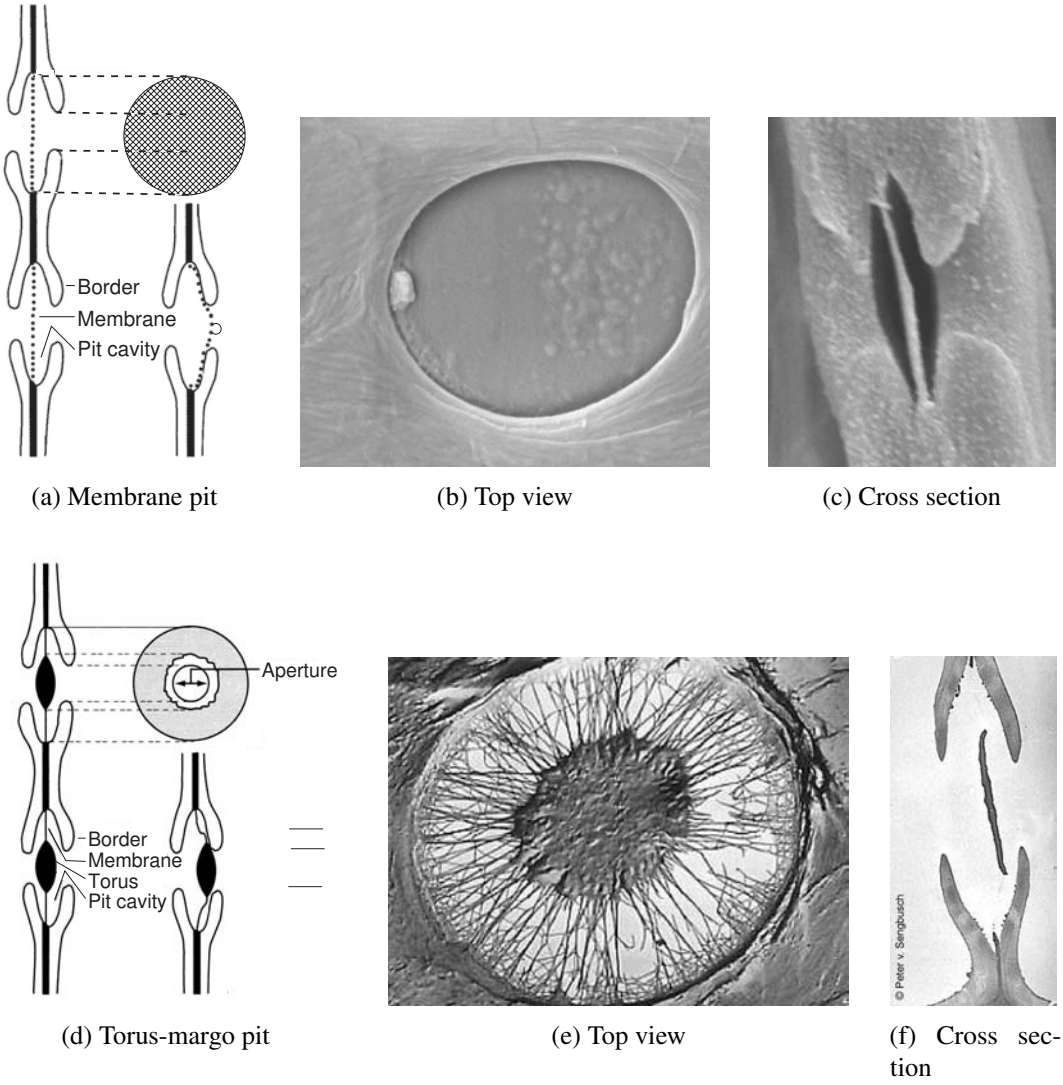

(a) Membrane pit (b) Top view (c) Cross section

(d) Torus-margo pit (e) Top view (f) Cross section

Figure 2.13: Differences and similarities between membrane pits (a,b,c) and torus-margo pits (d,e,f). The membranes in membrane pits possess many tiny pores through which the xylem water flows. During embolism, strongly curved gas/water interfaces develop in these pores. In torus-margo pits the water flows through the permeable and elastic margo. During embolism, the flowing water pushes the impermeable torus against the pit opening closing effectively the aperture. (Illustrations: (a) and (d) are from [24], (b) and (c) are by A. Roth-Nebelsick, Tübingen, (e) and (f) by Peter v. Sengbusch, Hamburg.)

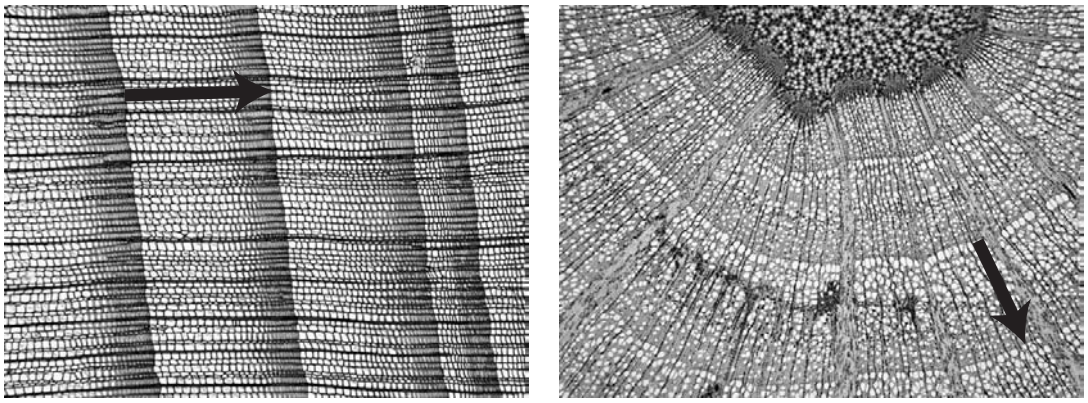

(a) *Abies alba* (b) *Fagus silvatica*

Figure 2.14: Transverse sections of the xylem of *Abies alba* and *Fagus silvatica*. Arrows denote annual rings and point from earlywood to latewood.
(a) *Abies alba*, a gymnosperm, has only narrow conduits (tracheids). The left (lighter) part of each annual ring is composed of earlywood tracheids, the right (darker) part consists of latewood tracheids which are thinner and have thicker walls than the earlywood.
(b) The xylem of *Fagus silvatica*, an angiosperm, is built up from narrow and wide vessel elements. The earlywood consists mostly of wide and only few narrow vessels. During the growth season the number of wide vessels decreases in favour of narrow vessels which make up most of the latewood. (Photographs by H. Reichenauer, Mikroskopische Gesellschaft Wien.)

also a few non-seed plants like *Pteridium* — developed another conduit type, the vessels, which are typically much wider than the tracheids, with radii in the range $25\,\mu\text{m} \ldots 250\,\mu\text{m}$. One reason (among others) for developing vessels is probably a compromise between (i) economising building material and (ii) security of water supply.

(i) The Law of Hagen-Poiseuille predicts for a viscous fluid flowing through a tube of length L that the volume flow rate Q is proportional to the fourth power of the tube radius r

$$Q = \frac{\pi r^4}{8 \eta L} \Delta p \tag{2.22}$$

(η: dynamic fluid viscosity, Δp: pressure difference between the ends of the tube). Thus, assuming a constant "driving pressure" Δp, the ratio of the flow rates through a tracheid of radius $r_{tracheid}$ and a vessel of radius $r_{vessel} = k\, r_{tracheid}$ is

$$\frac{Q_{vessel}}{Q_{tracheid}} = k^4 \tag{2.23}$$

For most angiosperms, $k = 6 \ldots 7$, hence $Q_{vessel}/Q_{tracheid} \approx 1300 \ldots 2500$, a tremendous gain of flow rate! On the other hand, there are costs: a wider tube needs more building material. If the tube's wall is thin compared to its radius, the volume of its building material is $V^{mat} \approx 2\pi r\, t\, L$ (t: thickness of tube wall, L: length of tube). If we require the strength of the tube to be independent from its radius — which is a reasonable first approximation — the wall thickness t must scale according to $t = \alpha r$

with α = const. (see [68]), hence $V^{mat} = 2\pi\alpha L\, r^2$, and

$$\frac{V^{mat}_{vessel}}{V^{mat}_{tracheid}} = k^2 \tag{2.24}$$

Thus, for $k = 6 \ldots 7$, the vessel/tracheid ratio of the cost of building material is (in terms of volume) $V^{mat}_{vessel}/V^{mat}_{tracheid} \approx 36 \ldots 49$. Division of equations (2.23) and (2.24) implies that the "gain/cost" ratios of vessels and tracheids are related as

$$\frac{Q_{vessel}}{V^{mat}_{vessel}} = k^2\, \frac{Q_{tracheid}}{V^{mat}_{tracheid}} \tag{2.25}$$

with $k = r_{vessel}/r_{tracheid}$. Now we calculate how many tracheids can be replaced by one vessel, if the water is to flow at the same rate. Denoting by n the number of tracheids equivalent to one vessel we start with

$$Q_{vessel} = n\, Q_{tracheid} \tag{2.26}$$

compare with equation (2.23) and find:

$$n = k^4 \tag{2.27}$$

The meaning of this is: transporting water at a fixed flow rate Q by one vessel instead of using k^4 tracheids, is k^2 times cheaper (in terms of building material). Or, applied to the above cited typical angiosperm values for $k = r_{vessel}/r_{tracheid} \approx 6 \ldots 7$: using one vessel instead of $1300 \ldots 2500$ tracheids, is $36 \ldots 49$ times cheaper (see also [31])!

(ii) The obvious question is now: why did the angiosperms not give up investing in narrow conduits (comparable to tracheids, with respect to diameter)? One (partial) answer comes from biomechanis: The gymnosperm's tracheids serve not only as water conduits, they provide also mechanical strength. This important requirement sets an upper limit to their radii. In angiosperm wood the task of providing mechanical strength has been shifted to an independent anatomical structure, the fibres. Therefore, angiosperm vessels may become much wider than gymnosperm tracheids.

But security of water supply may also be an important factor for keeping a certain proportion of narrow conduits: There is reason to believe that the most vulnerable parts of a conduit are the pit membranes (see also section 2.4.2.1). If one assumes that (a) each pit membrane fails (e.g. by giving way to air seeding) during a given time interval with probability w, and that (b) the pits are distributed over the pit surface at a uniform (area based) density μ, then the total risk of failure of a conduit of radius r amounts to

$$W = w\, \mu\, 2\pi L\, r \tag{2.28}$$

Writing down this equation once for narrow (with $r = r_{narrow}$) and once for wide vessels (with $r = r_{wide}$), dividing both versions and inserting $r_{wide} = k\, r_{narrow}$ leads to

$$W_{wide} = k\ W_{narrow} \tag{2.29}$$

that is, embolism in a wide vessel is more probable by a factor $k = 6 \ldots 7$, than in a narrow vessel. This result suggests that the angiosperms are wise to rely not exclusively on vessels with wide lumina although this would be cheaper (in terms of building material) and more efficient (in terms of flow rate). Keeping a minimum number of narrow vessels should be interpreted as a precaution, to be on the safe side if the wide vessels fail.

2.4.3 Restoration of conductivity

Furthermore, plants have developed repair mechanisms which are able (i) to remove the air introduced by the air seeding process, and, (ii) to reestablish the conductivity of an embolised conduit segment. This will be described in detail below and in the publication presented as section 5.1.

2.4.3.1 Repair model for conduits with membrane pits

In the following, we provide a brief summary of the repair model for membrane pits. According to the idea of Holbrook and Zwieniecki ([33]), a "reverse meniscus" can develop between a gas bubble in the pit chamber and the water in an embolized conduit if the sum of the contact angle θ and pit chamber angle α is greater than 90° (see Figure 2.15). The interface then exerts pressure onto the water and not onto the gas and is probably able to hydraulically isolate the embolized vessels. Whether this isolating effect is physically feasible was considered by Konrad and Roth-Nebelsick ([38]) by analyzing the dynamics of the embolizing bubbles in the conduit lumen (lumen bubbles, "LB" in the following formulae) and the bubbles within the pit chamber (pit bubbles, "PB" in the following formulae).

In short, the basic results are as follows (see [38] for further details). Figure 2.15 depicts schematically the situation after a vessel has failed: the liquid pressure within the vessel has attained a positive value $p_s > 0$, one or more lumen bubbles have developed and pit bubbles (pit bubble, gas bubbles sucked into the pits) isolate the failed vessel hydraulically from its intact neighbours, which still maintain a negative value $p_i < 0$ of the xylem sap pressure. Because the gas phase resides in a lumen bubble on the concave side of the liquid/gas-interface, in a pit bubble, however, on the convex side, different versions of the Young-Laplace-Equation result for both bubble types:

$$p_{LB} = p_s + \frac{2\gamma}{R_{LB}} > p_s \tag{2.30}$$

$$p_{PB} = p_s - \frac{2\gamma}{R} < p_s \tag{2.31}$$

$R_{LB} > 0$ and $R > 0$ denote the radii of curvature of the liquid/gas-interfaces (which coincides in the case of the lumen bubble with the bubble radius) and γ denotes the surface tension of an air/xylem-sap interface.

Because the molecules of a perfect gas exchange (by definition) no attractive forces, we can state $p_{LB} > 0$ and $p_{PB} > 0$. Together with equations (2.30) and (2.31) this leads to

$$p_{LB} > p_s > p_{PB} > 0 \tag{2.32}$$

If there has been a massive influx of air (for example, after local damage of the xylem) the following assumptions seem to be justified: (i) the pressure p_s within the embolized vessel is roughly the same as the atmospheric pressure p_{atm},

$$p_s \approx p_{atm} \tag{2.33}$$

and, (ii) the fictitious pressure C_b/k_H of air molecules dissolved within the xylem sap of the vessel adjacent to the embolized one is smaller as or at most approximately equal to the

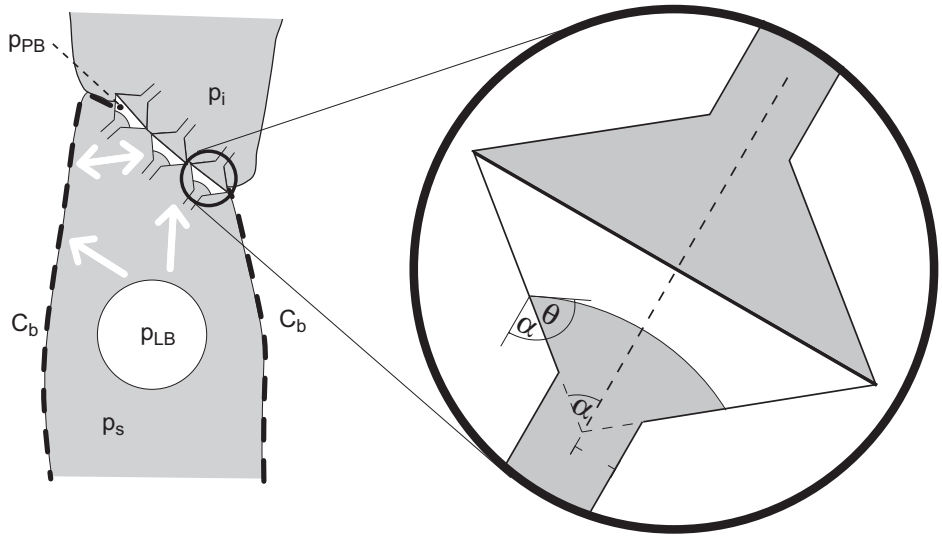

Figure 2.15: Left: Schematic representation of an embolized vessel (lower part of figure) filled with xylem sap under positive pressure p_s and an intact vessel (upper part of figure) filled with liquid under tension (negative pressure p_i). Gaseous contents of lumen (pressure p_{LB}) and pits (pressure p_{PB}) are in white colour. White arrows symbolize diffusional currents between the lumen bubble, the pit bubbles and the adjacent conduits. The broken line along the border of the vessel indicates a constant air concentration C_b in the xylem sap of the adjacent conduits.
Right: Schematic representation of pit valve mechanism. The pit connection between two conduits is shown in longitudinal section. Lower conduit: embolized, positive pressure. Upper conduit: functional, water in it under tension. Black area: porous pit membrane. White area: gas. Grey-shaded area: water. α: half-opening angle of pit chamber. θ: contact angle between pit wall and xylem sap.

atmospheric pressure p_{atm} (C_b denotes the concentration of dissolved air molecules, k_H is Henry's constant),

$$\frac{C_b}{k_H} \lesssim p_{atm} \tag{2.34}$$

From equations (2.32), (2.33) and (2.34) we conclude that either of the following chains of inequalities holds:

$$p_{LB} \gtrsim \frac{C_b}{k_H} \gtrsim p_{PB} \tag{2.35}$$

$$p_{LB} \gtrsim p_{PB} \gtrsim \frac{C_b}{k_H} \tag{2.36}$$

These pressure differences are the driving forces for the following diffusional currents (white arrows in Figure 2.15): (i) from the lumen bubble to the vessel border (because of $p_{LB} \gtrsim C_b/k_H$), (ii) from the lumen bubble to the pit bubbles (because of $p_{LB} > p_{PB}$), and, (iii) from the vessel border to the pit bubbles, (if $C_b/k_H \gtrsim p_{PB}$) or into the opposite direction (if $p_{PB} \gtrsim C_b/k_H$). In either case, the lumen bubble loses molecules (essentially to the vessel border) and its radius R_{LB} decreases, whereupon p_{LB} increases (via equation (2.30)), thus accelerating the process of emptying the lumen bubble. Since the pit bubbles are supplied

with molecules by diffusional currents from the lumen bubble (and perhaps from the vessel border), they do not dissolve and maintain hydraulic isolation of the embolized vessel until the lumen bubble completely disappears. Then, the “supply current" from the lumen bubble to the pit bubbles necessarily ceases and the pit bubbles also dissolve, partially into the neighboring intact vessel and partially into the vessel being repaired. As soon as the pit bubbles have dissolved, the water molecules in the intact and repaired vessels come into contact and they exchange attractive forces. Thus, the cohesion between adjacent water molecules and the tension gradient of the water potential reestablish themselves. There is theoretical evidence [38] that this last, critical stage of the refill process leads in most cases *not* to new embolism.

During various stages of this repair process, the pit bubbles suffer invariably from mechanical perturbations. Because the pit bubbles' existence rests on the assumption of an equilibrium between expanding and contracting pressures, it is of significance to investigate their behaviour under perturbations, or, in other words, the stability of the equilibrium they represent. This has been discussed in the paper presented as section 5.2.

2.4.3.2 Repair model for conduits with torus-margo pits

As has been described in section 2.4.2, torus-margo pits show a valve-like behaviour in that they close when the water flow rate Q exceeds a critical flow rate Q_{crit}. The water pressure in the embolising conduit element has by then increased considerably. If order to describe the behaviour of the inflating bubble by the methods explained in section 2.3.2 it has to be taken into account that water pressure p_s depends (i) on the (instantaneous) bubble radius R and (ii) on the elasticity of the conduit walls which have to sustain (and are deformed by) the water pressure difference between adjacent embolised and intact conduits. (They should bulge towards the latter.) This is done by adding appropriate terms to equation (2.9). An analysis similar to that in section 2.3.2 reveals that the additional terms produce a third equilibrium radius (the expressions R_{stab} and R_{inst} given in (2.12) are no longer exactly but still approximately valid). It represents stable equilibrium without any conditions on initial radii, initial air molecules content etc. of the embryonic bubble (see publication presented as section 5.3).

3 Gas exchange between leaves and atmosphere

By some reason, plants never developed membranes which are permeable for CO_2-molecules but not for H_2O-molecules. Hence, both molecular species may diffuse through the openings in the leaf surface ("stomata") which connect the interior of the leaf with the atmosphere (see Figure 3.1). Nonetheless, stomata seem to exist predominantly to supply the assimilation machinery within the leaf with sufficient CO_2, the raw material of photosynthesis, apart from water and sunlight. But transpiration is not entirely unwelcome: (i) It serves to cool leaf surfaces which might otherwise be damaged by overheating. (ii) The process of photosynthesis consumes water which is brought up into the crown of the tree by transpiration. (iii) Nutrients are transported upwards together with the transpiration stream. In plant physiology, one is interested to obtain quantitative values for transpiration rate and assimilation rate because from them conclusions can be drawn with respect to the ecophysiological performance of a given species.

Extant plants can always be put into a greenhouse which allows to study a plants' reaction on the variation of environmental variables like humidity, CO_2-concentration, temperature, wind or insolation. With fossil and (meanwhile) extinct plants this direct, experimental, approach does not work. If, however, the leaf anatomy is known from fossil findings, the transpiration rate can be reconstructed with the help of the laws of diffusion from the fossilised evidence. The assimilation rate can be reconstructed, too, if a "mechanistic" model of photosynthesis is coupled with the diffusion model.

Mechanistic models rely on principles of physics which are universal in time and space and on biochemical pathways which change very slowly, compared with a plant species' life-span. They connect parameters describing leaf anatomy, the mechanism of photosynthesis and environmental conditions including stomatal density ν (= number of stomata per leaf area) and (palaeo)atmospheric CO_2-concentration C_a. Thus, it becomes feasible to derive the relation between ν and C_a from this mathematical framework in terms of a mathematical function.

The derivation of a mechanistic ν/C_a-relation is motivated by the observation (see [71]) that — comparing only leaves from the same species — stomatal density can be used as a proxy for the temporal development of atmospheric CO_2. From the fossil record it is known that the stomatal density of leaves of a given species changes according to atmospheric CO_2-level. It is intuitively clear that lower atmospheric CO_2 requires more leaf openings if the tree's "hunger" for assimilation products remains approximately constant. If, on the other hand, atmospheric CO_2 increases, a leaf can do with less stomata and — in order to reduce "construction expenses" — the plant equips new leaves with a reduced number of stomata. This line of thought will be followed later on by applying an optimisation scheme to the assimilation and transpiration rates of a plant.

Mechanistic models surpass the purely phenomenological transfer functions obtained

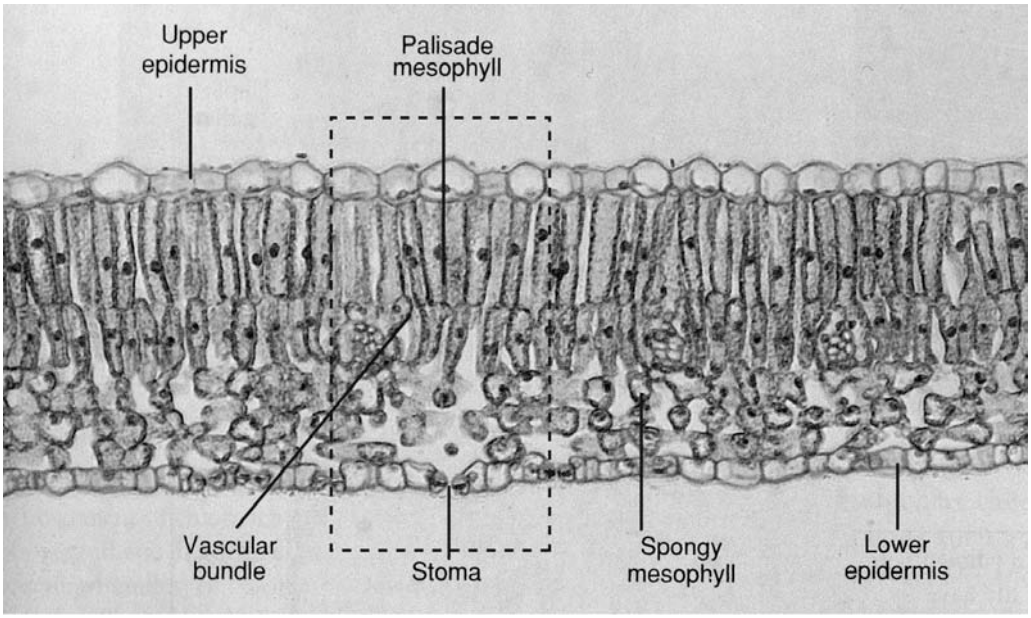

Figure 3.1: Cross section through a leaf of *Syringa vulgaris*. See also Figure 3.2. (Photograph taken from [47].)

from v/C_a-relations of extant plants in predictive power because (i) they supply information from physics and chemistry not available from the fossil record, and, (ii) they exploit causal connections between v and C_a. Moreover, mechanistic models allow (iii) to explore systematically the sensitivity of the v/C_a-relation against variation of parameters like temperature or leaf morphology. With phenomenologically obtained transfer functions, this is not possible.

3.1 Diffusion of water vapour and carbon dioxide in plant leaves

3.1.1 Fick's laws

The movement of water vapour and carbon dioxide in plants is governed by the process of diffusion, i.e. the tendency of gases and fluids to equalize differences in molecular concentration by establishing a molecular current from areas of high to areas of low concentration. Fick's first law

$$\mathbf{j} = -S \operatorname{grad} c \tag{3.1}$$

states that the flux $\mathbf{j}$ (number of molecules diffusing in time through area normal to the direction of movement) should be proportional to (i) the concentration gradient and (ii) an effective conductance S which depends on the properties of the diffusing molecules and on the medium through which they propagate.

Note: In what follows, c stands either for the concentration w of water vapour or the concentration C of carbon dioxide.

The Diffusion Equation (also known as Fick's second law) is derived from applying the

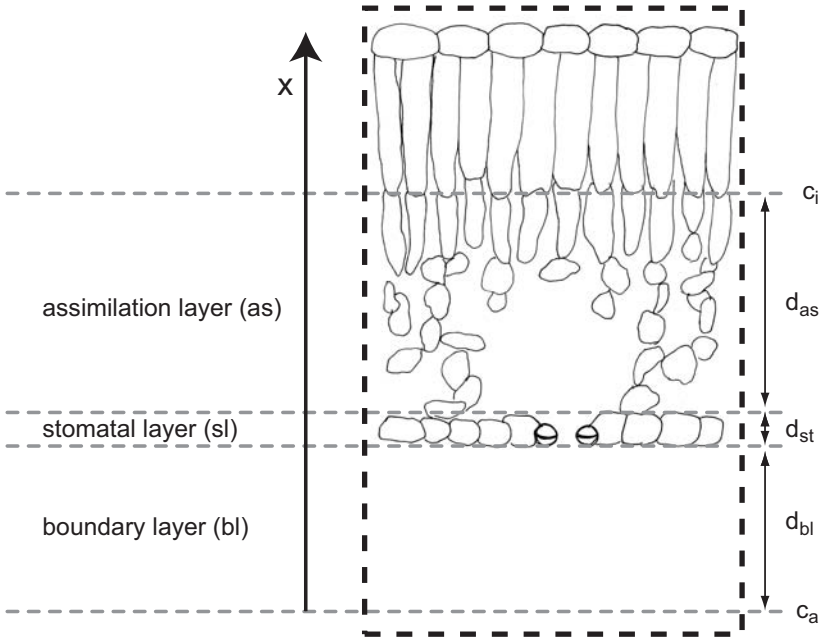

Figure 3.2: Schematic cross section through a leaf. Detail of Figure 3.1. (Drawing by Birgit Binder, Tübingen.)

principle of mass conservation to Fick's first law. It reads

$$\Sigma = \frac{\partial c}{\partial t} + \operatorname{div}(S \operatorname{grad} c) \tag{3.2}$$

If the source (or sink) term $\Sigma = \Sigma(x, y, z, t, c)$ is independent of or at most a linear function of c and if the effective conductance $S = S(x, y, z)$ and appropriate boundary conditions for c are prescribed, the diffusion equation (3.2) has exactly one solution for the concentration $c = c(x, y, z, t)$ of water vapour or carbon dioxide. Once $c = c(x, y, z, t)$ is calculated the flux $\mathbf{j}(x, y, z, t)$ follows from (3.1).

3.1.2 Approximations

It is impossible to solve (3.2) in all generality for realistic conditions, because the complex network of voids and channels which form the intercellular air space (see Figures 3.2 and 3.1), the principal gateway for carbon dioxide and water vapour, implies very complex boundary conditions for (3.2). If, however, we claim that c and $\mathbf{j}$ shall be correct only down to dimensions of a few diameters of a typical cell, we can employ approximations which lead to symmetries that allow for drastic simplifications in (3.2) and (3.1). In that case, we can apply (i) the porous medium approach and assume that (ii) the effective conductance S remains constant within the functionally different tissue layers of a plant leaf. We may furthermore assume (iii) stationary conditions.

(i) The **Porous Medium Approximation** is widely used (but seldom stated explicitly) as a tool in Applied Geology in order to describe the flow of water (via Darcy's law) or the transport processes of contaminants in soils and aquifers (via Fick's laws) (see,

for instance, [30]). It was developed by engineers who deal with industrial processes which take place in porous media ([2]) and later on applied to plant leaf tissue (see [54] and the review [53] and literature cited therein).

The central idea of the porous medium approach is the replacement of the discontinuous arrangement of cells and voids inside the real plant by a fictitious tissue whose continuous material properties are partly attributable to the cells and partly to the voids of the real plant. This is achieved by an averaging process which reduces the complex geometrical details of the cell and void architecture to just two quantities, the porosity n and the tortuosity τ, defined by

$$n := \frac{V_p}{V} \qquad \text{and} \qquad \tau := \frac{l_e}{l} \tag{3.3}$$

V_p and V are pore volume resp. total volume of a volume element. l_e denotes the length of the actual path which a molecule has to follow in order to move from one given point to another and l denotes the (geometrically) shortest distance between these same points. The effective conductance S is defined in terms of n, τ and the free air coefficient of diffusion D as

$$S := D\,\frac{n}{\tau^2} \tag{3.4}$$

Notice, that $D = D_{\mathrm{CO_2}}$ or $D = D_{\mathrm{H_2O}}$, depending on whether diffusion of CO_2- or H_2O-molecules is treated.

(ii) **Constancy of effective conductance:** Plant leaves consist of several tissue layers (see stomatal and assimilation layers in Figure 3.2). Due to the anatomical structure of leaves porosity n and tortuosity τ change more or less abruptly between adjacent layers, but vary only slightly within the individual layers. The effective conductance, defined by $S := D\,n/\tau^2$, should behave similarly, i.e. S = const. *within* a given layer.

(iii) We focus on **stationary** situations, i.e. we assume that the term $\partial c/\partial t$ on the righthand side of equation (3.2) is much smaller than and can be neglected against the term $\operatorname{div}(S\,\operatorname{grad} c)$. This is true if molecules diffusing from a region of high towards a region of low concentration do not experience an appreciable change in the "concentration pattern" around them during their journey.

Water vapour molecules, for example, need roughly a time $t \approx l^2/(4\,D^{air}_{\mathrm{H_2O}}) = 0.01\,\mathrm{s}$ to cover the distance $l \approx 1\,\mathrm{mm}$ from the interior of a leaf to free atmosphere. Under normal weather conditions one can assume that atmospheric humidity needs a longer time to change appreciably (within the plant it is constant anyway). Since carbon dioxide molecules are heavier than water molecules, they move slightly slower in air than water vapour molecules, they need for the same distance $t \approx l^2/(4\,D^{air}_{\mathrm{CO_2}}) = 0.017\,\mathrm{s}$. Atmospheric CO_2-content is practically constant during this time-span, and CO_2-concentration at the assimilating sites, too. Even if its getting dark, the process of assimilation takes much longer than 0.017 s to decrease considerably.

Upon application of these assumptions the differential equation (3.2) simplifies to

$$\Sigma = S\left(\frac{\partial^2 c}{\partial x^2} + \frac{\partial^2 c}{\partial y^2} + \frac{\partial^2 c}{\partial z^2}\right) \tag{3.5}$$

The source (or sink) term Σ (if present) and the concentration c are functions of the coordinates (x, y, z). Leaves are flat objects whose lateral dimensions (a few centimeters) are about a factor 10^4 greater than stomatal radii (a few micrometers). Together with the layered structure of leaves this implies:

(i) The general direction of the diffusional flux is perpendicular to the leaf plane, i.e. parallel to the x-axis, if we orient the coordinate system such that the y- and z-axes are parallel to the leaf plane (we ignore possible small deviations from this general direction near the leaf edge).

(ii) In the coordinate system defined in (i) all quantities appearing in equations (3.5) and (3.1) depend only on the coordinate x, but not on y or z.

Then the three-dimensional partial differential equation (3.5) reduces to a one-dimensional ordinary differential equation for $c(x)$

$$\Sigma(x) = S \, \frac{d^2c(x)}{dx^2} \tag{3.6}$$

which must be solved separately for each of the three layers depicted in Figure 3.2 (assimilation layer (as), stomatal layer (sl) and boundary layer (bl)). If the source (or sink) term $\Sigma(x)$ is not too involved this can be done by direct integration. Fick's first law (3.1) simplifies in a similar way

$$\mathbf{j}(x) = -S \, \frac{dc}{dx}(x) \tag{3.7}$$

where the flux $\mathbf{j}$ is directed parallel to the x-axis.

3.1.3 Temperature dependance of the coefficients of diffusion

The coefficients of diffusion depend on T.

$$D_{\mathrm{CO_2}} = \left(\frac{T}{273.15}\right)^{1.8} \times 1.33 \times 10^{-5} \, \frac{\mathrm{m}^2}{\mathrm{s}} \tag{3.8}$$

$$D_{\mathrm{H_2O}} = \left(\frac{T}{273.15}\right)^{1.8} \times 2.13 \times 10^{-5} \, \frac{\mathrm{m}^2}{\mathrm{s}} \tag{3.9}$$

are (see [50]) good approximations for the range $T = 273.15\,\mathrm{K} \ldots 313.15\,\mathrm{K}$ (resp. $0\,^\circ\mathrm{C} \ldots 40\,^\circ\mathrm{C}$).

3.1.4 Sources and sinks

Within boundary layer and stomatal layer we may assume $\Sigma(x) = 0$, both for CO_2- and H_2O-molecules. With respect to the assimilation layer two different approaches are feasible:

(i) The cells from which the liquid water vapourises are — at least on the level of the porous medium approximation — uniformly distributed throughout the assimilation layer. The same holds for the carbon dioxide assimilating cells within the tissue of the assimilation layer. Thus, $\Sigma(x) \neq 0$ both for CO_2 and H_2O.

(ii) The upper surface of the spongy mesophyll (the broken line, denoted c_i in Figure 3.2, see also Figure 3.1) serves as (idealised) source of water vapour and as sink for carbon dioxide molecules. Within the assimilation layer (as depicted in Figure 3.2) holds $\Sigma(x) = 0$. Speaking in mathematical terms: the sinks and sources which are in (i) *within* the region where equation (3.6) with $\Sigma(x) \neq 0$ is valid, are now shifted to the boundary of this region and formulated as boundary conditions to be imposed on the solution of (3.6) with $\Sigma(x) = 0$.

The second approach may appear less accurate than the first. It allows, however, mathematical simplifications which are nearly indispensable in the paper presented as section 5.6.

3.1.5 One-dimensional, source-free solutions of the diffusion equation with translational symmetries

In the publication presented as section 5.6 it is assumed (see Figure 3.2) that *within* the three compartments assimilation layer (as), stomatal layer (sl) and boundary layer (bl) neither sources nor sinks of water vapour or carbon dioxide exist, hence $\Sigma(x) = 0$. In this case equation (3.6) becomes *very* simple

$$0 = S \, \frac{d^2 c}{dx^2}(x) \tag{3.10}$$

with the readily obtained solutions

$$c_{as}(x) = a_{as}\, x + b_{as} \qquad c_{st}(x) = a_{st}\, x + b_{st} \qquad c_{bl}(x) = a_{bl}\, x + b_{bl} \tag{3.11}$$

and, from equation (3.7),

$$j_{as}(x) = -S_{as}\, a_{as} \qquad j_{st}(x) = -S_{st}\, a_{st} \qquad j_{bl}(x) = -S_{bl}\, a_{bl} \tag{3.12}$$

where it is understood that positive fluxes j_k ($k = as, sl, bl$) flow parallel, negative fluxes antiparallel to the x-axis (c.f. Figure 3.2). The a_k and b_k are arbitrary constants. Their values are calculated from requiring (i) that the c_k and j_k (from equations (3.11) and (3.12)) are continuous at the planes separating adjacent boundary layers, and, (ii) that c_{bl} and c_{as} attain the values c_a and c_i, respectively, at the lower and upper boundary of the region depicted in Figure 3.2.

The effective conductances S_k differ from layer to layer. They are defined in analogy to (3.4) as

$$S_{as} := D \, \frac{n_{as}}{{\tau_{as}}^2} \tag{3.13}$$

and similar expressions for for (sl) and (bl). D denotes either D_{H_2O} or D_{CO_2}.

Applying the continuity conditions we find (i) that the flux does *not* depend explicitly on x, and, (ii) that $j_{as} = j_{st} = j_{bl} =: j$. It is given as

$$j = \frac{D \; (c_i - c_a)}{\left(\dfrac{d_{bl}{\tau_{bl}}^2}{n_{bl}} + \dfrac{d_{st}{\tau_{st}}^2}{n_{st}} + \dfrac{d_{as}{\tau_{as}}^2}{n_{as}} \right)} \tag{3.14}$$

whose righthand side is composed of three factors: (i) the "driving force" (i.e. the concentration difference) $c_i - c_a$, (ii) the properties of the diffusing molecules, contained in D, the coefficient of diffusion, and, (iii) the denominator which is built up from the anatomical properties of the leaf and the atmospheric boundary layer.

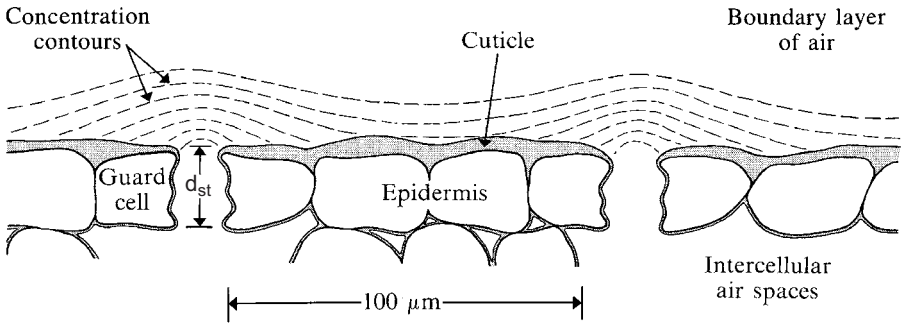

Figure 3.3: A typical plant epidermis. The broken lines depict the concentration contours of water vapour and carbon dioxide. (Drawing from [50].)

The quantities in (iii) can be specified more explicitly (c.f. Figures 3.2 and 3.3):

- **Boundary layer:** Obviously, porosity and tortuosity attain the very simple values

$$n_{bl} = 1 \qquad \text{and} \qquad \tau_{bl} = 1 \tag{3.15}$$

  d_{bl} depends (see [50]) on the wind velocity v_{wind} and a typical leaf length l according to the empirical formula (m and s denote the units meter and second, respectively)

$$d_{bl} = 4 \times 10^{-3} \, \frac{\mathrm{m}}{\sqrt{s}} \, \sqrt{\frac{l}{v_{wind}}} \tag{3.16}$$

- **Stomatal layer:** The porosity of the stomatal layer can be expressed in terms of the cross-sectional area of a stoma a_{st} and the stomatal density ν as

$$n_{st} = a_{st} \, \nu \tag{3.17}$$

  Since the stomata are relativily straight openings without bends we find for their tortuosity

$$\tau_{st} = 1 \tag{3.18}$$

  d_{st} is a combination of the geometrical thickness d_{st}^{geom} and a correction $\sqrt{a_{st}/\pi}$ which is due to the fact that the surfaces of constant CO_2 and H_2O concentration bulge out from the stomata into boundary layer and intercellular airspace (see [50]). Thus,

$$d_{st} = d_{st}^{geom} + \sqrt{a_{st}/\pi} \tag{3.19}$$

- **Assimilation layer:** Values for porosity, tortuosity and thickness of the layer should be obtained by measurements from specimen. Typical values are of the order of $n_{as} \approx 0.35$, $\tau_{as} \approx 1.571$ and $d_{as} \approx 200\,\mu\mathrm{m}$.

Insertion of the universally applicable expressions (3.15), (3.17) and (3.18) into equation (3.14) results in a somewhat simplified, intermediate version of (3.14)

$$j = \frac{\nu a_{st}\, D\ (c_a - c_i)}{\left[d_{bl} + d_{as}\frac{\tau_{as}^2}{n_{as}}\right]\nu a_{st} + d_{st}} \tag{3.20}$$

Writing down expression (3.20) separately for water vapour ($c_i = w_i$, $c_a = w_a$ and $D = D_{H_2O}$) and carbon dioxide ($c_i = C_i$, $c_a = C_a$ and $D = D_{CO_2}$) results in

$$j_{H_2O} = \frac{\nu a_{st}\, D_{H_2O}}{\left[d_{bl} + d_{as}\frac{\tau_{as}^2}{n_{as}}\right]\nu a_{st} + d_{st}} \times (w_a - w_i) \tag{3.21}$$

and

$$j_{CO_2} = \frac{\nu a_{st}\, D_{CO_2}}{\left[d_{bl} + d_{as}\frac{\tau_{as}^2}{n_{as}}\right]\nu a_{st} + d_{st}} \times (C_a - C_i) \tag{3.22}$$

where d_{bl} and d_{st} are as given in (3.16) and (3.19), respectively. To keep notation simple we define the first factor on the right hand side of (3.22) as the total conductance with respect to CO_2

$$g := \frac{\nu a_{st}\, D_{CO_2}}{\left[d_{bl} + d_{as}\frac{\tau_{as}^2}{n_{as}}\right]\nu a_{st} + d_{st}} \tag{3.23}$$

Employing the definition $a := D_{H_2O}/D_{CO_2}$ the total conductance with respect to H_2O (i.e. the first factor on the right hand side of (3.21)) becomes ag.

Since we restrict our model to stationary conditions all carbon dioxide molecules entering the plant become eventually assimilated, hence $j_{CO_2} = A$ where A denotes the assimilation rate (= number of assimilated molecules per leaf surface area and time). Equation (3.22) can now be rewritten in the more compact form

$$A = g\ (C_a - C_i) \tag{3.24}$$

Turning to equation (3.21) we note two facts: (i) Stationary conditions imply $-j_{H_2O} = E$, with E representing the transpiration rate (= number of transpired molecules per leaf surface area and time). The minus sign in front of j_{H_2O} is due to the orientation of the coordinate system (see Figure 3.2): Ingoing fluxes (like j_{CO_2}, if assimilation dominates respiration) are counted as positive, outgoing fluxes (like j_{H_2O}) as negative. The minus sign ensures that E attains positive values. (ii) Because w_i is defined as the water vapour concentration around the transpiring mesophyll cells it equals the saturation value of water vapour concentration in air (equivalent to 100 % relative humidity). This depends on temperature T. The Clausius-Clapeyron equation provides an approximate (but for our purposes good enough) expression for $w_i^{sat}(T)$ (see [56], [50])

$$w_i^{sat} := \frac{u}{T}\exp\left(-\frac{v}{T}\right) \tag{3.25}$$

with $u = 2.035 \times 10^{10}\,\mathrm{mol/m^3}$ and $v = 5306$ (T in Kelvin). Inserting the definitions (3.23) and $a = D_{H_2O}/D_{CO_2}$ and the equation $w_i = w_i^{sat}$ into (3.21) we find

$$E = ag\ (w_i^{sat} - w_a) \tag{3.26}$$

In view of (3.16) we may state: if the anatomic parameters and the environmental parameters T and v_{wind} are prescribed, equation (3.26) represents a functional relation between transpiration rate E and atmospheric water vapour concentration w_a. That is, if either of E or w_a is given the other one can be calculated from (3.26).

In contrast to (3.26), expression (3.24) represents only an intermediate result: it relates — in analogy to (3.26) — A to C_i. C_i, however, does not attain a fixed value comparable to w_i^{sat}. It is rather coupled to A by a second relation expressing the intensity of photosynthesis. This will be further discussed below (see section 3.2).

3.1.6 Axisymmetric solutions with sources

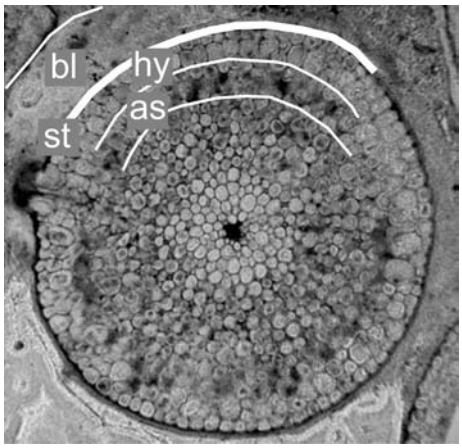

Figure 3.4: Cross-section through an axis of *Rhynia gwynne-vaughanii* and schematic representation of the relevant layers in the tissue. Only the tissue layers which are relevant for the model are indicated. The radius of the axis amounts to 1.4 mm. (Photograph: Hans Steur, `http://www.xs4all.nl/~steurh`.)

The rhyniophytic plants from the Lower Devonian (see Figure 2.2) which are the subjects of the publications presented as sections 5.4 and 5.5 have no leaves, they consist simply of aerial axes which function like the cylindrical photosynthetic stems of extant *Equisetum*, *Ephedra* or *Casuarina* or the flat leaves of modern angiosperms. Therefore, they possess (see Figure 3.4) an axial symmetry — other than most leaves of modern angiosperms with their translational symmetries with respect to the leaf surface. The equations resulting from Fick's Laws must be modified accordingly. Rhyniophytic plants possess also an additional layer, the hypodermal layer, containing channels which connect the stomata with the assimilating tissue (see Figure 3.4. Moreover, the approach in these publications followed the first of the alternatives outlined in section 3.1.5: It assumes that carbon dioxide sinks (i.e. $\Sigma \neq 0$) are uniformly distributed throughout the assimilation layer.

3.2 Assimilation of carbon dioxide within plant leaves

We use the Farquhar model of assimilation (see [25], [27]) for C_3-plants which gives the assimilation rate A in terms of C_i (the carbon dioxide concentration inside the leaf, see Figure 3.2), the irradiance I, and various other variables:

$$A = \left(1 - \frac{\Gamma}{C_i}\right) \min\{W_c, W_j\} - R_d \tag{3.27}$$

with

$$W_c := V_{max} \frac{C_i}{C_i + K_c \left(1 + \frac{p_o}{K_o}\right)}$$

$$W_j := \left(\frac{2}{9} J\right) \frac{C_i}{C_i + \frac{7}{3}\Gamma}$$

where

$$J := \frac{Q_2 + J_{max} - \sqrt{(Q_2 + J_{max})^2 - 4\,\Theta_{PSII}\,Q_2\,J_{max}}}{2\,\Theta_{PSII}}$$

and

$$Q_2 := Q\,\alpha_l\,\Phi_{PSII,max}\,\beta \tag{3.28}$$

The expression $\min\{W_c, W_j\}$ denotes the smaller of W_c and W_j for given values of C_i and J. The variables and parameters used in (3.27) are defined in Table 3.1. Defining

$$q = \begin{cases} V_{max} & \text{if } W_c < W_j \\ \frac{2}{9} J & \text{if } W_c > W_j \end{cases} \tag{3.29}$$

and

$$K = \begin{cases} K_c \left(1 + \frac{p_o}{K_o}\right) & \text{if } W_c < W_j \\ \frac{7}{3}\Gamma & \text{if } W_c > W_j \end{cases} \tag{3.30}$$

expression (3.27) can be written in the more compact form

$$A = q\,\frac{C_i - \Gamma}{C_i + K} - R_d \tag{3.31}$$

Most of the variables defining photosynthesis depend on the leaf temperature T (measured in Kelvin). In order to quantify their temperature dependance we use the parametrisations given by Bernacchi et al. ([8]):

$$\begin{aligned}
J_{max} &= J_{max,25\,^\circ\mathrm{C}} \times \mathrm{e}^{\left(17.57 - \frac{5236.760760}{T}\right)} \times \mu\mathrm{mol/m^2/s} \\
K &= k_{25\,^\circ\mathrm{C}} \times K_c\,(1 + p_o/K_o) \\
K_c &= \mathrm{e}^{\left(38.05 - \frac{9553.420009}{T}\right)} \times \mu\mathrm{mol/mol} \\
K_o &= \mathrm{e}^{\left(20.30 - \frac{4375.593855}{T}\right)} \times \mathrm{mmol/mol} \\
p_o &= 210\,\mathrm{mmol/mol} \\
R_d &= R_{d,25\,^\circ\mathrm{C}} \times \mathrm{e}^{\left(18.72 - \frac{5579.543675}{T}\right)} \times \mu\mathrm{mol/m^2/s} \\
V_{max} &= V_{max,25\,^\circ\mathrm{C}} \times \mathrm{e}^{\left(26.35 - \frac{7857.546634}{T}\right)} \times \mu\mathrm{mol/m^2/s} \\
\Gamma &= \gamma_{25\,^\circ\mathrm{C}} \times \mathrm{e}^{\left(19.02 - \frac{4549.992181}{T}\right)} \times \mu\mathrm{mol/mol} \\
\Theta_{PSII} &= 0.76 + 0.018\,T - 3.7 \times 10^{-4}\,\mathrm{T}^2 \\
\Phi_{PSII,max} &= 0.352 + 0.022\,T - 3.4 \times 10^{-4}\,\mathrm{T}^2
\end{aligned} \tag{3.32}$$

Table 3.1: Parameters defining photosynthesis.

Symbol	Unit	Quantity
A	$\mu mol/m^2/s$	Assimilation rate per leaf area
J	$\mu mol/m^2/s$	Rate of electron transport
J_{max}	$\mu mol/m^2/s$	Maximum rate of electron transport
K_o	mmol/mol	Michaelis-Menten constant of oxygenation
K_c	µmol/mol	Michaelis-Menten constant of carboxylation
p_o	mmol/mol	Partial pressure of oxygen
Q	$\mu mol/m^2/s$	Photosynthetic photon flux density
R_d	$\mu mol/m^2/s$	Mitochondrial respiration rate in the light
V_{max}	$\mu mol/m^2/s$	Maximum RuBP-saturated rate of carboxylation
W_c	$\mu mol/m^2/s$	Rubisco limited rate of carboxylation
W_j	$\mu mol/m^2/s$	RuBP-limited rate of carboxylation
α_l	–	Total leaf absorbance
β	–	Fraction of absorbed quanta reaching PSII
Γ	µmol/mol	CO_2-compensation point in the absence of dark respiration
Θ_{PSII}	–	Convexity term for electron transport rates
$\Phi_{PSII,max}$	–	Maximum dark-adapted quantum yield of PSII

T is measured in Kelvin. The factors $V_{max,25\,°C}$, $R_{d,25\,°C}$, $J_{max,25\,°C}$, $k_{25\,°C}$ and $\gamma_{25\,°C}$ which are part of the expressions V_{max}, R_d, J_{max}, K and Γ must be known (or calibrated). (The introduction of $k_{25\,°C}$ and $\gamma_{25\,°C}$ represents a slight extension of the formulas of Bernacchi et al.. The exact version of their formulas is recovered by setting $k_{25\,°C} = 1$ and $\gamma_{25\,°C} = 1$.)

3.3 Coupling diffusion and assimilation

We resume now the discussion of expression (3.24) from the end of section 3.1.5. Having derived now a second relation between A and C_i we can use (3.24) and (3.31) to eliminate C_i from the function representing A.

Equating expressions (3.24) and (3.31) leads to a quadratic equation for C_i with solutions

$$C_i = \frac{1}{2g}\left\{g\,(C_a - K) - (q - R_d) \pm \sqrt{[g\,(C_a - K) - (q - R_d)]^2 + 4g\,(gKC_a + q\Gamma + KR_d)}\right\} \tag{3.33}$$

Since the solution with the minus sign in front of the root symbol leads to negative concentrations C_i we discard it. Employing the meaningful solution to eliminate C_i from equation (3.24) in favour of C_a and g we arrive at the following expression for the assimilation rate:

$$A = \frac{1}{2}\left\{g\,(C_a + K) + (q - R_d) - \sqrt{[g\,(C_a - K) - (q - R_d)]^2 + 4g\,(gKC_a + q\Gamma + KR_d)}\right\} \tag{3.34}$$

This expression is analogous to (3.26) for the transpiration rate. If the anatomic parameters of the plant leaf and the environmental parameters T and v_{wind} are prescribed, equation (3.34) connects assimilation rate A and atmospheric carbon dioxide concentration C_a, although this is a much more complicated relation than (3.26). Similarly as above: if either of A or C_a is given the other one can be calculated from (3.34).

3.4 Optimisation principle, derivation of optimum conductance $g(C_a)$

As explained at the beginning of section 3 it is desirable ro derive a functional relation between stomatal density ν and atmospheric carbon dioxide concentration C_a. *If* the assimilation rate A is known, expression (3.34) can be solved for g which leads — in connection with definition (3.23) — to the desired result. In general, however, A is *not* known independently from (3.34). Fortunately, it turns out that the information which is necessary to calculate $\nu(C_a)$ can also be supplied by an optimisation principle acting on the transpiration and assimilation rates given in equations (3.26) and (3.34).

In habitats where water supply is not unlimited it is imperative for plants to maximise assimilation while keeping the amount of transpired water low. It appears, however, that plants do not maximise assimilation with respect to the instantaneous water use efficiency A/E. They rather optimise assimilation and transpiration in a way that takes into account diurnal or even seasonal changes of e.g. temperature, humidity and irradiance. The rationale behind the optimisation scheme is that a plant may be better off keeping open its stomata in the morning when humidity is still high rather than during the afternoon heat, although irradiance is then more intense (and assimilation would be more productive) than in the morning. Formally, such a behaviour can be expressed by the statements

$$\int_{\Delta t} A(t)\,dt = \text{maximum} \quad \text{and} \quad \int_{\Delta t} E(t)\,dt = W_0 \tag{3.35}$$

which have to be fulfilled simultaneously. Δt stands for a reasonable time span (like one day or one season) and W_0 denotes the water supply (per leaf area) available during this time span. It is furthermore understood that the quantities w_a, q, Γ, K and g appearing in expressions (3.26) and (3.34) for E and A depend either explicitly on time t, or implicitly via the time-dependent temperature $T(t)$.

Since a plant can regulate its stomatal conductance by adjusting stomatal density ν or stomatal area a_{st} (or both) we may choose the total conductance g which encompasses both effects (see equation (3.23)) as the variable whose temporal behaviour is to be calculated from the optimisation procedure. The time dependence of the quantities w_a, q, Γ and K we assume, however, as being explicitly or implicitly prescribed.

In order to calculate the conductance $g(t)$ which maximises $\int_{\Delta t} A(t)\,dt$ under the constraint $\int_{\Delta t} E(t)\,dt = W_0$ we apply the method of Lagrangian multipliers (from the Calculus of Variation of Mathematical Physics, see e.g. [1], for slightly different formulations leading to the same results see [19], [20], [28], [13], [45], [10]). The optimisation procedure starts with

forming the expression

$$\begin{aligned} L &= A - \lambda E \\ &= \frac{1}{2g}\left\{g\left(C_a + K\right) + \left(q - R_d\right) - \sqrt{\left[g\left(C_a - K\right) - \left(q - R_d\right)\right]^2 + 4g\left(gKC_a + q\Gamma + KR_d\right)}\right\} \\ &\quad - \lambda a g\left(w_i^{sat} - w_a\right) \end{aligned} \tag{3.36}$$

where the second line emerges from substitution of A and E by expressions (3.34) and (3.26). (In mathematical terminology, the arbitrary constant λ is called the Lagrangian multiplier and $\int_{\Delta t} E(t)\,dt = W_0$ is the constraint of the problem.) Then we calculate

$$\frac{d}{dt}\frac{\partial L}{\partial \dot{g}} = \frac{\partial L}{\partial g} \tag{3.37}$$

where $\dot{g} \equiv \frac{dg}{dt}$. The last equation constitutes an ordinary differential equation of second order for the conductance $g(t)$. In a last step the Lagrangian multiplier λ is calculated by evaluating the constraint $\int_{\Delta t} E(g(t))\,dt = W_0$ with the help of the now known conductance $g(t)$.

Inspection of expressions (3.34) and (3.26) shows that both A and E depend on g but neither of them depends on $\dot{g}$. Hence, equation (3.37) reduces to

$$0 = \frac{\partial L}{\partial g} \tag{3.38}$$

This implies two important simplifications: (i) The differential equation (3.37) of the generic case reduces to a mere algebraic equation for $g(t)$, and, (ii) in order to solve equation (3.38) for $g(t)$ the time dependencies of the quantities w_a, q, Γ and K need not be known explicitly.

Applying the optimisation scheme to equation (3.36) results in

$$\begin{aligned} g = \frac{1}{\left(C_a + K\right)^2}\Bigg\{ &\sqrt{\frac{q\left(K + \Gamma\right)\left[C_a\left(q - R_d\right) - \left(q\Gamma + KR_d\right)\right]}{\left[C_a + K - \lambda a\left(w_i^{sat} - w_a\right)\right]\lambda a\left(w_i^{sat} - w_a\right)}}\left[C_a + K - 2\lambda a\left(w_i^{sat} - w_a\right)\right] \\ &+ \left(q - R_d\right)C_a - \left(q\Gamma + KR_d\right) - q\left(K + \Gamma\right)\Bigg\} \end{aligned} \tag{3.39}$$

A few remarks concerning structure and properties of g and the functions derived from it (like A and C_i) are appropriate:

3.4.1 Conductance $g(C_a)$

(i) **General behaviour of** $g(C_a)$: To be meaningful, g obtained from the optimisation procedure (equation (3.39)) should be compatible with expression (3.23) where g was defined in terms of plant anatomy: Since minimum mechanical strength is certainly a more restricting constraint for a plant leaf than maximum stomatal conductance, the maximum number of stomata a leaf can accomodate without losing too much of its mechanical strength sets an upper limit $g_{max}^{mech} := f\left[D_{\mathrm{CO_2}}/\left(d_{st} + d_{bl} + d_{as}\frac{\tau_{as}^2}{n_{as}}\right)\right]$ to g. (The factor in brackets follows from the — mechanically absurd — condition

that the leaf surface is completely covered with stomatal openings. This assumption implies for the porosity of the leaf surface $n_{st} = va_{st} = 1$ and — by (3.23) — the expression in brackets. The factor f is inserted to remedy this absurdity by taking care of the leaf strength in a general way. Instead of considering any details we simply assume $0 < f < 1$). Similarly, negative values of g — even if recommended by the mathematics behind g — are not meaningful and should be discarded as artefacts. Altogether, the function

$$\tilde{g}(t) = \begin{cases} g_{max}^{mech} & \text{if } g > g_{max}^{mech} \\ 0 & \text{if } g < 0 \\ g & \text{else} \end{cases} \tag{3.40}$$

represents an optimum of the temporal variation of leaf conductance in the following sense: if a plant regulates its (total) conductance according to it during a given time span Δt, it achieves the highest possible output of assimilation products $\int_{\Delta t} A(t)\,dt$ while not exceeding the water budget $W_0 = \int_{\Delta t} E(t)\,dt$ which is disposable during Δt.

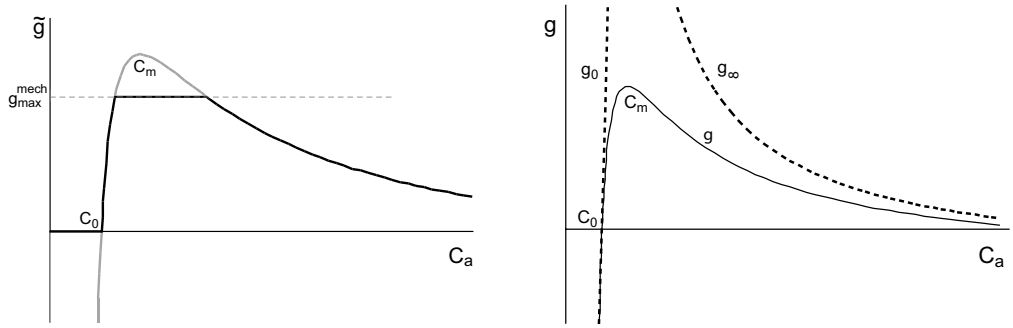

(a) (b)

Figure 3.5: (a) Generic behaviour of $g(C_a)$. $g(C_a)$ has one zero located at $C_0 := \frac{q\Gamma + KR_d}{q - R_d} + \lambda\, a\left(w_i^{sat} - w_a\right)$. For $C_a \to \infty$ it approaches asymptotically the C_a-axis. The black line illustrates g as defined by (3.40), the grey line depicts g as given in (3.39).
(b) g and its first order approximations g_0 and g_∞ as given in equations (3.42) and (3.43).

Figure 3.5 illustrates the generic behaviour of $g(C_a)$. It becomes zero at

$$C_0 := \frac{q\Gamma + KR_d}{q - R_d} + \lambda\, a\,(w_i^{sat} - w_a) \tag{3.41}$$

approaches asymptotically zero for $C_a \to \infty$ and has a maximum at $C_m > C_0$.

Series expansion of g around C_0 (for small C_a) and for large values of C_a leads to the

approximate expressions (see Figure 3.5)

$$C_a \approx C_0 : \qquad g \approx g_0 := \frac{(q - R_d)^2}{2\,q\,(K + \Gamma)\,\lambda\,a\left(w_i^{sat} - w_a\right)}\,(C_a - C_0) + \ldots \tag{3.42}$$

$$C_a \to \infty : \qquad g \approx g_\infty := \left[(q - R_d) + \sqrt{\frac{(q - R_d)\,q\,(K + \Gamma)}{\lambda\,a\left(w_i^{sat} - w_a\right)}}\right]\frac{1}{C_a} + \ldots \tag{3.43}$$

(ii) $g(C_a)$ **in the limit** $w_a \to w_i^{sat}$: For $w_a \to w_i^{sat}$ (i.e. the atmosphere in the canopy is saturated with water vapour), g approaches infinity. This is to be expected: In that case transpiration does not take place and bounding conductance to finite values by any sort of regulation would be tantamount to limiting CO_2 influx from the atmosphere into the leaves.

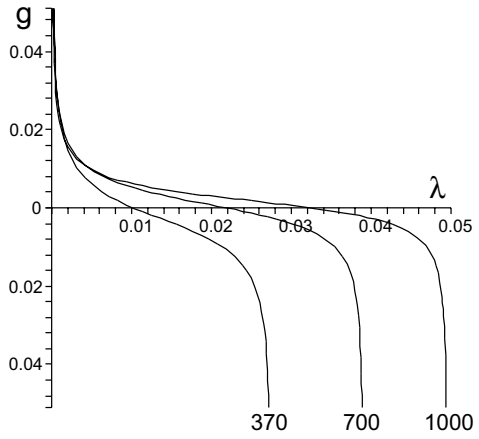

Figure 3.6: Optimum conductance g as a function of the Lagrangian multiplier λ for C_a = 370 µmol/mol, C_a = 700 µmol/mol and C_a = 1000 µmol/mol. Only values of λ between the pole at $\lambda = 0$ common to the three curves and their zeros (where the curves intersect the λ-axis) are meaningful since only they lead to positive values of the conductance g. The acceptable range of λ increases with the atmospheric CO_2 concentration C_a.

(iii) **Dependence of** $g(C_a)$ **on the Lagrangian multiplier** λ: If the photosynthetic parameters attain realistic values and if C_a fulfills the inequality $C_a \geq (q\Gamma + KR_d)/(q - R_d)$ (which happens to be the case for realistic parameter values) the function $g(\lambda)$ looks as in Figure 3.6. Poles are located at $\lambda = 0$ and at $\lambda = (C_a + K)/(a(w_i^{sat} - w_a))$, a zero is found at

$$\lambda_0 = \frac{1}{a\left(w_i^{sat} - w_a\right)}\left(C_a - \frac{(q\Gamma + KR_d)}{(q - R_d)}\right) \tag{3.44}$$

Only values of λ in the range $\lambda = 0 \ldots \lambda_0$ are meaningful since only they lead to positive values of the conductance g. From Figure 3.6 it is obvious that the acceptable range of λ increases with the atmospheric CO_2 concentration C_a. The behaviour of $g(\lambda)$ suggests that λ represents in some way the "cost of water": Small values of λ

are related to high values of the optimum conductance g which indicates that high transpiration values are tolerable which implies in turn that water is easily (without high costs) supplied. g is lower for higher values of λ, meaning that the necessity to avoid transpiration is more severe. In other words, water is more expensive.

For values of C_a, K, w_a and λ satisfying the relation

$$\lambda \ll \frac{C_a + K}{a\left(w_i^{sat} - w_a\right)} \tag{3.45}$$

it is possible to derive an approximate relation between water supply W_0 and λ without explicit knowledge of the time dependencies hidden in g: We expand (3.39) in a Taylor series with respect to λ and find that for small λ (small in the sense of (3.45)) the dominating terms are

$$g \approx \frac{\alpha(t)}{\sqrt{\lambda}} + \beta(t) \tag{3.46}$$

where

$$\alpha(t) := \sqrt{\frac{q\,(K+\Gamma)\left[C_a\,(q-R_d) - (q\Gamma + KR_d)\right]}{(C_a+K)^3\,a\left(w_i^{sat} - w_a\right)}}$$

$$\beta(t) := \frac{C_a\,(q-R_d) - (q\Gamma + KR_d) - q\,(K+\Gamma)}{(C_a+K)^2} \tag{3.47}$$

α and β depend on time because the assimilation parameters q, R_d, K and Γ, and the atmospheric and saturated water concentrations w_a and w_i^{sat}, respectively, are functions of time t (see the definitions (3.30) and the temperature dependencies given in (3.32)).

Using (3.46) in the transpiration rate $E = a\,g\,\left(w_i^{sat} - w_a\right)$ (defined in (3.26)) we find from equation (3.35) for the water supply available in the time span Δt

$$\begin{aligned} W_0 &= \int_{\Delta t} E(t)\,dt = \int_{\Delta t} a\,g\,\left(w_i^{sat} - w_a\right)\,dt \\ &= \frac{1}{\sqrt{\lambda}} \int_{\Delta t} a\,\alpha(t)\,\left(w_i^{sat} - w_a\right)\,dt + \int_{\Delta t} a\,\beta(t)\,\left(w_i^{sat} - w_a\right)\,dt \\ &= \frac{A}{\sqrt{\lambda}} + B \end{aligned} \tag{3.48}$$

where A and B represent the two integrals over t. Solving for λ, we obtain

$$\lambda = \frac{A^2}{(W_0 - B)^2} \tag{3.49}$$

which corroborates the interpretation of λ as representing the "cost of water": the more water W_0 is available during the time span Δt, the smaller is λ. For more detailed discussions on the interpretation of λ see [19], [20], [21], [28] and [13].

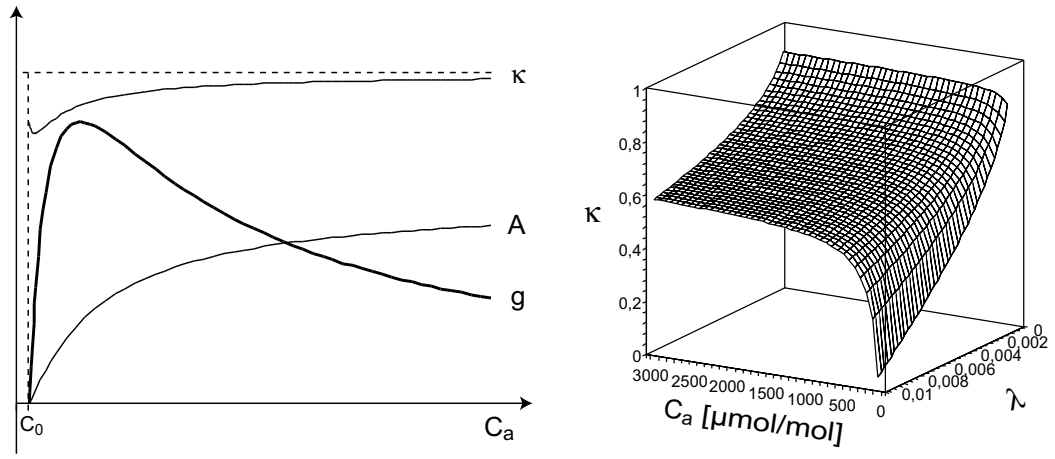

(a) (b)

Figure 3.7: (a) g, A and κ as a function of C_a for $C_0 < C_a < \infty$. g and A share a zero at $C_0 := \frac{q\Gamma + KR_d}{q - R_d} + \lambda a \left(w_i^{sat} - w_a\right)$. All three functions approach for $C_a \to \infty$ asymptotic values: $g \to 0$, $A \to (q - R_d)$ and $\kappa \to \kappa_\infty$ (see equation (3.58)).
(b) κ as a function of λ and C_a.

3.4.2 Assimilation rate $A(t)$

The optimum assimilation rate $A(t)$ related to $g(t)$ follows from substitution of expression (3.39) into equation (3.34)

$$A = \frac{1}{(C_a + K)} \left\{ C_a (q - R_d) - (q\Gamma + KR_d) - \sqrt{\frac{q (K + \Gamma) \left[C_a (q - R_d) - (q\Gamma + KR_d)\right] \lambda a \left(w_i^{sat} - w_a\right)}{\left(C_a + K - \lambda a \left(w_i^{sat} - w_a\right)\right)}} \right\} \tag{3.50}$$

Similarly as $g(C_a)$, $A(C_a)$ has a zero at (see Figure 3.7)

$$C_0 = \frac{q\Gamma + KR_d}{q - R_d} + \lambda a \left(w_i^{sat} - w_a\right) \tag{3.51}$$

Asymptotically, it behaves according to

$$\lim_{C_a \to \infty} A = q - R_d \tag{3.52}$$

As is to be expected, this result coincides with the corresponding limit of expression (3.31) giving A as a function of C_i

$$\lim_{C_i \to \infty} A(C_i) = \lim_{C_i \to \infty} \left(q \, \frac{C_i - \Gamma}{C_i + K} - R_d \right) = q - R_d \tag{3.53}$$

Expanding expression (3.50) for A in a series with respect to λ we find the following structure

$$A = a_0 + a_1 \sqrt{\lambda} + a_3 \sqrt{\lambda}^{\,3} + a_5 \sqrt{\lambda}^{\,5} + \cdots \tag{3.54}$$

where the a_k are functions of the parameters in expression (3.50) (apart from λ).

3.4.3 Transpiration rate $E(t)$

The optimum transpiration rate $E(t)$ was defined in equation (3.26) as a multiple of g according to $E = ag\left(w_a - w_i^{sat}\right)$. Hence, it shares many properties with g, as given in expression (3.39). Expansion in a series with respect to λ results in

$$E = e_{-1}\frac{1}{\sqrt{\lambda}} + e_0 + e_1\sqrt{\lambda} + e_3\sqrt{\lambda}^{\,3} + e_5\sqrt{\lambda}^{\,5} + \cdots \tag{3.55}$$

The e_k are functions of the parameters in expression (3.39), they do not depend on λ.

3.4.4 CO_2-ratio κ

In a similar way, we find from (3.33) the carbon dioxide concentration $C_i(t)$ within the leaves corresponding to the optimum variation of leaf conductance (3.39). Dividing the result by C_a we obtain $\kappa := C_i/C_a$, the ratio between the CO_2 concentrations inside and outside of the plant

$$\begin{aligned}\kappa = \frac{1}{C_a\left[q(K+\Gamma) - \lambda a\left(w_i^{sat} - w_a\right)(q - R_d)\right]} \Big\{ & C_a\, q(K+\Gamma) - \lambda a\left(w_i^{sat} - w_a\right)(q\Gamma + KR_d) \\ & - \sqrt{\left[C_a + K - \lambda a\left(w_i^{sat} - w_a\right)\right]\left[C_a\left(q - R_d\right) - (q\Gamma + KR_d)\right]\, q(K+\Gamma)\,\lambda a\left(w_i^{sat} - w_a\right)} \Big\}\end{aligned} \tag{3.56}$$

κ behaves in an interesting way (see Figures 3.7): κ is smaller than its asymptotic value

$$\kappa_\infty := \lim_{C_a\to\infty}\kappa = \frac{1}{1 + \sqrt{\lambda a\left(w_i^{sat} - w_a\right)\,\dfrac{q - R_d}{q\,(K+\Gamma)}}} \tag{3.57}$$

$$= \frac{1}{1 + \sqrt{\lambda a\left(1 - \dfrac{R_d}{q}\right)\left[\dfrac{w_i^{sat} - w_a}{K+\Gamma}\right]}} \tag{3.58}$$

within the complete interval $C_0 < C_a < \infty$. κ's only extremum — a minimum — is located just a little bit right of C_0. For C_a-values right of the minimum we find that κ increases slowly towards its asymptotic value κ_∞. Thus, the value of κ differs nowhere very much from the value of κ_∞. This property allows us to examine κ_∞ instead of κ in order to seek understanding why values of κ lie seldom outside of the range $\kappa \approx 0.6 \ldots 0.8$, apparently irrespective of species and palaeoatmospheric CO_2-content (C_i/C_a ratios of fossil plants can be calculated from the relative amounts of ^{12}C and ^{13}C isotopes in the fossilized plant material).

(i) The ratio $a = D_{H_2O}/D_{CO_2}$ is independent of species, temperature, time and space. D_{H_2O} and D_{CO_2} themselves are functions of T, but in exactly the same way (see (3.9)), hence a is independent of T.

(ii) The cost of water, λ, is also independent of species and temperature. It depends, however, on climate and weather conditions and may be different in different habitats.

(iii) The expression in parentheses under the root sign in (3.58) is very close to one. This is due to the fact that — for reasonable temperatures — $R_d/q \lessapprox 0.02$. That is, omitting R_d/q produces an error $\lessapprox 2\,\%$. (Notice that q stands for either V_{max} or $(2/9)\,J$ (see (3.30)).)

(iv) The expression in brackets in (3.58) is species independent because its constituents have this property (for K and Γ see expressions (3.32), for w_i^{sat} (3.25)). They depend merely on temperature, but all in a very similar way, provided that we assume that the *absolute* atmospheric humidity w_a is a constant fraction of w_i^{sat} which is equivalent to a constant relative humidity. Then, the temperature dependence of the bracket is less pronounced than the temperature dependencies of the individual terms. (For a relative humidity of 50 %, the value of the bracket is in the range $30 \ldots 13$, corresponding to the temperature interval $0\,°\mathrm{C} \ldots 40\,°\mathrm{C}$.)

Recalling that all parameters appearing in κ_∞ are independent of C_a, we may conclude that variations in κ_∞ are caused chiefly by variations in the cost of water, λ, which are due to a periodically changing or weather dependent availability of ground water or rain. Seasonalities in the atmospheric humidity w_a and variations in the temperature T have a tendency to cancel out each other and have therefore probably a minor impact on the value of κ_∞. In view of the observation that the values of κ and κ_∞ differ nowhere very much, these results apply also to κ.

Reviewing the expressions for g, A, E, κ and κ_∞ we find that the quantities λ, w_a and w_i^{sat} which describe the amount of water available for the plant do appear without exception in form of the product $\lambda a\left(w_i^{sat} - w_a\right)$. This opens up a formal way to replace the *three* variables λ, w_a and w_i^{sat} by just *one* variable, namely κ_∞. Solving (3.58) for $\lambda a\left(w_i^{sat} - w_a\right)$ we obtain

$$\lambda a\left(w_i^{sat} - w_a\right) = \frac{q\,(K+\Gamma)}{q - R_d}\;\frac{(1-\kappa_\infty)^2}{{\kappa_\infty}^2} \tag{3.59}$$

Insertion of this result into (3.39) produces

$$g = \frac{1}{(C_a+K)^2}\left\{\sqrt{\frac{C_a\,(q-R_d) - (q\Gamma + KR_d)}{C_a\,(q-R_d) - (q\Gamma + KR_d) + q\,(K+\Gamma)\left(\frac{2\kappa_\infty - 1}{{\kappa_\infty}^2}\right)}}\;\left(\frac{\kappa_\infty}{1-\kappa_\infty}\right)\right.$$
$$\left.\times\left[(C_a+K)\,(q-R_d) - 2\,q\,(K+\Gamma)\,\frac{(1-\kappa_\infty)^2}{{\kappa_\infty}^2}\right] + (q-R_d)\;C_a - (q\Gamma + KR_d) - q\,(K+\Gamma)\right\} \tag{3.60}$$

and similar expressions for A, E and κ. The quantity λ depends on precipitation, evaporation, ground water regime and maybe more parameters which are difficult to assess experimentally. There may be situations when measurements on κ_∞ are more easily performed. In applying (3.60) it should be kept in mind, however, that κ_∞ still depends on temperature, humidity and water supply, even if one can assume that it is usually within the range $\kappa \approx 0.6 \ldots 0.8$.

3.5 Diurnal variations of assimilation and transpiration rates and of water use efficiency

The diurnal variations of the "input functions" insolation $Q(t)$, temperature $T(t)$ and atmospheric water vapour concentration $w_a(t)$ cause similar variations of the quantities conductance $g(t)$, assimilation rate $A(t)$, transpiration rate $E(t)$ and water use efficiency $WUE(t) := A(t)/E(t)$. We illustrate this by adapting the fictitious (but nonetheless realistic) temporal variations of the input functions depicted in Figure 3.8. For the effect on $g(t)$, $A(t)$, $E(t)$ and $WUE(t)$ consult Figures 3.9 and 3.10.

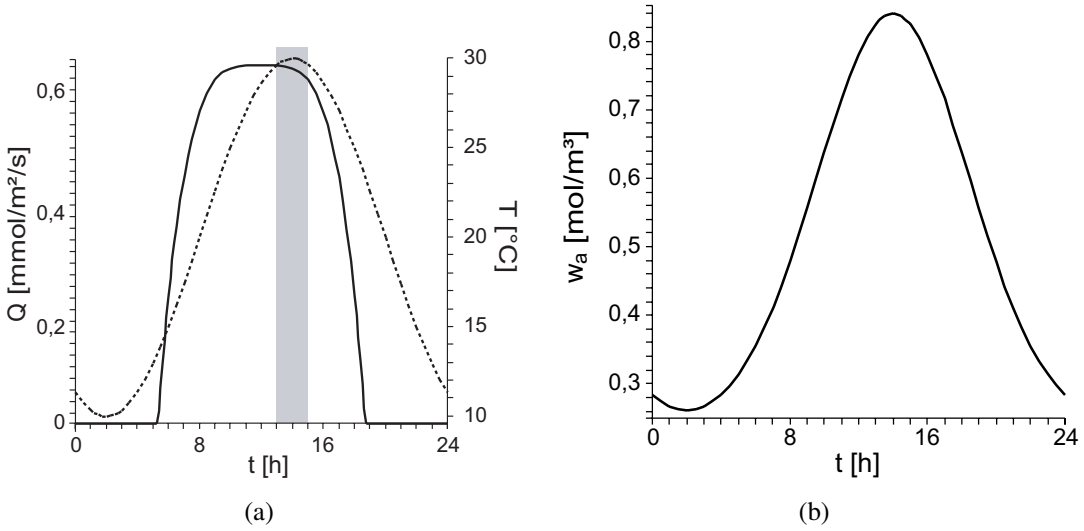

Figure 3.8: Diurnal variations of (a) photon flux density $Q(t)$ (solid line) and temperature $T(t)$ (dotted line) and (b) atmospheric humidity $w_a(t)$ used as input functions for the plots of conductance $g(t, C_a)$ shown in Figure 3.9 ($t = 0$ h and $t = 24$ h denote midnight). $w_a(t)$ shown in (b) corresponds to a constant relative humidity of 50 %. $Q(t)$ is centered around its maximum at $t = 12$ h, $T(t)$ and $w_a(t)$ are centered around their maxima at $t = 14$ h. The input functions determine the time dependence of the assimilation parameters q, R_d, K and Γ which occur in $g(t, C_a)$ and the atmospheric and saturated water concentrations w_a and w_i^{sat} via the definitions (3.30) and the temperature dependencies given in (3.32).

Obviously, λ affects the absolute values but not the structural behaviour of these functions. It can be seen from Figure 3.10 that the assimilation rate $A(t)$ depends less pointedly on λ than the transpiration rate $E(t)$. Clearly, this asymmetry entails that the water use efficiency $WUE(t) = A(t)/E(t)$ increases along with λ, as is to be expected from the interpretation of λ as the cost of water. Mathematically, the different sensitivity of $A(t)$ and $E(t)$ with respect to λ can be understood from expressions (3.54) and (3.55), the series expansions of both quantitites with respect to λ: the leading term in the expansion of $A(t)$ is a constant which dominates $A(t)$ for small λ. Hence, variations in λ have only small effects on $A(t)$. $E(t)$, however, is (for small λ) dominated by the term $e_{-1}/\sqrt{\lambda}$ which decreases if λ increases. From the viewpoint of plant physiology, the loose coupling of $A(t)$ to λ is appropriate: since the plant requires a constant supply of assimilation products in order to survive, it would be dangerous if $A(t)$ depended too strongly on the water availability λ. The properties of $A(t)$

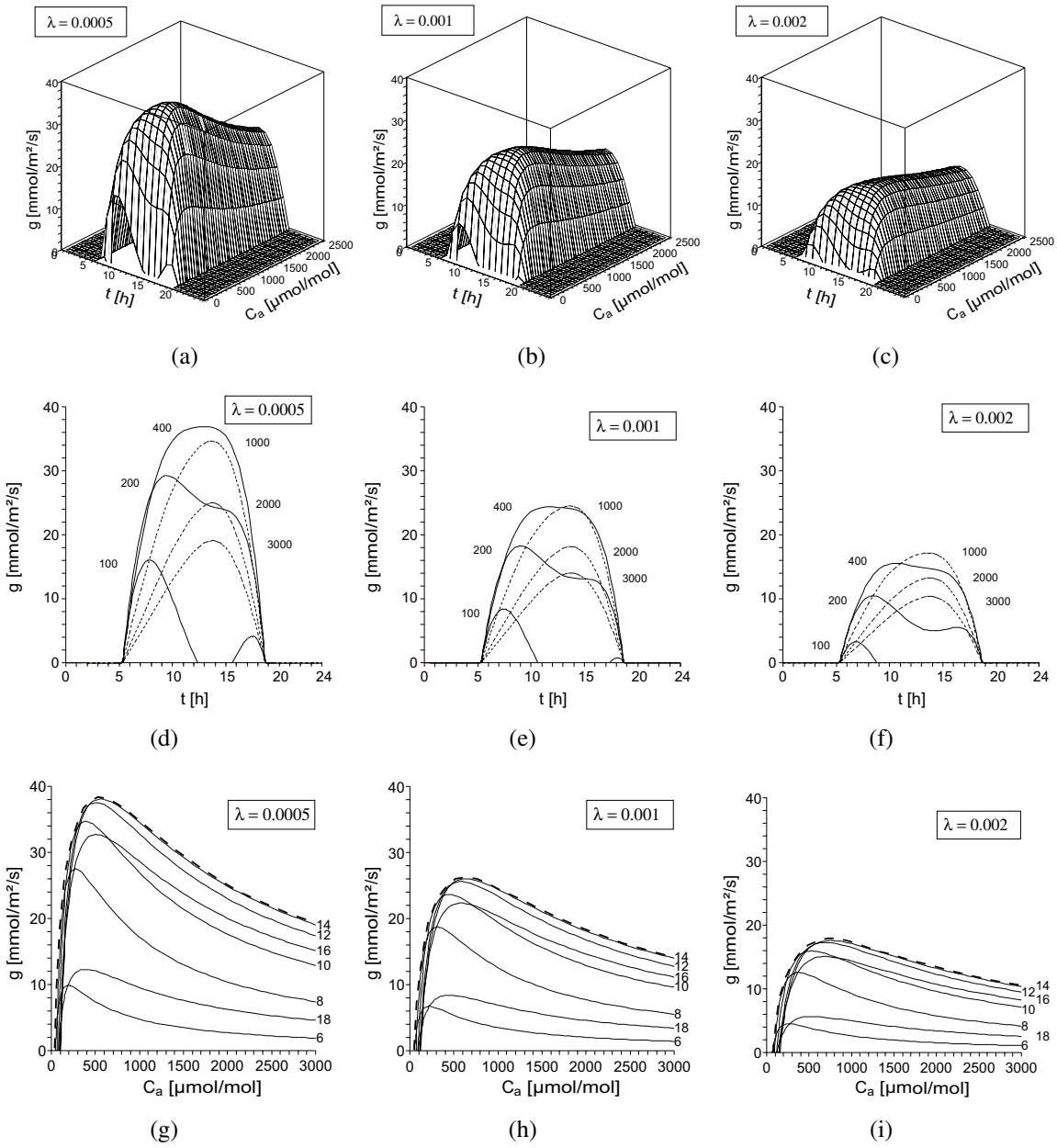

Figure 3.9: Upper row: Conductance $g(t, C_a)$ as a function of t (diurnal variations) and atmospheric CO_2 concentration C_a for (a) $\lambda = 0.0005$, (b) $\lambda = 0.001$ and (c) $\lambda = 0.002$ (λ represents the cost of water). $g(t, C_a)$ is calculated according to (3.39) from diurnal variations of $Q(t)$, $T(t)$ and $w_a(t)$ as shown in Figure 3.8. C_a is given in units of µmol/mol. $t = 0$ and $t = 24$ denote midnight.
Centre row: Slices through the three-dimensional surfaces $g(t, C_a)$ of the upper row with C_a held constant. Numbers close to the maxima of the curves give C_a in units of µmol/mol (1000 µmol/mol, 2000 µmol/mol and 3000 µmol/mol correspond to the broken curves). Obviously, small values of λ (i.e. cheap water) are in favour of high values of optimum conductance g.
Lower row: Slices through the three-dimensional surfaces $g(t, C_a)$ of the upper row with t held constant. Numbers close to the curves indicate the time of day. The assumption of darkness between 19 h in the evening and 5 h in the morning implies $g = 0$. Broken lines indicate the envelopes around the families of curves. The envelopes represent the functions $g_{max}(C_a)$ used in (3.62). Geometrically, they can be obtained by projecting the "crests" of the "mountains" of the upper row along the t-axis into the (g, C_a)-plane.

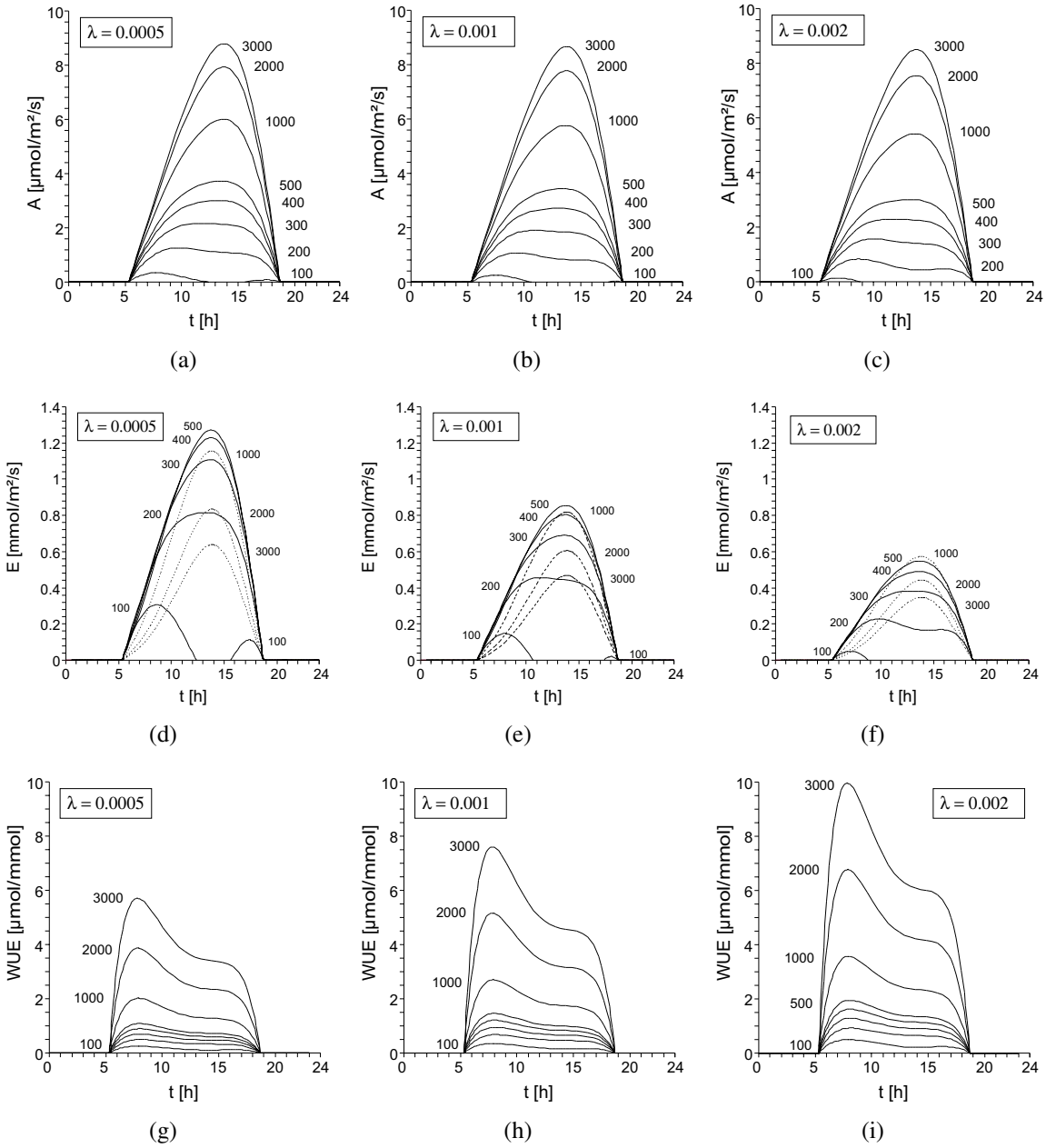

Figure 3.10: Assimilation rate $A(t)$ (a,b,c), transpiration rate $E(t)$ (d,e,f) and water use efficiency $WUE(t) := A(t)/E(t)$ (g,h,i) as a function of t (diurnal variations) for various values of the cost of water λ. $A(t)$, $E(t)$ and $WUE(t)$ are calculated according to (3.50) and (3.26) from the diurnal variations of $Q(t)$, $T(t)$ and $w_a(t)$ shown in Figure 3.8. The atmospheric CO_2 concentration C_a is held constant along each curve. Numbers close to the maxima of the curves give C_a in units of µmol/mol (1000 µmol/mol, 2000 µmol/mol and 3000 µmol/mol correspond to the broken curves). C_a is given in units of µmol/mol. $t = 0$ h and $t = 24$ h denote midnight.
Upper row: Optimum assimilation rate $A(t)$ for (a) $\lambda = 0.0005$, (b) $\lambda = 0.001$ and (c) $\lambda = 0.002$.
Centre row: Optimum transpiration rate $E(t)$ for (d) $\lambda = 0.0005$, (e) $\lambda = 0.001$ and (f) $\lambda = 0.002$.
Lower row: water use efficiency $WUE(t)$ for (g) $\lambda = 0.0005$, (h) $\lambda = 0.001$ and (i) $\lambda = 0.002$.

and $E(t)$ are illustrated by the series of pictures (d,e,f) and (g,h,i), respectively, in Figure 3.10.

3.6 Reconstruction of palaeoatmospheric CO_2 from fossil stomatal density

3.6.1 General Considerations

The optimisation principle rests merely on a plausible assumption about favourable water and assimilation management. The mathematics representing it is completely independent of any physiological mechanisms by which a plant might regulate the conductance g as predicted by expression (3.39). Plant physiology tells us that two methods of regulation are in use: (i) The short-term or diurnal regulation of conductance g is done by the stomata whose guard cells are perfectly suited to react quickly and efficiently by varying the stomatal cross section a_{st} in the range $0 \ldots a_{st}^{max}$. (ii) Medium-term to long-term adjustments of conductance can be realised by increasing or decreasing the stomatal density ν.

Turning to the calculation of $\nu(C_a)$ we insert (3.19) into (3.23) and solve for ν

$$\nu = \frac{1}{a_{st}} \left(\frac{\left[d_{st}^{geom} + \sqrt{\frac{a_{st}}{\pi}} \right] g}{D_{\mathrm{CO}_2} - \left[d_{bl} + d_{as} \frac{\tau_{as}^2}{n_{as}} \right] g} \right) \tag{3.61}$$

Then we substitute expression (3.16)

$$d_{bl} = 4 \times 10^{-3} \, \frac{\mathrm{m}}{\sqrt{s}} \, \sqrt{\frac{l}{v_{wind}}}$$

and g from (3.40). The result is quite long which is why we do not give it here explicitly. If we would also insert the temperature dependencies of assimilation, diffusion and water vapour saturation according to equations (3.32), (3.9) and (3.25), respectively, the expressions would become unreadable. (In parentheses, we recommand to perform any calculations with a computer programme which is capable of symbolic manipulations.) Using (3.61) to exploit fossil values of ν as a proxy for palaeoatmospheric C_a requires to take care of the different time scales involved in (3.61):

- Wind speed v_{wind}, atmospheric humidity w_a, insolation Q and (leaf) temperature T (i.e. the weather) change on a day-to-day basis, or, to put it differently, they vary according to a diurnal rhythm which must be provided as input for the optimisation procedure expressed by equations (3.35) (that is, if the conductances for CO_2 and H_2O are to be calculated explicitly). Actually, the plant puts into effect the optimisation strategy by varying the cross-section a_{st} which alters in turn the conductance $g(t)$, according to equation (3.23).

- The (palaeo)atmospheric CO_2-concentration C_a changes medium-term to long-term (apart from the summer/winter differences in moderate latitudes due to growth period which are of no interest here). Variations in stomatal density ν belong also to this time scale: as stated above, the short-term regulation of conductance is performed by

adjusting the stomatal cross section a_{st}. If, however, all stomata are fully opened a necessary further increase in conductance (in order to put the optimisation strategy into effect) can be realised only by investing in additional stomata. This takes much longer than varying the stomatal cross section a_{st}, hence deciduous plants may wait for the next season to add stomata to their leaves. On the other hand, stomata are more expensive in terms of building expenses than ordinary epidermis cells. Therefore, a plant which realises that its stomata have never been fully opened during a season will conclude that lower stomatal density ν will do and accordingly equip next years leaves with less stomata.

- The definition of the morphospecies relies on the approximate constancy of characteristic anatomical traits (while ignoring minor variations on the level of the individuum, or anatomic differences between sun leaves and shadow leaves, for instance). Hence, the numerical values of anatomical parameters like d_{st}^{geom}, d_{as}, n_{as} and τ_{as} (but not ν or a_{st}!) of a given species can be expected to scatter around mean values which remain approximately constant within the lifetime of this species. Similarly, the biochemistry of C_3-photosynthesis has probably not changed since the appearance of the first land plants during the Palaeozoic. Hence, although the quantities given in equations (3.32) vary — due to their temperature dependence — diurnally, the biochemical structure as such has probably remained unchanged.

The essence of these considerations is as follows: Secular variations of the atmospheric CO_2-concentration cause long-term variations of ν, diurnal variations of temperature, insolation, atmospheric humidity and wind speed cause short-term variations of a_{st}. The time-scales of both variations differ by three orders of magnitude, i.e. they can be treated as being effectively independent of one another.

Since fossilised leaves provide information on a_{st}^{max} but not on the continuously fluctuating values of a_{st} this feature is very favourable if we want to reconstruct C_a from fossil ν via expression (3.61). The separation of short-term and long-term variations can be achieved as follows: The considerations outlined above imply that the maximum stomatal cross-section a_{st}^{max} corresponds to the maximum conductance g_{max} which is realised during the *diurnal* variations of v_{wind}, Q, w_a and T at least once per day (see Figure 3.9). When these events occur relation (3.61) takes the form

$$\nu = \frac{1}{a_{st}^{max}} \left(\frac{\left[d_{st}^{geom} + \sqrt{\frac{a_{st}^{max}}{\pi}} \right] g_{max}}{D_{CO_2} - \left[d_{bl} + d_{as} \frac{\tau_{as}^2}{n_{as}} \right] g_{max}} \right) \tag{3.62}$$

with

$$d_{bl} = 4 \times 10^{-3} \, \frac{\mathrm{m}}{\sqrt{s}} \, \sqrt{\frac{l}{v_{wind}}}$$

Since $v_{wind}(t)$, $Q(t)$, $w_a(t)$ and $T(t)$ are supposed to be explicitly known (as are — via their dependence on temperature — the photosynthetic parameters q, K, Γ and R_d), we can calculate from equation (3.39) the (short-term) maximum conductance g_{max} and the time t_{max}

when it occurs. Because the diurnal variation of g involves a much shorter time-scale than its secular variation caused by changes in the atmospheric CO_2-concentration, C_a can be held constant when t_{max} is calculated. In principle, this can be done by solving $dg/dt = 0$ for $t = t_{max}$. This may, however, be cumbersome or even impossible if g is a complicated function of t. Once t_{max} is known it is inserted back into expression (3.39), resulting in $g_{max}(C_a)$, a relation between C_a and g_{max} which is not explicitly dependent on time. Substitution of $g_{max}(C_a)$ in (3.62) concludes the derivation of $\nu(C_a)$.

The procedure of obtaining $g_{max}(C_a)$ can also be understood geometrically: Each one of subfigures (g), (h) and (i) (i.e. the lower row) of Figure 3.9 depicts a family of curves $g(t, C_a)$. The family is generated by assigning different values to the parameter t. From Differential Geometry, it is well known (see, e.g. [41]) that the envelope of this family of curves can be calculated from (i) the condition $dg(t, C_a)/dt = 0$, plus, (ii) the relation $g(t, C_a)$ itself. Comparing the upper and lower rows of Figure 3.9 it is evident that the envelope curves $g_{max}(C_a)$ (depicted in the lower rows as broken lines) can be obtained by projecting the "crests" of the "mountains" of the upper row parallel to the t-axis into the (g, C_a)-plane.

The lower row of Figure 3.9 shows that the "mountain crest" $g_{max}(C_a)$ can be approximated by just one representative, $g(\hat{t}, C_a)$, of the curves family of curves $g(t, C_a)$, provided $t = \hat{t}$ is appropriately chosen (in the case of Figure 3.9 the obvious choice would be $\hat{t} \approx 14\,\mathrm{h}$).

Applying the approximation $g_{max}(C_a) = g(\hat{t}, C_a)$ (with $\hat{t}$ defined by $T(\hat{t}) = T_{max}$) simplifies the calculation of g_{max} from equation (3.39) considerably: (i) The diurnal temperature cycle $T(t)$ need not be known in detail, it is sufficient to know the (average) daily maximum temperature T_{max} during the vegetation period. (ii) We may assume that under normal circumstances the daily temperature maximum is caused by solar insolation which is coupled with a high flux density Q of photosynthetic active photons (c.f. Figure 3.8, for Q see Table 3.1 and expressions (3.28)). Then the first alternative of expression (3.29) is valid, implying, that we have to know only two assimilation parameters explicitly in order to calculate g_{max} from equation (3.39), namely $V_{max,25\,^\circ\mathrm{C}}$ and $R_{d,25\,^\circ\mathrm{C}}$.

Summarising these intermediate results: In order to calculate stomatal density ν as a function of atmospheric CO_2 concentration C_a from equation (3.62) we need to know (or estimate) the following parameters:

(i) The assimilation parameters q, R_d, K and Γ.

(ii) The average maximum temperature T_{max} during the vegetation period.

(iii) The atmospheric humidity w_a.

(iv) The "cost of water" λ.

(v) The wind speed v_{wind}.

(vi) The leaf anatomic parameters: maximum stomatal area a_{st}^{max}, depth of stomatal opening d_{st}^{geom}, thickness of assimilation tissue d_{as}, tortuosity of assimilation tissue τ_{as}, porosity of assimilation tissue n_{as} and average leaf length l (implying — together with v_{wind} — the thickness of the boundary layer d_{bl}).

In order to calculate g_{max} from (3.39) only the quantities (i) through (iv) must be known. The first of these is species specific, the other three describe the environment.

The leaf anatomic parameters in (vi) can be obtained from fossil material as accurately as the quality of the material allows (with respect to a_{st}^{max} see, however, section 3.6.2.3). The assimilation parameter in (i) must be taken from an extant relative of the plant under consideration. The environmental parameters in (ii) to (v) are probably the most difficult to obtain because they are part of the climatic scenario one wants to unravel.

If values of the environmental parameters are unobtainable, equation (3.62) provides at any rate a quantitative link between the parameters T_{max}, w_a, λ and v_{wind} and the atmospheric CO_2-concentration C_a. This link may be exploited e.g. by sensitivity studies and give some insight into the "hierarchy" of the environmental parameters involved (see Section 3.6.3, below).

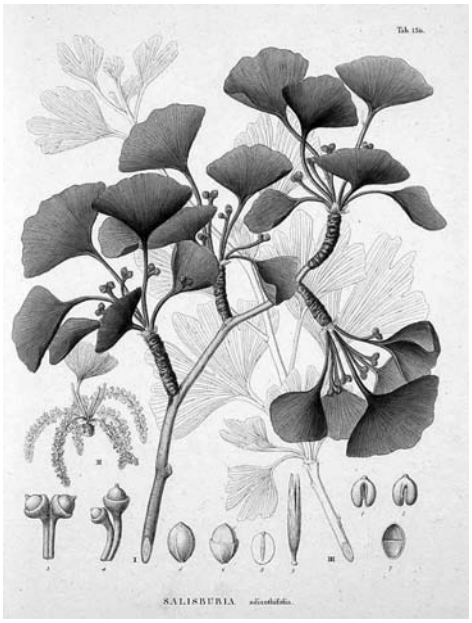

(a) Leaves and twigs of *Ginkgo biloba*.

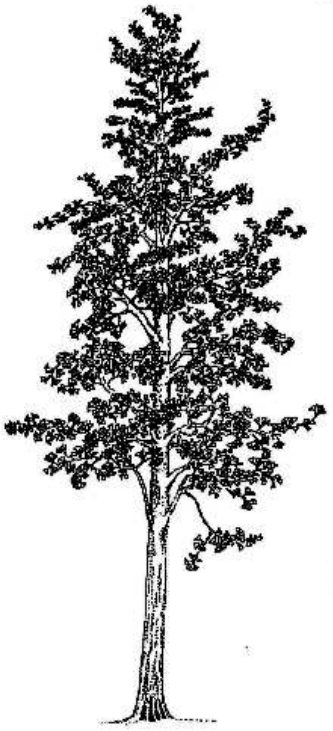

(b) Habit of *Ginkgo biloba*.

Figure 3.11: *Ginkgo biloba* (Illustrations: (a) from "Flora Japonica" by Siebold & Zuccarini, Leiden 1835/42.) (b) from [70].)

3.6.2 Calibration of $\nu(C_a)$ with respect to *Ginkgo biloba*

Before we can apply equation (3.62) to stomatal data of fossil leaves in order to reconstruct palaeoatmospheric CO_2 concentrations we have to calibrate equation (3.62) with respect to the plant species from which the fossil leaves come. As an example, we do the calibration for *Ginkgo biloba* (see Figure 3.11).

Overdieck and Strassemeyer ([52]) investigated an adult *Ginkgo biloba* tree growing in the field in Berlin. They provide measurements of the assimilation rate $A(C_i)$ and of the stomatal conductance (with respect to water vapour) $g_{s\,H_2O}(C_a)$ (see Figure 3.12 and Table

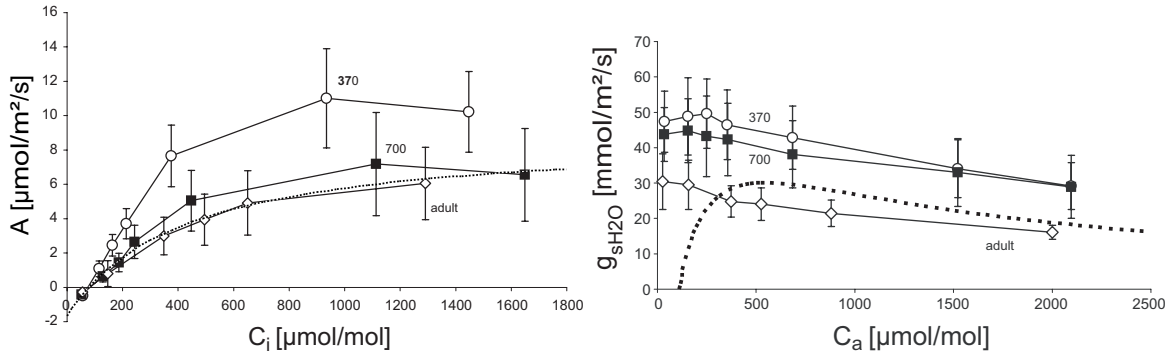

(a) (b)

Figure 3.12: Calculation of (a) q, R_d, K and Γ and (b) λ from data points included in Figures 1 and 2 of [52]. The data are related to three groups of *Ginkgo biloba* plants. Open circles: Saplings grown for 2 years at $C_a \approx 370\,\mu\text{mol/mol}$. Filled diamonds: Saplings grown for 2 years at $C_a \approx 700\,\mu\text{mol/mol}$. Open squares: Values of an adult *Ginkgo biloba* growing in the field (Berlin) at $C_a \approx 370\,\mu\text{mol/mol}$.
(a) The dotted curve represents the function $A(C_i)$ (see (3.63)). q, R_d, K and Γ were obtained by the least squares method according to (3.64) from the (C_i, A) data pairs of Table 3.2.
(b) The dotted curve represents the function $g_{s\mathrm{H_2O}}(C_a)$. λ was obtained by the least squares method (according to (3.65)) from the $(C_a, g_{s\,\mathrm{H_2O}})$ data pairs of Table 3.2.

3.2). The measurements were carried out at a temperature of $T = 27.3\,^\circ\text{C}$ and at a relative atmospheric humidity of 50 %. We use the data points related to $A(C_i)$ to calculate the assimilation parameters q, R_d, K and Γ via the least squares method. Once these are known, we obtain in a second step the quantity λ from the data points related to $g_{s\mathrm{H_2O}}(C_a)$. Finally, we use leaf anatomy to obtain $\nu(C_a)$.

3.6.2.1 Calculation of q, R_d, K and Γ

In order to calculate q, R_d, K and Γ we apply the method of least squares to equation (3.31)

$$A(C_i) = q\,\frac{C_i - \Gamma}{C_i + K} - R_d \tag{3.63}$$

q and K were defined in equations (3.29) and (3.30). If the rate of carboxylation is limited by Rubisco activity and not by insolation — which we may assume in our case, see Figure 3.8 — they are given as $q = V_{max}$ and $K = K_c\,(1 + p_o/K_o)$. First, we form from equation (3.63) and the six data points $(C_{i,k}, A_k)$ of Table 3.2 the sum

$$\sigma_A^2 = \sum_k \left[A(C_{i,k}) - A_k\right]^2 \tag{3.64}$$

σ_A^2 constitutes a measure for the deviation of the curve $A(C_i)$ from the data points $(C_{i,k}, A_k)$, (k = all data points). It depends on the four unknown quantities q, R_d, K and Γ. In order to obtain a "best fit" of the curve representing equation (3.63) to the data points, we have to locate the minimum of σ_A^2 ("nonlinear regression"). The minimum is characterised by the

value of the quadrupel (q, R_d, K, Γ) for which the four partial derivatives of σ_A^2 with respect to q, R_d, K and Γ vanish simultaneously. This system of four equations can readily be solved. Employing the temperature dependencies given by Bernacchi et al. ([8]) in expressions (3.32) the solutions are normalised to the temperature $T = 25\,°\mathrm{C}$. For the results see Table 3.3. The dotted curve in Figure 3.12(a) represents $A(C_i)$ emerging from reinsertion of the values representing the minimum of (3.64) into equation (3.63).

Table 3.2: Data pairs (C_i, A) and $(C_a, g_{s\,\mathrm{H_2O}})$ from [52] used to calculate the quantities (q, R_d, K, Γ) and λ, respectively, via the least squares method. The data were obtained at a temperature $T = 27.3\,°\mathrm{C}$ and a relative atmospheric humidity of 50 %.

C_i	55.5	145	340	492	647	1287	µmol/mol
A	-0.26	0.81	3.13	3.93	4.9	6.11	µmol/m^2/s
C_a	25	163	375	525	875	2000	µmol/mol
$g_{s\,\mathrm{H_2O}}$	31	29	25	24	22	17	mmol/m^2/s

3.6.2.2 Calculation of λ

In order to proceed with the calibration of $g(C_a)$ we need a numeric value of the Lagrangian multiplier λ which represents the cost of water. We obtain it in an indirect way from the data points $(C_{a,k}, g_{s\,\mathrm{H_2O},k})$ (k = all data points) given in Table 3.2 according to measurements of Overdieck and Strassemeyer ([52], Figure 3.12(b) displays the stomatal conductance $g_{s\,\mathrm{H_2O}}$ as a function of C_a).

Similarly as above we use nonlinear regression in order to obtain a "best fit" of the curve $g_{s\,\mathrm{H_2O}}(C_a)$ to the data points of Table 3.2. Using the relation $g_{s\,\mathrm{H_2O}} \approx g_{\mathrm{H_2O}} = ag$ (with $a = D_{\mathrm{H_2O}}/D_{\mathrm{CO_2}}$) we start with the expression

$$\sigma_g^2 = \sum_k \left[a\, g(C_{a,k}) - g_k\right]^2 \tag{3.65}$$

which depends on λ, the only parameter in $g(C_a)$ which is not yet fixed. Proceeding as above, the minimum of σ_g^2 is found at $\lambda = 1.17 \times 10^{-3}$. The dotted curve in Figure 3.12(b) represents $g_{s\mathrm{H_2O}}(C_a) \equiv a\, g(C_a)$ obtained from this value for λ.

In forming σ_g^2 we ignored the data point which corresponds to $C_a = 25\,\mu\mathrm{mol/mol}$. The formal reason for this omission is that the expression under the root sign in (3.39) becomes negative for $C_a = 25\,\mu\mathrm{mol/mol}$ which would lead to imaginary values of the conductance g. In physiological terms the omission is justified by the fact that the atmospheric CO_2 concentration $C_a = 25\,\mu\mathrm{mol/mol}$ implies a negative assimilation rate $A(C_a)$. Most probably, however, a plant tries to avoid a negative assimilation rate because otherwise it would lose water vapour *and* already assimilated carbon dioxide. Thus, in the framework of an optimisation scheme the data point with $C_a = 25\,\mu\mathrm{mol/mol}$ is to be viewed as an artefact and it is to be expected that the plant actually closes its stomata. (Note, that this conclusion is in agreement with expression (3.40).)

Table 3.3: Photosynthetic, environmental and anatomical parameters used to calculate $\nu(C_a)$ of *Ginkgo biloba* from equation (3.62). The temperature dependent quantities q, R_d, K and Γ refer to $T_{max} = 19.07\,°C$ (Values at other temperatures can be calculated from the expressions given in (3.32)).

Symbol	Value	Unit	Quantity	Source/Remarks
Photosynthetic parameters:				
q	4.28	$\mu mol/m^2/s$	see (3.31) and (3.32)	[52], [8], Table 3.2
R_d	0.11	$\mu mol/m^2/s$	see (3.31) and (3.32)	[52], [8], Table 3.2
K	205	$\mu mol/mol$	see (3.31) and (3.32)	[52], [8], Table 3.2
Γ	43	$\mu mol/mol$	see (3.31) and (3.32)	[52], [8], Table 3.2
$V_{max,25\,°C}$	7.34	—	see (3.32)	[52], [8], Table 3.2
$R_{d,25\,°C}$	0.16	—	see (3.32)	[52], [8], Table 3.2
$k_{25\,°C}$	0.48	—	see (3.32)	[52], [8], Table 3.2
$\gamma_{25\,°C}$	1.37	—	see (3.32)	[52], [8], Table 3.2
Environmental parameters:				
v_{wind}	3	m/s	Wind speed	rough estimate for Berlin
w_a	637	mmol/mol	Atmospheric humidity	equivalent to a relative humidity of 50 %, average value for Berlin during growth period [52]
T_{max}	19.07	°C	Leaf temperature	average value maximum temperature for Berlin during growth period [52]
λ	1.57×10^{-3}	—	"Cost of water"	[52], Table 3.2
Anatomical parameters:				
d_{st}^{geom}	31.9 ± 3.7	µm	Depth of stomatal opening, see Figures 3.3 and 3.13	own measurements
w_{st}^{max}	1.0	µm	Maximum width of stomatal opening	inferred (see text)
h_{st}^{cl}	14.3 ± 3.0	µm	Length of closed stomatal pore, see Figure 3.13	own measurements
h_{st}	13.3	µm	Length of stomatal opening (related to w_{st}^{max}, calculated from equation (3.68))	
a_{st}^{max}	36.44	μm^2	Maximum stomatal area	
d_{as}	218 ± 32	µm	Thickness of assimilation tissue, see Figure 3.13	own measurements
τ_{as}	1.571	—	Tortuosity of assimilation tissue	rough estimate
n_{as}	0.35	—	Porosity of assimilation tissue	rough estimate
l	84 ± 11	mm	Average leaf length	own measurements

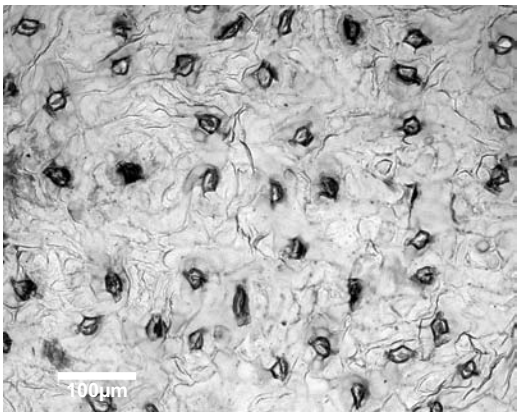

(a) Lower surface of a leaf with stomata.

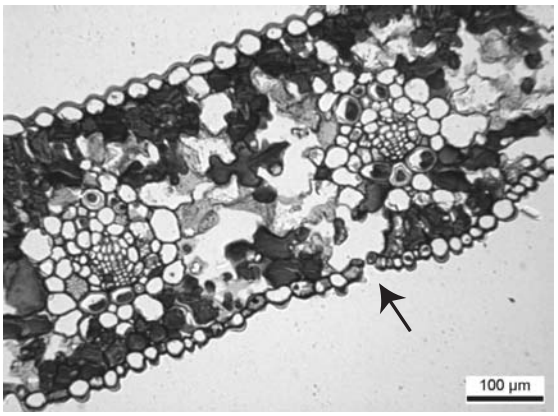

(b) Cross-section through a leaf with stoma (arrow).

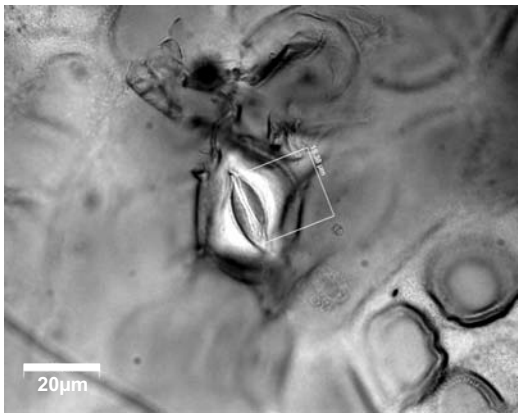

(c) Stoma from the Goethe tree in Weimar.

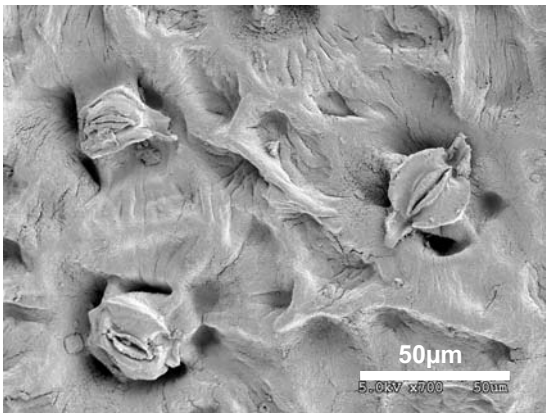

(d) Stomata from a fossil *Ginkgo* leaf.

Figure 3.13: *Ginkgo biloba* (Illustrations by Anita Roth-Nebelsick, Tübingen.)

3.6.2.3 Calculation of a_{st}^{max} resp. w_{st}^{max}

Apparently, stomata close when leaves are shed. Hence, direct measurements of the maximum stomatal area a_{st}^{max} of fossil leaves are impossible. Even for leaves of extant trees it is difficult to measure a_{st} or a_{st}^{max}.

The length h_{st}^{cl} of a closed stoma can easily be assessed from photographs as in Figure 3.13. Data of the temporal (diurnal) development of the width w_{st} of a stomatal opening (or of its maximum width w_{st}^{max}), however, are not so easily obtained. The reason is, as mentioned above, that leaves close their stomata when picked. Accordingly, we found only one value for w_{st}^{max} in the literature: Copeland ([18]) reports with respect to *Ginkgo biloba* that "the widest open pore I have observed measured 3.5 µm", but he gives neither other values nor a mean value nor any statistics for w_{st}^{max}.

Before pursuing this problem further we discuss another aspect of calculating stomatal area from length and width of the stomatal opening. We describe the stomatal opening as an ellipse with half axes $h_{st}/2$ and $w_{st}/2$. From geometry it is well known that this ellipse has the area

$$a_{st}^{max} = \frac{\pi}{4} h_{st} w_{st} \tag{3.66}$$

and the circumference

$$U = 2\,h_{st}\,E\,(e) \tag{3.67}$$

where $E(e) = \int_0^{\pi/2} \sqrt{1 - e^2 \sin^2\psi}\; d\psi$ and $e = \sqrt{1 - [w_{st}/h_{st}]^2}$ denote the complete elliptic integral of the second kind and the numeric eccentricity of the ellipse, respectively (see e.g. [1]). From the literature, it appears that the tissue which forms the inner strand of the stomatal opening is flexible against bending but not against stretching. This implies that the circumference U of the stomatal opening is (approximately) unaffected by any changes in the degree or shape of the stomatal opening, i.e. U = const.. Since we assume that the circumference of the stomatal opening is constant, irrespective of the current stomatal width, we may conclude from the closed stoma $U = 2\,h_{st}^{cl}$. Insertion of this constraint into equation (3.67) leads to

$$2\,h_{st}^{cl} = 2\,h_{st}\,E\left(\sqrt{1 - \left[\frac{w_{st}}{h_{st}}\right]^2}\right) \tag{3.68}$$

This is a transcendental equation for h_{st} which can not be solved in all generality. If, however, values of w_{st} (or, more interestingly, w_{st}^{max}) and h_{st}^{cl} are given (see Table 3.3) numerical solutions are readily obtained (as in Table 3.3).

3.6.2.4 Calculation of $\nu(C_a)$

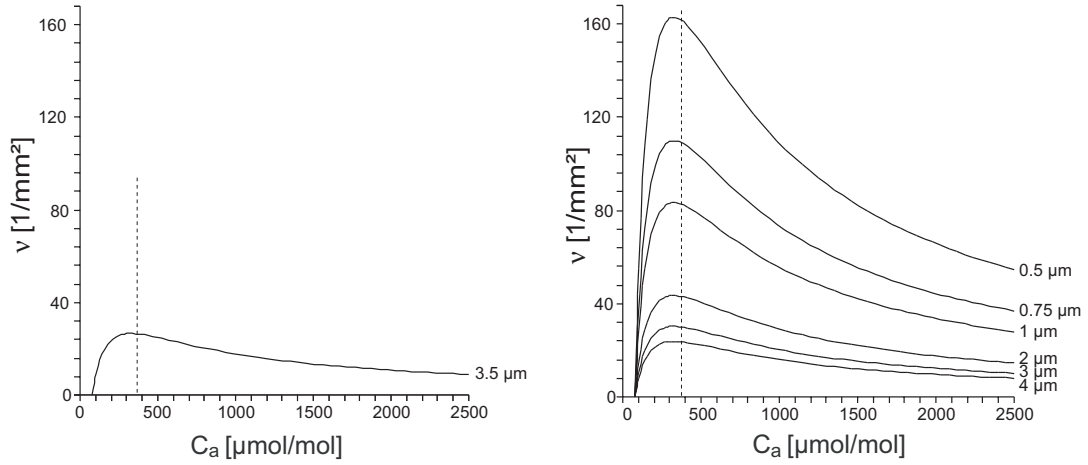

Figure 3.14: $\nu(C_a)$-curve calculated from expression (3.62). The atmospheric CO_2 concentration $C_a^{\text{now}} \approx 370\,\mu\text{mol/mol}$ is indicated by a vertical broken line. Parameters used (except w_{st}^{max}) are as in Table 3.3. (a) $w_{st}^{max} = 3.5\,\text{mm}^{-2}$. (b) The maximum stomatal width w_{st} is varied as indicated by the labels to the right of the curves.

Having nearly all ingredients at hand (we regard our knowledge of a_{st}^{max} resp. w_{st}^{max} still as preliminary) we can calculate the optimal $\nu(C_a)$-dependence for an adult *Ginkgo biloba* growing at an temperature $T_{max} = 19.07\,°\text{C}$ (average maximum temperature of the growth

period) in the field in Berlin. Inserting D_{CO_2} (from equation (3.9)) and the quantities given in Table 3.3 into expression (3.62) leads to Figure 3.14(a). According to our approach, it depicts the $\nu(C_a)$-curve calculated from the optimisation prodecure. In other words, it predicts the stomatal density of a multitude of fictitious *Ginkgo biloba* trees which are all identical to and grow — apart from atmospheric CO_2 concentration — in the same environment as the real adult *Ginkgo biloba* which has been examined by [52] in Berlin. Figure 3.14(b) shows what happens to the $\nu(C_a)$-curve of Figure 3.14(a) if the stomatal width w_{st} is varied. (The accompanying values of a_{st} can be calculated according to equations (3.66) through (3.68).)

The value $\nu(C_a = 370\,\mu\text{mol/mol}) = 27\,\text{mm}^{-2}$ predicted for $w_{st}^{max} = 3.5\,\mu\text{m}$ is probably too low. For stomatal densities of adult *Ginkgo biloba* we found the following sources (We exclude data of *Ginkgo biloba* saplings because their photosynthetic parameters are different from those of adult plants (see [52] and [5])):

(i) Overdieck and Strassemeyer give no definite value for the stomatal density of the individuum which they investigated in [52]. They merely cite Napp-Zinn ([49]) who cites in turn two other sources which provide stomatal densities of *Ginkgo biloba*, but without information on the corresponding temperatures, humidities and atmospheric CO_2 values: The first source (published in the year 1865 when $C_a \approx 290\,\mu\text{mol/mol}$, according to ice core data) claims $\nu = 120\,\text{mm}^{-2}$. The second source (published 1963 when $C_a \approx 320\,\mu\text{mol/mol}$, according to direct measurements) gives the range $\nu = 110\,\text{mm}^{-2} \ldots 140\,\text{mm}^{-2}$. In comparison with other sources these stomatal densities appear very high.

(ii) Data compiled by Royer ([58]) including 34 adult *Ginkgo biloba* which have been examined between the years 1856 ($C_a = 288\,\mu\text{mol/mol}$) and 2000 ($C_a = 369\,\mu\text{mol/mol}$) are in the range $\nu = 56\,\text{mm}^{-2} \ldots 157\,\text{mm}^{-2}$ with a mean value $\overline{\nu} = (87 \pm 19)\,\text{mm}^{-2}$.

(iii) Extant ($C_a = 366\,\mu\text{mol/mol}$) adult *Ginkgo biloba* in China investigated by Sun et al. ([64]) had stomatal densities $\nu = 78\,\text{mm}^{-2} \ldots 98\,\text{mm}^{-2}$, the shade leaves ($\overline{\nu} = 83\,\text{mm}^{-2}$) scattering over the whole range and the sun leaves ($\overline{\nu} = 96\,\text{mm}^{-2}$) clustering towards the upper limit.

Since the data base of the last two sources seems to be much broader than that of the first source, we calibrate w_{st}^{max} via equation (3.62) from the requirement that $\nu(C_a = 370\,\mu\text{mol/mol})$ should reproduce the mean values of the stomatal density cited in (ii) and (iii). $\overline{\nu} = 83\,\text{mm}^{-2}$ implies $w_{st}^{max} = 1.0\,\mu\text{m}$ (see Figure 3.14(b)) which we will henceforth apply.

3.6.3 Sensitivity of $\nu(C_a)$ against fluctuations of the photosynthetic, environmental and anatomical parameters

Because the fossil record provides usually only limited amounts of data it is little wonder that the accuracy of this data can often not be assessed by proper statistical methods or remains even dubious. Thus, if one wants to reconstruct $\nu(C_a)$-curves from fossil data it is helpful to know to what extent uncertainties in the photosynthetic, environmental and anatomical parameters influence the $\nu(C_a)$-curves obtained from equation (3.62).

We calculate now for *Ginkgo biloba* families of $\nu(C_a; \xi)$-curves which are generated by assigning various values to one of these parameters (we denote it ξ) while keeping the other

parameters constant at the values listed in Table 3.3. Putting it slightly different: we use the real *Ginkgo biloba* of Table 3.3 (or, rather, the $\nu(C_a)$-curve related to it) as starting point and generate an assortment of fictitious trees by varying the parameters of Table 3.3 one at a time through a range of hypothetical values. The fictitious trees are quantified by their $\nu(C_a;\xi)$-curves. Comparison of the $\nu(C_a;\xi)$-curves of the real and the fictitious trees allows to identify the most sensitive parameters. (We understand sensitivity in the sense that small deviations in the parameter value ξ cause large deviations in the stomatal density ν.)

In a reconstruction of $\nu(C_a)$-curves from fossil data this information is important. The degree of sensitivity establishes a hierarchy of the parameters: if reliable results are desired, the most sensitive parameters should be known with great accuracy, for the less sensitive parameters rough estimates of their values may be sufficient. If the desired accuracy can not be achieved (which is closer to the palaeontological reality) this hierarchy of sensitivity provides at least a tool to assess the reliabilty of the calculated results.

3.6.3.1 Sensitivity of $\nu(C_a)$ against fluctuations of the photosynthetic parameters

Figure 3.16 shows that the stomatal density ν is most sensitive against variations of the parameter q. Variations in K, produce a much smaller change of ν, and the effects of varying R_d and Γ are — compared with q — almost negligible.

3.6.3.2 Sensitivity of $\nu(C_a)$ against fluctuations of the environmental parameters

Of the environmental parameters, the wind speed v_{wind} has the least impact on ν (see Figure 3.17). The curves $\nu(C_a; v_{wind})$ are virtually indistinguishable for a very wide range of wind speeds. Only if v_{wind} approaches zero $\nu(C_a; v_{wind})$ increases somewhat. In this limit, however, expression (3.16) for the thickness d_{bl} of the boundary layer loses its meaning (the limit $\lim_{v_{wind}\to 0} d_{bl} = \infty$, implied by (3.16), is certainly unphysical).

Variations of atmospheric humidity w_a and cost of water λ cause very similar effects: the maxima of both $\nu(C_a; w_a)$ and $\nu(C_a;\lambda)$ increase and become sharper if humidity increases resp. if water becomes cheaper.

If the temperature T increases, the maxima of $\nu(C_a; T)$ increase, too, they become however less pronounced and shift to higher C_a-values.

3.6.3.3 Sensitivity of $\nu(C_a)$ against fluctuations of the anatomical parameters

Inspection of Figure 3.18 reveals that the anatomical parameters describing the assimilating tissue do not strongly influence the $\nu(C_a)$-curve. (Notice that the values $d_{as} = 1000\,\mu\text{m}$, $d_{as} = 1000\,\mu\text{m}$, $\tau_{as} = 5$ and $\tau_{as} = 4$ are absurdly high.) Still less important is the leaf length l. Area and thickness of the stomatal opening have a much stronger impact on $\nu(C_a)$ (see Figure 3.15).

Conclusion

Summarising, we may state that of the 14 parameters we have investigated in Figures 3.15 through 3.18 the following cause major modifications of the $\nu(C_a)$-curve:

- The photosynthetic parameters q (and, of secondary importance, K).

- The atmospheric humidity w_a, the cost of water λ and the temperature T.
- Area a_{st} and thickness d_{st} of the stomatal pore.

The dominance of the the environmental parameters which indicate the availability of water is no surprise: it is the central idea of the optimum principle that assimilation and transpiration are strongly interconnected and that the means for their regulation are number density and geometry of the stomatal pores.

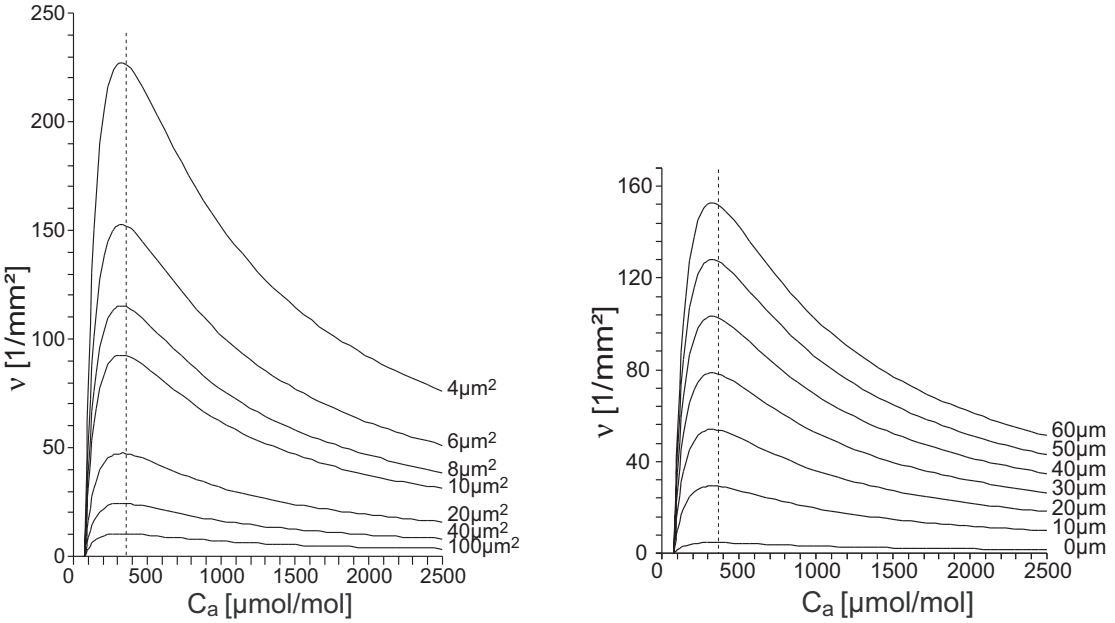

(a) $\nu(C_a; a_{st})$ a_{st}: stomatal area

(b) $\nu(C_a; d_{st})$ d_{st}: depth of stomatal pore

Figure 3.15: Dependance of $\nu(C_a)$-curves on the anatomical parameters. Parameters used (except those which are varied) are as in Table 3.3 and related to the adult *Ginkgo biloba* tree investigated in [52] in Berlin. Values of varied quantities are indicated by the labels to the right of the curves. The present atmospheric CO_2 concentration $C_a \approx 370\,\mu\text{mol/mol}$ is indicated by a vertical broken line. (See also Figure 3.18.)

3.6.4 Reconstruction of palaeoatmospheric CO_2 from fossil leaves of *Ginkgo biloba*

We make no attempt to perform a serious reconstruction of palaeoatmospheric CO_2 from fossil leaves of *Ginkgo biloba* (Figure 3.19 shows a sample of such leaves). We shall rather give an example which illustrates the problems arising from the fact that stomatal density ν is not a function of palaeoatmospheric CO_2 alone. The examples given in section 3.6.3 included a strong dependence on the (palaeo)atmospheric water vapour concentration and on the cost of water which is related to (palaeo)precipitation, (palaeo)evaporation and the (palaeo) ground water regime.

These interconnections imply that the relation $\nu(C_a)$ can not be inverted unambiguously: Knowledge of ν alone is not sufficient to reconstruct the palaeoatmospheric C_a. The inversion

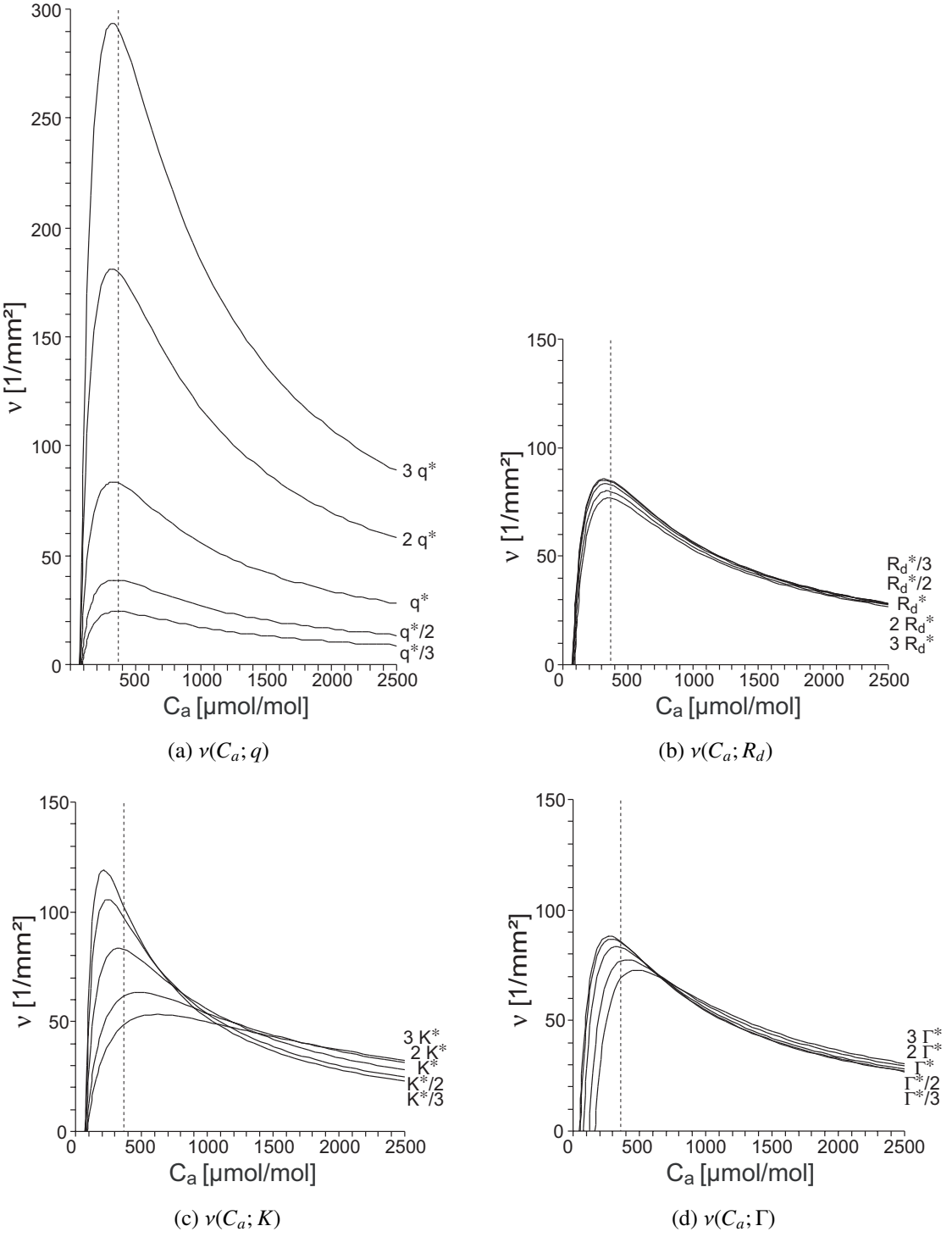

(a) $\nu(C_a; q)$

(b) $\nu(C_a; R_d)$

(c) $\nu(C_a; K)$

(d) $\nu(C_a; \Gamma)$

Figure 3.16: Dependance of $\nu(C_a; \xi)$-curves on the photosynthetic parameters $\xi = q, R_d, K$ and Γ. Parameters are as in Table 3.3 and related to the adult *Ginkgo biloba* tree investigated in [52] in Berlin. Each family of $\nu(C_a; \xi)$-curves is generated by substituting $\xi = \xi^*/3, \xi^*/2, \xi^*, 2\,\xi^*, 3\,\xi^*$ into equation (3.62) where ξ^* is the parameter value given in Table 3.3. The present atmospheric CO_2 concentration $C_a \approx 370\,\mu\text{mol/mol}$ is indicated by vertical broken lines.

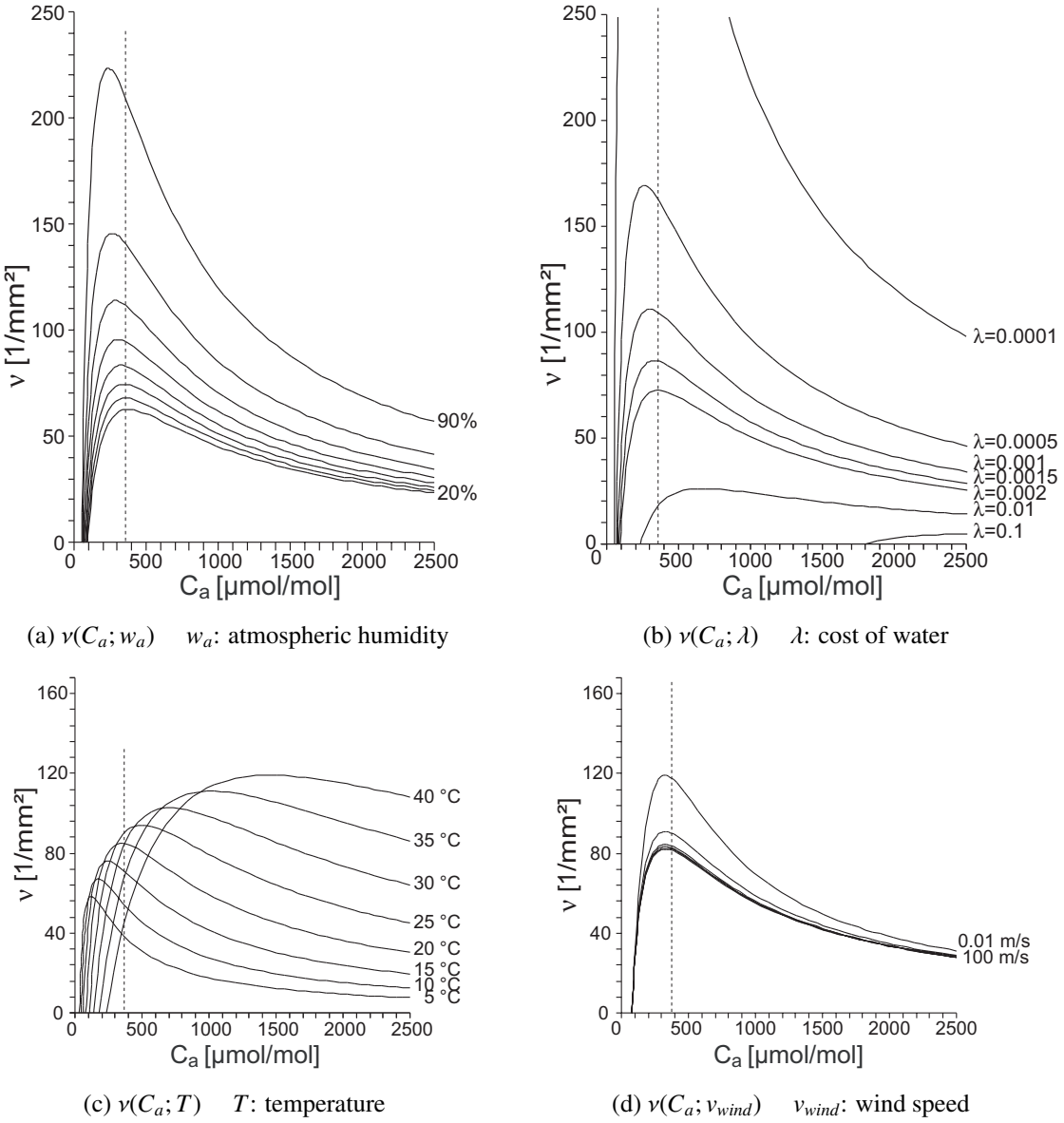

(a) $\nu(C_a; w_a)$ w_a: atmospheric humidity

(b) $\nu(C_a; \lambda)$ λ: cost of water

(c) $\nu(C_a; T)$ T: temperature

(d) $\nu(C_a; v_{wind})$ v_{wind}: wind speed

Figure 3.17: Dependance of $\nu(C_a; \xi)$-curves on the environmental parameters atmospheric humidity, cost of water, temperature, and wind speed. Parameters used (except those which are varied) are as in Table 3.3 and related to the adult *Ginkgo biloba* tree investigated in [52] in Berlin. Values of varied quantities are indicated by the labels to the right of the curves. The present atmospheric CO_2 concentration $C_a \approx 370\,\mu\text{mol/mol}$ is indicated by a vertical broken line.
(a) The (relative) atmospheric humidity varies from 20 % to 90 % in steps of 10 %.
(b) The cost of water varies. $\lambda = 0.0001\,,\ 0.0005\,,\ 0.001\,,\ 0.0015\,,\ 0.002\,,\ 0.01$ and 0.1 .
(c) The temperature varies from 5 °C to 40 °C in steps of 5 °C.
(d) The wind speed is varied. Values of v_{wind} are 0.01 m/s, 0.1 m/s, 1 m/s, 3 m/s, 10 m/s, 100 m/s (from upper- to lowermost curve).

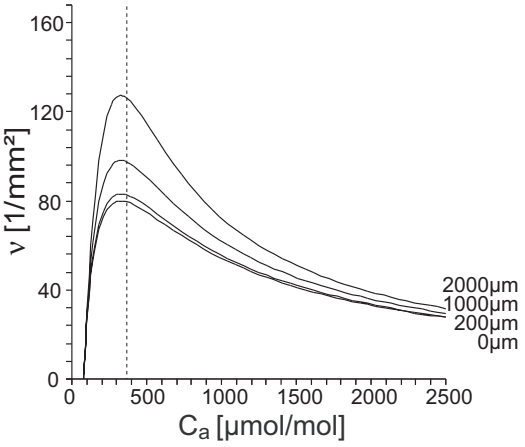

(a) $\nu(C_a; d_{as})$ d_{as}: thickness of assimilating tissue

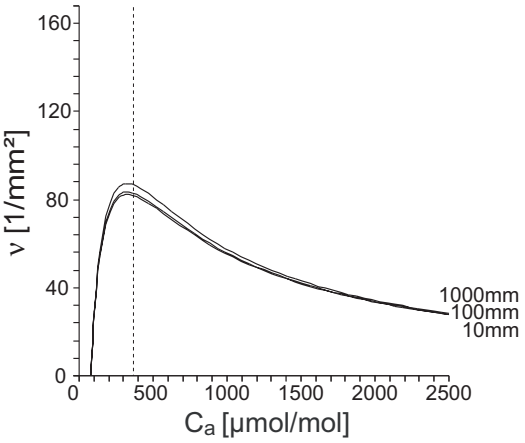

(b) $\nu(C_a; l)$ l: length of a leaf

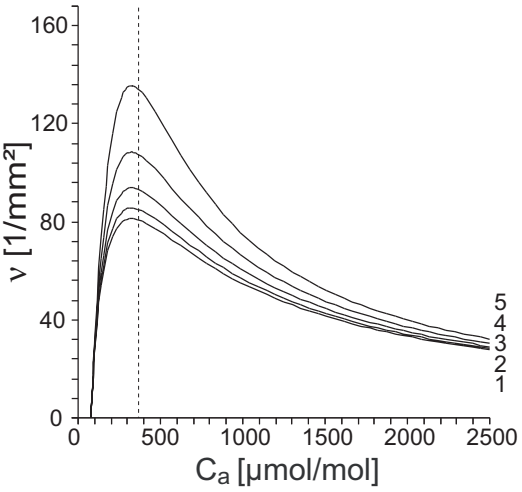

(c) $\nu(C_a; t_{as})$ t_{as}: tortuosity of assimilating tissue

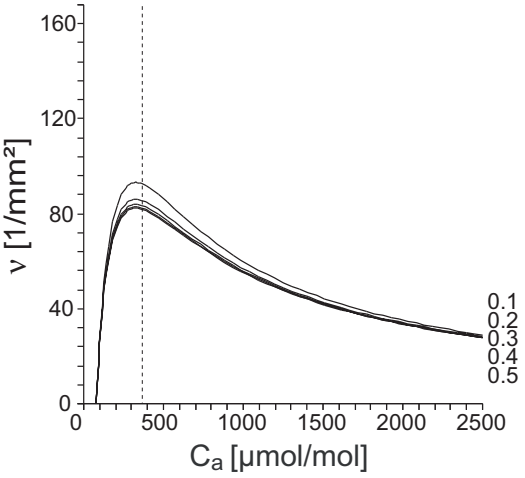

(d) $\nu(C_a; n_{as})$ n_{as}: porosity of assimilating tissue

Figure 3.18: Dependance of $\nu(C_a)$-curves on the anatomical parameters. Parameters used (except those which are varied) are as in Table 3.3 and related to the adult *Ginkgo biloba* tree investigated in [52] in Berlin. Values of varied quantities are indicated by the labels to the right of the curves. The present atmospheric CO_2 concentration $C_a \approx 370\,\mu\text{mol/mol}$ is indicated by a vertical broken line. (See also Figure 3.15.)

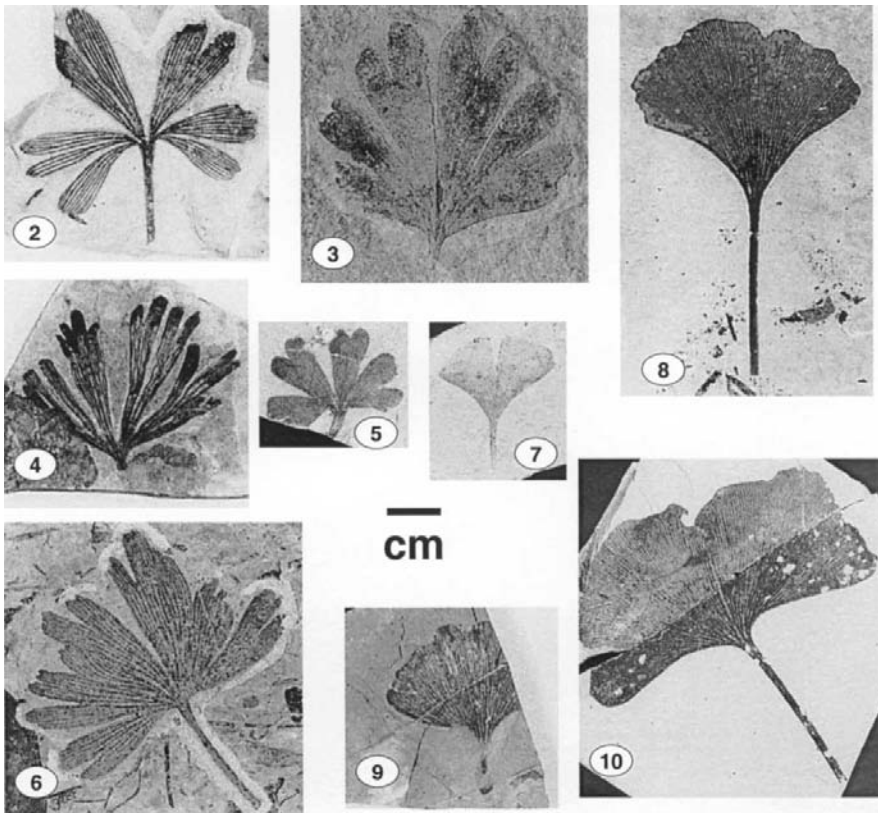

Figure 3.19: Various Eocene *Ginkgo* leaf fossils from the Pacific Northwest (see [48]). (2): *Ginkgo dissecta* sp.nov., holotype. (3) *Ginkgo dissecta* sp.nov. (4) *Ginkgo dissecta* sp.nov., paratype. (5) *Ginkgo dissecta* sp.nov. (6) *Ginkgo dissecta* sp.nov. (7) *Ginkgo biloba*. (8) *Ginkgo biloba*. (9) *Ginkgo biloba*. (10) *Ginkgo biloba*. (Photographs from [48].)

requires independent information on the parameters which have been demonstrated in section 3.6.3 to exert great influence on ν. Most important is information on the environment, e.g. on the temperature and the availability of water.

In cases where the palaeoatmospheric CO_2 is already known expression (3.62) can be used as palaeothermometer or palaeohygrometer (provided values of w_a resp. T can be obtained from independent sources).

Figure 3.20(b) demonstrates the influence of temperature, atmospheric humidity and water availability on the reconstruction of palaeoatmospheric CO_2 from stomatal density of fossilised leaves which grew during the Palaeocene and the Eocene (Figure 3.20(a), data are from Royer [58]). Calculation of C_a has been done by solving equation (3.62) numerically after inserting the values for ν, T, w_a and λ supplied in Figure 3.20(a) and indicated to the right of the curves in Figure 3.20(b). Values of the other parameters are from Table 3.3.

Figure 3.20 allows to draw the following implications:

- Although the absolute C_a-values predicted by the four curves in Figure 3.20(b) diverge grossly, the curves are very similar in their structure (notice, for instance, the sequence of maxima and minima).

- Misjudging the palaeotemperature by 10 °C may lead to C_a-values which are wrong by a factor 2.5. Errors of similar magnitude follow from erroneous values of w_a or λ.

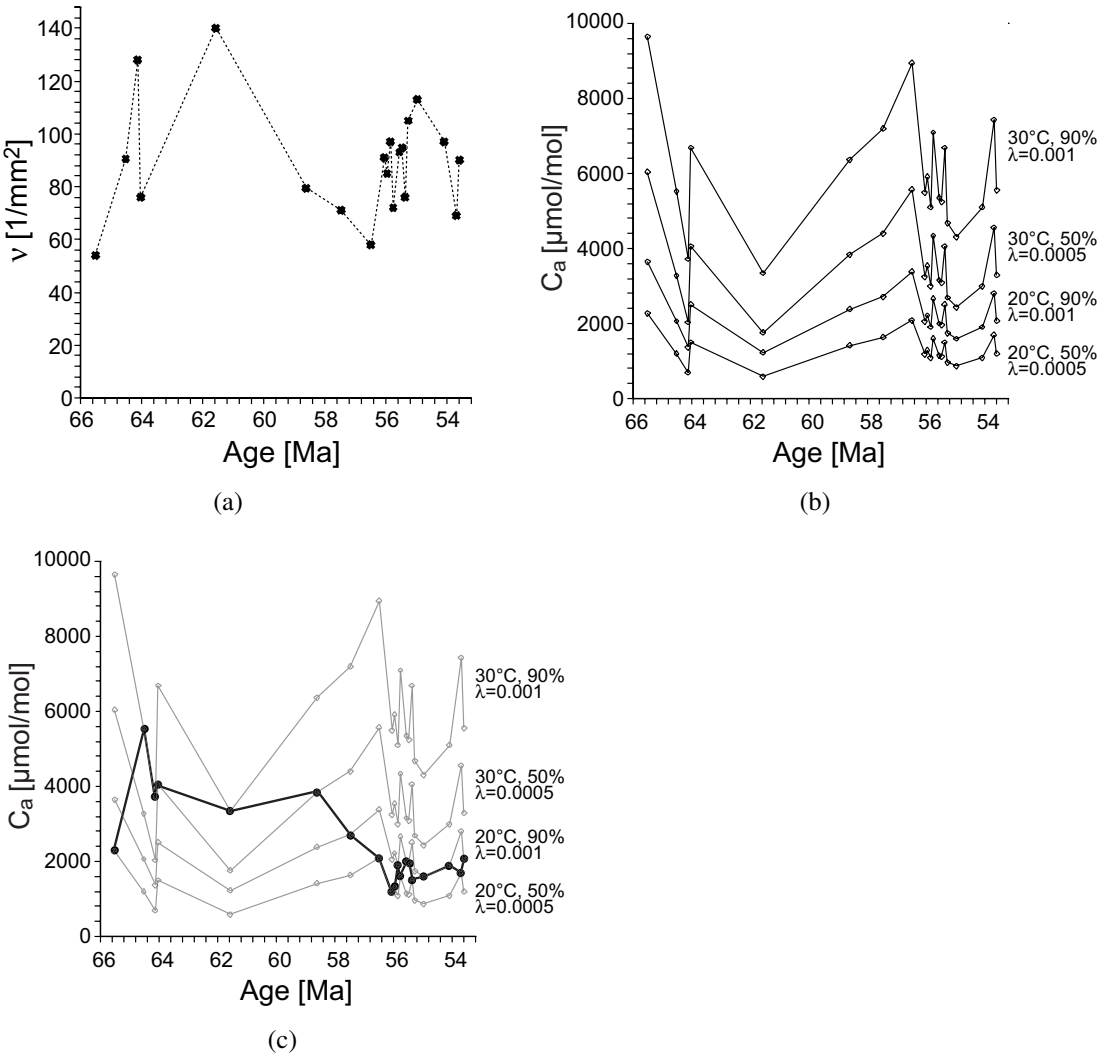

Figure 3.20: (a) Stomatal densities of fossilised leaves from the Palaeocene and Eocene (data points are from Royer [58], broken lines indicate merely interpolations between data points).
(b) Reconstruction of palaeoatmospheric CO_2 from the stomatal densities depicted in (a). The values of temperature, atmospheric humidity and cost of water λ used in calculating C_a from expression (3.62) are indicated to the right of the curves.
(c) Variations in environmental conditions may lead to a $C_a(t)$-curve (black line) which is quite different from $C_a(t)$-curves (grey lines) for which constant environmental conditions are assumed.

- A variation in environmental conditions may lead to a temporal development of palaeoatmospheric CO_2 which is quite different from the development under (supposedly) constant environmental conditions (see Figure 3.20(c)).

3.7 Obtaining $g(C_a)$ and $\nu(C_a)$ from a simplified model

Discussing the CO_2-ratio $\kappa = C_a/C_i$ in section 3.4.4 we realised that the product $\lambda a \left(w_i^{sat} - w_a\right)$ which consists of several variables can be replaced by the single quantity $\kappa_\infty = \lim_{C_a \to \infty} C_i/C_a$. We also saw that (i) κ_∞ represents an upper boundary of $\kappa(C_a)$ and that (ii) $\kappa(C_a)$ deviates for no value of C_a very much from κ_∞. These observations suggest that it should be possible to deduce an expression for $g(C_a)$ not only from the optimisation principle introduced in section 3.4 but also from the more simple condition that the ratio $\kappa = C_i/C_a$ should attain the same constant value $\overline{\kappa}$ for all C_a. Put differently, one *assumes* proportionality between C_i and C_a. The benefit of this assumption will be a mathematically much simpler model for the relation between ν and C_a than the one presented in equation (3.61). The price to be paid for simplicity is, of course, accuracy.

In order to derive this simpler relation we start as in section 3.4 by equating expressions (3.24) and (3.31) for the assimilation rate A. Solving for g and replacing C_i via the relation $C_i = \overline{\kappa}\, C_a$ we obtain immediately the equivalent of equation (3.39):

$$g = \frac{\overline{\kappa}\, C_a\,(q - R_d) - (q\Gamma + KR_d)}{(1 - \overline{\kappa})\, C_a\,(\overline{\kappa}\, C_a + K)} \tag{3.69}$$

Proceeding as in section 3.4, i.e. equating expressions (3.69) and (3.23) and solving for ν completes the derivation of $\nu(C_a)$:

$$\nu = \xi\, \frac{\overline{\kappa}\, C_a\,(q - R_d) - (q\Gamma + KR_d)}{\eta\, {C_a}^2\, \overline{\kappa}\,(1 - \overline{\kappa}) + C_a\,[\eta K(1 - \overline{\kappa}) - \overline{\kappa}(q - R_d)] - (q\Gamma + KR_d)} \tag{3.70}$$

where

$$\xi := \frac{d_{st}\, {\tau_{st}}^2}{a_{st}\,(d_{bl} + d_{as}\, {\tau_{as}}^2/n_{as})} \qquad \text{and} \qquad \eta := \frac{D_{CO_2}}{(d_{bl} + d_{as}\, {\tau_{as}}^2/n_{as})} \tag{3.71}$$

Inserting $C_i = \overline{\kappa}\, C_a$ into equation (3.31) we find for the assimilation rate

$$A = q\, \frac{\overline{\kappa}\, C_a - \Gamma}{\overline{\kappa}\, C_a + K} - R_d \tag{3.72}$$

The asymptotic values for $C_a \to \infty$ are the same as in section 3.4:

$$\lim_{C_a \to \infty} g = 0 \tag{3.73}$$

$$\lim_{C_a \to \infty} C_i = \infty \tag{3.74}$$

$$\lim_{C_a \to \infty} A = q - R_d \tag{3.75}$$

$$\lim_{C_a \to \infty} \nu = 0 \tag{3.76}$$

We emphasize that the complex model and the simple model employ the submodels diffusion and assimilation in exactly the same way. The complex model, however, draws additional information from the optimisation approach and *derives* that the ratio $\kappa = C_i/C_a$ is more or less constant, while the simple model takes this fact simply for granted. This establishes a clear hierarchy: the complex model can be used to justify the simple model but not *vice versa*. Figure 3.21 illustrates the different predictions of the two models if applied to *Ginkgo biloba*.

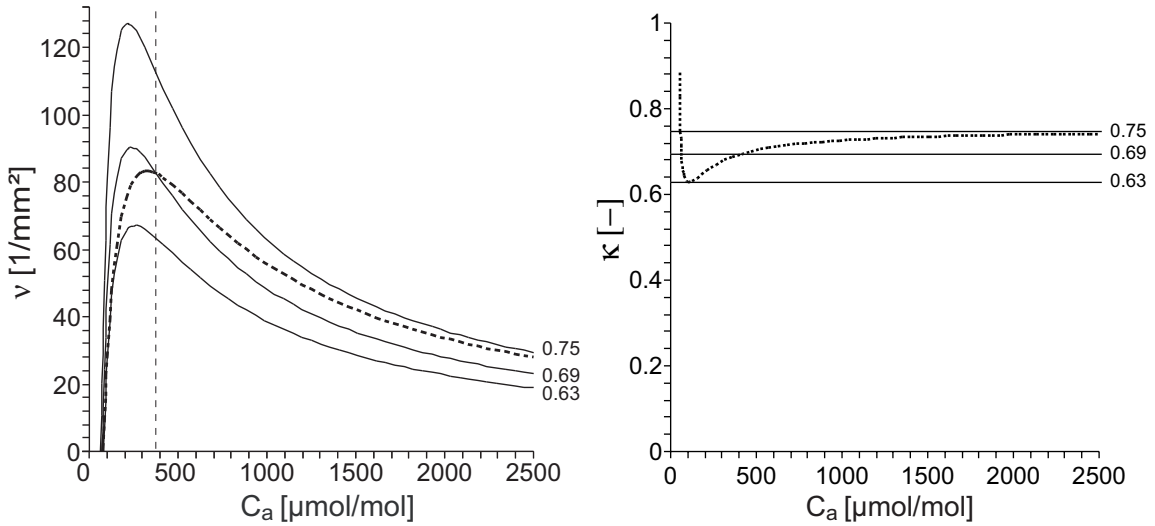

(a) (b)

Figure 3.21: (a) $\nu(C_a)$ curves derived from the optimisation principle (expression (3.61), broken line) and from the simple model (expression (3.70), solid lines). The solid curves have been obtained with the C_i/C_a-ratios $\overline{\kappa} = \kappa_\infty = 0.75$, $\overline{\kappa} = 0.69$ and $\overline{\kappa} = 0.63$. Other parameters are as in Table 3.3. The value $\overline{\kappa} = 0.69$ has been fixed from the requirement that the curve obtained via the optimisation principle intersects the curve representing the simple model at $C_a = 370\,\mu\text{mol/mol}$ (vertical broken line).
(b) $\kappa(C_a)$ curve according to the optimisation principle (expression (3.56), broken line) and straight lines, representing the simple model (solid lines with $\overline{\kappa} = \kappa_\infty = 0.75$, $\overline{\kappa} = 0.69$ and $\overline{\kappa} = 0.63$).

4 Bibliography

[1] Arfken, G. (1970): Mathematical Methods for Physicists. Academic Press, New York.

[2] Aris, R. (1975): The mathematical theory of diffusion and reaction in permeable catalysts. The theory of the steady state. Oxford University Press, London.

[3] Beerling, D.J., Woodward, F.I. (1995): Leaf stable carbon isotope composition records increased water-use efficiency of C_3 plants in response to atmospheric CO_2 enrichment. Functional Ecology **9**, 394–401.

[4] Beerling, D.J., Woodward, F.I. (1997): Changes in land plant function over the Phanerozoic: reconstructions based on the fossil record. Botanical Journal of the Linnean Society **124**, 137–153.

[5] Beerling, D.J., McElwain, J.C., Osborne, C.P. (1998): Stomatal responses of the 'living fossil' *Ginkgo biloba* L. to changes in atmospheric CO_2 concentrations. J. of Exp. Bot., **49**, 1603–1607.

[6] Beerling, D.J., Osborne, C.P., Chaloner, W.G. (2001): Evolution of leaf from in land plants linked to atmospheric CO_2 decline in the late Palaeozoic era. Nature **419**, 352–354.

[7] Beerling, D.J., Royer, D.L. (2002): Reading a CO_2 signal from fossil stomata. New Phytologist **153**, 387–397.

[8] Bernacchi, C.J., Pimentel, C., Long, S.P. (2003): *In vivo* temperature response functions of parameters required to model RuBP-limited ohotosynthesis. Plant, Cell and Environment **26**, 1419–1430.

[9] Berner, R.A., Kothvala, Z. (2001): GEOCARBIII: A revised model of atmospheric CO_2 over Phanerozoic time. American Journal of Science **301**, 182–204.

[10] Berninger, F., Mäkelä, A., Hari, P. (1996): Optimal Control of Gas Exchange during Drought: Empirical Evidence. Annals of Botany **77**, 469–476.

[11] Bodenstedt, F. (1881): Die Lieder und Sprüche des Omar Châjjam. Schlettersche Buchhandlung, Breslau. (zitiert nach: `http://www.omarkhayyamnederland.com`)

[12] Brecht, B. (1981): Die Gedichte von Bertolt Brecht in einem Band. Suhrkamp Verlag, Frankfurt am Main.

[13] Buckley, T.N., Miller, J.M., Farquhar, G.D. (2002): The Mathematics of Linked Optimisation for Water and Nitrogen Use ina Canopy. Silva Fennica **36**, 639–669.

[14] Carlquist, S. (2001): Comparative wood anatomy. Berlin, Heidelberg, New York.

[15] von Caemmerer, S., Evans, J.R. (1991): Determination of the average partial pressure of CO_2 in chloroplasts from leaves of several C_3 plants. Australian Journal of Plant Physiology. **18**, 287–306.

[16] Chapman, D.C., Rand, R.H., Cooke, J.R. (1977): A Hydrodynamical Model of Bordered Pits in Conifer Tracheids. Journal of Theoretical Biology **206**, 91–107.

[17] Choat, B., Ball, M., Luly, J., Holtum, J. (2003): Pit Membrane Porosity and Water Stress-Induced Cavitation in Four Co-Existing Dry Rainforest Tree Species. Plant Physiology **131**, 41–48.

[18] Copeland, E.B. (1902): The Mechanism of Stomata. Annals of Botany, **16**, 327–364.

[19] Cowan, I.R. (1977): Stomatal behaviour and environment. Adv. Bot. Res. **4**, 117–228.

[20] Cowan, I.R., Farquhar G.D. (1977): Stomatal function in relation to leaf metabolism and environment. Symposia of the Society for Experimental Biology **31**, 471–505.

[21] Cowan, I.R. (2002): Fit, Fitter, Fittest; Where Does Optimisation Fit In?. Silva Fennica **36**, 745–754.

[22] Debenedetti, P. G. (1996): Metastable Liquids. Princeton University Press, Princeton, New Jersey.

[23] Edwards, D., Kerp, H., Hass, H. (1998): Stomata in early land plants: an anatomical and ecophysiological approach. Journal of Experimental Botany **49**, 255–278.

[24] Esau, K. G. (1962): Anatomy of Seed Plants. Wiley, New York.

[25] Farquhar, G.D., von Caemmerer, S., Berry, J.A. (1980): A biochemical model of photosynthetic CO_2 assimilation in leaves of C_3 species. Planta **149**, 78–90.

[26] Farquhar, G.D., Ehleringer, J.R., Hubick, K.T. (1989): Carbon isotope discrimination and photosynthesis. Annual Review of Plant Physiology and Plant Molecular Biology **40**, 503–537.

[27] Farquhar, G.D., von Caemmerer, S., Berry, J.A. (2001): Models of Photosynthesis. Plant Physiology **125**, 42–45.

[28] Farquhar, G.D., Buckley, T.N., Miller, J.M. (2002): Optimal Stomatal Control in Relation to Leaf Area and Nitrogen Content. Silva Fennica **36**, 625–637.

[29] Fforde, J. (2005): Something Rotten. Hodder & Stoughton, London.

[30] Grathwohl, P. (1998): Diffusion in natural media: Contaminant Transport, Sorption/Desorption and Dissolution Kinetics, Kluwer Academic Publishers, Boston.

[31] Hacke, U.G., Sperry, J.S., Wheeler, J.K., Castro, Laura (2006): Scaling of angiosperm xylem structure with safety and efficiency. Tree Physiology **26**, 689–701.

[32] Holbrook, N.M., Ahrens, E.T., Burns, M.J., Zwieniecki, M.A. (2001): In vivo observation of cavitation and embolism repair using magnetic resonance imaging. Plant Physiol. **126**, 27–31.

[33] Holbrook, N.M., Zwieniecki, M.A. (1999): Embolism repair and xylem tension. Do we need a miracle? Plant Physiol. **120**, 7–10.

[34] Hopkins, W.G., Hüner, N.P.A (2004): Introduction to Plant Physiology. John Wiley and Sons.

[35] Jagger, M., Richards, K. (1967): Sitting On A Fence. (Text according to `http://www.keno.org/stones_lyrics/Sittingonafence.htm`)

[36] Körner, C. (1988): Does Global Increase of CO_2 Alter Stomatal Density? Flora **181**, 253-257.

[37] Konrad, W., Roth-Nebelsick, A., Kerp, H., Hass, H., (2000): Transpiration and assimilation of Early Devonian land plants with axially symmetric telomes — simulations on the tissue level. Journal of Theoretical Biology **206**, 91–107.

[38] Konrad, W., Roth-Nebelsick, A. (2003): The dynamics of gas bubbles in conduits of vascular plants and implications for embolism repair. Journal of Theoretical Biology **224**, 43–61.

[39] Konrad, W., Roth-Nebelsick, A. (2005): The Significance of Pit Shape for Hydraulic Isolation of Embolized Conduits of Vascular Plants During Novel Refilling. J. Biol. Physics **31**, 57–71.

[40] Konrad, W., Roth-Nebelsick, A. (2006): Embolism formation and repair in vascular plants: the role of cell wall mechanics, in: Proceedings of the Fifth Plant Biomechanics Conference, Editor: Lennart Salmén, Stockholm, p. 417–422 (Volume II).

[41] Kreyszig, E. (1991): Differential Geometry, Dover Publications, New York

[42] Landau, L.D. and Lifschitz, E.M. (1989): Lehrbuch der Theoretischen Physik VII, Elastizitätstheorie. Akademie-Verlag, Berlin.

[43] Larcher, W. (1997): Physiological plant ecology. 3rd ed. Springer Verlag, New York.

[44] Lösch, R. (2001): Wasserhaushalt der Pflanzen. Quelle und Meyer, Wiebelsheim.

[45] Mäkelä, A., Berninger, F., Hari, P. (1996): Optimal Control of Gas Exchange during Drought: Theoretical Analysis. Annals of Botany **77**, 461–467.

[46] Maris, H., Balibar, S. (2000): Negative pressures and cavitation in liquid helium. Physics Today **53**, 29–34.

[47] Moore, R., Clark, W.D., Vodopich, D.S. (1998): Botany. McGraw-Hill Book Company, Boston.

[48] Mustoe, G.E. (2002): Eocene *Ginkgo* leaf fossils from the Pacific Nortwest. Canadian Journal of Botany **80**, 1078–1087.

[49] Napp-Zinn, K. (1966): Anatomie des Blattes. I. Blattanatomie der Gymnospermen. Borntraeger, Berlin.

[50] Nobel, P.S. (1999): Physicochemical and environmental plant physiology. 2nd ed. Academic Press, New York.

[51] Oertli, J.J. (1971): The stability of water under tension in the xylem. Zeitschrift fuer Pflanzenpysiologie **65**, 195–209.

[52] Overdieck, D., Strassemeyer, J. (2005): Gas exchange of *Ginkgo biloba* leaves at different CO_2 concentration levels. Flora **200**, 159–167.

[53] Parkhurst, D.F. (1994) Diffusion of CO_2 and other gases inside leaves. New Phytol. **126**, 449–479.

[54] Parkhurst, D.F. & Mott, K.A. (1990) Intercellular Diffusion Limits to CO_2 Uptake in Leaves. Plant Physiol. **94**, 1024–1032.

[55] Pickard, W.F. (1981): The ascent of sap in plants. Prog. Biophys. molec. Biol. **37**, 181–229.

[56] Reif, F. (1974): Fundamentals of statistical and thermal physics. McGraw-Hill.

[57] Roedel, W. (1994): Physik unserer Umwelt: Die Atmosphäre. Springer-Verlag, Heidelberg.

[58] Royer, D.L. (2003): Estimating latest Cretaceous and Tertiary atmospheric CO_2 from stomatal indices. Geological Society of America Special Paper **369**, 79–93.

[59] Shen, F., Gao, R., Liu, W., Zhang, W. (2002): Physical analysis of the process of cavitation in xylem sap. Tree Physiology **22**, 655–659.

[60] Shen, F., Wenji, L., Rongfu, G., Hu, H. (2003): A careful analysis of gas bubble dynamics in xylem. J. Theoretical Biology **225**, 229–233.

[61] Stein, W.E., Mannolini, F., VanAller Hernick, L., Landing, E., Berry, C.M. (2007): Giant cladoxylopsid trees resolve the enigma of the Earth's earliest forest stumps at Gilboa. Nature **446**, 904–907.

[62] Stewart, W.E., Rothwell, G.W. (1993): Paleobotany and the Evolution of Plants. Cambridge University Press, Cambridge.

[63] Strasburger, E. (1998): Lehrbuch der Botanik. 34. Auflage, Spektrum Akademischer Verlag, Heidelberg.

[64] Sun, B., Dilcher, D.L., Beerling, D.J., Zhang, C., Yan, D., Kowalski, E., (2003): Variation in *Ginkgo biloba* L. leaf characters across a climatic gradient in China. PNAS, **100**, 7141–7146.

[65] Taiz, L., Zeiger, E. (2006): Plant Physiology. Sinauer Associates, Sunderland, Massachusetts.)

[66] Richter, H., Cruiziat, P.: A Brief History of the Study of Water Movement in the Xylem. at `http://3e.plantphys.net` (accompanying: Taiz, L., Zeiger, E. (2006): Plant Physiology. Sinauer Associates, Sunderland, Massachusetts.)

[67] Temperley, H.N.V., Trevena, D.H. (1993): Metastability of the Liquid-Vapor Transition and Related Effects. Journal of Statistical Physics **77**, 501–508.

[68] Young, W.C., Budynas, R.G. (2002): Roark's Formulas for Stress and Strain. McGraw-Hill, New York.

[69] Waechter, F.K. (1997): Da bin ich. Diogenes Verlag, Zürich.

[70] Willis, K.J., McElwain, J.C. (2002): The Evolution of Plants. Oxford University Press, Oxford.

[71] Woodward, F.I. (1986): Stomatal numbers are sensitive to increase in CO_2 from preindustrial levels. Nature **327**, 617–618.

5 Publications

5.1 Konrad, W., Roth-Nebelsick, A.: *The Dynamics of Gas Bubbles in Conduits of Vascular Plants and implications for embolism repair*, Journal of Theoretical Biology 224 (2003), p. 43–61.

Available online at www.sciencedirect.com
SCIENCE DIRECT®
Journal of Theoretical Biology 224 (2003) 43–61
Journal of Theoretical Biology
www.elsevier.com/locate/jtbi

The dynamics of gas bubbles in conduits of vascular plants and implications for embolism repair

W. Konrad, A. Roth-Nebelsick*

Institut für Geowissenschaften, Sigwartstrasse 10, D-72076 Tübingen, Germany

Received 5 September 2002; received in revised form 13 March 2003; accepted 14 March 2003

Abstract

Pressure-induced tensions in the xylem, the water conducting tissue of vascular plants, can lead to embolism in the water-conducting cells. The details and mechanisms of embolism repair in vascular plants are still not well understood. In particular, experimental results which indicate that embolism repair may occur during xylem tension cause great problems with respect to current paradigms of plant water transport. The present paper deals with a theoretical analysis of interfacial effects at the pits (pores in the conduit walls), because it was suggested that gas–water interfaces at the pit pores may be involved in the repair process by hydraulically isolating the embolized conduit. The temporal behaviour of bubbles at the pit pores was especially studied since the question of whether these pit bubbles are able to persist is of crucial importance for the suggested mechanism to work. The results indicate that (1) the physical preconditions which are necessary for the suggested mechanism appear to be satisfied, (2) pit bubbles can achieve temporal stability and therefore persist and (3) dissolving of bubbles in the conduit lumen may lead to the final breakdown of the hydraulic isolation. The whole process is, however, complex and strongly dependent on the detailed anatomy of the pit and the contact angle.

Keywords: Xylem; Water conduction; Embolism; Pits

1. Introduction

According to the cohesion-tension theory, upward water flow in land plants is generated by a pressure gradient originating in the water loss of transpiring leaves (Zimmermann, 1983; Tyree and Ewers, 1991). This mechanism may cause large tension gradients in the xylem, the water-conducting tissue of vascular plants although the magnitude of the tension is still under debate (Pickard, 1981; Holbrook et al., 1995; Pockman et al., 1995; Steudle, 2001). This paper will concentrate on an important aspect of xylem tension: the development of gas bubbles within the xylem conduits, the tracheids or vessels, which lead to blockage of water transport (Tyree and Sperry, 1989; Tyree and Yang, 1990; Milburn, 1991).

It is generally assumed that an embolism develops from an initially small, air filled cavity in the xylem. Numerous pores (pits), which represent gaps in the secondary cell wall, exist on the walls of tracheids or vessels. A porous membrane, the pit membrane, is located in the centre of the pits. According to the "air seeding hypothesis", air is drawn through the pores of the pit membrane into a functioning conduit and leads to embolism which prevents further water transport inside the now embolized conduit (Sperry and Tyree, 1988).

The xylem is able to recover from embolism (Tyree et al., 1999; Holbrook et al., 2001). It is assumed that one important factor is represented by the (positive) root pressure which removes the gas filled spaces within the conduits by forcing the bubbles into solution, because the xylem pressure has to exceed a certain threshold value for bubble dissolution, depending on the radius of the conduits (Tyree et al., 1999). A corresponding physical model is based on the pressure values and the geometry of the conduits (Yang and Tyree, 1992). Embolism recovery occurs, in fact, frequently

*Corresponding author. Institute for Geosciences, University of Tuebingen, Sigwartstrasse 10, Tuebingen 72076, Germany. Tel.: +49-7071-2973061; fax: +49-7071-295217.
E-mail address: anita.roth@uni-tuebingen.de (A. Roth-Nebelsick).

0022-5193/03/$ - see front matter © 2003 Elsevier Ltd. All rights reserved.
doi:10.1016/S0022-5193(03)00138-3

over night or during rain periods when pressure values inside the xylem favour bubble solution (Magnani and Borghetti, 1995). In vines, embolism recovery is observed during spring when high root pressures occur (Ewers et al., 1991; Cochard et al., 1994). Stem pressure can also be involved in embolism reversal (Sperry et al., 1988).

There is recent evidence that embolism represents a frequent and regular phenomenon during daily xylem water transport and can be removed (i) very quickly (within minutes) and (ii) possibly under xylem tension, that is, during transpiration (Salleo et al., 1996; McCully, 1999; Tyree et al., 1999). Experimental indications that embolism repair may occur under xylem tension represent a serious problem within the current paradigms of water transport. The various single questions arising through this observation are: (i) how does water move into an embolized conduit when negative pressures exist in the adjacent functioning conduits and (ii) how can under these circumstances pressure values be achieved in the embolized conduit which allow for bubble dissolution? Recently, it was suggested that (i) living cells within the xylem would be able to supply embolized conduits with water, and (ii) surface properties and pit geometry of the conduits cause special interfacial effects which lead to hydraulic isolation and contribute to bubble dissolution (Holbrook and Zwieniecki, 1999).

Anatomical studies carried out by Zwieniecki and Holbrook (2000) corroborate this suggestion, because contact angle and pit geometry are in agreement with the physical pre-conditions of this model. However, no further physical analysis of this putative mechanism, which relies heavily on thermodynamic processes, exists so far. The temporal course of bubble growth or bubble dissolution is especially of crucial importance to embolism repair. The present paper concentrates on a detailed physical analysis of the interfacial processes which can take place if bubbles appear in xylem conduits. This analysis includes the temporal behaviour of bubbles in the lumen of xylem conduits, interfacial effects which can be expected at the pit and how these effects influence pressure within "pit bubbles" and their temporal dynamics. The analysis starts with the consideration of a simple spherical bubble and the results will be integrated into the exploration of which requirements are necessary for a successful "valve" function of a bubble situated at a pit pore.

2. Dynamics of a spherically symmetric bubble

2.1. Volume, surface tension, pressure and number of gas molecules of a spherically symmetric bubble

In the following sections, it will be described how the temporal behaviour of a gas bubble immersed in a liquid can be derived from parameters such as bubble volume, pressure inside and outside the bubble, surface tension, temperature and dissolution dynamics of the gas molecules inside the bubble. We consider a spherically symmetric gas bubble of radius R. Its volume (cf. Fig. 1) is

$$V = \frac{4\pi}{3} R^3. \tag{1}$$

The pressure p inside the bubble (cf. Fig. 2) is given by the Young–Laplace equation as the sum of the pressure p_s in the surrounding liquid and a second term which stems from the surface tension γ of the gas/liquid interface,

$$p = p_s + \frac{2\gamma}{R}. \tag{2}$$

By treating the gaseous content of the bubble as an ideal gas, we can calculate the number n of gas molecules inside

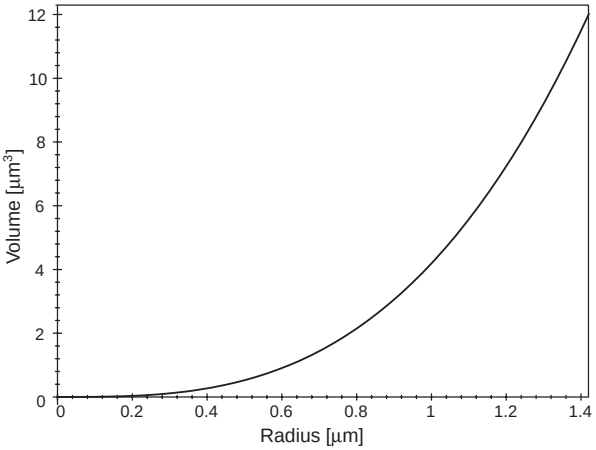

Fig. 1. Bubble volume V as a function of bubble radius R, according to Eq. (1) (cases 1–4, see text).

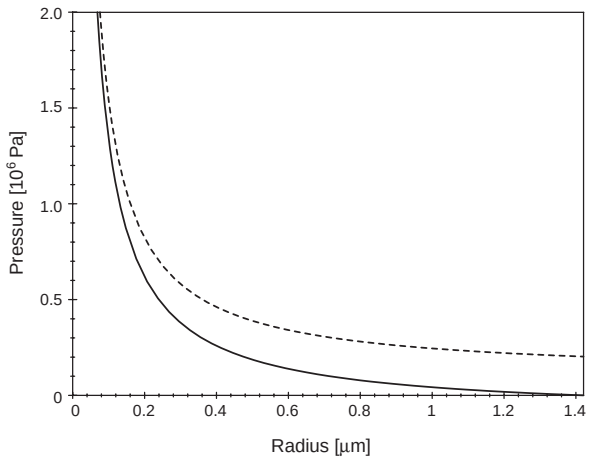

Fig. 2. Pressure p in the bubble as a function of bubble radius R, according to Eq. (2). The pressure p_s in the surrounding liquid amounts to $p_s = 101\,325$ Pa (broken line, cases 1 and 2) and $p_s = -101\,325$ Pa (solid line, cases 3 and 4), respectively (see text). Surface tension of water: $\gamma = 0.072$ N/m.

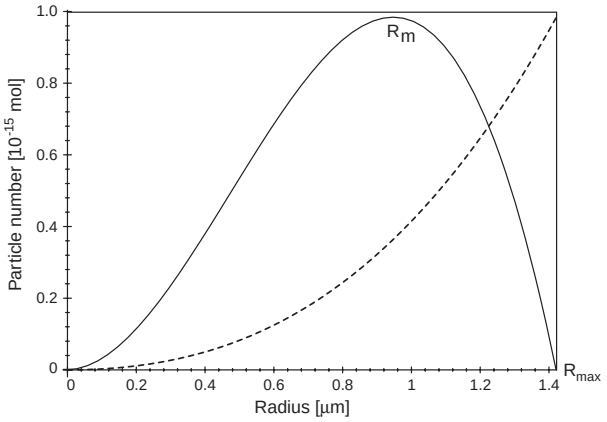

Fig. 3. Particle number n in the bubble as a function of bubble radius R, according to Eq. (3). The pressures p_s in the surrounding liquid have values $p_s = 101\,325$ Pa (broken line, cases 1 and 2) and $p_s = -101\,325$ Pa (solid line, cases 3 and 4), respectively. Absolute temperature: $T = 298$ K, gas constant: $\mathscr{R} = 8.314$ m^{3}Pa/mol/ K.

the bubble from the equation for a perfect gas (note that $\mathscr{R}$ represents the gas constant and not a radius, T denotes absolute temperature, cf. Fig. 3):

$$n = \frac{pV}{\mathscr{R}T} = \frac{1}{\mathscr{R}T}\frac{4\pi}{3}(p_s R^3 + 2\gamma R^2). \tag{3}$$

Before inspecting Eq. (3) further, we notice that the surface tension γ is always positive, whereas the pressure p_s in the liquid is not, because negative pressures can occur in the xylem. The cases $p_s > 0$ and $p_s < 0$ lead to quite different behaviour, as will become evident in the following sections.

Eq. (3) shows that $n(R)$ becomes zero at $R = 0$, whatever value p_s attains. We first consider the case of $p_s > 0$. This means for the plant that no xylem tension exists. This is the case, for example, during the night or in periods of rainfall and high humidity. A positive xylem pressure implies that $n(R)$ is a positive and monotonically increasing function of R for $R \geqslant 0$. No bubble (and therefore no gas particles) exist for $R = 0$, but for $R > 0$ an expanding bubble can house increasing numbers of gas particles. This behaviour is illustrated by Fig. 3. According to Eq. (2), the pressure p inside the bubble then approaches the pressure p_s of the surrounding liquid asymptotically with increasing bubble radius. Now we consider the case $p_s < 0$. Negative xylem pressure (i.e. xylem tension) can occur in the xylem during transpiration and/or water stress. For $p_s < 0$, the function $n(R)$ has a second zero on the positive R-axis at

$$R_{max} := \frac{2\gamma}{-p_s}. \tag{4}$$

This is depicted by Fig. 3. In the case of $p_s < 0$, the function $n(R)$ is thus positive only if R lies in the interval $0 \leqslant R \leqslant -2\gamma/p_s$. Since $n(R)$ is a continuous function, it must attain an extremum for some R-value within this interval, which lies at

$$R_m := -\frac{4\gamma}{3p_s}. \tag{5}$$

Insertion of Eq. (5) into Eq. (3) returns that the maximum number of gas molecules, which can be accomodated in a spherically symmetric bubble surrounded by a liquid at negative pressure, depends only on the temperature T, the gas constant $\mathscr{R}$, the pressure $p_s < 0$ (the negative xylem pressure) and the surface tension γ of the gas/liquid interface. The maximum number of gas molecules is given by

$$n_{max} := \frac{2\pi\gamma}{\mathscr{R}T}\left(\frac{8\gamma}{9p_s}\right)^2. \tag{6}$$

The existence of this maximum can be understood in terms of physics. The gas molecules with their inherent tendency to expand the volume that they occupy, are "kept together" by (i) the surface tension and (ii) the pressure p_s of the surrounding liquid as long as the latter quantity is positive. A negative liquid pressure p_s, however, acts "in the same direction" as the (potentially) expanding gas particles and the confinement of the gas molecules must be provided solely by the surface tension term in Eq. (2). Since the volume and the surface of a sphere are proportional to R^3 and R^2, respectively, and the former grows more rapidly with R than the latter, it is intuitively evident that the surface tension will be dominated by the volume pressure beyond a certain R-value. Consequently, the number of particles which can be accomodated within the bubble without risk of bursting is limited.

We summarize at the end of this section that under negative xylem pressure:

(i) a gas bubble can only contain a certain maximum number of gas molecules and
(ii) the radius of a gas bubble has an upper limit.

2.2. Physical basis of temporal bubble behaviour

We now proceed to the dynamics of the bubble. Our goal is to calculate $R(t)$, i.e. the temporal behaviour of the radius of the bubble. Once $R(t)$ is known, the functions $V(t)$, $p(t)$ and $n(t)$ can be derived from relations (1), (2) and (3).

For the sake of simplicity, we assume that the gas particles inside the bubble and the external liquid belong to different chemical species, i.e. air inside the bubble and water outside. This simplification limits our model to embolism events caused by "air seeding". This is a reasonable limitation, resting on two arguments: (i) There is evidence that most embolism events are caused by "air seeding" (Sperry et al., 1996), (ii) although water

molecules tend to vaporize into bubbles consisting initially only of air, their fraction of the total particle content will usually remain small, because it is proportional to the ratio between the water vapour pressure and the total pressure in the bubble. Thus, if the latter amounts to $p = 1$ atm $= 101\,325$ Pa, at a temperature of 25°C only about 3.2% of the particles in the bubble are water molecules. Under this assumption the dynamic behaviour of the bubble rests upon two physical effects:

(i) when gas contacts a liquid at an interface, gas particles dissolve into the liquid according to Henry's Law which states that the (partial) pressure of the gas (inside the bubble) p and the concentration C_R of the dissolved gas particles in the liquid in the near vicinity of the bubble (which is the meaning of the index R) are proportional to each other (see Fig. 4):

$$C_R = k_H p, \tag{7}$$

(ii) if the concentration of dissolved gas particles in the surrounding liquid deviates from the value C_R, diffusional currents, directed from areas of higher to areas of lower concentration arise.

As the combined result of both processes we expect that gas particles are transported either out of and away from the gas bubble or into the opposite direction. This process continues until an equilibrium situation is attained.

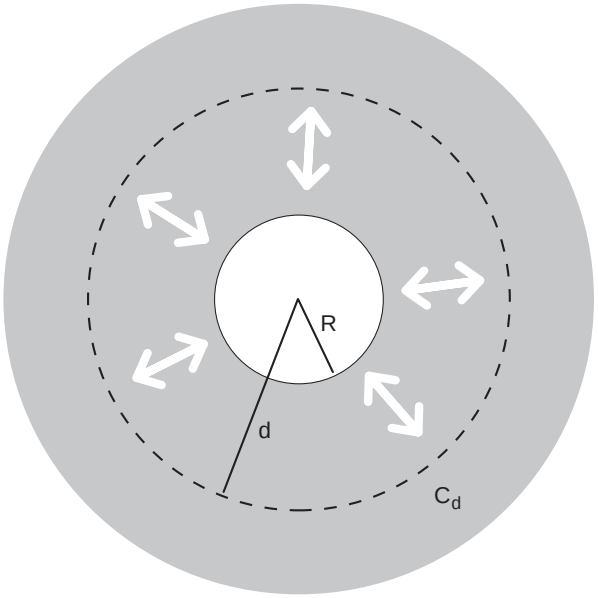

Fig. 4. Schematic representation of a gas bubble (white) of radius R immersed in a liquid (grey). Outside of a sphere of radius d (broken line) the air concentration in the liquid is held at a constant value C_d. In general, this gives rise to a radial diffusional current (white arrows).

2.3. Calculation of temporal evolution of spherically symmetric bubbles

Our starting point to calculate $R(t)$ is the observation, that changes in the number n of gas particles in the bubble must be generated by the diffusional current I, as long as no other processes take place which consume (or produce) gas particles. The corresponding equation reads as

$$-\frac{\mathrm{d}n}{\mathrm{d}t} = I. \tag{8}$$

Since we adopt the convention that a positive diffusional current transports particles *away* from the bubble, Eq. (8) contains a minus sign. By means of the chain rule of differentiation we conclude

$$-\frac{\mathrm{d}n}{\mathrm{d}t} = -\frac{\mathrm{d}n}{\mathrm{d}R}\frac{\mathrm{d}R}{\mathrm{d}t} = I, \tag{9}$$

which implies the equation

$$\frac{\mathrm{d}t}{\mathrm{d}R} = -\frac{\mathrm{d}n/\mathrm{d}R}{I}. \tag{10}$$

$n(R)$ is already explicitly given in Eq. (3). If the current I can also be written as a function of R, the R-dependence of the right-hand side of Eq. (10) can be calculated and the integration

$$t(R) = -\int \frac{\mathrm{d}n/\mathrm{d}R}{I(R)}\,\mathrm{d}R \tag{11}$$

can be performed. The calculation of $I(R)$ is provided in the Section A.1. Fig. 5 illustrates the results concerning

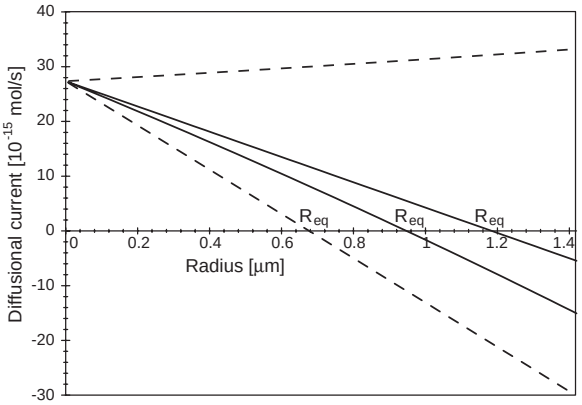

Fig. 5. Diffusional currents directed into or out of the bubble as a function of bubble radius. The four curves correspond to cases 1–4 (see text). The equilibrium radius R_{eq} is defined in Eq. (17) and characterizes the bubble radius where diffusion ceases. The pressure p_s in the surrounding liquid and the pressure p_d (equivalent to the air concentrations C_d at a radial distance $d = 15$ µm from the bubble) have the following values: $p_s = 101\,325$ Pa, $p_d = 91\,193$ Pa (case 1, upper broken line) $p_s = 101\,325$ Pa, $p_d = 253\,313$ Pa (case 2, lower broken line) $p_s = -101\,325$ Pa, $p_d = 20\,265$ Pa (case 3, lower solid line) and $p_s = -101\,325$ Pa, $p_d = 11\,458$ Pa (case 4, upper solid line), respectively. Effective diffusion coefficient of air in water: $S = 1.95 \times 10^{-9}$ m^2/s, Henry's Law constant: $k_H = 7.75 \times 10^{-6}$ mol/m^3/Pa.

$I(R)$ for four different cases (explained in the following sections). Insertion of Eqs. (A.9) and (A.10) (from Appendix A) into Eq. (11) and subsequent integration leads to

$$t(R) = \alpha(R - R_0) + \beta(R^2 - R_0^2) + \delta(R^3 - R_0^3) + \varepsilon \log\left(\frac{R - R_{eq}}{R_0 - R_{eq}}\right). \quad (12)$$

R_0, the constant of integration in Eq. (12), is defined by $t(R_0) = 0$. Thus, R_0 denotes the bubble radius at time $t = 0$. The greek letters in Eq. (12) represent combinations of the constants $\mathscr{R}$, γ, S and k_H and the parameters T, R_{eq}, R_m and d.

$$\alpha := \frac{2}{3\mathscr{R}TSdk_H}\frac{R_{eq}}{R_m}(d - R_{eq})(R_m - R_{eq}), \quad (13)$$

$$\beta := \frac{-1}{3\mathscr{R}TSdk_H}\frac{R_{eq}}{R_m}(R_m - R_{eq} + d), \quad (14)$$

$$\delta := \frac{2}{9\mathscr{R}TSdk_H}\frac{R_{eq}}{R_m}, \quad (15)$$

$$\varepsilon := \frac{2}{3\mathscr{R}TSdk_H}\frac{R_{eq}^2}{R_m}(d - R_{eq})(R_m - R_{eq}), \quad (16)$$

with R_{eq} as the "equilibrium radius" ($R = R_{eq}$ implies $I = 0$, as is shown in Section A.2)

$$R_{eq} := \frac{2\gamma k_H}{C_d - k_H p_s} = \frac{2\gamma}{p_d - p_s}. \quad (17)$$

The pressure $p_d := C_d/k_H$ has been introduced in the last expression purely for mathematical convenience. (Physically, it can be interpreted as the partial pressure of (gaseous) air which is in equilibrium with (liquid) xylem sap containing air molecules in a concentration C_d.) The "equilibrium radius" R_{eq} defined in Eq. (17) represents the "final" radius of a bubble in those cases, in which diffusion ceases after some time. A closer inspection of Eqs. (12) and (A.11) (of Appendix A) reveals that four qualitatively different cases of bubble behaviour exist:

$$\begin{aligned} &\text{Case 1}: \quad 0 < p_d < p_s, \\ &\text{Case 2}: \quad 0 < p_s < p_d, \\ &\text{Case 3}: \quad p_s < -2p_d < 0, \\ &\text{Case 4}: \quad -2p_d < p_s < 0. \end{aligned} \quad (18)$$

Eq. (12) gives the time t as a function of the bubble radius R. This may appear to be strange at first sight, but as Eq. (12) is built up from a polynomial in R and a logarithmic term containing R, R cannot be expressed as a function of t. For the problem of exploring the temporal development of a bubble it is completely irrelevant whether the radius or the time is the independent variable.

The temporal behaviour of the bubbles for the four different cases is illustrated in Figs. 6, 7, 8 and 9. A short discussion of the different cases will be provided in the following sections.

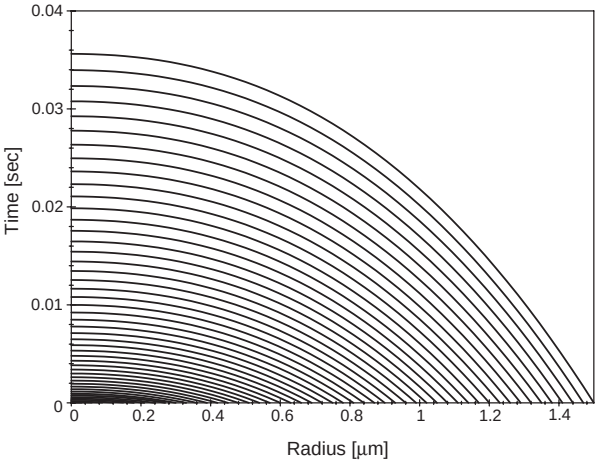

Fig. 6. Temporal development of a spherically symmetric gas bubble which is coupled by diffusion to a gas reservoir at constant pressure. The bubble radius R is drawn along the abscissa, time t along the ordinate. Each curve starts for $t = 0$ at an initial radius R_0. In case 1, the present case, every curve either terminates at $R = 0$ (because the corresponding bubble has dissolved) or it extends till infinity. Figures were obtained from Eq. (12) by insertion of the following parameter values $d = 15$ μm, $p_e = 101\,325$ Pa, $p_d = 91\,193$ Pa (case 1).

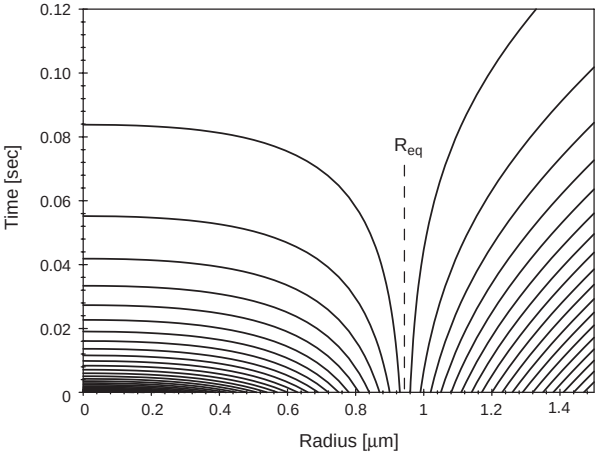

Fig. 7. Temporal development of a spherically symmetric gas bubble which is coupled by diffusion to a gas reservoir at constant pressure. The bubble radius R is drawn along the abscissa, time t along the ordinate. Each curve starts for $t = 0$ at an initial radius R_0. In case 2, the present case, every curve either terminates at $R = 0$ (for values of R_0 small enough), or it extends till infinity (because the corresponding bubble expands forever). R_{eq} denotes the bubble radius where diffusion ceases (for detailed explanation see text). Figure was obtained from Eq. (12) by insertion of the following parameter values $d = 15$ μm, $P_e = 101\,325$ Pa, $P_d = 253\,313$ Pa (case 2).

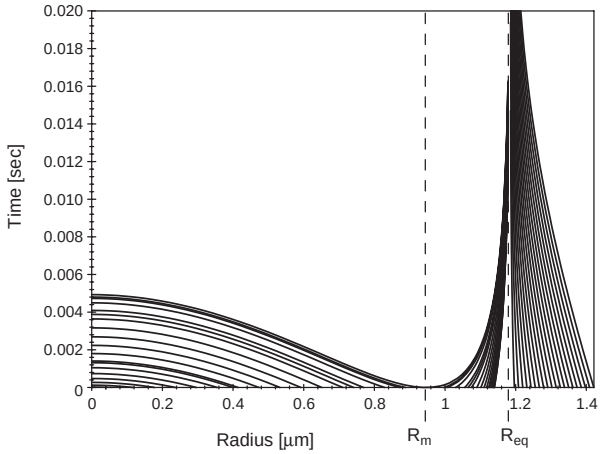

Fig. 8. Temporal development of a spherically symmetric gas bubble which is coupled by diffusion to a gas reservoir at constant pressure. The bubble radius R is drawn along the abscissa, time t along the ordinate. Each curve starts for $t = 0$ at an initial radius R_0. In case 3, the present case, every curves either terminates at $R = 0$ (for value of R_0 small enough), or it extends till infinity (because the corresponding bubble stops its expansion, if the diffusional current ceases). R_m denotes the radius at which the capacity of the bubble to host particles is at its maximum. R_{eq} denotes the bubble radius where diffusion ceases (for detailed explanation see text). Figure was obtained from Eq. (12) by insertion of the following parameter values $d = 15$ µm, $P_e = -101\,325$ Pa, $P_d = 20\,265$ Pa (case 3).

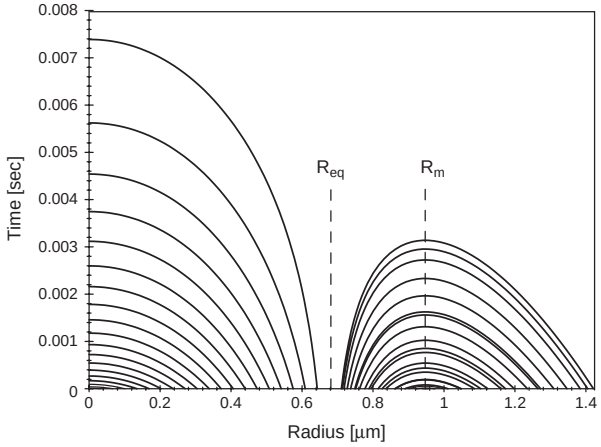

Fig. 9. Temporal development of a spherically symmetric gas bubble which is coupled by diffusion to a gas reservoir at constant pressure. The bubble radius R is drawn along the abscissa, time t along the ordinate. Each curve starts for $t = 0$ at an initial radius R_0. The curves with $R > R_{eq}$ is case 4, the present case, are physically impossible and will be discussed in the Appendix A. R_m denotes the radius at which the capacity of the bubble to host particles is at its maximum. R_{eq} denotes the bubble radius where diffusion ceases (for detailed explanation see text). Figures were obtained from Eq. (12) by insertion of the following parameter values $d = 15$ µm, $P_e = -101\,325$ Pa, $P_d = 111\,458$ Pa (case 4).

2.4. Discussion of temporal evolution of spherically symmetric gas bubbles

Case 1 (*see Fig.* 6): For a positive pressure $0 < p < p_s$ of the liquid surrounding the gas bubble, the bubble will disappear after some time. According to the Young–Laplace equation and Henry's Law, the concentration of dissolved gas particles in the liquid in the near vicinity of the bubble is greater than their concentration at $r = d$. Hence, the diffusional current $I > 0$ is directed out of the bubble (see Fig. 5 or Eq. (A.9)). By losing gas molecules, the radius of the bubble decreases (see Fig. 3 or Eq. (3)), and the pressure inside increases (see Fig. 2 or Eq. (2)), which results in an ongoing efflux of particles of the bubble until it has dissolved. The "dissolution time" can either be taken from Figs. 6 and 7 (as the intersection of any curve starting at $R_0 < R_{eq}$ and the t-axis) or it can be calculated by setting $R = 0$ in Eq. (12). This case is realized in the xylem if, for example, small bubbles dissolve during the night or/and under root pressure.

Case 2 (*see Fig.* 7): For $R_0 < R_{eq}$ the $t(R)$-curves show the same features as in case 1.

A bubble of the initial radius $R_0 > R_{eq}$, however, will not dissolve but grow (in principle indefinitely). $R_0 > R_{eq}$ implies that the concentration of the dissolved gas particles adjacent to the bubble is smaller than their concentration at $r = d$. Thus, the diffusional current $I < 0$ is directed into the bubble (Fig. 5), the particle number $n(R)$ in the bubble increases and—according to Fig. 3—also its radius. This leads to a decreasing bubble pressure (Fig. 2) and to a diffusional current $I < 0$. This case represents conduit bubbles which cannot be dissolved due to, for example, inability of the plant to produce significant root pressure or large conduits which allowed for the development of correspondingly large bubbles (for example, after pit membrane damage by fatigue, Hacke et al., 2001). The large vessels of ring-porous woods are usually irreversibly blocked by embolism events and new functioning vessels are formed in the following growing season.

Case 3 (*see Fig.* 8): The (R, t)-plot (Fig. 8) shows a more complex structure than in the preceding cases. For $R < R_m$ the interpretation is equal to case 1. This means that bubbles with an initial radius smaller than R_m dissolve despite $p_s < 0$. For $R_m < R < R_{eq}$, the diffusional current $I > 0$ is directed out of the bubble (Fig. 5). However, due to the existence of the maximum $n_{max} = n(R_m)$, the loss of particles leads to an increase in R (Fig. 3). This leads to a decrease of p (Fig. 2) and a subsequent decrease of $I > 0$. The process of particle loss slows down as R approaches R_{eq} asymptotically and stops eventually—in theory after an infinite, in reality after a finite amount of time.

A similar behaviour develops for $R > R_{eq}$. Since $I < 0$ is directed into the bubble (Fig. 5), n increases and R decreases (Fig. 3). This leads to an increase in p (Fig. 2), which slows down the particle influx via $I < 0$. Again, R

approaches R_{eq} and the whole process stops in an "asymptotic" manner at $R = R_{eq}$. We may say, that the equilibrium at $R = R_{eq}$ is stable in case 3, because after a small perturbation of the bubble radius (say, to a new radius $R = R_{eq} + \rho$ with $|\rho| \ll R$) the equilibrium at $R = R_{eq}$ will restore. A formal derivation of this statement will be provided in Section A.3.

Case 4 (*see Fig.* 9): For $R < R_{eq}$ the interpretation is as in case 1, that is, the bubble will dissolve after a certain time interval.

If $R > R_{eq}$ in Fig. 9, the bubble appears to show an "impossible" behaviour: time appears to "stop" at $R = R_m$ for all curves who start at a $R_0 > R_{eq}$. In all other cases, the (R, t)-curves behave as expected: they extend either to temporal infinity (at $R = R_{eq}$ or for $R \to \infty$) or they intersect after a finite "dissolution time" with the t-axis, because the bubbles have shrunk to the radius $R = 0$, i.e. they have completely dissolved. The strange behaviour of bubbles with $R_0 > R_{eq}$ shown in Fig. 9 can be traced to the fact that for this special case the equations presented in this paper have been stressed beyond their "physical limit". This will be discussed in the following.

From Figs. 5 and 3 we see that for every $R > R_{eq}$ the diffusional current is directed into the bubble and that this influx of particles makes the bubble radius approach $R = R_m$, which represents the radius with the maximum of n. At $R = R_m$ the current $I < 0$ still transports particles into the bubble, although it cannot accomodate additional particles. The strange behaviour of the (R, t)-curves in Fig. 9 is an attempt of our mathematical framework to deal with this contradiction although the validity of Eq. (8) (which states that the bubbles's only way to lose particles is by means of a diffusional flux out of the bubble) is already exhausted at $R = R_m$.

What happens in reality is that the bubble deals with the breakdown of Eq. (8) by splitting up into "daughter bubbles". This behaviour is certainly beyond the limits of Eq. (8). Once the daughter bubbles have formed, they *do* again obey Eq. (8), until they reach the radius $R = R_m$ (which may or may not happen) and the splitting event repeats.

It is impossible to predict the number, sizes and respective particle contents of the daughter bubbles within the framework of the actual equations. Still, we may be confident that the gross number of all particles within all bubbles present is the same before and after a splitting event. Eq. (3) connects the number of particles in a bubble n with its radius R. Viewed as an equation for R, Eq. (3) has two real solutions (that is, if R_m is positive, a negative R_m implies one real solution). Thus, even if the number of particles within a bubble "born" in a splitting event would be known in advance, the ambiguity with respect to its radius would remain.

We now provide a short summary of this section. Four different cases of bubble evolution arise, depending on xylem pressure and air concentration in the xylem sap. Under positive xylem pressure, the bubble can dissolve or it can grow (cases 1 and 2). Under negative xylem pressure, bubbles with sufficiently small initial radii dissolve (cases 3 and 4), the bubbles can grow asymptotically until an equilibrium radius $R = R_{eq}$ is reached (case 3), or splitting of the bubbles can occur (case 4). The temporal development of a bubble with $R > R_{eq}$ in case 4 can be characterized as a succession of time intervals with predictable behaviour, punctuated by events with unpredictable outcome. It is possible to calculate from Eq. (8) (or, rather from its solution, Eq. (12)), when the next bubble splitting event will occur. It is, however, not possible to calculate when the event following the next one will take place. Since we do not really need this information for our present considerations, it suffices to keep in mind, that whenever in case 4 the bubble radius attains the value $R = R_m$, our central vehicle of prediction (i.e. Eq. (8)) is superseded by a process, whose outcome is only partially predictable. The temporal course of splitting events is further discussed in Section A.2.

3. Dynamics of an axially symmetric pit bubble

3.1. Background and basics of repair scenario

The model of Holbrook and Zwieniecki (1999) and Zwieniecki and Holbrook (2000) comprises the following components (see Fig. 10):

(i) The positive pressure in the embolized conduit (in contrast to the negative pressures within the functioning conduits) promotes the dissolution of the gas bubble.
(ii) The process of dissolution is enhanced by the surface tension of the liquid/gas interface which adds to the pressure of the liquid.
(iii) If the resulting pressure in the gas bubble is sufficiently high, a diffusional flux of dissolved air molecules to the adjacent conduits develops.
(iv) The pits connecting embolized and functioning conduits show a special geometry. Their shape leads to hydraulic isolation of the embolized vessel from the adjacent conduits, because the effect of surface tension of the liquid/gas interface and the pressure of the liquid diminish each other. Therefore, dissolution of the bubbles at/within the pits (termed as "pit bubbles", PB, throughout the rest of the paper) is less effective if compared to the dissolution of the bubbles within the conduit lumen (termed as "lumen bubbles", LB, throughout the rest of the paper). In fact the pressure difference between them may cause a diffusional current which "feeds" the PB at expense of the LB.

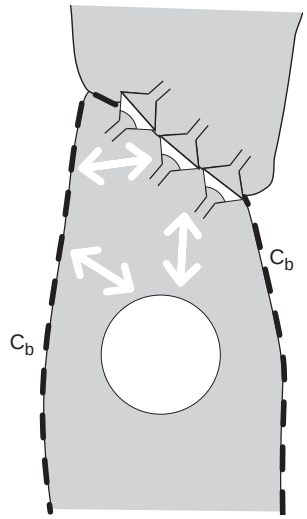

Fig. 10. Schematic representation of an embolized vessel (lower part of figure) filled with xylem sap under positive pressure p_e and an intact vessel (upper part of figures) filled with liquid under tension (negative pressure). White: gas. White arrows symbolize diffusional currents between the LB, the PBs and the adjacent conduits. The broken line along the border of the vessel indicates a constant air concentration C_b in the xylem sap of the adjacent conduits. This figure depicts the realistic situation.

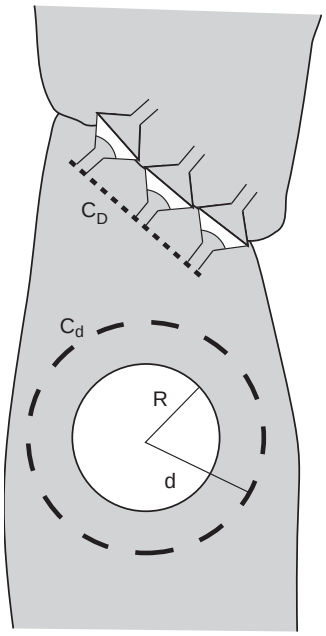

Fig. 11. Schematic representation of an embolized vessel (lower part of figure) filled with xylem sap under positive pressure p_e and an intact vessel (upper part of figure) filled with liquid under tension (negative pressure). White: gas. The broken lines labelled c_d and c_D denote the reservoirs of constant air concentration to which the PBs and the LB, respectively, are coupled by diffusion. This figure depicts the approximate treatment of the situation.

The success of this model depends largely on the question if the dissolution of the "embolizing bubbles" can be completed before the hydraulic isolation of the embolized vessel fails due to the dissolution of the PB. Therefore, the temporal behaviour of both spherically symmetric LB and of axially symmetric PB is of central significance to embolism repair and to the general dynamics of bubbles in xylem conduits.

Since an exact mathematical description of the situation is impossible and a near-exact treatment requires extensive use of numerical mathematics (which is beyond the scope of this contribution), we pursue an approximate quantitative approach to the processes which are happening after an air seeding event.

In reality (see Fig. 10) LB and PB interact, because generally the pressures in the LB and in the PB are not the same and they are both different from the pressure C_b/k_H, equivalent to the air concentration C_b in the adjacent conduits. Therefore, diffusional currents between all three develop, which couple the dynamics of the LB and the PB. Fig. 11 indicates the approximations we employ (i) to break up this coupling on the mathematical level and (ii) to obtain simple boundary conditions on simply shaped geometrical forms, exhibiting a high degree of symmetry. We assume that the LB exchanges particles only with a sphere of radius d around the LB where the air concentration in the liquid has the constant value C_d. Similarly, the row of PB is supposed to have diffusional contact only to a "bar" at a distance D from the pit necks. Thus, the constant air concentration C_b of the adjacent conduits has been replaced by the constant air concentration C_d which is also present in the embolized vessel, with the exception of the sphere of radius d around the LB. In a sense, the constant air concentration C_D at distance D from the pit necks replaces the diffusional current between the LB and the PB. The dynamics of the LB and the PB are no longer coupled.

The following part of the paper concentrates on the putative "valve" function of PB. Hereby, the results of the analysis of LB dynamics are used as basis for the far more complex problem of the interfacial effects at the PB. We discuss the dynamics of a PB under the aspect of achieving the hydraulic isolation of an embolized vessel from its intact neighbours. Thus, we assume that the liquid in the embolized vessel is under a positive pressure $p_e > 0$ while in its intact neighbour conduit (on the other side of the pit) a negative pressure $p_i < 0$ remains.

3.2. Compatibility conditions between pit geometry and pressure difference across the interface

A gas/liquid interface within a cone-shaped pit may be realized according to Holbrook and Zwieniecki (1999) and Zwieniecki and Holbrook (2000) as in

Fig. 12: the area between the gas/liquid interface (in the embolized side of the pit) and the membrane is filled with gas and the interface bulges towards the pit membrane.

An interface is capable to maintain hydraulic isolation of an embolized vessel only if the pit geometry and the pressures concerned fulfil several conditions (see Fig. 12):

(i) the gas/liquid interface should bulge towards the pit membrane,
(ii) the gas/liquid interface should not touch the pit membrane, because then hydraulic isolation of the embolized vessel would break down,
(iii) if the gas/liquid interface is situated at the mouth of the pit neck, it should not retreat further,
(iv) the pressure in the gaseous part of the pit should be positive, because we assume it to be filled with an ideal gas and ideal gases do not exhibit attractive forces between their constituents,
(v) the interface should be able to provide the required pressure difference.

In order to formulate these conditions in mathematical terms we characterize the position of the interface by the variable l (i.e. the distance between interface and membrane, measured along the "side" of the pit as in Fig. 12). Trigonometric relations allow then the expression of R in terms of the contact angle θ, the parameters s and α (characterizing the shape of the pit) and the variable l:

$$R = \frac{s - l\sin\alpha}{-\cos(\alpha+\theta)}. \tag{19}$$

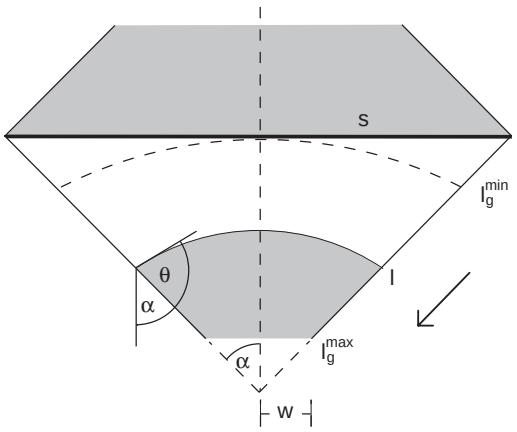

Fig. 12. Schematic representation of a pit, isolating an intact (upper part of figure) from an embolized vessel (lower part of figure). The quantity l characterizes the position of the gas/liquid interface, $l = 0$ = position of the membrane.

white: air, grey: water, s: radius of pit membrane, θ: contact angle, α: pit opening half-angle, w: radius of pit neck, l_g^{min}: minimum value of l due to condition (22), l_g^{max}: maximum value of l due to condition (23).

θ and α are restricted by definition and geometry, respectively, to the intervals (see also Fig. 12):

$$0 \leqslant \theta \leqslant \pi \quad \text{and} \quad 0 \leqslant \alpha \leqslant \frac{\pi}{2}. \tag{20}$$

The conditions now read as

(i) $$\theta + \alpha > \frac{\pi}{2}. \tag{21}$$

If condition (21) is fulfilled, R is positive: Eq. (20) implies $\pi/2 < \alpha + \theta \leqslant 3\pi/2$. The cosine is negative on this interval.

(ii) Assuming that the membrane remains flat under all circumstances (which cannot be taken for granted, because the membrane must necessarily sustain the high pressure difference between the intact vessel and the gaseous interior of the pit, see Fig. 12), geometric relations (consult Fig. 12) imply the following conclusion:

$$l \geqslant s\frac{1-\sin(\alpha+\theta)}{\sin\alpha - \cos\theta} =: l_g^{min}. \tag{22}$$

(iii) Denoting the radius of the pit neck by w, Fig. 12 implies

$$l \leqslant \frac{1}{\sin\alpha}(s - w) =: l_g^{max}. \tag{23}$$

(iv) Denoting the pressures in the intact and embolized vessels by $p_i < 0$ and $p_e > 0$, respectively, the Young–Laplace equation takes the form:

$$p = p_e - \frac{2\gamma}{R} = p_e + 2\gamma\frac{\cos(\alpha+\theta)}{s - l\sin\alpha}. \tag{24}$$

Recalling that the pressure is positive in the embolized vessel ($p_e > 0$) and negative in the intact one ($p_i < 0$), Eq. (24) implies that values of the expression $2\gamma/R$ which are too large result in a negative pressure in the gas bubble within the pit. The condition

$$p \geqslant 0 \tag{25}$$

transforms upon use of Eq. (24) into a geometric condition on l:

$$l \leqslant \frac{1}{\sin\alpha}\left(s + \frac{2\gamma}{p_e}\cos(\alpha+\theta)\right) =: l_p^{max}. \tag{26}$$

(v) The maximum pressure difference Δp^{max} which can, in principle, be sustained by the interface (while bulging into the required direction and obeying condition (21), ignoring, however, restriction (26)), is identical to the maximum of the expression $2\gamma/R$. This lies at $l = l_g^{max}$ (i.e. at the mouth of the pit neck), because $2\gamma/R$ increases for increasing values of l, as is evident from Eqs. (19)

and (20). Thus,

$$\Delta p^{max} = \frac{2\gamma}{R}\bigg|_{l=l_g^{max}} = -\frac{2\gamma\cos(\alpha+\theta)}{w}. \quad (27)$$

As the pressure p in the gaseous part of the pit cannot drop below $p=0$, a sufficient condition to be met by the gas/liquid interface is given by the relation

$$\Delta p^{max} \geqslant p_e, \quad (28)$$

which can be obtained formally by insertion of Eq. (27) into Eq. (24) and setting $p=0$.

Results (ii)–(v) summarize to the following relations ($\min(x,y)$ denotes the smaller of x and y):

$$l_g^{min} \leqslant l \leqslant \min(l_g^{max}, l_p^{max}) \quad \text{and} \quad \Delta p^{max} \geqslant p_e. \quad (29)$$

Eqs. (29) can be read as compatibility conditions between the quantities defining the pit and the pressure p_e: an interface can only be realized, if the conditions

$$l_g^{min} \leqslant \min(l_g^{max}, l_p^{max}) \quad \text{and} \quad \Delta p^{max} \geqslant p_e \quad (30)$$

are satisfied.

Since Eqs. (28), (27), (19) and the definition of l_g^{max} (Eq. (23)) lead to the statements $(\Delta p^{max} \geqslant p_e \Rightarrow l_g^{max} \geqslant l_p^{max})$ and $(\Delta p^{max} \geqslant p_e \Rightarrow \min(l_g^{max}, l_p^{max}) = l_p^{max})$, conditions (30) for the existence of an interface can be rephrased in the form

$$\Delta p^{max} \geqslant p_e \quad \text{and} \quad l_g^{min} \leqslant l_p^{max}. \quad (31)$$

Employing the definitions of the quantities Δp^{max}, l_g^{min} and l_p^{max}, conditions (31) can be cast into the form

$$\frac{2\gamma}{s}\frac{\sin\alpha - \cos\theta}{\cos\alpha} \leqslant p_e \leqslant \frac{2\gamma}{w}(-\cos(\alpha+\theta)) \quad (32)$$

which is especially well suited to enquire into the effects of changes in the pit defining quantities s, w and α or in the contact angle θ on the acceptable range of p_e.

3.2.1. Comparison with measurements

Values of the maximum pressure differences reported in the literature amount to $p_e \approx 150\,000$ Pa. The magnitude of values concerning the contact angle θ and the pit opening half-angle α appear to amount roughly to $\theta \approx 50°$ and $\alpha \approx 75°$, respectively, and the radii of the pit membrane and the pit neck are given as $s \approx 2.5$ μm and $w \approx 0.5$ μm (Zwieniecki and Holbrook, 2000; van Ieperen et al., 2001). The maximum pressure difference and the boundaries of the l-interval resulting from these values are found from Eqs. (27), (22), (23) and (26): $\Delta p^{max} = 165\,190$ Pa, $l_g^{min} = 1.39$ μm, $l_g^{max} = 2.07$ μm, $l_p^{max} = 2.02$ μm. Application of conditions (30) yields the following result:

$$l_g^{min} = 1.392\ \mu\text{m} < 2.02\ \mu\text{m} = l_p^{max} = \min(l_g^{max}, l_p^{max}), \quad (33)$$

$$\Delta p^{max} = 165\,190\ \text{Pa} \geqslant 150\,000\ \text{Pa} \approx p_e, \quad (34)$$

that is, with the pit data given above, all conditions are met and we can proceed to the analysis of the PB dynamics.

3.3. Volume, surface tension, pressure and number of gas molecules of a pit bubble

We shall explore the dynamics of a PB with the same framework applied to the LB (Section 2).

The volume of a PB is obtained from Fig. 12 by adding and subtracting cones and sections of a sphere as (see also Fig. 13)

$$V = \begin{cases} \frac{\pi}{3} l^2 \left(\frac{\cos\alpha}{-\cos(\alpha+\theta)}\right)\{3s\sin\theta - l[2\sin\alpha\sin\theta \\ \quad + \cos\alpha\cos\theta]\} \quad \text{if } 0 \leqslant l \leqslant l_g^{min}, \\ \frac{\pi}{3} s^3 \cot\alpha \\ \quad -\frac{\pi}{3}\left(\frac{s - l\sin\alpha}{-\cos(\alpha+\theta)}\right)^3 \{\cot\alpha[-\cos(\alpha+\theta)]^3 + \\ \quad [1-\sin(\alpha+\theta)]^2[2+\sin(\alpha+\theta)]\} \quad \text{if } l \geqslant l_g^{min}. \end{cases} \quad (35)$$

Eq. (35) is more complex than its counterpart, Eq. (1). The simplicity of the latter is due to: (i) the spherical symmetry of the LB (a sphere is completely described by its radius, for the still axisymmetric geometry of a pit, however, the three variables s, w and α are required), and (ii) the fact, that in the case of a spherically symmetric bubble the radius of curvature of its surface coincides with the radius of the bubble.

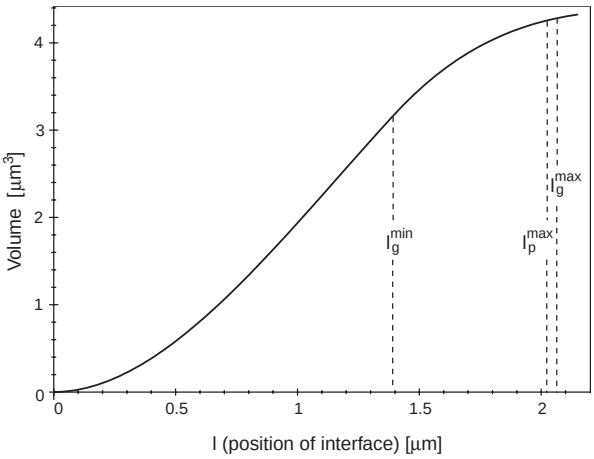

Fig. 13. Bubble volume V as a function of parameter l, according to Eq. (35) (cases A and B, see text). l (position of the air/water interface) is restricted to the interval $l_g^{min} < l < \min(l_p^{max}, l_g^{max})$ (for definitions see text). $\theta = 50°$, $\alpha = 75°$, $s = 2.5$ μm, $w = 0.5$ μm.

The pressure p inside the PB (cf. Fig. 14) is given by the Young–Laplace equation as

$$p = p_e - \frac{2\gamma}{R} = p_e - 2\gamma\left(\frac{-\cos(\alpha+\theta)}{s - l\sin\alpha}\right). \quad (36)$$

Eq. (36) is similar to Eq. (2) (provided the variable p_s in Eq. (2) attains negative values) in that the right-hand sides of both equations become zero for some value of R (respectively l) and the dynamics which develops is quite similar in both cases.

The number n of gas molecules inside the bubble follows from the equation for a perfect gas (cf. Fig. 15),

$$n = \frac{pV}{\mathscr{R}T} \quad (37)$$

with p and V as provided by Eqs. (35) and (36). A closer inspection of Eq. (37) would reveal that $n(l)$ has two zeros and a maximum within the interval $0 \leqslant l \leqslant s/\sin\alpha$. The zeros are inherited from the functions $V(l)$ and $p(l)$. The maximum follows because (i) the left zero derives from $V(l)$ and the right one from $p(l)$, (ii) $V(l)$ and $p(l)$ are continuous functions of l, and, (iii) $\mathrm{d}V/\mathrm{d}l \geqslant 0$ and $\mathrm{d}p/\mathrm{d}l \leqslant 0$ for $0 \leqslant l \leqslant s/\sin\alpha$. As $\mathrm{d}n/\mathrm{d}l$ is a polynomial of fourth degree in l, attempts to calculate the position l_m of n_{max} on the l-axis lead to uncomfortably long expressions. Therefore, we restrict the treatment to define l_m by the equation $n(l_m) = n_{max}$ and to illustrate the situation by Fig. 15.

The principle result of this section is that a PB can—similarly as a LB under negative liquid pressure—contain only a certain maximum number of gas molecules without bursting immediately.

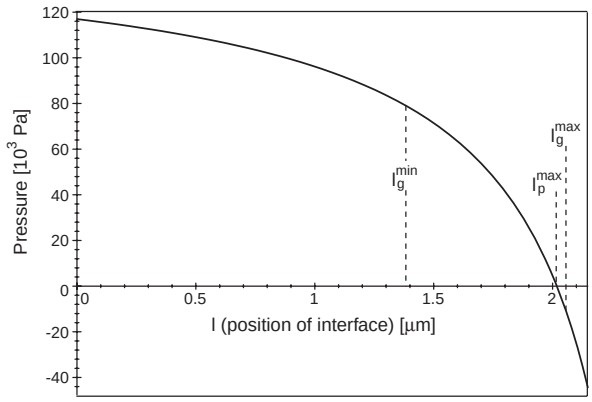

Fig. 14. Pressure p in the PB as a function of l, according to Eq. (36). The pressure p_e in the surrounding liquid amounts to $p_e = 150\,000$ Pa (cases A and B, see text).

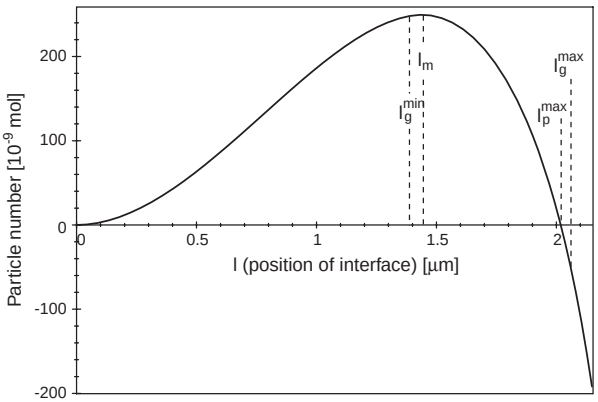

Fig. 15. Particle number n in the bubble as a function of l, according to Eq. (37). The pressure in the surrounding liquid has the value $p_e = 150\,000$ Pa (cases A and B, see text). Absolute temperature $T = 298$ K.

3.4. Dynamics of a cone-shaped pit

Our goal is to calculate $l(t)$. As before, we assume that changes in the number n of gas particles in the bubble are exclusively due to the diffusional current I:

$$-\frac{\mathrm{d}n}{\mathrm{d}t} = I. \quad (38)$$

This can be reformulated as

$$-\frac{\mathrm{d}n}{\mathrm{d}t} = -\frac{\mathrm{d}n}{\mathrm{d}l}\frac{\mathrm{d}l}{\mathrm{d}t} = I, \quad (39)$$

from which we conclude

$$\frac{\mathrm{d}t}{\mathrm{d}l} = -\frac{\mathrm{d}n/\mathrm{d}l}{I} \quad (40)$$

and

$$t(l) = -\int \frac{\mathrm{d}n/\mathrm{d}l}{I(l)}\,\mathrm{d}l, \quad (41)$$

provided the diffusional current $I(l)$ is known. $I(l)$ is calculated in Section A.4 as Eq. (A.28) and depicted by Fig. 16. $n(l)$ is already provided by (37), insertion of

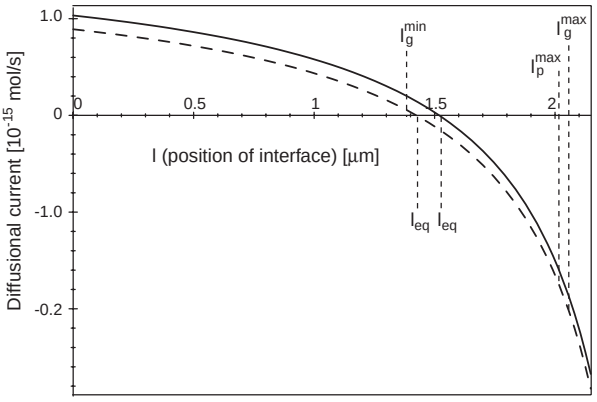

Fig. 16. Diffusional current directed into or out of the pit as a function of interface position l. The two curves correspond to cases A (broken line) and B (solid line). The equilibrium position l_{eq} is defined in Eq. (43) and characterizes the position of the interface where diffusion ceases. The pressures p_e in the surrounding liquid and the pressure p_D (equivalent to the air concentrations C_D at a distance D from the pit) amount to $p_e = 150\,000$ Pa, $p_D = 70\,000$ Pa (case A, solid line) and $p_e = 150\,000$ Pa, $p_D = 76\,500$ Pa (case B, broken line), respectively. For the description of cases A and B, see text.

dn/dl (from Eq. (37)) and $I(l)$ into Eq. (40) shows that the integrand is a rational function in l, which consists of a polynomial of fifth degree in the numerator over a polynomial of third degree in the denominator. Subsequent integration leads to a transcendental function in l with the following structure:

$$\begin{aligned} t(l) = & \frac{1}{\delta_1 l + \delta_0} \times \{[\xi_1 l + \xi_0] \\ & \times \log(\lambda_1 l + \lambda_0) + [\Xi_1 l + \Xi_0] \log(\Lambda_1 l + \Lambda_0) \\ & + \nu_4 l^4 + \nu_3 l^3 + \nu_2 l^2 + \nu_1 l + \nu_0\} \\ & - \frac{1}{\delta_1 l_0 + \delta_0} \times \{[\xi_1 l_0 + \xi_0] \\ & \times \log(\lambda_1 l_0 + \lambda_0) + [\Xi_1 l_0 + \Xi_0] \log(\Lambda_1 l_0 + \Lambda_0) \\ & + \nu_4 l_0^4 + \nu_3 l_0^3 + \nu_2 l_0^2 + \nu_1 l_0 + \nu_0\}. \end{aligned} \quad (42)$$

l_0, the constant of integration in Eq. (42), is defined by $t(l_0) = 0$. Thus, l_0 denotes the position of the interface at time $t = 0$. The greek letters in Eq. (42) represent lengthy combinations of the constants $\mathscr{R}$, γ, S and k_H and the parameters T, l_{eq}, l_m, α, θ, s, w, C_D and D. The "equilibrium interface position" ($l = l_{eq}$ implies $I = 0$ and $p_D = C_D k_H$) is found to be

$$l_{eq} := \frac{1}{\sin\alpha}\left(s + \frac{2\gamma}{p_e - p_D}\cos(\alpha + \theta)\right). \quad (43)$$

Figs. 17 and 18 illustrate the two distinct cases of pit behaviour which are possible, according to Eq. (42). Which case is realized depends on the relation between l_{eq} and l_m (the value of the parameter l at maximum number of molecules in the PB):

$$\begin{aligned} &\text{Case A}: \quad l_{eq} \geqslant l_m, \\ &\text{Case B}: \quad l_{eq} \leqslant l_m. \end{aligned} \quad (44)$$

Comparison with Figs. 8 and 9 shows, that the PB behaves in entire analogy with a spherical bubble immersed in a liquid under negative pressure. Since cases A and B correspond to cases 3 and 4, respectively, a discussion of cases A and B can be omitted. We merely mention, that in case B, PB with their interface positioned initially at an $l_0 > l_{eq}$ should be treated as

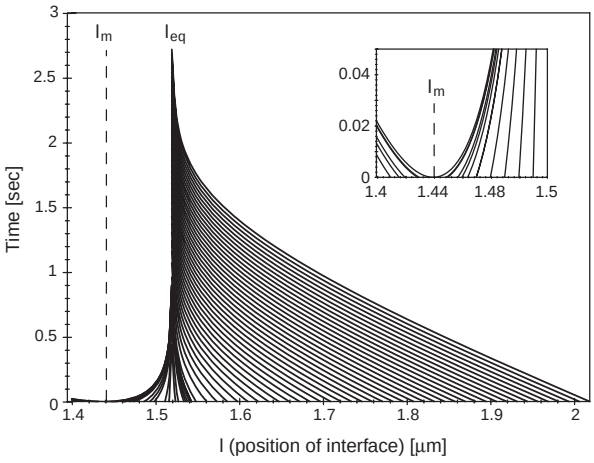

Fig. 17. Temporal development of an axisymmetric gas bubble in a pit which is coupled by diffusion to a gas reservoir at constant pressure. The insets show magnified details for small values of l and t. Time t is represented by the ordinate, the interface positions l by the abscissa. The abscissa terminates at the left at $l = l_g^{min}$ (for smaller l-values the interface would touch the pit membrane) and at the right at $l = l_p^{max}$ (greater l-values would lead to negative pressures within the gas bubble). l_m and l_{eq} denote the interface positions where the capacity of the bubble to host particles is at its maximum and where diffusion ceases, respectively. Each curve starts for $t = 0$ at an interface initial position l_0. Curves with $l_0 < l_m$ (see inset) describe PBs which dissolve, whereas curves starting at an $l_0 > l_m$ extend to temporal infinity, thus indicating that the interface approaches the equilibrium value $l = l_{eq}$. (case A, left). l_m and/or l_{eq} may be smaller than $l = l_g^{min}$ or greater than $l = l_p^{max}$. Their location depends on the values of p_e (pressure of the surrounding liquid) and p_D (pressure equivalent to the concentration $C_D = p_D k_H$ of gas particles in the surrounding liquid at a distance D from the pit). Since we want the figure to give a full picture of all effects possible, rather than to represent realistic cases, we have chosen $p_e = 150\,000$ Pa and $p_D = 70\,000$ Pa. Absolute temperature is $T = 298$ K. This case A illustrates.

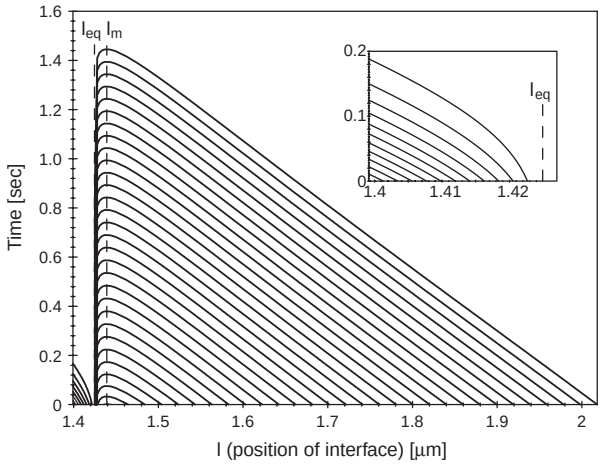

Fig. 18. Temporal development of an axisymmetric gas bubble in a pit which is coupled by diffusion to a gas reservoir at constant pressure. The insets show magnified details for small values of l and t. Time t is represented by the ordinate, the interface positions l by the abscissa. The abscissa terminates at the left at $l = l_g^{min}$ (for smaller l-values the interface would touch the pit membrane) and at the right at $l = l_p^{max}$ (greater l-values would lead to negative pressures within the gas bubble). l_m and l_{eq} denote the interface positions where the capacity of the bubble to host particles is at its maximum and where diffusion ceases, respectively. Each curve starts for $t = 0$ at an interface initial position l_0. PBs with their interface positioned initially at an $l_0 < l_{eq}$ (see inset) dissolve in the course of time while curves starting with an $l_0 > l_{eq}$ describe what happens if our system of equations exceeds its limits of competence. The problem can be resolved in the same way as in case 4 (Section 2 and Appendix A). l_m and/or l_{eq} may be smaller than $l = l_g^{min}$ or greater than $l = l_p^{max}$. Their location depends on the values of p_e (pressure of the surrounding liquid) and p_D (pressure equivalent to the concentration $C_D = p_D k_H$ of gas particles in the surrounding liquid at a distance D from the pit). Since we want the figure to give a full picture of all effects possible, rather than to represent realistic cases, we have chosen $p_e = 150\,000$ Pa and $p_D = 76\,500$ Pa (case B, right). Absolute temperature is $T = 298$ K. This depicts case B.

artefacts of our system of equations, rather than reality, in the same sense as their counterparts in case 4. A physically acceptable resolution of the problem with case B—the PB splits into daughter bubbles—follows the same principles as in case 4 (see also Section A.2).

The essential result of this section is that the PB can develop temporal stability (and only under this condition it can act as valve) if certain combinations of p_e and p_D exist in the conduit.

4. Bubble dynamics after air seeding events

4.1. Air seeding without embolism

An air seeding event does not necessarily embolize an intact vessel. If, according to Sections 2.1 and 2.3, the air sucked into the vessel develops into a (spherical) bubble which contains at most $n_{max} = (2\pi\gamma/\mathscr{R}T)(8\gamma/9p_s)^2$ particles, chances are good that the bubble behaves as described in cases 3 and 4: For $R_0 < R_m$ in case 3 and for $R_0 < R_{eq}$ in case 4 the bubble should have dissolved after some time.

For $R_0 > R_m$ in case 3, however, it should approach the equilibrium radius R_{eq}, and thus exist—in principle—indefinitely long. Within the framework of our equations (which quite naturally does not encompass all possible effects), a limited number of such non-expanding bubbles may be tolerated in an operating vessel. They can, however, disturb the metastable state of xylem tension and lead to its breakdown.

4.2. Repair after embolism

If, however, a bubble with $R_0 > R_{eq}$ develops according to case 4, or a bubble tries to form, which would contain $n > n_{max}$ particles, things are different: Then (in case 4, only when the radius $R = R_m$ has been reached) the expansion tendency of the gas particles due to their statistical movements inevitably outweighs the surface tension. Thus an equilibrium between the forces connected with both effects—which is a necessary condition for a bubble to establish itself—cannot be achieved. As discussed in Section A.2, the bubble will probably split up into daughter bubbles, which may or may not dissolve. The exact result of this situation is unpredictable, but it may well happen that repeated bursting of bubbles into daughter bubbles causes the water (which is in a metastable state under negative pressure) to "collapse" into a stable state. As a result, a positive water pressure establishes within the vessel and small gas bubbles drift into the pits connecting the embolizing vessel with its still intact neighbours. In the end, the ability of the vessel to conduct water has broken down completely.

According to the model of Holbrook and Zwieniecki (shortly described in Section 3.1) the repair scenario should now be initiated. In view of our results we reexamine three crucial aspects of the model, namely the questions (i) under which circumstances a diffusional flux of dissolved air molecules to the adjacent conduits establishes, (ii) whether the embolized vessel remains hydraulically isolated during the dissolution process, and (iii) how and when this hydraulic isolation breaks down.

(i) As the liquid pressure p_e is positive in an embolized vessel, it behaves according to cases 1 or 2 (notice, that when cases 1 and 2 are employed to describe a LB in an embolized vessel, p_s and p_e denote the same pressure). For $p_d < p_e$ case 1 is realized and the LB dissolves for all initial radii R_0 (see Fig. 6, notice that dissolution is not restricted to the R_0-values of the figure, e.g. a bubble with $R_0 =$ 50 μm needs under otherwise identical conditions about 20 s for dissolution). For $p_d > p_e$ case 2 (Fig. 7) is realized and the LB dissolves only if $R_0 < R_{eq}$ (which is in view of Eq. (17) equivalent to the condition $p_e < p_d < p_e + 2\gamma/R_0$), otherwise (for $p_d > p_e + 2\gamma/R_0$) it expands until it fills the lumen completely.

Since the concentration C_d of air dissolved in the xylem sap has in most cases presumably a value such that the condition $p_d < p_e$ is satisfied (recall that p_d is defined by $C_d = k_H\, p_d$), a LB will quite probably dissolve after some time, provided the embolized bubble remains hydraulically isolated during the dissolution process.

(ii) In terms of Figs. 17 and 18 an interface maintains hydraulic isolation (in principle) indefinitely long, if its (l,t)-curve approaches $l = l_{eq}$. Curves, which intersect the vertical line $l = l_g^{min}$ indicate hereby, that the interface touches the membrane and that hydraulic isolation fails due to bursting of the PB. If case A is realized, interfaces initially at a $l_0 < l_m$ do not isolate, those initially at a $l_0 > l_m$ do. Interfaces which behave according to case B are unsuited for isolation purposes, because they either (for $l_0 < l_{eq}$) move towards and touch eventually the membrane, or (for $l_0 > l_{eq}$) they run through a sequence of splitting events in the sense of Section A.2.

Consulting Fig. 19, we see that the relative positions of l_g^{min}, l_g^{max}, l_p^{max} and l_m depend on the pressure p_e. We furthermore observe, that for $p_e < p_e^{crit}$ (with $p_e^{crit} \approx 135\,000$ Pa for the values of the pit geometry and the contact angle chosen in Section 3) l_m is smaller than l_g^{min}. In view of Fig. 17, which illustrates case A, the inequality $p_e < p_e^{crit}$ implies that curves with $l_0 < l_m$ (leading to isolation failure) do not exist, that is, all interfaces approach

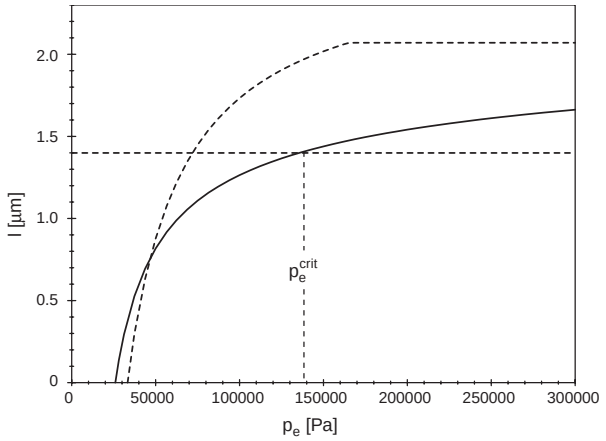

Fig. 19. $\min(l_g^{max}, l_p^{max})$ (curved broken line), l_g^{min} (straight broken line) and l_m (solid line) as functions of the pressure p_e in the xylem sap. $l_m(p_e)$ and l_g^{min} intersect at $p_e = p_e^{crit}$. The values of the pit geometry and the contact angle chosen in Section 3 imply $p_e^{crit} \approx 135\,000$ Pa.

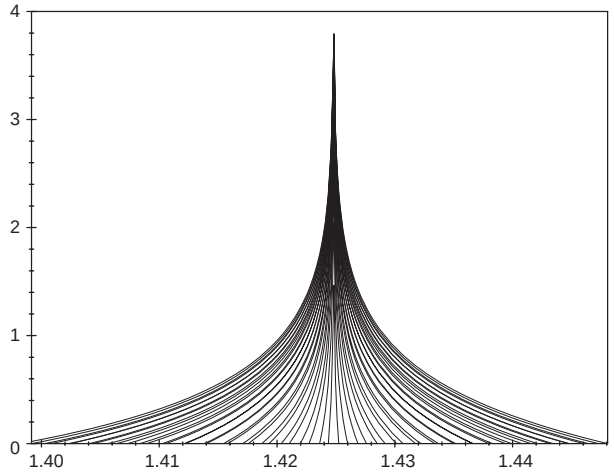

Fig. 20. Sequence of (t, l)-curves for the p_D-value 1500 Pa. Time $t(\Delta)$ is drawn along the ordinate, the interface position l (µm) along the abscissa. The pressure of the xylem sap is $p_e = 75\,000$ Pa. The sequence of Figs. 20–22 illustrate a section of the curve $l_{eq}(p_D)$ in Fig. 23. The parameter values in this figure satisfy $l_m < l_g^{min} < l_{eq}$. The present figure (and Fig. 21) describe pits which preserve hydraulic isolation (every interface approaches $l = l_{eq}$, reaches it after at most 3.5 s and stays there infinitely).

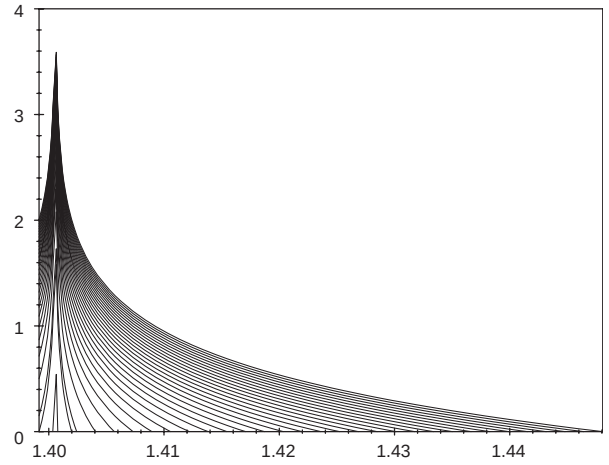

Fig. 21. Sequence of (t, l)-curves for the p_D-value 3000 Pa. Time t (s) is drawn along the ordinate, the interface positions l (µm) along the abscissa. The pressure of the xylem sap is $p_e = 75\,000$ Pa. The sequence of Figs. 20–22 illustrate a section of the curve $l_{eq}(p_D)$ in Fig. 23. The parameter values in this figure satisfy $l_m < l_g^{min} < l_{eq}$. Fig. 20 and the present figure (Fig. 21) describe pits which preserve hydraulic isolation (every interface approaches $l = l_{eq}$, reaches it after at most 3.5 s and stays there infinitely).

l_{eq} (preserving isolation). Related to Fig. 18, which illustrates case B, condition $l_m < l_g^{min}$ (which is equivalent to $p_e < p_e^{crit}$) implies that all curves intersect the vertical line $l = l_g^{min}$, which means failure of isolation. Since case B is defined via the condition $l_{eq} < l_m$, we conclude: if the pit is exposed to the pressure $p_e < p_e^{crit}$, hydraulic isolation is preserved as long as the relation $l_{eq} > l_g^{min}$ is valid. When l_{eq} drops below l_g^{min}, isolation fails almost immediately (see Figs. 20–22).

This result is a general one, although we do not give explicitly p_e^{crit} as a function of the contact angle θ, the pit opening half-angle α and the radii s and w of pit membrane and pit neck, respectively. This is, because $p_e^{crit}(\theta, \alpha, s, w)$ is equivalent to and would have to be solved for from the equation $l_m = l_g^{min}$, which is possible in principle but beyond the scope of the present contribution.

We should point out that the values of the pressures p_e and p_D (or, rather, the "boundary concentration" $C_D = k_H p_D$ of air in water) leading to Figs. 17 and 18 were primarily chosen with respect to the purpose of illustrating all possible aspects of cases A and B. In an embolized vessel, a value of the pressure p_e of the xylem sap around 1 atm = 101 325 Pa appears to be not unreasonable, because it is the pressure of the atmosphere. Even if the plant is capable somehow to exert an additional pressure on the embolized vessel, the value $p_e^{crit} \approx 135\,000$ Pa leaves some margin for the relation $p_e < p_e^{crit}$ to be satisfied. Remember, however, that the value of $p_e^{crit}(\theta, \alpha, s, w)$ is species dependent.

(iii) Figs. 23 and 24 (and, more generally, Eq. (43) upon differentiation with respect to p_D) show that l_{eq} is a monotonically decreasing function of p_D. That is, there are values of p_D which satisfy the unequality $l_{eq}(p_D) > l_g^{min}$ (implying that the respective interface maintains hydraulic isolation). If we increase p_D, the value of $l_{eq}(p_D)$ decreases and reaches eventually values $l_{eq}(p_D) < l_g^{min}$ (which indicate the loss

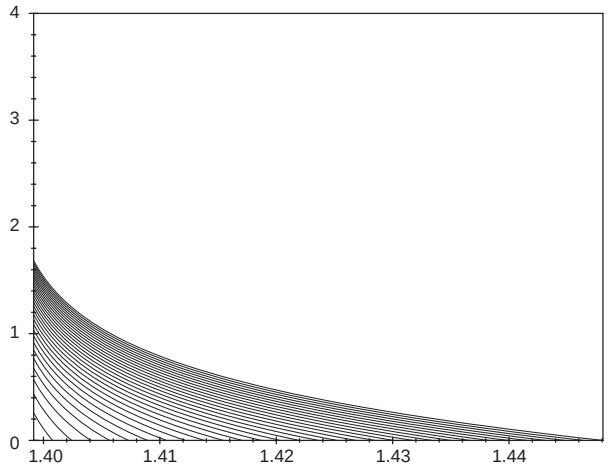

Fig. 22. Sequence of (t, l)-curves for the p_D-value 3250 Pa. Time t (s) is drawn along the ordinate, the interface positions l (μm) along the abscissa. The pressure of the xylem sap is $p_e = 75\,000$ Pa. The sequence of Figs. 20–22 illustrate a section of the curve $l_{eq}(p_D)$ in Fig. 23. The present figure is based upon the relation $l_m < l_{eq} < l_g^{min}$. The pits considered by this figure become permeable because every interface approaches the pit membrane and touches it after at most 1.7 s.

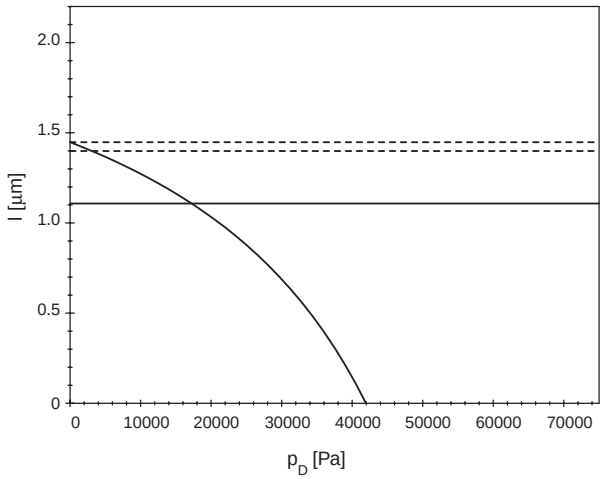

Fig. 23. $\min(l_g^{max}, l_p^{max})$ (upper broken line), l_g^{min} (lower broken line), l_m (solid line, horizontal) and l_{eq} (solid line, curved) as functions of the pressure p_D, which stands for the air concentration $C_D = k_H p_D$ in the xylem sap at a distance D from the pit neck (see Figs. 11 and 26). The gas/liquid interface in a pit provides hydraulic isolation, if (i) l_m lies below the lower broken line (i.e $l_m < l_g^{min}$), and (ii) $l_{eq}(p_D)$ lies between the broken lines (i.e. $l_g^{min} < l_{eq} < \min(l_g^{max}, l_p^{max})$). In the present figure, $p_e = 75\,000$ Pa, that is, $p_e < p_e^{crit}$. Thus, condition (i) is fulfilled and the gas/liquid interface in the PB behaves as in case A (see Fig. 17). Figs. 20–22 are related to Fig. 23, the present figure in that the former can be viewed as "realizations" of the latter for different values of the variable p_D. In Figs. 20 and 21 conditions (ii) is also fulfilled and hydraulic isolation thus realized, in Fig. 22 it is not.

of the isolation ability of the pit, as explained above).

Recalling from Fig. 2 (or from the Young–Laplace equation) that the pressure within a

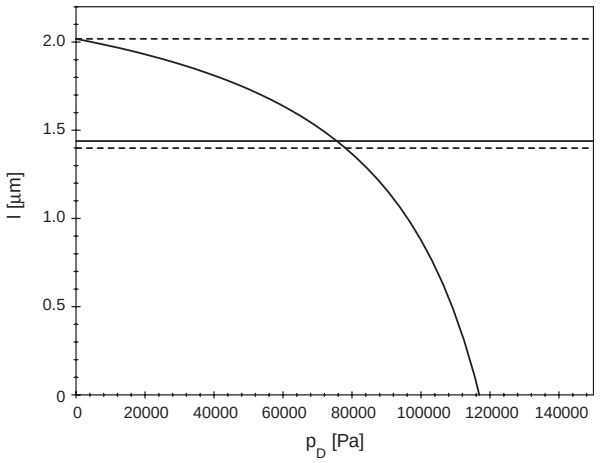

Fig. 24. $\min(l_g^{max}, l_p^{max})$ (upper broken line), l_g^{min} (lower broken line), l_m (solid line, horizontal) and l_{eq} (solid line, curved) as functions of the pressure p_D, which stands for the air concentration $C_D = k_H p_D$ in the xylem sap at the distance D from the pit neck (see Figs. 11 and 26). The gas/liquid interface in a pit provides hydraulic isolation, if (i) l_m lies below the lower broken line (i.e $l_m < l_g^{min}$), and (ii) $l_{eq}(p_D)$ lies between the broken lines (i.e. $l_g^{min} < l_{eq} < \min(l_g^{max}, l_p^{max})$). In the present figure, $p_e = 150\,000$ Pa, that is, $p_e > p_e^{crit}$. Thus, condition (i) is not fulfilled and the gas/liquid interface in the PB behaves as in case A (see Fig. 18). Hydraulic isolation cannot be achieved, although condition (ii) is fulfilled for a wide range of p_D-values. The values of the pit geometry and the contact angle chosen in Section 3 imply $p_e^{crit} \approx 135\,000$ Pa.

spherical bubble grows rapidly with decreasing bubble radius, Henry's Law implies an increasing air concentration in the liquid around the LB during the dissolution process, in fact, it culminates at the moment when the LB disappears.

We propose, that the combination of both effects cause the breakdown of hydraulic isolation as the last act of the repair process. We cannot become more specific at this point, because the mathematics we have used so far is too simple to express (or predict) the time of isolation breakdown as a function of pit geometry, vessel geometry, contact angle, of the pressures involved and of the number of particles trapped initially in an LB. The reason for the complexity of these processes is primarily due to the diffusional currents which evolve between the LB, the PB and the adjacent conduits (see Fig. 10). To describe the situation more accurately, the diffusion equation must be solved in at least two dimensions and more sophisticated approximations for the boundary conditions must be employed.

5. Final conclusions

This first physical analysis provides evidence that (i) the preconditions for the mechanism are satisfied

(within the chosen parameters), (ii) temporally stable PB can establish and that (iii) the breakdown of the pit bubbles can be initiated by the final stage of the repair process. The results summarized so far thus indicate that the mechanism suggested by Holbrook and Zwieniecki (1999) is principally able to cause hydraulic isolation of an embolized conduit. The results, however, also show that the underlying physical processes are very complex and depend heavily on the geometric properties of the pits, on the developing contact angle and on the gas concentration in the sap. Further analyses of the bubble behaviour in xylem conduits are expected to yield a more detailed understanding of the involved mechanisms and of the role of interfacial effects. Since the considered processes cannot be observed directly, theoretical analyses of this subject are an indispensable tool for improving our knowledge of the significance of interfacial effects for plant water transport.

Appendix A

A.1. Diffusion equation and diffusion current $I(R)$ in a spherically symmetric situation

For the sake of simplicity, we assume the following (see Fig. 4): (i) The gas bubble is surrounded by an (imaginary) sphere-shaped closed surface with radius d which resides completely within the vessel lumen. This sphere serves as source or sink for the diffusing gas particles. (ii) Outside of this closed surface the concentration of dissolved gas particles is kept constant at the value C_d. Thus, we restrict the process of diffusion to a spherical section of the vessel lumen which contains the gas bubble, and we assume that the air concentration in the xylem sap exterior to this section remains constant. Due to this auxiliary construction the whole system is spherically symmetric and can conveniently be parametrized with the radial coordinate r, the distance to the centre of the bubble.

In order to calculate $I(R)$ we first have to solve the diffusion equation for the area between $r = R$ and d.

The time-independent diffusion equation for spherical symmetry reads as

$$\frac{1}{r^2}\frac{\mathrm{d}}{\mathrm{d}r}\left(r^2\frac{\mathrm{d}C}{\mathrm{d}r}\right) = 0. \tag{A.1}$$

The general solution of this equation contains two arbitrary constants, a and b,

$$C(r) = a + \frac{b}{r}. \tag{A.2}$$

The solution $C(r)$ is subject to the boundary conditions

$$C(R) = C_R \quad \text{and} \quad C(d) = C_d. \tag{A.3}$$

C_R means the concentration of air in the near vicinity of the bubble and C_d denotes the (constant) concentration of air in the liquid, the xylem sap (as depicted in Fig. 4). Application of the boundary conditions (A.3) results in

$$C(r) = \frac{C_d d - C_R R}{d - R} + \frac{Rd}{d - R}(C_R - C_d)\frac{1}{r}. \tag{A.4}$$

The current density $\vec{j}$ of the gas particles diffusing through the liquid follows from (A.4) according to Fick's Law

$$\vec{j} = -S\,\mathrm{grad}\,C, \tag{A.5}$$

where S represents the effective conductance of the liquid for the diffusing substance. Due to spherical symmetry only the radial component of $\vec{j}$ remains,

$$j(r) = -S\frac{\mathrm{d}C(r)}{\mathrm{d}r} = S\frac{Rd}{d - R}(C_R - C_d)\frac{1}{r^2}. \tag{A.6}$$

The (total) current I including all gas particles diffusing into or out of the gas bubble is given by integration over the (closed) surface of a sphere centered at $r = 0$ with a radius r_a which may lie anywhere in the interval $R < r_a < d$:

$$I = \oint \vec{j}\cdot d\vec{A} = j(r_a)r_a^2\int_0^{\pi}\sin\theta\,\mathrm{d}\theta\int_0^{2\pi}\mathrm{d}\phi$$
$$= 4\pi j(r_a)r_a^2 = 4\pi S\frac{Rd}{d - R}(C_R - C_d). \tag{A.7}$$

Eq. (A.7) states that the gas bubble is in equilibrium with the environment (i.e. no gas particles are exchanged), when there is no diffusion current. How C_R is dependant on R follows from Henry's Law (7) and the Young–Laplace equation (2),

$$C_R = k_H p_s + \frac{2\gamma k_H}{R}. \tag{A.8}$$

This one-to-one relation between C_R and R is the basis of the geometric characterization of the equilibrium situation $C_R = C_d$ (equivalent to $I = 0$ by (A.7)) via the "equilibrium radius" $R_{eq} = 2\gamma/(p_d - p_s)$ of definition (17): Substitution of $R = R_{eq}$ in (A.8) leads to $C_R = C_d$ and hence to $I = 0$.

Eventually, after insertion of Eqs. (A.8) and (17) we obtain the explicit R-dependence of Eq. (A.7)

$$I(R) = 8\pi S\gamma k_H\frac{d}{R_{eq}}\frac{R_{eq} - R}{d - R}. \tag{A.9}$$

For the evaluation of the integral in Eq. (11) we need a second ingredient beneath $I(R)$. Using Eq. (5) in order to eliminate p_s in favour of R_m from $\mathrm{d}n/\mathrm{d}R$ we obtain

$$\frac{\mathrm{d}n}{\mathrm{d}R} = \frac{16\pi\gamma}{3\mathscr{R}T}\frac{R}{R_m}(R_m - R). \tag{A.10}$$

We note that the interpretations of the quantities R_m and R_{eq} are significant only if the relations $p_s < 0$ and $p_d - p_s > 0$, respectively, are valid, i.e. if the xylem pressure is negative. Eqs. (5) and (17), however, can and will be viewed as formal definitions of R_m and R_{eq} also for positive xylem pressure, in the sense of a shorthand

notation. Interpretations in terms of radii are, however, not valid then.

By using Eqs. (A.9) and (A.10) we obtain from Eq. (10)

$$\frac{dt}{dR} = \frac{-2}{3\mathscr{R}TSdk_H}(d-R)R\frac{R_{eq}}{R_m}\frac{R_m-R}{R_{eq}-R}, \tag{A.11}$$

the desired integrand of Eq. (11).

A.2. Detailed discussion of a lumen bubble (LB) according to case 4

Fig. 25 gives a more realistic picture of the temporal development of a case 4-bubble than Fig. 9. The upper part of the figure shows the number of particles $n(R)$ in the bubble, its lower part represents typical examples on a bubble's (R,t)-path (the path given here describes the fate of just one bubble, the sister or daughter bubbles do not appear). The (R,t)-path consists of two types of curves:

- the curves $0\rightarrow 1-$, $1+\rightarrow 2-$, $2+\rightarrow 3-$, $2'+\rightarrow 3'$, and beyond $3+$ represent time segments, which are predicted by Eq. (8),
- the straight lines $1-\rightarrow 1+$, $2-\rightarrow 2+$, $2-\rightarrow 2'+$ and $3-\rightarrow 3+$ stand for the "jumps" in radius R caused by the formation of daughter bubbles whenever the bubble radius R takes on the value $R=R_m$.

The quantities Δn_1, Δn_2, $\Delta n_{2'}$ and Δn_3 in the upper part of the figure are related to the numbers of particles lost from the considered bubble during the splitting events $1-\rightarrow 1+$, $2-\rightarrow 2+$, $2-\rightarrow 2'+$ and $3-\rightarrow 3+$.

The bubble's route through the (R,t)-plain evolves as follows:

- Starting at a radius $R=R_0$ (point 0) the bubble develops according to Eq. (8) until it undergoes a non-predictable splitting event at $1-$. Then it loses Δn_1 particles, which forces its radius to jump to one of the two solutions of Eq. (3) for $n=n_{max}-\Delta n_1$. We suppose that the value R_{1+} is realized.
- Curve $1+\rightarrow 2-$ again obeys Eq. (8), at $2-$ the bubble experiences a second splitting, the particle loss amounts to Δn_2. Again, the bubble radius may jump to either of the two R-values R_{2+} or $R_{2'+}$.
- If the bubble happens to "choose" the latter value, the diffusional current, which has procured particles so far, is from now on directed out of the bubble, and the bubbles fate is, according to Eq. (8), to evaporate particles until its existence ceases at $3'$.
- If the bubble radius takes on the latter value, the diffusional current is again directed into the bubble, the curve $2+\rightarrow 3-$ evolves according to Eq. (8), a third splitting of the bubble occurs at $3-$, combined with a particle loss Δn_3, and so on.

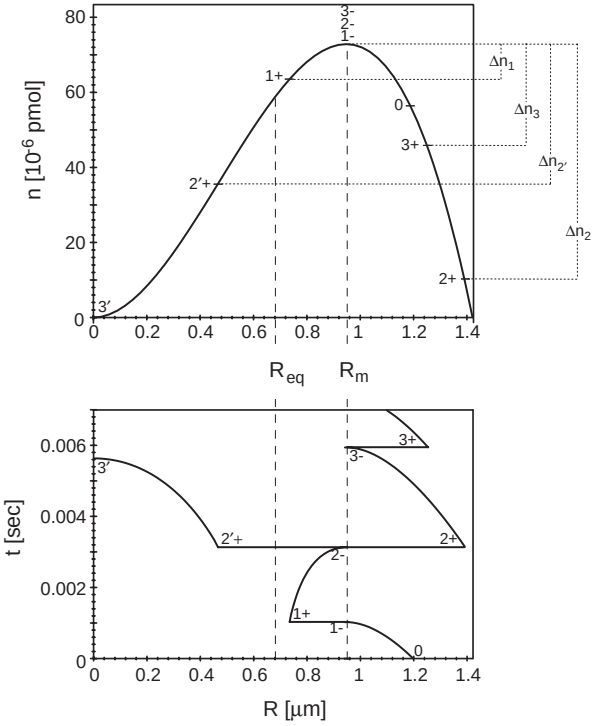

Fig. 25. Upper part: Particle number $n(R)$ as a function of bubble radius R of a gas bubble in a liquid (case 4, i.e. $0<R_{eq}<R_m$, equivalent to $0<-p_s<p_d$). Lower part: Possible (t,R)-path of a gas bubble in case 4 (for explanation see text).

A.3. Stability of the diffusional equilibrium at $R=R_{eq}$

In order to shed some light onto the nature of the equilibrium characterized by $I=0$, or, in geometric terms, by $R=R_{eq}$, we examine the system's behaviour if it is initially in equilibrium (i.e. no diffusional current) and then slightly perturbed. In order to define this we expand Eq. (8) about $R=R_{eq}$ after setting $R(t)=R_{eq}+\rho(t)$. Since we assume $|\rho|\ll R$ it is sufficient to keep only the linear terms in ρ. The expansions

$$n(R)\approx n(R_{eq})+n'(R_{eq})\cdot\rho, \tag{A.12}$$

$$I(R)\approx I(R_{eq})+I'(R_{eq})\cdot\rho \tag{A.13}$$

(a prime stands for differentiation with respect to R) reduce upon differentiation with respect to t (which is characterized by a dot) and in view of the condition of equilibrium $I(R_{eq})=0$ to

$$\dot{n}(R)\approx n'(R_{eq})\cdot\dot{\rho}, \tag{A.14}$$

$$I(R)\approx I'(R_{eq})\cdot\rho. \tag{A.15}$$

Insertion into Eq. (8) and reorganization leads to the linear first order differential equation

$$\dot{\rho}+\frac{I'(R_{eq})}{n'(R_{eq})}\rho=0 \tag{A.16}$$

with the readily obtained solution

$$\rho(t) = \rho_0 \exp\left(-\frac{I'(R_{eq})}{n'(R_{eq})}t\right). \tag{A.17}$$

ρ_0, the constant of integration, characterizes the radial distance by which the bubble has been disturbed initially, at $t = 0$.

The interpretation of the result (A.17) is straightforward: An initial perturbation ρ_0 "dies out" with an characteristic "decay time" $\tau := n'(R_{eq})/I'(R_{eq})$ if the expression

$$\frac{n'(R_{eq})}{I'(R_{eq})} = \frac{2}{3\mathscr{R}TSdk_H} R_{eq}^2 (d - R_{eq}) \frac{R_{eq} - R_m}{R_m}, \tag{A.18}$$

in the exponent in Eq. (A.17) is (strictly) positive. If it is negative, the initial perturbation ρ_0 grows unboundedly with time.

As all parameters in the first factor on the right-hand side of Eq. (A.18) are positive and as the relations $R_{eq} > 0$ and $d > R_{eq}$ are valid by assumption, the sign of Eq. (A.18) depends on the signs of R_m and of the difference $R_{eq} - R_m$. The results are given in the following table (the "case-labels" refer to table (18))

$$\begin{aligned}
&\text{Unstable equilibrium}: \quad \rho(t) \to \infty \quad \text{if } R_m < 0 \quad \text{(case 2)},\\
&\qquad\qquad\qquad\qquad\quad \rho(t) \to \infty \quad \text{if } R_m > 0\\
&\qquad\qquad\qquad\qquad\quad \text{and } R_{eq} < R_m \quad \text{(case 4)}.\\
&\text{Stable equilibrium}: \quad \rho(t) \to 0 \quad \text{if } R_m > 0\\
&\qquad\qquad\qquad\qquad\quad \text{and } R_{eq} > R_m \quad \text{(case 3)}
\end{aligned} \tag{A.19}$$

A.4. Diffusion equation and diffusion current $I(l)$ in an axisymmetric situation

In order to calculate $I(l)$ we first have to solve the diffusion equation in the area where transport of gas particles via diffusion occurs. For the sake of simplicity, we rely on the following assumptions and approximations (see Fig. 26):

(i) No gas particles diffuse across the walls of the pit and of the pit channel.
(ii) Diffusional transport of gas particles through xylem sap is restricted to the embolized side of the pit (that is, the pit membrane is supposed to be dense).
(iii) At a distance $z = z_- := -D$ from the pit and beyond (i.e. for $z \leqslant z_-$) the concentration of dissolved gas particles in the liquid is kept constant at the value $C_D = p_D k_H$.
(iv) The gas/liquid interface at position l coincides approximately with a section of a (fictitious) sphere of radius $r = r_+ := (s/\sin\alpha) - l$ (for $\theta = \pi/2$ the coincidence is exact).
(v) The section of a (fictitious) sphere of radius $r = r_- := w/\sin\alpha$ coincides in an approximate sense with the (equally fictitious) flat(!), circular disc of radius w at $z = z_+ := w\cot\alpha$.

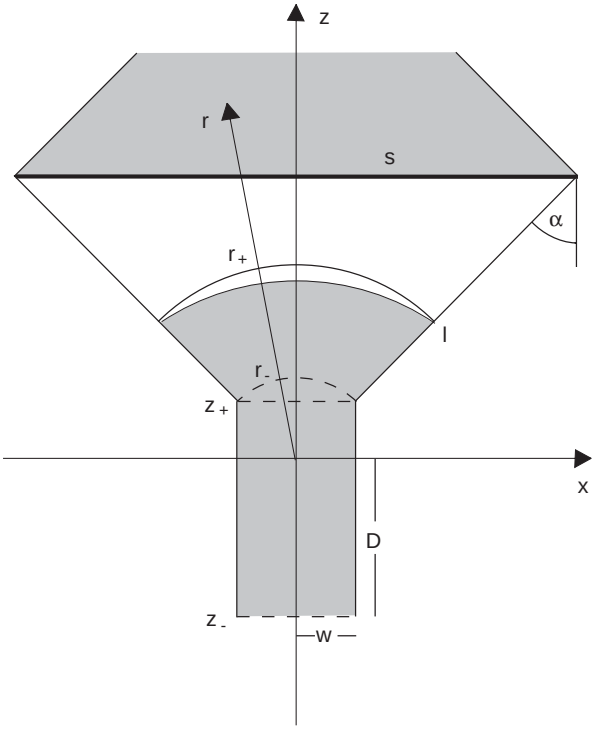

Fig. 26. Coordinates used in Section A.4. The z-axis is axis of symmetry. The origin of the coordinate system is at the (fictitious) tip of the pit cone. Thus, the spherical surfaces defined by $r = r_-$ and r_+ intersect the pit cone at right angles. The gas/liquid interface (characterized by l) is also a section of a sphere, but of radius R (as defined in Eq. (19), R is not shown here). Its centre coincides with the origin of the coordinate system only in the special case $\theta = \pi/2$. For $\theta < \pi/2$ it is on the negative, for $\theta > \pi/2$ on the positive part of the z-axis, respectively.

Diffusional currents connect the gaseous space (white) and the plane $z = z_-$, on which the air concentration C_D is held constant.

gray: water, l: position of the gas/liquid interface, s: radius of pit membrane, θ: contact angle, α: pit opening half angle, w: radius of pit neck, D: length of pit channel.

Thus, we employ a similar auxiliary construction as above, which allows us to work with (i) one-dimensional versions of the diffusion equation (and hence simple, analytic solutions) on two spatial "patches", and (ii) very simple boundary conditions. On the patch defined by $r_- \leqslant r \leqslant r_+$ the time-independent diffusion equation for spherical symmetry reads as

$$\frac{1}{r^2}\frac{\mathrm{d}}{\mathrm{d}r}\left(r^2 \frac{\mathrm{d}C}{\mathrm{d}r}\right) = 0, \tag{A.20}$$

with general solution

$$C(r) = a + \frac{b}{r}. \tag{A.21}$$

On the patch with $z_- \leqslant z \leqslant z_+$ the cylinder symmetric equivalent of Eq. (A.20) is

$$\frac{d^2C}{dz^2} = 0, \tag{A.22}$$

with solution

$$C(z) = A + Bz. \tag{A.23}$$

a, b, A and B are arbitrary constants which are calculated from the boundary conditions

$$C(r_+) \approx C_l \quad \text{and} \quad C(z_-) = C_D, \tag{A.24}$$

and the conditions of continuity for particle concentration and particle current

$$C(r_-) \approx C(z_+) \quad \text{and} \quad I(r_-) \approx I(z_+). \tag{A.25}$$

Eqs. (A.24) and (A.25) are the formalized versions of assumptions (iii)–(v). Assumption (ii) ("no-flow boundary") is automatically fulfilled by Eqs. (A.21) and (A.23). Application of Eqs. (A.24) and (A.25) to the general solutions (A.21) and (A.23), use of Henry's Law

$$C_l = pk_H, \tag{A.26}$$

and Fick's Law

$$\vec{j} = -S\, grad\, C, \tag{A.27}$$

and an integration similar to that leading from Eq. (A.16) to Eq. (A.17) results in

$$I(l) = 2\pi S k_H w^2 \sin\alpha \frac{(s - l\sin\alpha)(p_e - p_D) + 2\gamma\cos(\alpha + \theta)}{(s - l\sin\alpha)[w(1 + 3\cos\alpha) + 2D\sin\alpha] - w^2(1 + \cos\alpha)}. \tag{A.28}$$

References

Cochard, H., Ewers, F., Tyree, M.T., 1994. Water relations of a tropical vinelike bamboo (*Rhipidocladum racemiflorum*): root pressures, vulnerability to cavitation and seasonal changes in embolism. J. Exp. Bot. 45, 1085–1089.

Ewers, F.W., Fisher, J.B., Fichtner, K., 1991. Water flux and xylem structure in vines. In: Putz, F.E. and Mooney, H.A. (Eds), The Biology of Vines. Cambridge University Press, Cambridge.

Hacke, U.G., Stiller, V., Sperry, J.S., Pittermann, J., McCulloh, K., 2001. Cavitation fatigue: embolism and refilling cycles can weaken the cavitation resistance of xylem. Plant Physiol. 125, 779–786.

Holbrook, N.M., Zwieniecki, M.A., 1999. Embolism repair and xylem tension. Do we need a miracle? Plant Physiol. 120, 7–10.

Holbrook, N.M., Burns, M.J., Field, C.B., 1995. Negative xylem pressure in plants: a test of the balancing pressure technique. Science 270, 1193–1194.

Holbrook, N.M., Ahrens, E.T., Burns, M.J., Zwieniecki, M.A., 2001. In vivo observation of cavitation and embolism repair using magnetic resonance imaging. Plant Physiol. 126, 27–31.

van Ieperen, W., Nijsse, J., Keijzer, C.J., van Meeteren, U., 2001. Induction of air embolism in xylem conduits of pre-defined diameter. J. Exp. Bot. 358, 981–991.

Magnani, F., Borghetti, M., 1995. Interpretation of seasonal changes of xylem embolism and plant hydraulic resistance. Plant Cell Environ. 18, 689–696.

McCully, M.E., 1999. Root xylem embolisms and refilling. Relation to water potentials of soil, root and leaves, and osmotic potentials of root xylem sap. Plant Physiol. 119, 1001–1008.

Milburn, J.A., 1991. Cavitation and embolisms in xylem conduits. In: Raghavendra, A.S. (Ed.), Physiology of Trees. Wiley, New York, pp. 163–174.

Pickard, W.F., 1981. The ascent of sap in plants. Prog. Biophys. Molec. Biol. 37, 181–229.

Pockman, W.T., Sperry, J.S., OLeary, J.W., 1995. Sustained and significant negative water pressure in xylem. Nature 378, 715–716.

Salleo, S., LoGullo, M., Depaoli, M., Zippo, M., 1996. Xylem recovery from cavitation-induced embolism in young plants of Laurus nobilis: a possible mechanism. New Phytol. 132, 47–56.

Sperry, J.S., Tyree, M.T., 1988. Mechanism of water stress-induced xylem embolism. Plant Physiol. 88, 581–587.

Sperry, J.S., Donnelly, J.R., Tyree, M.T., 1988. Seasonal occurrence of xylem embolism in sugar maple (*Acer saccharum*). Am. J. Bot. 75, 1212–1218.

Sperry, J.S., Saliendra, N.Z., Pockman, W.T., Cochard, H., Cruiziat, P., Davis, D., Ewers, F.W., Tyree, M.T., 1996. New evidence for large negative xylem pressures and their measurement by the pressure chamber method. Plant Cell Environ. 19, 427–436.

Steudle, E., 2001. The cohesion–tension mechanism and the acquisition of water by plant roots. Annu. Rev. Plant Physiol. Plant Mol. Biol. 52, 847–875.

Tyree, M.T., Ewers, F., 1991. The hydraulic architecture of trees and other woody plants. New Phytol. 199, 345–360.

Tyree, M.T., Sperry, J.S., 1989. Vulnerability of xylem to cavitation and embolism. Annu. Rev. Plant Physiol. Plant Mol. Biol. 40, 19–38.

Tyree, M.T., Yang, S., 1990. Water-storage capacity of Thuja, Tsuga and Acer stems measured by dehydration isotherms: the contribution of capillary water and cavitation. Planta 182, 420–426.

Tyree, M.T., Salleo, S., Nardini, A., LoGullo, M.A., Mosca, R., 1999. Refilling of embolized vessels in young stems of laurel: do we need a new paradigm? Plant Physiol. 120, 11–21.

Yang, S., Tyree, M.T., 1992. A theoretical model of hydraulic conductivity recovery from embolism with comparison to experimental data on Acer saccharum. Plant Cell Environ. 15, 633–643.

Zimmermann, M.H., 1983. Xylem Structure and the Ascent of Sap. Springer, Berlin.

Zwieniecki, M.A., Holbrook, N.M., 2000. Bordered pit structure and vessel wall surface properties. Implications for embolism repair. Plant Physiol. 123, 1015–1020.

5.2 Konrad, W., Roth-Nebelsick, A.: *The Significance of Pit Shape for Hydraulic Isolation of Embolized Conduits of Vascular Plants During Novel Refilling*, Journal of Biological Physics 31 (2005), p. 57–71.

Journal of Biological Physics 31: 57–71, 2005.
DOI: 10.1007/s10867-005-6094-0

The Significance of Pit Shape for Hydraulic Isolation of Embolized Conduits of Vascular Plants During Novel Refilling

W. KONRAD and A. ROTH-NEBELSICK*
Institut für Geowissenschaften, University of Tübingen, Sigwartstrasse 10, D-72076 Tübingen, Germany
*(*Author for correspondence, e-mail: anita.roth@uni.tuebingen.de)*

Abstract. During plant water transport, the water in the conducting tissue (xylem) is under tension. The system is then in a metastable state and prone to bubble development and subsequent embolism blocking further water transport. It has recently been demonstrated, that embolism can be repaired under tension (= novel refilling). A model (Pit Valve Mechanism = PVM) has also been suggested which is based on the development of a special meniscus in the pores (pits) between adjacent conduits. This meniscus is expected to be able to isolate embolized conduits from neighbouring conduits during embolism repair. In this contribution the stability of this isolating meniscus against perturbations is considered which inevitably occur in natural environments. It can be shown that pit shape affects the stability of PVM fundamentally in the case of perturbation. The results show that a concave pit shape significantly supports the stability of PVM. Concave pit shape should thus be of selective value for species practicing novel refilling.

Key words:

1. Introduction

According to the Cohesion-Tension Theory, upward water flow in land plants is generated by a water potential gradient driven by transpiring leaves [1, 2]. This mechanism can cause large tension gradients in the xylem, the water-conducting tissue of vascular plants [3–5]. Because it is in a metastable state, this system can be easily disturbed by the development of gas bubbles within these conduits, blocking transport of the water [6–8]. The water-transporting conduits of the xylem are tracheids or vessels formed by dead lignified cells with a typical radius of $30\,\mu\text{m} \ldots 100\,\mu\text{m}$. The conduits are not laterally tight capillaries. Their walls are strewn with pores (=pits) which represent lateral channels between adjacent conduits. Water can flow through these pits from one conduit to a neighbour conduit. The pit channel between two adjacent conduits is separated by a porous membrane (=pit membrane) which represents the primary wall.

There are several possible mechanisms of bubble development during plant water transport [4, 9] It is, however, generally assumed that embolism events develop in many cases from an initially small, gas filled cavity in the xylem. This pre-existing bubble is drawn through the pores of the pit membrane into a functioning conduit (the "air seeding hypothesis," [10]). The expansion of the gaseous space stops when the gas bubble reaches the conduit pits. This process leads to embolism preventing any further water transport. There is recent evidence that embolism occurs frequently during daily xylem water transport and can be removed (1) very quickly (within minutes) and (2) – at least in several species – under xylem tension, that is, during transpiration [11–14]. The last observation, termed as "novel refilling," is difficult to explain [12, 15]. The following questions arise:

1. How is it possible that water moves into an embolized conduit when negative pressures exist in the adjacent functioning conduits? According to the pressure gradient (higher pressure in the embolized conduit than in the non-embolized conduits), water should rather flow out of the embolized conduit than into it.
2. How is it possible under these circumstances to achieve bubble dissolution in the embolized conduits, i.e. how can the positive pressures needed for refilling coexist with tension?
3. How is hydraulic continuity restored?

It has recently been suggested that (1) living cells within the xylem can supply embolized conduits with water needed for refilling [16] and (2) the surface properties and the pit geometry of the conduits cause interfacial effects which lead to hydraulic isolation and contribute to bubble dissolution [17]. This mechanism is termed as Pit Valve Mechanism (=PVM) throughout the rest of this paper. According to [17], novel refilling would thus rely on (1) a biological basis and (2) a physical basis represented by PVM. A biophysical analysis of PVM concentrating on the temporal course of bubble growth or bubble dissolution during embolism repair has been recently presented [18]. The essence of the repair scenario is that a "reverse meniscus" (see Figure 1) can develop between a gas bubble in the pit chamber (termed as "PB", pit bubble, throughout the rest of this text) and the water in an embolized conduit if the contact angle and the geometry of the pit chamber are suitably related. The interface then exerts pressure upon the water and not upon the gas and is probably able to hydraulically isolate the embolized vessels from their intact neighbours, so that the high pressure required to drive the gas back into solution can be generated in the embolized conduit only. Although the study [18] demonstrated that PVM is principally possible there are still open questions concerning the reliability and biological relevance of PVM. One significant aspect is how stable PVM is against perturbations from external forces which inevitably occur in a natural environment (for example, mechanical vibrations caused by wind or animals) and how pit shape affects PVM. In this paper, the stability of PVM against perturbations and the influence of pit shape are investigated in detail. It will be demonstrated that pit shape is of high significance for the stability of PVM.

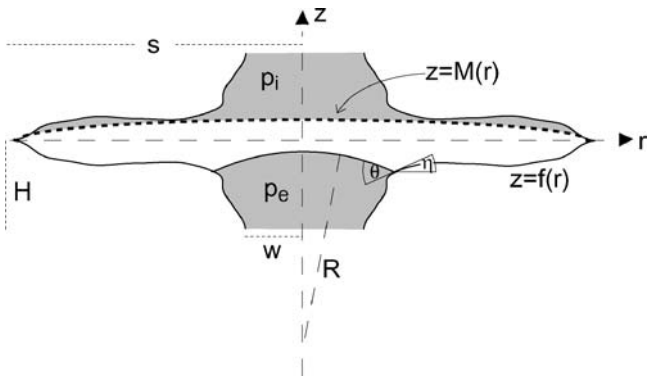

Figure 1. Section through a pit along its axis of symmetry. The shape of the pit is described by the function $z = f(\rho)$ (lower, right part of figure). The other parts of the pit shape arise from (1) mirror symmetry with respect to the $z = 0$-plane (upper, right part of figure) and (2) rotational symmetry around the z-axis (left part of figure). The function $z = M(\rho)$ describes the membrane, which bends because of the pressure difference between the embolized vessel (pressure $p_e > 0$) and the intact vessel (pressure $p_i < 0$) towards the latter. θ denotes the contact angle between water and pit wall. η is the angle between the tangent of the function $f(\rho)$ and the $z = 0$-plane, thus $\tan\eta = f'(\rho)$. s denotes the radius of the (unbent) pit membrane, w the radius of the pit mouth, and H the height of a half pit along its symmetry axis.

In the present article, we do not discuss PVM in general. For a general exposition as well as for the details of PVM we refer to [17, 18].

2. Concept of Stability for Axisymmetric Pit Bubbles

The reasoning in this section follows a line of thought given in Shen et al. [19] for spherically symmetric gas bubbles immersed in a liquid of either positive or negative pressure.

Our goal is to find a criterion which allows to decide whether or not a meniscus at a given position within a pit represents a point of stable or of unstable equilibrium with respect to small perturbations of the position of the meniscus.

If the gas bubble neither contracts nor expands, we may conclude that within the gas/liquid-interface an equilibrium exists between (1) the "confining" liquid pressure p_e, and (2) the "expansive" pressure $\tilde{p}$ exerted by the expansion seeking gas within the bubble plus the surface tension of the reverse meniscus of the PB which acts, due to the pit geometry, also in an "expansive" way.

We start from the equation of an ideal gas

$$\tilde{p} = \frac{\mathcal{R}T\,n}{V} \tag{1}$$

and from the Young–Laplace Equation

$$p = p_e - \frac{2\gamma}{R} \tag{2}$$

where the quantity R denotes the radius of curvature of the meniscus (the geometry is depicted in Figure 1) and expand $\tilde{p}$ and p in Taylor series with respect to V around the equilibrium value $V = V_0$,

$$\tilde{p}(V_0 + dV) = \tilde{p}(V_0) - \frac{\mathcal{R}T\ n}{{V_0}^2}\, dV + (\text{terms of order } (dV)^2 \text{ and higher}) \tag{3}$$

$$p(V_0 + dV) = p(V_0) + \frac{2\gamma}{{R_0}^2}\, \frac{dR}{dV}\bigg|_0\, dV + (\text{terms of order } (dV)^2 \text{ and higher}) \tag{4}$$

Retaining only terms linear in dV, we obtain

$$\delta p := \tilde{p}(V_0 + dV) - p(V_0 + dV) = \{\tilde{p}(V_0) - p(V_0)\} - \left[\frac{\mathcal{R}T\ n_0}{{V_0}^2} + \frac{2\gamma}{{R_0}^2}\, \frac{dR}{dV}\bigg|_0\right] dV \tag{5}$$

The expression in the braces in Equation (5) disappears because of the assumed equilibrium at $V = V_0$, i.e. $\tilde{p}(V_0) = p(V_0)$.

For an interpretation of Equation (5) recall that δp denotes the discrepancy between expansion and contraction seeking pressures which develop after a disturbance connected with a volume change dV. Simplifying the terms in the brackets with Equations (1) and (2) and applying the definition

$$\xi := \left[\frac{1}{V}\left(p_e - \frac{2\gamma}{R}\right) + \frac{2\gamma}{R^2}\frac{dR}{dV}\right]_0 \tag{6}$$

(each quantity is to be evaluated at its equilibrium value, denoted by the index 0), Equation (5) reads as

$$\delta p = -\xi\, dV \tag{7}$$

On inspection of Equation (7) we notice that two cases may be realized:

1. $\xi > 0$: In this case, an increase in bubble volume (i.e. $dV > 0$) implies $\delta p < 0$. That is, the initial (externally caused) increase in volume makes the contracting forces dominate the expanding forces, whereupon the bubble volume V returns to its equilibrium value V_0, provided, the system is undisturbed afterwards. A decrease in bubble volume (i.e. $dV < 0$), however, implies $\delta p > 0$, hence the bubble volume is expanded to the equilibrium value from which it was "perturbed away". Thus, if $\xi > 0$, equilibrium is restored irrespective of the sign of the perturbation dV.
2. $\xi < 0$: In this case, $dV > 0$ implies $\delta p > 0$ and $dV < 0$ implies $\delta p < 0$. The consequences are quite different from the previous case, because an increase in bubble volume ($dV > 0$) now leads to a strengthening of the expanding forces ($\delta p > 0$) leading to a further bubble expansion. Similarly, an initial decrease of

bubble radius reinforces the contracting forces resulting in a further contraction of the bubble, etc. Thus, once the equilibrium has been perturbed, it will never be restored.

From Equation (6) we draw the conclusions:

1. If p_e (the liquid pressure in the embolized conduit) is high enough, every pit bubble exhibits stable equilibrium.
2. As the difference $p_e - (2\gamma/R)$ represents via the Young-Laplace-Equation (2) the (necessarily positive) pressure in the PB, $dR/dV > 0$ implies $\xi > 0$. For $dR/dV < 0$, however, ξ may be positive or negative, depending on the absolute value of dR/dV. Thus, $dR/dV > 0$ is sufficient (although not necessary) for stability.

Further conclusions require more explicit prescriptions of the geometry of the pits to be investigated.

3. Pit Shape – General Considerations

Small variations in shape have a profound influence on stability, precise data of the morphology of pits are, however, difficult to obtain. Therefore, we approach the problem of PB stability from a more theoretical point of view: we apply the stability criterion Equation (7) to several "typical" but idealized pit forms and try to identify pit shapes which are able to support stability of PVM. Support for approach comes from the principle of natural selection which suggests that pit shapes fulfilling the stability criterion are more likely expressed by plants than those failing in this respect, provided, that embolism repair actually takes place and if stability in the sense defined above is a necessary prerequisite for it.

For the sake of simplicity, we assume axial symmetry of the pits (with the axis normal to the pit membrane) because then, any liquid/gas-interface figures as a section of a sphere of radius R. Figure 1 shows a pit connecting an intact (upper part of figure) and an embolized (lower part of figure) vessel. We introduce coordinates r (the distance from the symmetry axis) and z (identical with the symmetry axis).

The shape of the pit is described by the function $z = f(r)$ and, s, the radius of the (unbent) pit membrane, w, the radius of the pit mouth, and H, the height of a half pit along its symmetry axis. θ is the contact angle between water and pit wall. Finally, η denotes the angle between the tangent of the function $f(r)$ and the $z = 0$-plane, thus $\tan\eta = f'(r)$. $z = M(r)$ describes the shape of the membrane which is possibly bent towards the upper part of the pit.

The radius R of the meniscus developing in the lower part of the pit and the gas volume between meniscus and pit membrane can be calculated quite generally, if the contact angle θ and the pit shape $z = f(r)$ are given (and if $f(r)$ behaves sensible). Employing the definitions of the quantities θ and η, we infer with standard methods

of geometry for a meniscus touching the pit wall at position $(r, z) = (\rho, -\zeta)$:

$$R(\rho) = \frac{\rho}{\sin(\theta - \eta(\rho))} = \frac{\rho\sqrt{1 + f'(\rho)^2}}{\sin\theta - f'(\rho)\cos\theta} \tag{8}$$

Similarly, from formulas of trigonometry, the height $g(\rho)$ (measured along the z-axis) of the spherical segment denoted V_{kal} in Figure 2 is calculated as

$$g(\rho) = R(\rho)[1 - \cos(\theta - \eta)] = R(\rho)\left[1 - \frac{\cos\theta + f'(\rho)\sin\theta}{\sqrt{1 + f'(\rho)^2}}\right] \tag{9}$$

From Figure 2 it is apparent that the gas volume $V(\rho)$ within the PB can be obtained via $V = V_{\text{mem}} + V_{\text{int}} - V_{\text{kal}}$.

1. The volume V_{kal} follows from geometrical formulas related to spheres:

$$V_{\text{kal}}(\rho) = \frac{\pi}{3} g(\rho)^2 [3\,R(\rho) - g(\rho)] \tag{10}$$

2. V_{int} is calculated by cutting the volume into a stack of circular discs of radius $r(z)$ and of thickness dz, sharing the problem's symmetry around the z-axis. The connection between the z-position and the radius r of each disc is provided by the relation $z = f(r)$, hence,

$$V_{\text{int}}(\rho) = \pi \int_{-\zeta}^{0} f^{-1}(z)\,dz \tag{11}$$

where the integration is from $z = -\zeta$ (where the meniscus touches the pit wall) till the $z = 0$-plane. Application of the substitution rule of integration with respect to the relation $z = f(r)$ implies $dz = f'(r)\,dr$ (a prime denotes differentiation with respect to the argument), $f^{-1}(-\zeta) = \rho$ and $f^{-1}(0) = f(s)$,

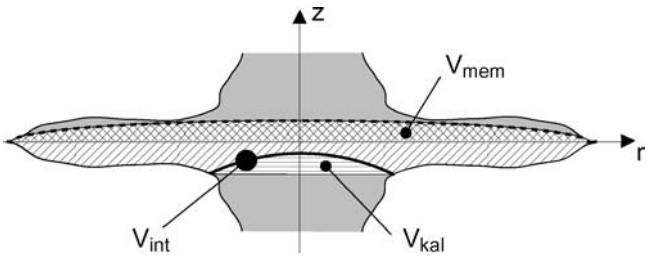

Figure 2. Volumes involved in the calculation of the gas volume within the pit (Equations (10) through (14)). Oblique cross hatching (V_{mem}) denotes the gas volume between the $z = 0$-plane and the distorted pit membrane, simple oblique hatching ($V_{\text{int}} - V_{\text{kal}}$) denotes the gas volume between the $z = 0$-plane and the gas/liquid interface and horizontal hatching designates the spherical segment V_{kal}. V_{kal} is filled with liquid, *not* with gas.

provided f is a one-to-one function. If so, V_{int} takes the form

$$V_{\text{int}}(\rho) = \pi \int_{\rho}^{s} r^2 \, f'(r)\, dr \tag{12}$$

The examples of the relation $z = f(r)$ we shall calculate below, are one-to-one functions.

3. V_{mem} is calculated similarly as V_{int} by exploiting first its symmetry with respect to the z-axis

$$V_{\text{mem}}(\rho) = \pi \int_{0}^{M(0)} r^2 \, dz = \pi \int_{s}^{0} r^2 \, M'(r)\, dr \tag{13}$$

and then using the substitution rule of integration with respect to the relation $z = M(r)$.

Collecting these contributions we arrive eventually at

$$\begin{aligned} V(\rho) &= V_{\text{int}}(\rho) - V_{\text{kal}}(\rho) + V_{\text{mem}}(\rho) \\ &= \pi \int_{\rho}^{s} r^2 \, f'(r)\, dr - \frac{\pi}{3} g(r)^2 [3\, R(r) - g(r)] + \pi \int_{s}^{0} r^2 \, M'(r)\, dr \end{aligned} \tag{14}$$

The "typical" pit forms we will consider share the following geometric properties: (1) the radius s of the (unbent) membrane, (2) the "mouth radius" w, and (3) the half height H (as measured along the symmetry axis). Thus, a curve $z = f(r)$ describing the pit shape has to pass through the points $(r, z) = (s, 0)$ and $(r, z) = (w, -H)$.

4. Shape of the Pit Membrane

Before proceeding with the analysis of the influence of pit shape on the stability of PVM, we have to consider the shape of the pit membrane. In a pit connecting two intact vessels, the membrane should be unbent, i.e. coincide with the plane $z = 0$. After an embolism has occurred and a PB isolates intact and embolized vessel from each other, the former vessel remains under negative pressure (typically $p_i \approx -4$ MPa $\ldots -1$ MPa) whereas the pressure p_e within the latter increases to a positive value, probably close to atmospheric pressure (i.e. $p_e \approx 0.1$ MPa), as explained in the introduction. The membrane therefore bulges towards the intact vessel and assumes the shape $z = M(r)$. In SEM pictures, deformed pit membranes can be observed [20]. Additionally, there are indications of pit membrane fatigue after embolism events due to strong mechanical load and deformation [21]. Thus, deviations from the original (unbent) shape of the pit membrane have to be taken into account.

We will now explore which shape of a bent pit membrane is appropriate, because the function $z = M(r)$ which contributes to the expression $V(r)$ for the gas

volume in the pit (Equation (13)) has to be determined as a prerequisite for calculating ξ (Equation (6)). The appropriate way to treat this situation would be to calculate the shape of the membrane caused by the pressure difference from the elasto-mechanical properties of pit membranes. Because these are – to the authors knowledge – not known, we examine two somewhat idealized cases that can be treated without this information.

1. We consider a very stiff membrane that remains in the $z = 0$-plane in spite of the pressure difference trying to bend it, i.e.

$$M(r) = 0 \tag{15}$$

2. For the sake of simplicity, we assume only the central part of the membrane to be undeformably stiff; its periphery, however, we assume to be very elastic. Then, the pressure difference pushes the membrane along the positive z-axis until its elastic periphery clings to the pit wall (desribed by the function $z = f(r)$) and the central part is located on the pit opening towards the intact vessel like a flat lid:

$$M(r) = \begin{cases} -f(w) & \text{if } 0 \le r \le w \\ -f(r) & \text{if } w \le r \le s \end{cases} \tag{16}$$

In both cases, the gas volume above the $z = 0$-plane contributes to $V(r)$ (as calculated in Equation (13)) only a constant term which is independent of the coordinate r and vanishes therefore from the derivative dV/dr. Thus, in the treatment we are going to apply, the second term in ξ (Equation (6)) is not affected by the reaction of the membrane to changes in the pressure difference of the gaseous content of the PB which occur after the event of embolism has taken place. The contribution of $M(r)$ to the first term in ξ (via $V(r)$) can be easily calculated.

5. Pit Shape – Examples

There is an infinity of shape-defining curves. We choose to describe curved pit walls by

$$f(r) = z_0 + \frac{b}{a}\sqrt{a^2 - (r_0 - r)^2} \tag{17}$$

which is part of an ellipse with centre $(r, z) = (r_0, z_0)$ and long and short half axes a and b, respectively (see Figure 3).

Four conditions are necessary to determine the four constants r_0, z_0, a and b. Two of them are derived from the condition that the pit curve should have its endpoints at $(r, z) = (s, 0)$ and $(r, z) = (w, -H)$. Insertion of these into Equation (17) gives

$$0 = f(s) = z_0 + \frac{b}{a}\sqrt{a^2 - (r_0 - s)^2} \tag{18}$$

$$-\frac{H}{2} = f(w) = z_0 + \frac{b}{a}\sqrt{a^2 - (r_0 - w)^2} \tag{19}$$

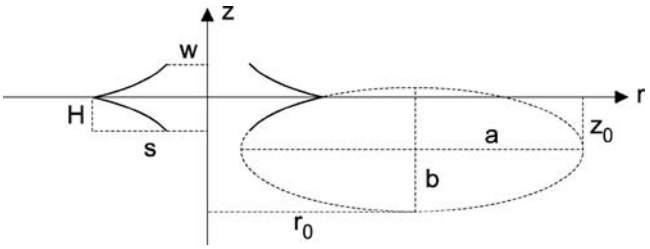

Figure 3. Pit, generated by rotating part of an ellipse around the symmetry axis of the pit, i.e. the z-axis. The general features of the pit shape are defined by the quantities s, w and H. Its detailed features are described by a section of the ellipse of Equation (17), which contains the four constants r_0, z_0, a and b. By adjusting their values appropriately, the real pit shape can be approximated.

The remaining two constants follow from other conditions: we could demand, for instance, that $f(r)$ touches two more prescribed points. Alternatively, we require $f(r)$ to form the angle η_s with the $z = 0$-plane at the point $r = s$ and, likewise, the angle η_w with the $z = -H$-plane at $r = w$. Employing Equation (17) this amounts to

$$\tan \eta_s = f'(s) = \frac{b}{a} \frac{r_0 - s}{\sqrt{a^2 - (r_0 - s)^2}} \tag{20}$$

$$\tan \eta_w = f'(w) = \frac{b}{a} \frac{r_0 - w}{\sqrt{a^2 - (r_0 - w)^2}} \tag{21}$$

Calculation of r_0, z_0, a and b from the system of Equations (18) to (21) completes pit shape determination.

We now consider four different pit forms. Three of them (Figures 4, 5 and 7) are derived from (17) by choosing specific values for η_s and η_w, the fourth one (Figure 6) is generated by rotating a straight line around the symmetry axis of the pit.

Concave pit (a), Figure 4 ($\eta_s = 0$, $\eta_w = \theta$):

$$f(r) = -\frac{H}{s - w - 2\,H \cot\theta} \left(s - w - H \cot\theta \right.$$
$$\left. - \sqrt{(s - w - H \cot\theta)^2 - (s - r)^2 \left(1 - \frac{2\,H \cot\theta}{s - w}\right)} \right) \tag{22}$$

Concave pit (b), Figure 5 ($\eta_s = 0$, $\eta_w = \pi/2$):

$$f(r) = -\frac{H}{s - w} \left(s - w - \sqrt{(s - w)^2 - (s - r)^2}\right) \tag{23}$$

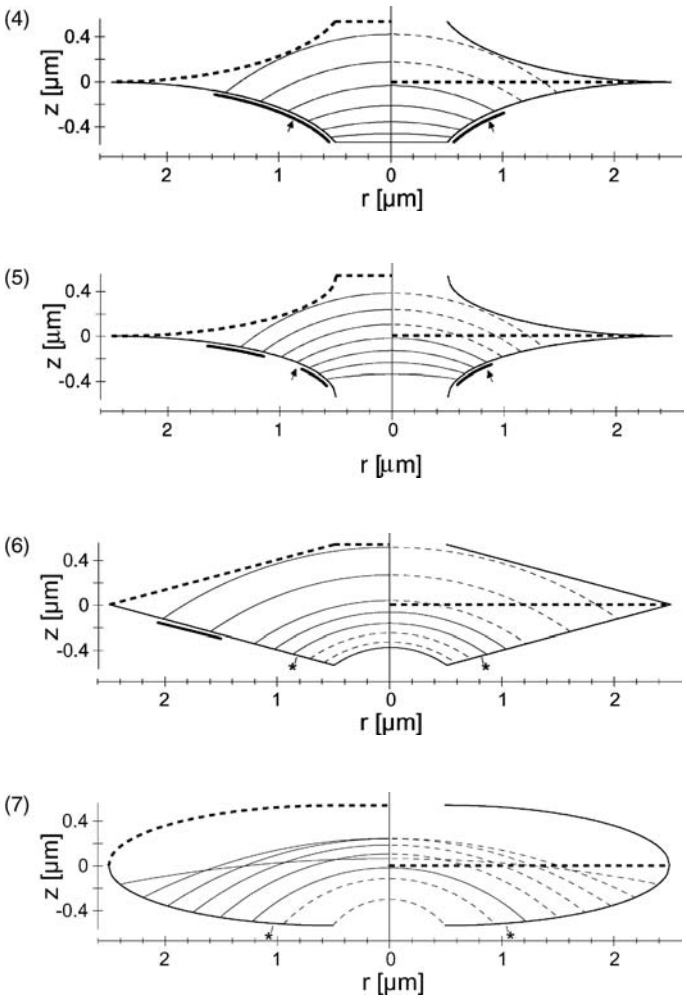

Figures 4–7. The four pit shapes of Equations (22) to (25) (for orientation see also Figure 1).
- Upper pits open into intact, lower pits open into embolized vessels.
- Right halves of the figures are related to a very stiff, immovable membrane (Equation (15)), left halves correspond to a partially stiff, partially elastic membrane adapting to the shape of the pit wall (Equation (16)).
- Membranes are indicated by thick, broken lines.
- Sectors of circles represent liquid/gas-interfaces. Thin, broken lines indicate interfaces which cannot exist, because they would touch the membrane (higher r-values, all figures) or because they imply negative pressures in the PB (lower r-values, between asterisks in Figure 6 [$r_\star = 0.83\ \mu$m] and Figure 7 [$r_\star = 1.03\ \mu$m]).
- Thick black strokes beneath the pit walls indicate possible positions of stable interfaces.
- Arrows point to minima of the interface radii of curvature $R(r)$ in Figure 4 ($r_\nearrow = 0.89\ \mu$m) and Figure 5 ($r_\nearrow = 0.85\ \mu$m).
- Values common to all figures: radius of pit membrane $s = 2.5\ \mu$m, radius of pit mouth $w = 0.5\ \mu$m, half height of pit $H = 0.54\ \mu$m, pressure within embolized vessel $p_e = 100\,000$ Pa (cf. Figure 1). All interfaces form the same contact angle ($\theta = 50^\circ$) with the pit wall.

Straight walled pit, Figure 6:

$$f(r) = -\frac{H}{s-w}(s-r) \tag{24}$$

Convex pit, Figure 7 ($\eta_s = \pi/2$, $\eta_w = 0$):

$$f(r) = -\frac{H}{s-w}(\sqrt{(s-w)^2 - (r-w)^2}) \tag{25}$$

The range of r is in all cases restricted to

$$w \leq r \leq s \tag{26}$$

6. Application of Stability Criterion – Effects of Pit Shape on PVM

Insertion of the definitions of pit and membrane shape (Equations (22) to (25) and Equations (15) or (16)) into Equations (8) to (9) allows explicit calculation of $R(r)$, $V(r)$ and $\xi(r)$. We do not give here the resulting, rather lengthy expressions, because the main results can be more easily obtained from Figures 4–7. These have been calculated for the following (common) values: Contact angle between interfaces and pit wall: $\theta = 50^\circ$, radius of pit membrane: $s = 2.5\,\mu$m, radius of pit mouth: $w = 0.5\,\mu$m, height of pit: $H = 0.54\,\mu$m, pressure within embolized vessel: $p_e = 100\,000$ Pa.

Before inspecting the results, we summarize conditions which are to be satisfied by successfully operating gas/liquid-interfaces:

1. Interfaces should bulge towards the intact vessel, that is, every interface at position $r = \rho$ should obey the inequality $\theta > \eta(\rho) = \arctan f'(\rho)$ (cf. Figure 1).
2. An interface should not touch the membrane, as otherwise water molecules from both sides of the membrane would come into contact, and the conductivity of the xylem sap through the membrane would be restored. This would lead to a breakdown of hydraulic isolation.
3. An interface should be stable, i.e. the inequality $\xi(\rho) > 0$ should be fulfilled for an interface at position ρ.
4. Being filled by a gas, the pressure in the PB should be positive. The condition $p > 0$ implies via the Young-Laplace Equation (2), $R(\rho) > 2\gamma/p_e \approx 1.44\,\mu$m. The numerical value is obtained upon insertion of $p_e = 100\,000$ Pa $\approx p_{atm}$.

Conditions (1) and (2) are related solely to geometric properties of a pit, whereas (3) and (4) also include the liquid pressure p_e in the embolized vessel.

It should be noted at this point that the results concerning stability presented so far, do apply not only to gas bubbles which consist solely of air molecules but also to bubbles including water vapour. This is possible because the underlying principles

of the model considerations presented above are not restricted to a special gas (apart from the assumption that they can be treated as an ideal gas).

In the following, the results depicted in Figures 4–7 will be analyzed with respect to the suitability of the different pit shapes for PVM. The degree of suitability is reflected by the ability of the pit shape to maintain stability of hydraulic isolation by obeying conditions (1)–(4).

We recall that the first term in ξ (Equation (6)) is necessarily (independent of pit shape) positive, if condition (4) is fulfilled. The second term in ξ, however, can attain both signs: for $dR/dV > 0$ it is positive, for $dR/dV < 0$ it is negative. Thus, the second term in ξ is shape-dependent, not in a very obvious way but – because of $dR/dV = (dR/d\rho)/(dV/d\rho)$ – rather through the ρ-dependance of the radius of curvature of the liquid/gas-interface $R(\rho)$ and of the gas volume $V(\rho)$.

The different degrees of suitability of the pit shapes of Figures 4–7 for maintaining stability during perturbation can be summarized as follows:

- Since all conditions apply, the concave pit with $\eta_w = \theta$ (Equation (22), Figure 4) is best suited to maintain stability of hydraulic isolation of an embolized vessel, at least for the parameter values given above. Notice, that for ρ-values between the arrows in Figure 4 the relation $dR/dV > 0$ holds, hence both terms in ξ are positive. ρ-values beyond the arrows are connected with $dR/dV < 0$, thus the second term in ξ is negative. Altogether, however, $\xi > 0$ is valid and stability is maintained.
- The concave pit with $\eta_w = 0$ (Equation (23), Figure 5) is very similar to the concave pit with $\eta_w = \theta$. The only difference lies in the "stability gap" in the case of the partially elastic membrane (left halve of Figure 5), which opens up because the balance between the positive first and negative second term in ξ is in this case more delicate.
- The pit with straight walls (Equation (24), Figure 6) exhibits stability only if the membrane is – at least partially – elastic. This can be understood as follows: The derivative $dR/dV = (dR/d\rho)/(dV/d\rho)$ is negative for all interfaces (as can be seen from inspection of Figure 6: obviously, $dV/d\rho$ is a decreasing function of ρ, whereas $dR/d\rho$ increases with ρ). Therefore, stability is restricted to ρ-values for which the gas volume $V(\rho)$ is comparatively small, and the first, positive, term in ξ becomes – due to its $1/V(\rho)$-dependancy – larger than the second, negative term. Figure 6 (left halve of Figure) shows that this occurs with higher ρ-values of the elastic membrane, because then the fluid/gas-interface lies relatively close to the upper pit wall, thus leaving little gas space $V(\rho)$.

  In contrast, the gas volume between the stiff membrane and an interface close to it (right part of Figure 6) is much larger and diminishes the positive first term in ξ to such an extent that ξ as a whole remains below zero. Comparison with the concave interfaces in Figures 4 and 5 reveals that straight walls are unfavourable with respect to minimizing the gas volume $V(\rho)$.

We note that interfaces with $r \leq 0.83\,\mu$m (indicated by an asterisk in the figure) generally violate condition (4) (the pressure in the PB should be positive) and therefore cannot exist.

- The convex pit (Equation (25), Figure 7) does not allow for stability since the derivative dR/dV is negative for all interfaces and the sum of both terms in ξ is negative even for a partially elastic membrane.

7. Concluding Remarks

The results of these theoretical studies demonstrate the significance of detailed pit shape for the functionality of PVM. Additionally to the basic prerequisite architecture – the funnel-shaped appearance – concave curvature of the pit chamber is beneficial for PVM, because it leads to the maintenance of the hydraulic isolation of the embolized pit under mechanical perturbations, which will inevitably occur in a natural environment (e.g. wind, animals). This effect is not restricted to a special gas and is thus applicable to both air and water vapour bubbles. As is also demonstrated in this study, the deformation of the pit membrane due to the strong pressure difference between functioning and embolized conduits also contributes to the stability of PVM. Hence, it may be speculated that interfacial effects in wood play a significant functional role in plant water transport under various aspects.

From this we draw the conclusion that PVM – if it is biologically relevant – should lead to concave pit shapes by natural selection. In order to verify this hypothesis, it will be necessary to collect detailed information about the shapes of real pits, preferably from SEM-pictures of undistorted xylem vessels of various species.

Further research should also address the possible functional implications of the numerous microstructures which are expressed by wood conduits, because the above results indicate that at least some of them may be involved in interfacial effects. Combined studies concerning physical, anatomical and ecophysiological aspects are expected to contribute significantly to our knowledge of fluid behaviour in wood on the micrometer/nanometer scale.

Acknowledgements

We thank the Federal State of Baden-Württemberg for partly supporting this study within the framework of the Competence Network “Biomimetics.” We thank James Nebelsick for carefully reading the manuscript.

Note Added in Proof

During the publication procedure of this manuscript, a new paper was published by Salleo et al. (2004) in which (1) novel refilling in *Laurus nobilis* L. was again confirmed and (2) the refilling process was interpreted to be dependent on living cells.

S. Salleo, Lo Gullo, M.A., Trifilo, P. and Nardini, A.: New evidence for a role of vessel-associated cells and phloem in the rapid xylem refilling of cavitated stems of *Laurus nobilis* L. Plant Cell Environ. **27** (2004), 1065–1076.

References

1. Tyree, M.T. and Ewers, F.: The Hydraulic Architecture of Trees and Other Woody Plants, *New Phytol.* **199** (1991), 345–360.
2. Zimmermann, M.H.: *Xylem Structure and the Ascent of Sap*, Springer-Verlag: Berlin (1983).
3. Holbrook, N.M., Ahrens, E.T., Burns, M.J. and Zwieniecki, M.A.: *In Vivo* Observation of Cavitation and Embolism Repair Using Magnetic Resonance Imaging, *Plant Physiol.* **126** (2001), 27–31.
4. Pickard, W.F.: The Ascent of Sap in Plants, *Prog. Biophys. Mol.. Biol.* **37** (1981), 181–229.
5. Pockman, W.T., Sperry, J.S. and OLeary, J.W.: Sustained and Significant Negative Water Pressure in Xylem, *Nature* **378** (1995), 715–716.
6. Milburn, J.A.: Cavitation and Embolisms in Xylem Conduits, in A.S. Raghavendra (ed.) *Physiology of Trees*, Wiley: New York.(1991), pp. 163–174.
7. Tyree, M.T. and Sperry, J.S.: The Vulnerability of Xylem to Cavitation and Embolism, *Annu. Rev. Plant Physiol., Plant Mol. Biol.* **40** (1989), 19–38.
8. Tyree, M.T. and Yang, S.: Water-Storage Capacity of *Thuja*, *Tsuga* and *Acer* Stems Measured by Dehydration Isotherms: The Contribution of Capillary Water and Cavitation, *Planta* **182** (1990), 420–426.
9. Hölttä, T., Vesala, T., Perämäki, M. and Nikinmaa, E.: Relationships Between Embolism, Stem Water Tension and Diameter Changes, *J. Theor. Biol.* **215** (2002), 23–38.
10. Sperry, J.S. and Tyree, M.T.: Mechanism of Water Stress-Induced Xylem Embolism, *Plant Physiol.* **88** (1988), 581–587.
11. Bucci, S.J., Scholz, F.G., Goldstein, G., Meinzer, F.C., Sternberg, L. and Da, S.L.: Dynamic Changes in Hydraulic Conductivity in Petioles of Two Savanna Tree Species: Factors and Mechanisms Contributing to the Refilling of Embolized Vessels, *Plant Cell Environ.* **26** (2003), 1633–1645.
12. Hacke, U.G. and Sperry, J.S.: Limits to Xylem Refilling Under Negative Pressure in *Laurus nobilis* and *Acer negundo*, *Plant Cell Environ.* **26** (2003), 303–311.
13. Salleo, S., LoGullo, M., Depaoli, M. and Zippo, M.: Xylem Recovery from Cavitation-Induced Embolism in Young Plants of *Laurus nobilis*: A Possible Mechanism, *New Phytol.* **132** (1996), 47–56.
14. Tyree, M.T., Salleo, S., Nardini, A., LoGullo, M.A. and Mosca, R.: Refilling of Embolized Vessels in Young Stems of Laurel: Do We Need a New Paradigm? *Plant Physiol.* **120** (1999), 11–21.
15. Steudle, E.: The Cohesion-Tension Mechanism and the Acquisition of Water by Plant Roots, *Annu. Rev. Plant Physiol., Plant Mol. Biol.* **52** (2001), 847–875.
16. Vesala, T., Hölttä, T., Perämäki, M. and Nikinmaa, E.: Refilling of a Hydraulically Isolated Embolized Xylem Vessel: Model Calculations, *Ann. Bot.* **91** (2003), 419-428.
17. Holbrook, N.M., Zwieniecki, M.A.: Embolism Repair and Xylem Tension. Do we need a Miracle? *Plant Physiol.* **120** (1999), 7–10.
18. Konrad, W. and Roth-Nebelsick, A.: The Dynamics of Gas Bubbles in Conduits of Vascular Plants and Implications for Embolism Repair, *J. Theor. Biol.* **224** (2003), 43–61.
19. Shen, F., Gao, R., Liu, W. and Zhang, W.: Physical Analysis of the Process of Cavitation in Xylem Sap, *Tree Physiol.* **22** (2002), 655–659.
20. Wheeler, E.A.: Intervascular Pit Membranes in *Ulmus* and *Celtis* Native to the United States, *IAWA Bulletin* **4** (1983), 79–88.

21. Hacke, U.G., Stiller, V., Sperry, J.S., Pittermann, J. and McCulloh, K.A.: Cavitation Fatigue. Embolism and Refilling Cycles Can Weaken the Cavitation Resistance of Xylem, *Plant Physiology* **125** (2001), 779–786.
22. Carlquist, S.: *Comparative Wood Anatomy*, Berlin, Heidelberg, New York, 2001.
23. Cochard, H., Ewers, F. and Tyree, M.T.: Water Relations of a Tropical Vinelike Bamboo (*Rhipidocladum racemiflorum*): Root Pressures, Vulnerability to Cavitation and Seasonal Changes in Embolism, *J. Exp. Bot.* **45** (1994), 1085–1089.
24. Ewers, F.W., Fisher, J.B. and Fichtner, K.: Water Flux and Xylem Structure in Vines, in F.E. Putz and H.A. Mooney (eds.) *The Biology of Vines*, Cambridge University Press, Cambridge (1991), pp. 127–160.
25. Fisher, J.B., Angeles, G., Ewers, F.W. and Lopez-Portillo, J.: Survey of Root Pressure in Tropical Vines and Woody Species, *Int. J. Plant Sci.* **158** (1997), 44–50.
26. Lösch, R.: Wasserhaushalt der Pflanzen. Quelle und Meyer (2001), Wiebelsheim.
27. Magnani, F. and Borghetti, M.: Interpretation of Seasonal Changes of Xylem Embolism and Plant Hydraulic Resistance, *Plant Cell Environ.* **18** (1995), 689–696.
28. Tyree, M.T., Fiscus, E.L., Wullschleger, S.D. and Dixon, M.A.: Detection of Xylem Cavitation in Corn Under Field Conditions, *Plant Physiol.* **82** (1986), 597–599.
29. Yang, S. and Tyree, M.T.: A Theoretical Model of Hydraulic Conductivity Recovery From Embolism With Comparison to Experimental Data on *Acer saccharum*, *Plant Cell Environ.* **15** (1992), 633–643.
30. Zwieniecki, M.A. and Holbrook, N.M.: Bordered Pit Structure and Vessel Wall Surface Properties. Implications for Embolism Repair, *Plant Physiol.* **123** (2000), 1015–1020.
31. Zwieniecki, M.A., Melcher, P.J. and Holbrook, N.M.: Hydraulic Properties of Individual Xylem Vessels of *Fraxinus americana*, *J. Exp. Bot.* **52** (2001), 257–264.

5.3 Konrad, W., Roth-Nebelsick, A.: *Embolism formation and repair in vascular plants: the role of cell wall mechanics*, in: Proceedings of the Fifth Plant Biomechanics Conference, Editor: Lennart Salmén, Stockholm (2006), p. 417–422 (Volume II).

5th Plant Biomechanics Conference – Stockholm, August 28 – September 1 2006

Embolism formation and repair in vascular plants: the role of cell wall mechanics.

Wilfried Konrad and Anita Roth-Nebelsick

University of Tübingen, Germany

Abstract

The water transport system of vascular plants is permanently endangered by the formation of gas bubbles. Such embryonic gas bubbles are created by the air seeding process, i.e. the penetration of air into a vessel from adjacent, air filled vessels/tracheids or — to a much lesser extent — by spontaneous vapourization of xylem water. Because the water in xylem conduits is under tension (negative pressure), an embryonic gas bubble introduced into the water column by either source may expand into embolism, the complete disruption of the water flow inside a conduit. Embryonic gas bubbles do not necessarily evolve in this way. Instead of causing embolism they may also collapse into an — at least temporarily — stable and harmless state or even dissolute completely. If, however, embolism has occurred, a repair mechanism may start which can be expected to restore conductivity of the conduit under favourable conditions. It can be shown that the fate of bubbles appearing in a conduit under negative pressure is affected by cell wall mechanics if the conduits possess torus-margo pits. In this contribution it is examined to what extent mechanical properties of the vessel cell wall (e.g. elasticity, thickness) influence the behaviour of embryonic gas bubbles (immediate collapse vs. development towards embolism) and the processes of embolism formation. For this purpose, behaviour and possible final states of embryonic gas bubbles are calculated in terms of (a) thickness and elastic properties of the vessel cell wall, (b) xylem water pressure, (c) the initial number of air molecules within an embryonic bubble, and (d) the initial bubble radius.

Introduction

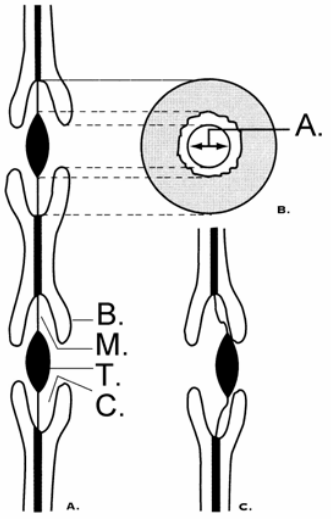

Fig. 1 (A) Two bordered pit pairs in the wall between two xylem tracheids, in side view. (B) Surface view. (C) A pressure difference — lower pressure to the right — pushes the torus against the border, thereby sealing the pit and preventing water movement.
A.:Aperture
B.: Border
M.: Pit membrane
T.: Torus
C.: Pit Cavity
(From K. Esau, Anatomy of Seed Plants*).*

Conifers possess valve-like pits (*see Fig. 1*): a pressure difference between the conduits they connect causes them to close. In this manner, an embolized conduit becomes hydraulically isolated from its

neighbours. (Also, certain angiosperms show pits with tori, such as, for example, some *Ulmus* species in their latewood (see [1]). Since it is, however, not clear whether they function in the same way as coniferous torus-margo pits, we will concentrate on coniferous wood throughout the rest of the text.) The sealing mechanism based on the torus-valve system differs from the typical angiosperm pit-membrane system since it immediately seals the embolizing conduit if a significant pressure drop develops. This rapid sealing of the tracheid has consequences for the subsequent interplay of forces acting upon the bubble and therefore on the process of embolization, because cell wall mechanics becomes significant. In this contribution, the effect of cell wall mechanics on bubble dynamics in conduits with torus-margo pits will be explored.

Physical background

After its creation by air seeding or spontaneous cavitation the development of a gas bubble is controlled by various expanding and contracting forces:

- Expanding forces: gas pressure of water vapour and air molecules and xylem water pressure (if negative)
- Contracting forces: surface force exerted by liquid/gas-interface at bubble surface and xylem water pressure (if positive)

n_a air molecules introduced into a tracheid form very rapidly a bubble of initial radius R, containing also $n_w = 4\pi R^3 p_w / (3\mathcal{R}T)$ water molecules, which vapourize almost instantaneously into the bubble (p_w: water vapour saturation pressure). Such an embryonic bubble develops further according to the following net force acting upon it (see also [2], [3])

$$F = \text{(contracting forces)} - \text{(expanding forces)} = 8\pi\gamma R + 4\pi R^2 p_s - 4\pi R^2 p_w - \frac{3\mathcal{R}T n_a}{R} \quad (1)$$

(p_s: xylem water pressure, T: temperature, $\mathcal{R}$: gas constant, γ: surface tension). The bubble radius R evolves according to the relation between the expanding and contracting forces:

$F < 0$: bubble expands
$F > 0$: bubble contracts
$F = 0$: bubble in equilibrium (stable or unstable)

An equilibrium radius R is called stable if the expanding and contracting forces react on a radial perturbation $\Delta R << R$ by restoring the bubble to the equilibrium radius R. Otherwise it is called unstable.

During gas bubble expansion, the distance between adjacent water molecules decreases because the xylem water occupies gradually less space. Macroscopically, this is equivalent to an increasing water pressure, i.e. p_s becomes less negative. The water pressure difference $p_s - p_0$ between embolizing and intact tracheids (the latter maintaining the initial water pressure p_0) induces (i) the closure of the "pit valves" (*Fig. 1*), and, (ii) a second effect: Since the tracheid walls are elastic they bulge towards the intact tracheids. Hence, the volume of the tracheids carrying the expanding bubble increases by an amount

$$\Delta V = V_0 (p_s - p_0)\, \mu \quad \text{with} \quad \mu := \frac{2 r_0}{d_0} \frac{1 - \sigma^2}{E} \quad (2)$$

which is calculated from the theory of elasticity (E: Young's modulus, σ: Poisson's number, d_0: thickness of tracheid wall, r_0: radius of undeformed tracheid, L_0: tracheid length, $V_0 = \pi r_0^2 L_0$: volume of undeformed tracheid (before air seeding), p_0: tracheid water pressure before air seeding). The

difference in tracheid volume fraction occupied by (liquid) water before and after the formation of the gas bubble (and including the compressibility κ of water) affects p_s according to the following equation (see *Fig. 2*):

$$p_s = p_0 + \frac{4\,\pi\,R^3}{3\,V_0\,(\kappa+\mu)} \tag{3}$$

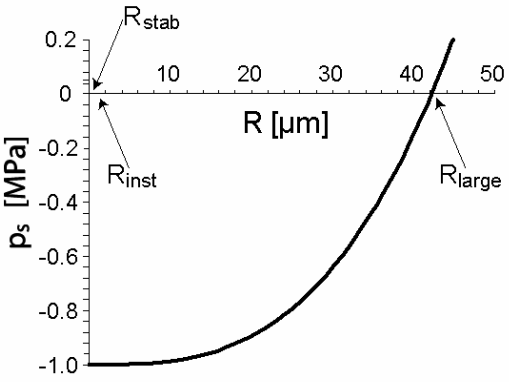

Fig. 2 Xylem water pressure p_s as function of bubble radius R as given in equation (3). R_{stab}= 0.047 µm and R_{inst} = 0.13 µm have been obtained by setting n_a = 0.5 n_{crit} in equation (5). R_{large} = 42.21 µm follows from equation (7).

Via intermolecular forces and volume change, the process of bubble expansion is thus interrelated with cell wall mechanics. In the following, it will be explored how cell wall mechanics influences bubble dynamics and therefore embolism formation. Insertion of equation (3) into (1) leads to a more general equation for the net force acting upon the gas bubble which includes the effects of cell wall properties.

$$F = \frac{16\,\pi^2}{3\,V_0\,(\kappa+\mu)}\,R^5 - 4\,\pi\,(p_w - p_0)\,R^2 + 8\,\pi\,\gamma\,R - \frac{3\,\mathcal{R}\,T\,n_a}{R} \tag{4}$$

The equilibrium radii at which a bubble ceases to expand (or shrink) are identified by setting $F = 0$ in equation (4). Closed solutions for this sixth order algebraic equation in R are not available. In the next section, approximate solutions for the interrelated system of bubble dynamics and cell wall mechanics will be presented and discussed.

Results and Discussion

Approximate solutions of equation (4) (restricted to $p_0 < p_w$) apply to either small or large bubbles

- **Small** *R* (necglecting first term in equation (4))

$$R_{stab} = \frac{R_{vap}}{3}\left(1 - 2\,\cos\left[\frac{1}{3}\,\arccos\left(1 - \frac{2\,n_a}{n_{crit}}\right) + \frac{\pi}{3}\right]\right)$$
$$R_{inst} = \frac{R_{vap}}{3}\left(1 + 2\,\cos\left[\frac{1}{3}\,\arccos\left(1 - \frac{2\,n_a}{n_{crit}}\right)\right]\right) \tag{5}$$

$$\text{with} \quad n_{crit} := \frac{128\,\pi\gamma^3}{81\,\mathcal{R}\,T}\,\frac{1}{(p_w - p_0)^2} \qquad \text{and} \qquad R_{vap} := \frac{2\,\gamma}{p_w - p_0} \tag{6}$$

- **Large** *R* (necglecting last two terms in equation (4))

$$R_{large} = \sqrt[3]{\frac{3}{4\,\pi}\,V_0\,(p_w - p_0)\,(\kappa + \mu)} \qquad (7)$$

R_{stab} and R_{inst} are meaningful only if the condition $n_a \leq n_{crit}$ is fulfilled. It should be noted that R_{large} is independent of n_a. Furthermore, only R_{large} (and therefore only a large nucleating bubble) depends via the quantity $\kappa+\mu$ defined in equation (2) on cell wall mechanics. The equilibrium radii R_{stab} and R_{large} are stable against radial perturbations $\Delta R << R$ whereas R_{inst} is unstable. Together with (4), this implies the stability diagram of *Fig. 3* summarizing bubble behaviour: The net force F acting on a bubble is positive (i.e. contractive) in the area between the lines R_{stab}, R_{inst} and the R -axis, and beyond $R = R_{large}$. In all other (n_a,R)-areas of *Fig. 3* expression F is negative, a bubble expands towards R_{large}. For typical values of $p_0 \approx -1$MPa, stable equilibrium radii are $R_{stab} \approx 0.047$ µm and $R_{large} \approx 42.21$ µm, that is, they differ by three orders of magnitude. Thus, according to (3), if a bubble expands towards the radius R_{stab} the water pressure p_s is nearly unaffected due to its small radius, whereas the expansion of a bubble towards R_{large} causes a drastic increase of p_s (*see Fig. 2*). A small bubble at R_{stab} thus does not lead to pit valve closure since it does not cause any pressure change, neither by embolism (because it is stable) nor by affecting p_s (because it is too small). Consequently, a conduit may tolerate bubbles at stable equlibrium R_{stab} for a long time without losing its conductivity.

Bubbles, however, which expand (or shrink) towards the stable equlibrium R_{large}, induce — due to the sharp increase in p_s during their expansion — the closure of the pit. This seals the tracheid segment hydraulically from its neighbours. A residing bubble of R_{large} can only develop with a sealing torus-margo pit.

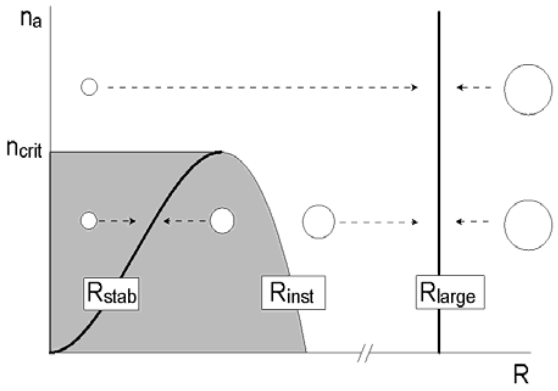

Fig. 3 Stability diagram for bubbles with initial radius R and initial air content n_a.
(i) Bubbles starting within the grey region expand or contract towards R_{stab} (solid curve, left).
(ii) Bubbles starting within other regions (white) expand or contract towards R_{large} (solid line, right).

Since R_{stab}, R_{inst} and R_{large} are solutions of $F = 0$ (equation (4)) they depend — although to a different extent — also on the parameters present in equation (4). Inspection of solutions (5) and (7) reveals the following: The positions of the lines representing R_{stab} and R_{inst} in *Fig. 3* vary only with the number n_a of air molecules injected by air seeding and with the pressure p_0 inside the tracheid before air seeding. R_{large}, however, depends also on the elastic properties of the tracheid wall, on the volume of the tracheid and on p_0: If E, d_0 or p_0 increases, R_{large} shifts to smaller values (*see Figs. 4 and 5*). If, however, r_0, L_0 or V_0 increases, R_{large} shifts to higher values (*Fig. 6*). A combination of a thicker or more rigid cell wall thus decreases the maximum radius of stable bubbles. Since smaller bubbles dissolve more readily under favourable conditions than larger bubbles, this may enhance the chances for embolism repair.

Fig. 6 shows that the connexion between R_{large} and r_0 is approximately linear for sufficiently high values of r_0. This can be understood from the structure of equations (7), (2) and the relation $V_0 = \pi\, r_0^2\, L_0$ for the tracheid volume, leading to $R_{large} \approx [3\, L_0\, (p_w - p_0)\, (1 - \sigma^2)/(2\, d_0 E)]^{(1/3)}\, r_0$. Remarkably, for typical numerical values of the quantities involved (given in *Table 1*), the value of the root is about 0.8. Hence, a bubble which has achieved stable equilibrium is “smaller” than the tracheid.

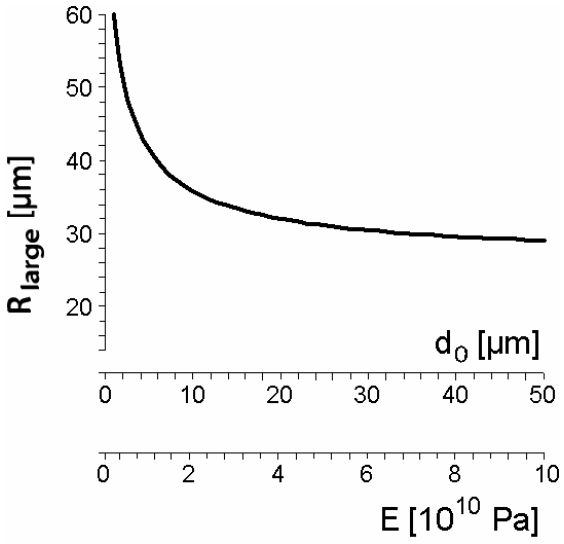

Fig. 4 Bubble radius R_{large} as function of (i) thickness d_0 of vessel wall (upper abscissa) and of (ii) Young's modulus E of the vessel wall (lower abscissa). See equations (7) and (2).

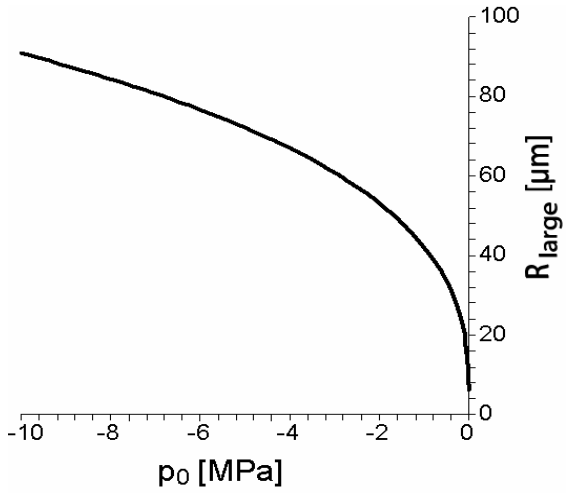

Fig. 5 Dependance of bubble radius R_{large} on initial water pressure p_0 within the vessel as given by equation (7).

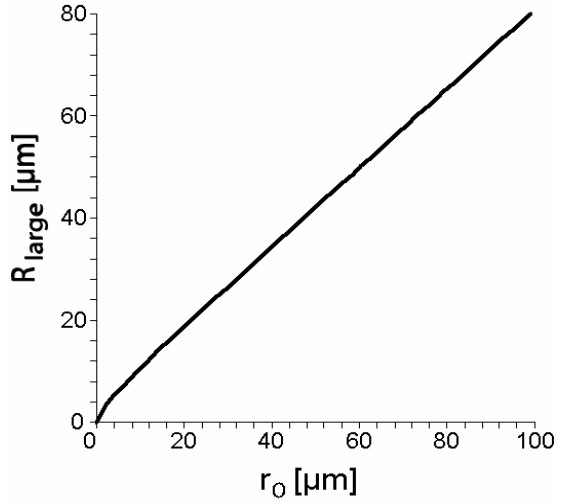

Fig. 6 Bubble radius R_{large} as function of vessel radius r_0. See equations (7), (2) and the relation $V_0 = \pi r_0^2 L_0$ for the vessel volume.

Conclusions

1. Embryonic bubbles introduced (e.g. by the air seeding process) into a tracheid possessing torus-margo pits expand (or contract) towards stable equilibrium at either bubble radius R_{stab} or R_{large}.
2. Bubbles expanding towards the radius R_{large} lead to immediate closure of the pit valves due to a pressure gradient developing between embolized and functioning tracheary element.
3. Stable bubbles with R_{large} can only form with sealing torus-margo pits.
4. R_{stab} depends only on the number n_a of air molecules injected by air seeding and on the water pressure p_0 inside the tracheid (before air seeding occured). R_{large} depends on the (elastic) properties of the tracheid wall (like Young's modulus E and wall thickness d_0) and on p_0, but not on n_a.
5. R_{large} decreases with increasing d_0, with increasing E-Modulus and with decreasing r_0. Small tracheids with thick walls may thus be favoured with respect to bubble dissolution.

Table 1 Numerical values used in the figures

Quantity	*Symbol*	*Value*
Tracheid water pressure before air seeding	p_0	-1 MPa
(Undeformed) tracheid radius	r_0	50 µm
Tracheid length	L_0	20×10^3 µm
Tracheid volume	V_0	1.57×10^8 µm^3
Thickness of tracheid wall	d_0	5 µm
Young's modulus of tracheid wall	E	10^4 MPa
Poisson's number of tracheid wall	σ	0.5
Compressibility of water	κ	5×10^{-10} Pa^{-1}

References

1. Shen, F., Gao, R., Liu, W. and Zhang, W. (2002) *Physical analysis of the process of cavitation in xylem sap.* Tree Physiology 22: 655–659.
2. Shen, F., Wenji, L., Rongfu, G., Hu, H. (2003) *A careful analysis of gas bubble dynamics in xylem.* Journal of Theoretical Biology 225: 229–233.
3. Jansen, S., Choat, B., Vinckier, S., Lens, F., Schols, P. and Smets, E. (2004): *Intervascular pit membranes with a torus in the wood of Ulmus (Ulmaceae) and related genera.* New Phytologist 163: 51-59.

5.4 Konrad, W., Roth-Nebelsick, A., Kerp, H., Hass, H.: *Transpiration and Assimilation of Early Devonian Land Plants with Axially Symmetric Telomes — Simulations on the Tissue Level*, Journal of Theoretical Biology 206 (2000), p. 91–107.

J. theor. Biol. (2000) **206,** 91–107
doi:10.1006/jtbi.2000.2107, available online at http://www.idealibrary.com on IDEAL®

Transpiration and Assimilation of Early Devonian Land Plants with Axially Symmetric Telomes—Simulations on the Tissue Level

W. Konrad*, A. Roth-Nebelsick*†, H. Kerp‡ and H. Hass‡

**Institut und Museum für Geologie und Paläontologie, Sigwartstr.* 10, *D*-72076 *Tübingen, Germany and*
‡*Abteilung Paläobotanik, Westfälische Wilhelms-Universität Münster, Hindenburgplatz* 57–59,
D-48143 *Münster, Germany*

(*Received on* 9 *December* 1999, *Accepted in revised form on* 12 *May* 2000)

Early terrestrial ancestors of the land flora are characterized by a simple, axially symmetric habit and evolved in an atmosphere with much higher CO_2 concentrations than today. In order to gain information about the ecophysiological interrelationships of these plants, a model dealing with their gaseous exchange, which is basic to transpiration and photosynthesis, is introduced. The model is based on gas diffusion inside a porous medium and on a well-established photosynthesis model and allows for the simulation of the local gas fluxes through the various tissue layers of a plant axis. Necessary parameters consist of kinetical properties of the assimilation process and other physiological parameters (which have to be taken from extant plants), as well as physical constants and anatomical parameters which can be obtained from well-preserved fossil specimens. The model system is applied to an Early Devonian land plant, *Aglaophyton major*. The results demonstrate that, under an Early Devonian CO_2 concentration, *A. major* shows an extremely low transpiration rate and a low, but probably sufficiently high assimilation rate. Variation of the atmospheric CO_2 concentration shows that the assimilation is fully saturated even if the CO_2 content is decreased to about one-third of the initial value. This result indicates that *A. major* was probably able to exist under a wide range of atmospheric CO_2 concentrations. Further applications of this model system to ecophysiological studies of early land plant evolution are discussed.

1. Introduction

Early land plants with a "rhyniophytic" habit represent the evolutive starting point of the extant terrestrial tracheophyte flora (Bateman *et al.*, 1998). As documented by the fossil record, they existed through the Silurian and Lower Devonian (about 420–380 million years ago). They are characterized by radially symmetric axes which are equipped with a central conducting bundle and which branch dichotomously (this axis type is termed telome, after Zimmermann, 1959). True roots are absent. The members of this constructionally primitive group with still unsolved systematic interrelationships (Kenrick & Crane, 1997), such as *Rhynia gwynne-vaughanii* or *Aglaophyton major*, existed in an atmosphere with a CO_2 concentration which was much higher than today (Berner, 1997). New data about the ecophysiological features of these plants not only improve our knowledge of land plant evolution and ancient ecosystems but more information concerning physiological behaviour of plants under high CO_2 concentrations is also valuable

†Author to whom correspondence should be addressed.

0022–5193/00/170091 + 17 $35.00/0

considering the current increase of carbon dioxide concentration in the atmosphere.

A more detailed knowledge about the gaseous exchange (i.e. transpiration and assimilation) of these plants is thus of increasing interest (Raven, 1994). For example, Raven (1977, 1993) estimated possible assimilation and transpiration rates of rhyniophytic plant axes. Beerling & Woodward (1997) calculated gaseous exchange of numerous fossil plants by treating the gas fluxes with the common approach of resistance models (analogous to electrical circuits, see, for example, Nobel, 1991).

In the present contribution, an approach which allows for the detailed simulation of the gas fluxes of rhyniophytic plants is introduced. With *A. major* serving as an example, we show how the local tracking of gas fluxes along the different tissues of the plant axis can be deduced from (i) assumptions based on the mechanism of diffusion and physical constants that have obviously not changed since Devonian times, (ii) anatomical and morphological properties of the plant available from well-preserved fossil remains, and (iii) assumptions concerning the mechanism of photosynthesis and the CO_2 conductance within the cells of the assimilation tissue. The kinetic properties of the assimilation process may have changed over the course of time. However, a radical difference between the kinetic properties of the key enzymes of extant C_3 plants and Devonian plants appears to be unlikely (Robinson, 1994). Thus, we may be confident that the characteristic amplitudes of assimilation parameters of extant C_3 plants overlap with those of Lower Devonian plants.

The approach presented in this article is in two respects superior to the widely used concept of describing molecular fluxes in analogy to the networks of electric currents: the latter method breaks down if (i) the molecular pathway shows axial or more complicated symmetry, and if (ii) mechanisms like carbon assimilation extract molecules from the CO_2 flux along its path.

The paper is organized as follows: first, we sketch the morphology of *A. major*, a typical rhyniophytic plant, that will serve as an example throughout the paper. Then we give a short discussion of the physics behind diffusion and indicate how the mathematical complexity of the resulting differential equation can be reduced by exploiting symmetries and approximations. Subsequently, we describe the assimilation model which will be used and the mathematical proceeding. Then the model is applied to the tissue organization of *A. major*. Finally, we give results and discuss the possible applications of the method.

2. Characteristics of *A. major*

The axes of *A. major* were approximately 20 cm high with a radius of about 2–2.5 mm (Edwards, 1986). The one-layered epidermis covered by a cuticle and equipped with a stomata is followed by an approximately two- to three-layered hypodermis. A narrow channel formed by the hypodermal cells is located directly under the stomatal pore. It should be noted that not all Lower Devonian species known so far show such a channel. The channel terminates in a small substomatal chamber leading to the system of intercellular air spaces. This system is extensive in the outer cortex which is approximately two to four cell layers thick.

The inner cortex extends to the central vascular bundle. The intercellular air spaces decrease considerably in size towards the axis centre. The spatial structure of the intercellular air spaces and anatomical details of the cells of the subhypodermal layer provide evidence that the assimilating cortex cells are located subhypodermally occupying the most peripheral region of the outer cortex (Edwards *et al.*, 1998). Thus, assimilation took place in the peripheral regions of the plant axis. For a more detailed description of the anatomy of early Devonian plants in general see, for example, Remy & Hass (1996), or Edwards *et al.* (1998).

A reconstruction of the gaseous exchange may be based on an axially symmetric slice of the axis system including all tissues from the assimilating sites outwards (see Fig. 1; note that the radial dimensions of the different layers considered in the figure do not represent the real thickness values of the tissues). The mathematical model describing the fluxes together with their generating mechanisms and its application to this geometry will be explained in the next sections.

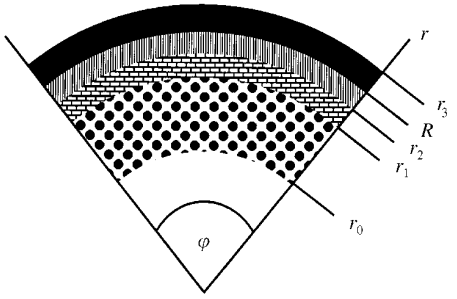

FIG. 1. A sector from the axis slice which represents the tissue model of *Aglaophyton major*. The mathematical model is applied to this system of tissue layers. Only the tissue layers which are considered by the mathematical model are shown. The other tissues, such as inner cortex or conducting tissues are not included. The z-axis is orientated perpendicularly to the illustration and thus not shown. Note that the radial dimensions of each layer as they are shown in the illustration do not reflect the real thickness values. Table 1 gives typical thickness values for each tissue layer. Boundary layer, (■); Stomatal layer, (▥); hypodermal layer, (▤); assimilation layer (⁘).

3. The Model

3.1. THE PROCESS OF DIFFUSION

The movement of water vapour and CO_2 in plants is governed by the process of diffusion, i.e. Fick's first law

$$\mathbf{j} = -S \operatorname{grad} C \tag{1}$$

($[\mathbf{j}] = \mathrm{mol\,m^{-2}\,s^{-1}}$, $[S] = \mathrm{m^2\,s^{-1}}$, $[C] = \mathrm{mol\,m^{-3}}$) which states that the current density $\mathbf{j}$ (number of molecules diffusing in unit time through unit area) should be proportional to (i) the concentration gradient and (ii) an effective conductance S which depends on the properties of the diffusing molecules and on the medium through which they propagate.

If CO_2 or water vapour diffuse through free air (in contrast to the network of air-filled voids between the plant cells) diffusion is not hindered by any spatial restrictions and eqn (1) reads as $\mathbf{j} = -D \operatorname{grad} C$, i.e. the effective conductance S equals the diffusion constant in free air, D ($D_{CO_2} = 1.51 \times 10^{-5}\,\mathrm{m^2\,s^{-1}}$, $D_{H_2O} = 2.42 \times 10^{-5}\,\mathrm{m^2\,s^{-1}}$). If, however, the diffusing molecules have to move along a lattice of interconnected channels, an averaging approach to this complex pathway,—the tortuosity τ—is necessary. This quantity is included into the effective conductance S in order to keep eqn (1) valid. A second correction to S—the porosity n—is imperative if eqn (1) is to be used in the framework of the porous medium approximation, which is appropriate for the simulation of the diffusion of gases in plant tissues (see Parkhurst, 1994). The porous medium approach will be discussed more in detail in a later section.

Both corrections result in

$$S = D\frac{n}{\tau^2}, \tag{2}$$

where $n := V_p/V$, with V_p being the pore volume and V the total volume of a volume element. $\tau := l_e/l$ is the tortuosity, with l_e denoting the length of the path which a molecule has to follow in order to move from one given point to another and l is the (geometrically) shortest distance between these same points.

The diffusion equation is derived by inserting Fick's first law into the principle of mass conservation. The result in polar coordinates (r, φ, z) reads as

$$S\frac{1}{r}\frac{\partial}{\partial r}\left(r\frac{\partial C}{\partial r}\right) + \frac{1}{r^2}\frac{\partial}{\partial \varphi}\left(S\frac{\partial C}{\partial \varphi}\right) + \frac{\partial}{\partial z}\left(S\frac{\partial C}{\partial z}\right)$$

$$-\frac{\partial C}{\partial t} + \frac{\partial S}{\partial r}\frac{\partial C}{\partial r} = -Q. \tag{3}$$

If the source (or sink) term $Q = Q(r, \varphi, z, t, C)$ ($[Q] = \mathrm{mol\,m^{-3}}$) is a linear function of C and if the effective conductance $S = S(r, \varphi, z)$ and appropriate boundary conditions are prescribed, the diffusion equation (3) has exactly one solution for the concentration $C = C(r, \varphi, z, t)$ of water vapour or CO_2 as a function of space and time within the whole plant or plant parts. Once $C = C(r, \varphi, z, t)$ is calculated the current density $\mathbf{j}(r, \varphi, z, t)$ follows from eqn (1).

For realistic conditions it is impossible to solve eqn (3) in all generality. In order to avoid unnecessary mathematical difficulties we use the porous medium approach (see below), assume

translatorial symmetry along the plants symmetry axis and stationary conditions. These approximations and some estimations of the possible errors caused by their application are discussed in the later section.

Aglaophyton is divided into various tissue layers (e.g. the stomatal and the hypodermal layer, see Fig. 1). Anatomical properties influencing the effective conductance S, such as porosity and tortuosity, change from one layer to the next more or less abruptly, but remain approximately constant within the individual layers. Thus, the effective conductance S is assumed to remain constant within each radial layer.

Due to these assumptions all terms but the first on the left-hand side (l.h.s.) of eqn (3) disappears and eqn (3) becomes the ordinary differential equation

$$\frac{1}{r}\frac{\mathrm{d}}{\mathrm{d}r}\left(r\frac{\mathrm{d}C}{\mathrm{d}r}\right) = -\frac{Q}{S}, \quad S = const., \quad C = C(r),$$

$$Q = Q(r, C(r)), \tag{4}$$

which will be central to our approach. Equation (1) becomes

$$j(r) = -S\frac{\mathrm{d}C(r)}{\mathrm{d}r}, \tag{5}$$

where j is defined by $\mathbf{j} = j\,\mathbf{e}_r$ and $\mathbf{e}_r$ is the unit vector along the r-coordinate. For each tissue layer of the axis slice, eqn (4) must be solved separately, after assigning appropriate values to S.

3.2. APPROXIMATIONS

3.2.1. *The Porous Medium Approach*

The overall structure of *Aglaophyton* consists of concentric layers which are built from smaller structures like cells and voids which obviously do not fit into the mathematically favourable picture of axial symmetry (with its sought for consequence that C and S do not depend on φ). In order to establish axial symmetry down to infinitely small structures, the porous medium approximation replaces the discontinuous arrangement of cells and voids inside the real plant by a fictitious tissue with continuous material properties which are constant in the φ direction and may vary in the r direction.

As a result of this averaging process, the permeability of a porous medium is described by two properties: (i) the porosity, which gives the percentage part of void space to the whole volume and (ii) the tortuosity. The latter quantity accounts for the fact, that a molecule cannot diffuse along a straight line but has to follow a complex network of pathways formed by the interconnected void spaces (see above). The porous medium approach was applied successfully by Parkhurst & Mott (1990) in order to study the intercellular CO_2 gradients inside the angiosperm leaves (see also the review by the Parkhurst, 1994).

3.2.2. *Stationarity*

We consider the steady state, i.e. C and S do not depend on the time ($= t$). This condition is not as restrictive as one might think: a concentration front of, say, water vapour needs a time $t \approx s^2/D_{H_2O} = 0.04\,\mathrm{s}$ to diffuse a distance $s = 1\,\mathrm{mm}$ through free air. (Diffusion constant $D_{H_2O} = 2.42 \times 10^{-5}\,\mathrm{m^2\,s^{-1}}$ at $T = 20^{\circ}\mathrm{C}$ and $p = 1\,\mathrm{atm}$.) The information that a change of humidity outside a plant (as caused by a sudden shower) took place needs roughly the same time to propagate it to the centre of *Aglaophyton*. Stationary conditions—on a perhaps different level—are thus re-established very quickly.

3.2.3. *Translatorial Symmetry*

As the height of *Aglaophyton* exceeds its radius by a factor of 100, we can assume that the fluxes of carbon dioxide and water vapour are oriented mainly radially, i.e. away from the plants symmetry axis. If we orientate the coordinate system in such a way that the z-axis coincides with the plant's symmetry axis, C and S do not depend on z. This is not quite true near the top and the bottom of the plant where the molecules do not move strictly radially. To estimate the error caused by ignoring this fact we assume that the flux through a given area of the plant's surface is

proportional to this area:

$$\text{error} \approx \frac{\text{flux through tips}}{\text{total flux}} \approx \frac{\text{area of tips}}{\text{total area}}$$

$$= \frac{2\pi R^2}{2\pi R^2 + 2\pi Rh} = \frac{R}{R+h} \approx \frac{R}{h} - \left(\frac{R}{h}\right)^2, \quad (6)$$

where we have used $R \ll h$. Typical values for *Aglaophyton* are $h \approx 20\,\text{cm}$ and $R \approx 2\,\text{mm}$, implying an error of about 1%.

3.3. PHOTOSYNTHESIS

Before solving eqn (4) for the assimilation layer we must specify the model of photosynthesis which will be applied, and connect it to eqn (4). We employ the photosynthetic models of Harley & Sharkey (1991) and Kirschbaum & Farquhar (1984) (both based on an older model of Farquhar *et al.*, 1980) to construct an explicit expression for the CO_2 sink $Q = Q(C)$ generated by assimilation. The core of the model consists of the equation

$$A^{chl}(q) = \left(1 - \frac{p_o}{2\tau\, q}\right) \min\{W_c(q), W_j(q)\}, \quad (7)$$

where

$$W_c(q) := \frac{q\, V_{max}}{q + K_c(1 + p_o/K_o)},$$

$$W_j(q) := \frac{q\, J}{4(q + p_o/\tau)},$$

$$J := \frac{\alpha I}{\sqrt{1 + (\alpha I/J_{max})^2}}$$

and $\min\{W_c(q), W_j(q)\}$ denotes the smaller of $W_c(q)$ and $W_j(q)$ for a given q. The carboxylation rate is limited by the activity of Rubisco ($W_c(q)$) or by the regeneration of Rubisco via electron transport ($W_j(q)$). Thus, this equation states that the net rate A^{chl} ($[A^{chl}] = \text{mol}\,\text{m}^{-2}\,\text{s}^{-1}$) of CO_2 flowing into (or out of) the chloroplasts depends on the partial pressure q ($[q] = \text{Pa}$) of CO_2 at the photosynthesizing sites inside the chloroplasts, as well as on p_o, α, τ, K_c, K_o, V_{max}, I, J and J_{max} which represent the various parameters of the photosynthesis model (Table 1). Respiration is not included in the model approach.

Equation (7) is qualitative in the sense (Parkhurst, 1994) that the functional form of $A^{chl}(q)$ is not derived from the first biochemical principles but may be chosen more or less arbitrarily as long as C_3-plant-specific features such as limitation of photosynthesis by Rubisco activity or by RuP_2 regeneration due to electron transport are maintained.

The implementation of the photosynthesis model (7) into the diffusion equation (4) requires the following tasks:

(i) $A^{chl}(q)$ is connected to Q by bookkeeping considerations which involve the porosity n_{as} (= percentage part of the volume of the assimilating tissue occupied by intercellular air spaces), the surface-to-volume ratio (a_{as}/v_{as}) of a typical cortex cell, and the ratio (a_{chl}/a_{as}) of the sum of the surfaces of all chloroplasts a_{chl} within one cortex cell to the surface a_{as} of this cell. These parameters have to be considered, because photosynthesis takes place in the chloroplast layer located peripherally of an assimilating cell. The CO_2 pathway thus includes the crossing of cell walls and cell membranes, a short distance in the cytosol and crossing of the chloroplast limiting membranes (see Nobel, 1991). The corresponding surface areas of these components have to be taken into account.

The result is

$$Q = -\left(\frac{a_{chl}}{a_{as}}\right)\left(\frac{a_{as}}{v_{as}}\right)(1 - n_{as})\, A^{chl}(q). \quad (8)$$

(ii) The partial pressure q of CO_2 inside the chloroplasts in eqn (7) should be replaced by the CO_2 concentration $C(r)$ in the intercellular air spaces of the assimilation layer. Following Parkhurst & Mott (1990) and Parkhurst (1994), we use

$$A^{chl} = g_{liq}(C(r)\, R_{gas}\, T - q), \quad (9)$$

TABLE 1
Aglaophyton *specific parameters*

Parameter	Value units	Abbreviation
Boundary values		
$C_{atm}^{CO_2}$	168 mmol m^{-3}	Atmospheric carbon dioxide concentration
$C_{atm}^{H_2O}$	480 mmol m^{-3}	Atmospheric water vapour concentration
$C_{sat}^{H_2O}$	960.3 mmol m^{-3}	Saturation value of water vapour at 20°C and 1 atm
V_l^m	1.805×10^{-8} m^3 mmol^{-1}	Molar volume of water at 20°C
γ	0.0728 Pa m	Surface tension of water at 20°C
Boundary layer		
r_3	2.685×10^{-3} m	Outer edge of the boundary layer
d_{bl}	0.435×10^{-3} m	Thickness of the boundary layer
v_{atm}	0.8 m s^{-1}	Atmospheric wind velocity
n_{bl}	1 —	Porosity of the boundary layer
τ_{bl}	1 —	Tortuosity of the boundary layer
Stomatal layer		
R	2.25×10^{-3} m	Radius of the plant
d_{st}	0.03×10^{-3} m	Depth of the stomatal pore
a_{st}	3.22×10^{-10} m^2	Surface area of the stomatal pore
v_{st}	1.0×10^{6} m^{-2}	Number density of the stomata
n_{st}	0.32×10^{-3} —	Porosity of the stomatal layer
τ_{st}	1.34 —	Tortuosity of the stomatal layer
Hypodermal layer		
r_2	2.22×10^{-3} m	Outer edge of the hypodermal layer
d_{hy}	0.075×10^{-3} m	Thickness of the hypodermal layer
h_{hy}	0.04×10^{-3} m	Long axis of the cross-section of the hypodermal channel
w_{hy}	0.03×10^{-3} m	Short axis of cross-section of the hypodermal channel
n_{hy}	0.96×10^{-3} —	Porosity of the hypodermal layer
τ_{hy}	1 —	Tortuosity of the hypodermal layer
Assimilation layer		
r_1	2.145×10^{-3} m	Outer edge of the assimilation layer
d_{as}	0.25×10^{-3} m	Thickness of the assimilation layer
r_0	1.895×10^{-3} m	Inner edge of the assimilation layer
σ	55×10^{-6} m	Radius of a cortex cell
(a_{as}/v_{as})	36 364 m^{-1}	Specific surface of a cortex cell
(a_{chl}/a_{as})	2.345 —	Sum of surfaces of all chloroplasts within a cortex cell over surface of one cortex cell
g_{liq}	0.5×10^{-3} mmol m^{-2} s^{-1} Pa^{-1}	Liquid-phase conductance for carbon dioxide in water from cell wall to chloroplast
n_{as}	0.35 —	Porosity of the assimilation layer
τ_{as}	1.57 —	Tortuosity of the assimilation layer
Photosynthesis		
p_o	20 260 Pa	Partial pressure of oxygen at chloroplasts
τ	2822 —	Specificity factor for Rubisco
V_{max}	0.38×10^{-3} mmol m^{-2} s^{-1}	Local maximum carboxylation rate
K_c	63.6 Pa	Michaelis–Menten constant for carboxylation
K_o	34 825 Pa	Michaelis–Menten constant for oxygenation
J	—mmol m^{-2} s^{-1}	Potential rate of electron transport
J_{max}	1.02×10^{-3} mmol m^{-2} s^{-1}	Light-saturated rate of electron transport
I	0.050 mmol m^{-2} s^{-1}	Irradiance
α	0.2–	Efficiency of light conversion

which is a spatially averaged analogue to Fick's first law (1). $R_{gas} = 8.3143\,\mathrm{m^3 Pa\,mol^{-1}\,{}^\circ C^{-1}}$ is the gas constant, $T = 293.15\,\mathrm{K}$ the absolute temperature in degrees Kelvin and g_{liq} ($[g_{liq}] = \mathrm{mol\,m^{-2}\,s^{-1}\,Pa^{-1}}$) denotes the effective conductance through the interior structures of the cortex cells. The value of g_{liq} must be estimated from extant plants (see Parkhurst & Mott, 1990). Equating eqns (7) and (9), solving this relation for q as a function of $C(r)$ and substituting the result back into eqn (9), would lead to an expression for A^{chl} in terms of $C(r)$, so that via eqn (8) the differential equation (4) for the CO_2 concentration in the assimilating region would be given explicitly.

The last step, however, leads to a nonlinear differential equation for $C(r)$, which cannot be solved in a closed form. In order to circumvent this problem, we make use of the freedom granted by the fact that $A^{chl}(q)$ is only of qualitative nature. That is, we replace $A^{chl}(q)$ as given by eqn (7) by a linear approximation $A^{chl}_{lin}(q)$, which retains the crucial features of eqn (7) and casts eqn (4) into an everywhere linear differential equation in C. Details of these manipulations can be found in Appendix A.

3.4. THE SOLUTION PROCEDURE

The layer specific versions of the diffusion equation (4) as they will be applied further on sum up to (bl = boundary layer, st = stomata layer, hy = hypodermal layer, as = assimilation layer)

$$\frac{\mathrm{d}^2 C_i}{\mathrm{d}r^2} + \frac{1}{r}\frac{\mathrm{d}C_i}{\mathrm{d}r} = \begin{cases} 0 & \text{if } r_1 \leqslant r \leqslant r_3 \quad (\text{i.e. } i = bl,\ st,\ hy), \\ \chi & \text{if } r_c \leqslant r \leqslant r_1 \quad (\text{i.e. } i = as), \\ k^2 C - \kappa & \text{if } r_0 \leqslant r \leqslant r_c \quad (\text{i.e. } i = as). \end{cases} \tag{10}$$

χ, k, and κ result from the application of the linear approximation to the photosynthesis model (see Appendix A for a detailed representation). r_c divides the assimilation layer into two areas, a peripheral and an inner zone. CO_2 production is allowed to take place only in the inner zone. The necessity and derivation of r_c is explained in Appendix A.

In mathematical terms, eqn (10) represents a boundary value problem. In order to solve it, we have to match layer specific solutions of eqn (10) in such a way that the overall solution $C(r)$ becomes a continuously differentiable function of r which assumes arbitrarily prescribed values for $C(r)$ (and—depending on the circumstances—perhaps $j(r)$) at the boundaries of the considered region.

General solutions of eqn (10) can be found in text books on Theoretical Physics (for example, Arfken, 1970 or Morse & Feshbach, 1953). In the case of CO_2 diffusion, they are cited in eqn (11) and for water vapour diffusion in eqn (12) [$I_n(x)$ and $K_n(x)$ denote the modified Bessel functions of, respectively, the first and second kind of order n according to the conventions of Abramowitz & Stegun (1972)]. The A_i and B_i (resp. a_i and b_i) are arbitrary constants to which definite values will be assigned during the matching procedure.

The physical basis of the continuity requirement lies in the mobility of the molecules in a gas (or a fluid), which prevents discontinuous concentrations and fluxes. Within the various layers, continuity is already guaranteed by the mathematical structure of eqn (10).

r	$C^{CO_2}(r)$	$j^{CO_2}(r)$
— r_3		
Boundary layer	$A_{bl} + B_{bl} \ln\left(\frac{r}{R}\right)$	$-S_{bl} \frac{B_{bl}}{r}$
— R		
Stomatal layer	$A_{st} + B_{st} \ln\left(\frac{r}{R}\right)$	$-S_{st} \frac{B_{st}}{r}$
— r_2		
Hypodermal layer	$A_{hy} + B_{hy} \ln\left(\frac{r}{R}\right)$	$-S_{hy} \frac{B_{hy}}{r}$
— r_1		
Intracellular air space (outer cortex)	$A_2 + B_2 \ln\left(\frac{r}{R}\right) + \frac{\chi}{4} r^2$	$-S_{as}\left[\frac{B_2}{r} + \frac{\chi}{2} r\right]$
— r_c		
	$A_1 I_0(kr) + B_1 K_0(kr) + \frac{\kappa}{k^2}$	$S_{as} k[-A_1 I_1(kr) + B_1 K_1(kr)]$
— r_0		

(11)

r	$C^{H_2O}(r)$	$j^{H_2O}(r)$
— r_3		
Boundary layer	$a_{bl} + b_{bl} \ln\left(\frac{r}{R}\right)$	$-S_{bl} \frac{b_{bl}}{r}$
— R		
Stomatal layer	$a_{st} + b_{st} \ln\left(\frac{r}{R}\right)$	$-S_{st} \frac{b_{st}}{r}$
— r_2		
Hypodermal layer	$a_{hy} + b_{hy} \ln\left(\frac{r}{R}\right)$	$-S_{hy} \frac{b_{hy}}{r}$
— r_1		

(12)

Critical areas, where continuity has to be ensured explicitly, are the boundaries which separate the layers. Therefore, we require at $r = r_2$: $A_{st} + B_{st}\ln(r_2/R) = A_{hy} + B_{hy}\ln(r_2/R)$ (for the concentration), and $-S_{st}B_{st}/\ r_2 = -\ S_{hy}B_{hy}/r_2$ (for the flux), and similar relations at $r = R$, r_1 and r_c. Analogous conditions apply for solutions (12) in the case of water vapour diffusion.

As boundary conditions at $r = r_0$ and $r = r_3$ we prescribe $j^{CO_2}(r_0) = 0$ and $C^{CO_2}(r_3) = C^{CO_2}_{atm}$ in the case of CO_2 ($C^{CO_2}_{atm}$ denotes the CO_2 concentration in the free atmosphere outside the boundary layer). In the case of water vapour diffusion, we assume that the inner cortex of *Aglaophyton* (which is almost free from intercellular spaces) is saturated with liquid water, that is supplied by the central vascular bundle and evaporates in the intercellular voids of the outer cortex. As the boundary condition at $r = r_1$ we require therefore $C^{H_2O}(r_1) = C^{H_2O}_{sat} \times \exp(-(2\,V^m_l\,\gamma)/(R_{gas}\,T\sigma))$ where $C^{H_2O}_{sat}$ is the saturation value of water vapour in air above a water surface. The exponential factor is supplied by the Kelvin-equation; σ denotes the radius of a typical cortex cell, V^m_l the molar volume of water and γ the surface tension in a boundary surface that separates air and liquid water. As boundary conditions at $r = r_3$ we define $C^{H_2O}_{bl}(r_3) = C^{H_2O}_{atm}$, i.e. we prescribe the water vapour concentration $C^{H_2O}_{atm}$ in the free atmosphere outside the boundary layer.

In order to calculate $C^{CO_2}(r)$ and $j^{CO_2}(r)$ explicitly, we insert the layer-specific solutions (11) into the continuity and boundary conditions. As the layer-specific solutions depend on the unknown constants A_i and B_i, a system of ten linear equations results for the ten A_i and B_i, which can be solved for the A_i and B_i by mathematical standard procedures. By this step, the A_i and B_i become functions of the parameters that describe the plants anatomy and its photosynthetical machinery. Thus, reinsertion of the A_i and B_i back into solutions (11) will complete the solution process: C^{CO_2} and j^{CO_2} depend now only on anatomical and photosynthetic parameters plus the variable r. a_i, b_i, $C^{H_2O}(r)$ and $j^{H_2O}(r)$ are calculated similarly.

The resulting expressions are very lengthy and will therefore not be presented here. Rather, the use of a computer code, such as MAPLE, is advised for all calculations.

4. Application of the Model to the Anatomy of *A. major*

So far, the model applies to every axially symmetric plant that qualifies for the approximations stated above. In the following, we will apply the model to *A. major*. For this purpose, porosity, tortuosity and other miscellaneous quantities are calculated for the various tissue layers of *A. major*.

4.1. BOUNDARY LAYER

The first barrier which has to be taken by a diffusing molecule is the boundary layer of air which envelopes the plant. If air (or a fluid) flows around an object, a velocity gradient develops due to the adhesion of the innermost air layer to the object (see, for example, Vogel, 1994). Thickness d_{bl} and the kind of the boundary layer (laminar or turbulent) influence its conductance. For the present case, we choose the approximation given in Nobel (1991) for a cylindrical body of radius R immersed in air with a (free air) wind velocity v:

$$d_{bl} = 5.8 \times 10^{-3} m \sqrt{\frac{2R}{v}\frac{1}{s}}. \qquad (13)$$

With R as the plants radius we define the outer edge of the boundary layer as

$$r_3 := R + d_{bl}. \qquad (14)$$

The thickness of the boundary layer depends on the wind velocity and increases with decreasing wind velocity. With zero wind velocity d_{bl} and r_3 become infinite. Mathematically, this is not a problem, but the application of eqn (13) makes physically no sense in the absence of wind. A thorough discussion of this point is beyond the scope of this paper. A corresponding sensitivity study, however, demonstrated that the thickness of the boundary layer has little influence on the results, because the main resistances to diffusion are offered by the various tissue layers.

As molecules move in air unhindered by any obstacles, porosity and tortuosity take the values

$$n_{bl} = 1 \quad \text{and} \quad \tau_{bl} = 1. \qquad (15, 16)$$

4.2. STOMATAL LAYER

The conductance of the stomatal layer depends on the stomatal density, the stomatal pore size and the diffusivity of the gas. We consider only the case of fully opened stomata, due to two reasons: (i) stomatal closure requires a corresponding regulation function which is not readily available for Devonian plants, and (ii) during the closing process the size of the stomatal pore may drop below a threshold value below which interactions between the diffusing molecules and the cell walls should be taken into account, that is, Fick's first law ought to be modified in this case (Jarman, 1974; Leuning, 1983).

r_2 denotes the inner edge of the stomatal layer, d_{st} the depth of stomatal pores and thus

$$r_2 := R - d_{st}. \tag{17}$$

Fossilized specimens of *Aglaophyton* provide values for the average area of stomatal pores, a_{st}, and for the number of stomata per unit surface area, v_{st}. In order to calculate the porosity we concentrate on a "slice" of length L along the symmetry axis. We approximate the stomatal layer between R and r_2 by a thin rectangular plate of thickness d_{st} and side lengths L and $\pi(R + r_2)$, where the latter is the arithmetic mean between the circumferences of the outer edge (at $r = R$) and the inner edge (at $r = r_2$) of the stomatal layer.

The volume of one stoma is $a_{st}d_{st}$, the number of stomata on the slice of length L is $v_{st}L\pi(R + r_2)$, and therefore, the pore volume V_p is given by $V_p = a_{st}d_{st}v_{st}L\pi(R + r_2)$. Because the total volume is $V = d_{st}L\pi(R + r_2)$ and $n_{st} = V_p/V$ we obtain

$$n_{st} = a_{st}v_{st}. \tag{18}$$

In the case of the stomatal layer, tortuosity results not from the obstacles inside the stomata, but from the following effect: within the boundary layer, the lines of equal concentration of water vapour or carbon dioxide are not exactly on concentric circles (with centres coinciding with the plant's symmetry axis) but bulge out over the stomata, so that molecules diffusing out of the stomata still experience stomatal conditions although they have already left the stomatal layer in a geometric sense. Nobel (1991, p. 397) approximates this effect by an effective pore radius

$$\rho_{st} = \sqrt{\frac{a_{st}}{\pi}}. \tag{19}$$

With $l_e = d_{st} + \rho_{st}$, $l = d_{st}$ and $\tau := l_e/l$ we obtain

$$\tau_{st} = \frac{d_{st} + \rho_{st}}{d_{st}} = 1 + \frac{\rho_{st}}{d_{st}} = 1 + \sqrt{\frac{a_{st}}{\pi d_{st}^2}}. \tag{20}$$

4.3. HYPODERMAL CHANNELS

If hypodermal channels are present, their contribution to the diffusion conductance has also to be considered. We denote the thickness of the hypodermis by d_{hy} and its lower edge, the boundary to the assimilation layer, by r_1. Thus,

$$r_1 := r_2 - d_{hy} = R - (d_{hy} + d_{st}). \tag{21}$$

The derivation of porosity follows the same ideas as above. Because every hypodermal channel is attached to exactly one stoma, the number of hypodermal channels on a slice of length L equals the number of stomata, $v_{st}L\pi(R + r_2)$. As the volume of one hypodermal channel is $a_{hy}d_{hy}$ the total pore volume of all channels reads as $V_p = a_{hy}d_{hy}v_{st}L\pi(R + r_2)$. The total volume now reads as $V = d_{hy}L\pi(r_1 + r_2)$, thus,

$$n_{hy} = \frac{V_p}{V} = a_{hy}v_{st}\frac{R + r_2}{r_1 + r_2}$$

$$= a_{hy}v_{st}\frac{2R - d_{st}}{2R - (2d_{st} + d_{hy})}, \tag{22}$$

where we have used eqns (17) and (21). Hypodermal channels usually show an elliptic cross-sectional shape with the longer axis, h_{hy}, oriented parallel to the z-axis, and the shorter axis, w_{hy}, lying in a plane of $z = const$.

Thus, $a_{hy} = (\pi/4)\,h_{hy}w_{hy}$ and

$$n_{hy} = \frac{\pi}{4}h_{hy}w_{hy}v_{st}\frac{2R - d_{st}}{2R - (2d_{st} + d_{hy})}. \tag{23}$$

Hypodermal channels contain no obstacles for diffusing molecules. Their tortuosity is therefore

$$\tau_{hy} = 1. \tag{24}$$

4.4. ASSIMILATION LAYER OF THE OUTER CORTEX

The outer cortex consists of cells that look roughly like cylinders. The longitudinal axis of these cells is parallel to the longitudinal axis of the plant. Thus, in cross-sectional view, the shape of these cells is similar to circular disks. Measurements of fossil specimens yield the following average value for the porosity:

$$n_{as} \approx 0.35. \tag{25}$$

In order to calculate the tortuosity of the outer cortex, we use a rough approximation: a molecule which diffuses around such a cell has to move along a half circular path with a distance r from the cell centre. The pathlength l_e amounts to $l_e = \pi r$, the direct distance is $l = 2r$, and the following average value therefore results in

$$\tau_{as} = \frac{l_e}{l} = \frac{\pi r}{2r} = \frac{\pi}{2} \approx 1.57. \tag{26}$$

For further reference we calculate the specific surface (a_{as}/v_{as}) of an infinite-long cylindrical cortex cell with radius σ

$$\left(\frac{a_{as}}{v_{as}}\right) = \frac{2\pi\sigma}{\pi\sigma^2} = \frac{2}{\sigma}. \tag{27}$$

The thickness of the assimilation layer is denoted as d_{as} and

$$r_0 := r_1 - d_{as} = R - (d_{as} + d_{hy} + d_{st}) \tag{28}$$

represents its inner edge.

The results for the quantity $S/D = n/\tau^2$ [see eqn (2)] which apply for CO_2 as well as for water vapour are thus for the various tissue layers $(S/D)_{bl} = 1$, $(S/D)_{st} = 1.8 \times 10^{-4}$, $(S/D)_{hy} = 9.6 \times 10^{-4}$ and $(S/D)_{as} = 0.12$.

All other necessary parameters are listed in Table 1. These include (i) anatomical properties, (ii) biochemical and physiological parameters and (iii) environmental parameters. The anatomical properties are derived from thin sections of fossil *A. major* specimens. In the case of the biochemical and physiological parameters p_0, α, τ, K_c, K_0, V_{max}, I, J and J_{max} values from extant C_3 plants are applied (data compiled from Harley & Sharkey, 1991, Harley *et al.*, 1992; Wullschleger, 1993). The chosen parameters for V_{max} and J_{max} are at the lower range for modern plants (Wullschleger, 1993). The corresponding values can be found in, for example, fern leaves or conifer needles. The environmental parameters represent a Lower Devonian atmosphere as described in the literature (Berner, 1997) and an arbitrarily chosen atmospheric humidity and wind velocity.

5. Results and Discussion

Using the *Aglaophyton* specific values from Table 1 results in the plots of Fig. 2 showing the local fluxes of water vapour and CO_2 against the radial coordinate r. It is apparent that the fluxes are quite smooth functions of r outside the assimilation layer. This is to be expected from the plants axial symmetry, which forces the fluxes to vary inversely proportional to r wherever sources or sinks are absent.

The local fluxes of CO_2 and water vapour at the plant surface give the assimilation rate and the transpiration rate per plant surface area. The

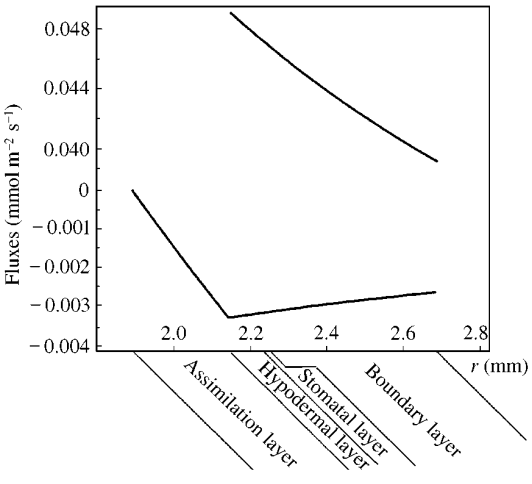

FIG. 2. Water vapour flux $j^{H_2O}(r)$ (above) and carbon dioxide flux $j^{CO_2}(r)$ (below) as a function of the radial coordinate r. $j^{CO_2}(r)$ is negative because it flows into the plant. Parameter values are as in Table 1.

value of the assimilation rate amounts to about 3.1 $\mu mol\,m^{-2}\,s^{-1}$, which is in the range of the results of Raven (1993) and Beerling & Woodward (1997). The value of the transpiration rate amounts to about 47 $\mu mol\,m^{-2}\,s^{-1}$. Both values are low, if compared to extant plants. Shade leaves of angiosperms, conifer needles or ferns show assimilation rates which lie in the range of about 6 $\mu mol\,m^{-2}\,s^{-1}$ (Larcher, 1997). The transpiration rate is extremely low, for example, as leaves of, extant herbaceous plants may reach transpiration rates of more than 5000 $\mu mol\,m^{-2}\,s^{-1}$ (Larcher, 1997). The tiny xylem strands of rhyniophytic plants thus appear to be sufficient due to the obviously low water demand of the plant axes.

The local concentrations of water vapour and CO_2 plotted in Fig. 3 against r behave less smoothly, because their gradients $dC(r)/dr = -(1/S)j(r)$ [from eqn (5)] are dominated by the factor $1/S$ which leaps considerably from layer to layer, exhibiting the proportions $1/S_{bl} : 1/S_{st} : 1/S_{hy} : 1/S_{as} \approx 1 : 5000 : 1000 : 8$. This causes steep gradients of both CO_2 and water vapour in the stomatal and hypodermal layers, whereas in the boundary layer and—in the case of CO_2—in the assimilation layer, the concentrations of both gases remain almost constant.

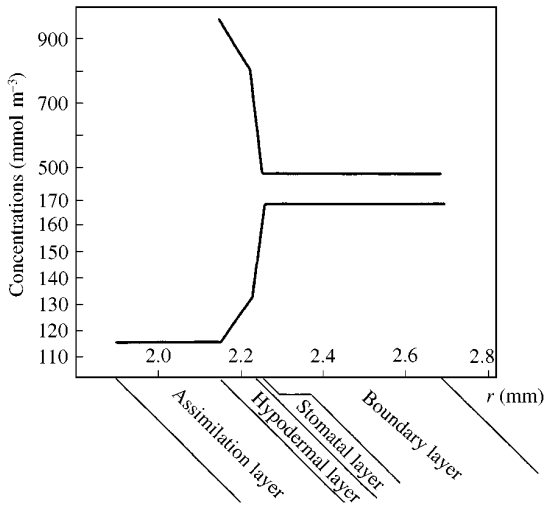

FIG. 3. Water vapour concentration $C^{H_2O}(r)$ (above) and carbon dioxide concentration $C^{CO_2}(r)$ (below) as a function of the radial coordinate r. Parameter values are as in Table 1.

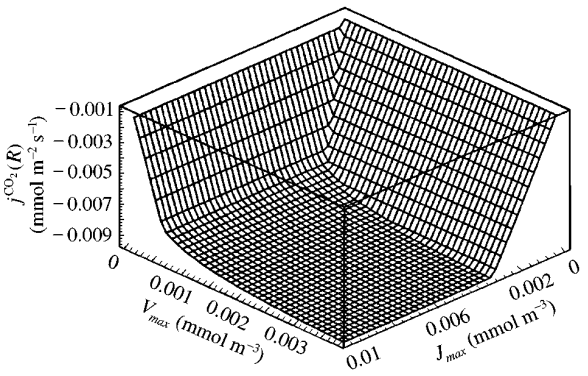

FIG. 4. Assimilation rate $j^{CO_2}(R)$ as a function of V_{max} and J_{max}. The original input values amount to $V_{max} = 0.38\ \mu mol\,m^{-2}\,s^{-1}$ and $J_{max} = 1.02\ \mu mol\,m^{-2}\,s^{-1}$. Other input values are as in Table 1.

As many input values represent estimations or are borrowed from extant plants, a number of sensitivity studies were carried out in order to yield an impression of how the results are influenced by smaller or greater changes of these input parameters. For these sensitivity studies, the calculations are repeated with one or two parameters of the whole set of input parameters increasing and decreasing systematically. Figure 4 shows the assimilation rate ($= j^{CO_2}(R)$) plotted against V_{max} and J_{max}. $j^{CO_2}(R)$ increases almost linearly with increasing V_{max} and J_{max} (with the other parameters remaining constant) up to a value of $j^{CO_2}(R)$ of about 8 $\mu mol\,m^{-2}\,s^{-1}$. At this point, V_{max} and J_{max} amount to about 0.4 and 3 $\mu mol\,m^{-2}\,s^{-1}$, respectively. Beyond this point, $j^{CO_2}(R)$ increases slowly approaching an upper limit of about 0.01 $mmol\,m^{-2}\,s^{-1}$. The values which are originally chosen for the simulations lead to a result which lies in the lower range of these possible values ($j^{CO_2}(R) = 3.1\ \mu mol\,m^{-2}\,s^{-1}$). The chosen input values of V_{max} and J_{max} are therefore located in the critical interval of possible values.

In another sensitivity study, the value of g_{liq}, the liquid-phase conductance for carbon dioxide in water (from the cell wall to the chloroplasts), was varied. The graph in Fig. 5 shows that the parameter of g_{liq} has no influence on the assimilation rate, until it reaches unrealistically low values. Note that the scale of g_{liq} ends at $5 \times 10^{-6}\ mmol\,m^{-2}\,s^{-1}\,Pa^{-1}$, a value much

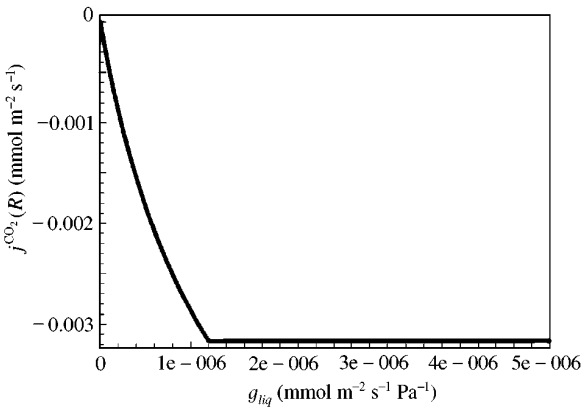

FIG. 5. Assimilation rate $j^{CO_2}(R)$ as a function of g_{liq}, the liquid-phase conductance for carbon dioxide in water. The scale of g_{liq} ends at 5×10^{-6} mmol m^{-2} s^{-1} Pa^{-1}, a value much lower than the original input value, $g_{liq} = 0.5 \times 10^{-3}$ mmol m^{-2} s^{-1} Pa^{-1}. All other parameter values are as in Table 1.

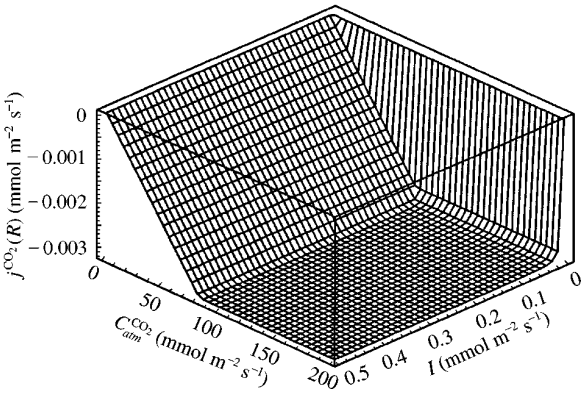

FIG. 6. Assimilation rate $j^{CO_2}(R)$ as a function of the irradiance I and the atmospheric carbon dioxide concentration $C_{atm}^{CO_2}$. The original input values amount to $I = 50$ μmol m^{-2} s^{-1} and $C_{atm}^{CO_2} = 168$ mmol m^{-2} s^{-1}. All other parameter values are as in Table 1.

lower than the chosen parameter taken from the literature.

The irradiance I was also varied (see Fig. 6). The results show that increasing I beyond the chosen input value has no influence on $j^{CO_2}(R)$. If I is decreased, however, $j^{CO_2}(R)$ decreases correspondingly. A lower irradiance value due to, for example, shading, thus decreases the assimilation rate.

These sensitivity studies demonstrate that increasing or decreasing input values may or may not have an effect on the simulation results, depending on the parameters. As many quantities must be estimated or taken from results obtained with extant plants, sensitivity studies can be used to identify critical parameters. The validity of obtained simulation results must then be checked by using additional criteria. Interestingly, the intercellular CO_2 concentration inside the assimilating tissue amounts to about 116 mmol m^{-3}, which corresponds to about 69% of the external value. Extant plants also show intercellular CO_2 concentrations which amount to 70% of the external value (von Caemmerer & Evans, 1991). The fact that the intercellular CO_2 concentration obtained by the calculations corresponds to this value thus indicates that the chosen input values represent reasonable estimations (see below).

If the water use efficiency (WUE), under stationary circumstances defined by

$$\text{WUE} := \frac{\text{number of } CO_2 \text{ molecules fixed}}{\text{number of } H_2O \text{ molecules transpired}} = \frac{|j^{CO_2}(R)|}{j^{H_2O}(R)} \tag{29}$$

is calculated, then we obtain a value of 0.068 which is 34 times higher than the typical values for extant C_3 plants (see, for example, Kramer, 1983). This high value is mainly due to the low transpiration rate of the rhyniophytic plant axis.

As stated by Edwards *et al.* (1998), the low stomatal density and the presence of the hypodermal layer should reflect a water-conserving strategy. In fact, the results demonstrate an extremely low water loss caused by the low stomatal density plus the additional resistance of the hypodermal layer. A direct comparison of rhyniophytic plants to extant plants in order to gain information about, for example, their environmental conditions is difficult and may lead to misinterpretations, because the primitive architecture of these earliest land plants is coupled to the pioneering colonization of the terrestrial environment (Edwards, 1998). As true roots were absent in rhyniophytic plants, they probably showed a low water-absorbing capacity. Mycorrhizal fungi were present in these plants. However, it is assumed that water absorption took place in the underground rhizoids of the plants.

Thus, the low water loss perhaps matched the probably low-water-absorbing capacity of these plants. Despite the low transpiration rate, the photosynthetic process reached assimilation rates which are low if compared to extant plants, but probably sufficiently high for rhyniophytic plant axes due to the high CO_2 content of the Lower Devonian atmosphere. Thus, as was stated by Edwards (1998), "it could be argued that high CO_2 concentration "permitted" the minimizing of numbers of stomata (…)".

As a high atmospheric CO_2 content probably represents a prerequisite for the evolution of early terrestrial plants such as *Aglaophyton major*, the question arises to which limit of the atmospheric CO_2 concentration rhyniophytic plants were able to exist. In order to study how the assimilation process changes with external CO_2 concentration, the latter is varied while all other parameters remain constant. Figure 6 illustrates the assimilation rate ($= CO_2$ flux into the plant surface) plotted against the atmospheric CO_2 concentration. The graph shows that the assimilation rate is roughly constant and fully saturated over a wide range of atmospheric CO_2 concentrations. Below a CO_2 concentration of about 81 mmol m^{-3} the assimilation rate decreases approximately linearly with decreasing atmospheric CO_2 content. Lower values than those which represent the upper limits or average values of the estimation range of Lower Devonian atmospheric CO_2 concentrations are thus sufficient for a saturation of the assimilation process and *Aglaophyton major* may well have been able to exist under a wide range of atmospheric CO_2 concentrations.

Because it is obviously impossible to conduct physiological measurements on fossil plants, some uncertainties exist for the present approach. This concerns mainly the biochemical parameters of photosynthesis. As noted above, assimilation parameters were chosen which lie in the lower range of extant C_3 plants. It is possible, for example, that the photosynthesis apparatus of rhyniophytic plants showed even lower parameters. It appears, however, reasonable to apply these values considering the fact that a wide range of C_3 plants such as conifers or ferns show parameters which are similar to the chosen values. This is supported by the resulting intercellular CO_2 concentration amounting to 69% of the external value. As discussed in Beerling & Woodward (1997), a corresponding ratio between internal and external CO_2 concentration is probably the common case for land plants, both past and present. This is supported by the relative constancy of $\delta^{13}C$ of terrestrially produced organic matter over the last 350 million years (Farquhar *et al.*, 1989). Another uncertainty is represented by such parameters as the resistance of the cell membranes to CO_2 or chloroplast content of the assimilating cells. However, the same ideas as above are valid for these parameters and it appears to be reasonable to choose the values of extant C_3 plants.

Another problem may be represented by the mycorrhizal fungi present in rhyniophytic plant axes (Taylor & Taylor, 1997). Quite probably the hyphae contributed at least to the nutrient supply of the plants, as is the case for extant mycorrhizae (Harley & Smith, 1983). Relevant to the present approach are possible influences on the following parameters: the volume (resp. porosity n_{as}) of the intercellular air spaces by simply occupying space and the permeability of the plant for external gases or fluids. The significance of the first effect may be investigated by carrying out sensitivity studies. In the case of the second effect, reasonable estimations about this possible effect would be needed. The actual model assumes that the stomatal pores are the main pathway for CO_2 and water vapour. If detailed information about the effects of the hyphae on the permeability of the plant axis became available, these could be easily introduced into the model system.

The approach presented in this paper allows readily for studying different taxa with different anatomical properties. Additionally, sensitivity studies are possible, allowing single parameters to be varied while the other values remain constant. Examples are shown in Figs 4, 5, & 6. In this way, considered environmental, anatomical and biochemical variables can be varied systematically and independently and the effects of these variations can be studied. Thus, functional studies become feasible which allow for comparisons of different taxa and to explore possible optima of the plant constructions. It is to be expected that further applications of this approach will yield numerous results concerning

ecophysiological and functional characteristics of the earliest land plants.

REFERENCES

ABRAMOWITZ, M. & STEGUN, I. (1972). *Handbook of Mathematical Functions.* New York: Dover Publications.

ARFKEN, G. (1970). *Mathematical Methods for Physicists.* New York: Academic Press.

BATEMAN, R. M., CRANE, P. R., DIMICHELE, W. A., KENRICK, P. R., ROWE, N. P., SPECK, T. & STEIN, W. (1998). Early evolution of land plants: phylogeny, physiology, and ecology of the primary terrestrial radiation. *Ann. Rev. Ecol. Systematics* **29,** 263–292.

BEERLING, D. J. & WOODWARD, F. L. S. (1997). Changes in land plant function over the Phanerozoic: reconstructions based on the fossil record. *Bot. J. Linn. Soc.* **124,** 137–153.

BERNER, R. A. (1997). The rise of plants and their effect on weathering and atmospheric CO_2. *Science* **276,** 544–545.

VON CAEMMERER, S. & EVANS, J. R. (1991). Determination of the average partial pressure of CO_2 in chloroplasts from leaves of several C_3 plants. *Austr. J. Plant Physiol.* **18,** 287–306.

EDWARDS, D. S. (1986). *Aglaophyton major*, a non-vascular land plant from the Devonian Rhynie Chert. *Bot. J. Linn. Soc.* **93,** 173–204.

EDWARDS, D. (1998). Climate signals in Paleozoic land plants. *Philos. Trans. R. Soc. Lond., Ser.* **B 353,** 141–157.

EDWARDS, D., KERP, H. & HASS, H. (1998). Stomata in early land plants: an anatomical and ecophysiological approach. *J. Exp. Bot.* **49,** 255–278.

FARQUHAR, G. D., VON CAEMMERER, S. & BERRY, J. A. (1980). A biochemical model of photosynthetic CO_2 assimilation in leaves of C_3 species. *Planta* **149,** 78–90.

FARQUHAR, G. D., EHLERINGER, J. R. & HUBICK, K. T. (1989). Carbon isotope discrimination and photosynthesis. *Ann. Rev. Plant Physiol. Plant Mol. Biol.* **40,** 503–537.

HARLEY, J. L. & SMITH, S. S. (1983). *Mycorrhizal Symbiosis.* New York: Academic Press.

HARLEY, P. C. & SHARKEY, T. D. (1991). An improved model of C_3 photosynthesis at high CO_2: reversed O_2 sensitivity explained the lack of glycerate re-entry into the chloroplast. *Photosynth. Res.* **27,** 169–178.

HARLEY, P. C., THOMAS, R. B., REYNOLDS, J. F. & STRAIN, B. R. (1992). Modelling the photosynthesis of cotton grown in elevated CO_2. *Plant, Cell Environ.* **15,** 271–282.

JARMAN, P. D. (1974). The diffusion of carbon dioxide and water vapour through stomata. *J. Exp. Bot.* **25,** 927–936.

KENRICK, P. & CRANE, P. R. (1997). The origin and early evolution of plants on land. *Nature* **389,** 33–39.

KIRSCHBAUM, M. U. F. & FARQUHAR, G. D. (1984). Temperature dependance of whole leaf photosynthesis in Eucalyptus pauciflora Sieb. ex Spreng. *Aust. J. Plant Physiol.* **11,** 519–538.

KRAMER, P. J. (1983). *Water Relations of Plants*, New York: Academic Press.

LARCHER, W. (1997). *Physiological Plant Ecology*, 3rd Edn. New York: Springer-Verlag.

LEUNING, R. (1983). Transport of gases into leaves. *Plant, Cell Environment* **6,** 181–194.

MORSE, P. M. & FESHBACH, H. (1953). *Methods of Theoretical Physics.* New York: McGraw-Hill Book Company.

NOBEL, P. S. (1991). *Physicochemical and Environmental Plant Physiology*. San Diego: Academic Press.

PARKHURST, D. F. (1994). Diffusion of CO_2 and other gases inside leaves. *Phytology* **126,** 449–479.

PARKHURST, D. F. & MOTT, K. A. (1990). Intercellular diffusion limits to CO_2 uptake in leaves. *Plant Physiol.* **94,** 1024–1032.

RAVEN, J. A. (1977). The evolution of vascular land plants in relation to supracellular transport processes. *Adv. Bot. Res.* **5,** 153–219.

RAVEN, J. A. (1993). The evolution of vascular plants in relation to quantitative functioning of dead water-conducting cells and stomata. *Biol. Rev.* **68,** 337–363.

RAVEN, J. A. (1994). The significance of the distance from photosynthesizing cells to vascular tissue in extant and early vascular plants. *Bot. J. Scotland* **47,** 65–81.

REMY, W. & HASS, H. (1996). New information on gametophytes and sporophytes of Aglaophyton major and inferences about possible environmental adaptations. *Rev. Palaeobot. Palynol.* **90,** 175–193.

ROBINSON, J. M. (1994). Speculations on carbon dioxide starvation, Late Tertiary evolution of stomatal regulation and floristic modernization. *Plant, Cell Environ.* **17,** 345–354.

TAYLOR, T. N. & TAYLOR, E. L. (1997). The distribution and interactions of some Paleozoic fungi. *Rev. Palaeobot. Palynol.* **95,** 83–94.

VOGEL, S. (1994). *Life in Moving Fluids.* Princeton: Princeton University Press.

WULLSCHLEGER, S. D. (1993). Biochemical limitations to carbon assimilation in C_3 plants—a retrospective analysis of the A/C_i curves from 109 species. *J. Exp. Bot.* **14,** 907–920.

ZIMMERMANN, W. (1959). *Die Phylogenie der Pflanzen.* Stuttgart: Fischer.

APPENDIX A

Linear Approximation of the Photosynthesis Model

As stated in the article, the nonlinearized version of the photosynthetic model consists of the equations

$$A^{chl}(q) = \left(1 - \frac{p_0}{2\tau q}\right) \min\{W_c(q), W_j(q)\}, \quad \text{(A.1)}$$

where

$$W_c(q) := \frac{q\, V_{max}}{q + K_c(1 + p_o/K_o)},$$

$$W_j(q) := \frac{q\, J}{4(q + p_o/\tau)},$$

$$J := \frac{\alpha I}{\sqrt{1 + (\alpha I/J_{max})^2}}$$

and $\min\{W_c(q), W_j(q)\}$ denotes the smaller of $W_c(q)$ and $W_j(q)$ for a given q.

We define the linear approximation $A^{chl}_{lin}(q)$ to eqn (A.1) by (i) the straight line through the points $(q, A^{chl}) = (0, A^{chl}(0))$ and $(q, A^{chl}) = (p_o/(2\tau), 0)$ and (ii) the straight line parallel to the q-axis with the asymptotic value $A^{chl} = \min\{V_{max}, J/4\}$. q_c denotes the q value of the intersection of (i) and (ii):

$$A^{chl}_{lin}(q) := \begin{cases} V_{max} & \begin{cases} \text{if } q_s \leqslant 0 \quad \text{and } J/4 > V_{max} \quad \text{and } q_c < q, \\ \text{if } q_s > 0 \quad \text{and } J/4 > V_{max} \quad \text{and } q_c < q, \end{cases} \\ \dfrac{J}{4} & \begin{cases} \text{if } q_s \leqslant 0 \quad \text{and } J/4 < V_{max} \quad \text{and } q_c < q, \\ \text{if } q_s > 0 \quad \text{and } J/4 < V_{max} \quad \text{and } q_c < q, \end{cases} \\ \dfrac{J(2\tau q - p_o)}{8p_o} & \begin{cases} \text{if } q_s \leqslant 0 \quad \text{and } J/4 < V_{max} \quad \text{and } 0 \leqslant q \leqslant q_c, \\ \text{if } q_s > 0 \quad \text{and } J/4 > V_{max} \quad \text{and } 0 \leqslant q \leqslant q_c, \end{cases} \\ \dfrac{K_o V_{max}(2\tau q - p_o)}{2\tau K_c(K_o + p_o)} & \begin{cases} \text{if } q_s \leqslant 0 \quad \text{and } J/4 > V_{max} \quad \text{and } 0 \leqslant q \leqslant q_c, \\ \text{if } q_s > 0 \quad \text{and } J/4 < V_{max} \quad \text{and } 0 \leqslant q \leqslant q_c, \end{cases} \end{cases} \tag{A.2}$$

with

$$q_c := \begin{cases} \dfrac{(J + 8V_{max})p_o}{2\tau J} & \text{if } q_s > 0 \quad \text{and } J/4 > V_{max}, \\ \dfrac{\tau K_c J(K_o + p_o) + 2V_{max} K_o p_o}{4V_{max}\tau K_o} & \text{if } q_s > 0 \quad \text{and } J/4 < V_{max}, \\ \dfrac{2\tau K_c(K_o + p_o) + K_o p_o}{2\tau K_o} & \text{if } q_s \leqslant 0 \quad \text{and } J/4 > V_{max}, \\ \dfrac{3\,p_o}{2\,\tau} & \text{if } q_s \leqslant 0 \quad \text{and } J/4 < V_{max}, \end{cases} \tag{A.3}$$

where

$$q_s := \frac{\tau K_c J(K_o + p_o) - 4V_{max} K_o p_o}{\tau K_o(4V_{max} - J)}. \tag{A.4}$$

Equating eqn (A.2) with

$$A^{chl} = g_{liq}(C\,R_{gas}\,T - q) \tag{A.5}$$

solving for q as a function of C and substituting back into eqn (A.2) we obtain an expression for $A^{chl}_{lin}(C)$. Inserting this result into

$$Q = -\left(\frac{a_{chl}}{a_{as}}\right)\left(\frac{a_{as}}{v_{as}}\right)(1 - n_{as})\,A^{chl}(q) \tag{A.6}$$

the diffusion equation (4) attains the following form in the assimilation layer:

$$\frac{\mathrm{d}^2 C}{\mathrm{d}r^2} + \frac{1}{r}\frac{\mathrm{d}C}{\mathrm{d}r} = \begin{cases} \chi & \text{if } r_c \leqslant r \leqslant r_1, \\ k^2\,C - \kappa & \text{if } r_0 \leqslant r \leqslant r_c. \end{cases} \tag{A.7}$$

χ, κ and k are defined by

$$\chi := \frac{1}{D_{CO_2}} \times \tau_{as}^2 \left(\frac{a_{chl}}{a_{as}}\right)\left(\frac{a_{as}}{v_{as}}\right)\frac{1-n_{as}}{n_{as}} \times \begin{cases} V_{max} & \text{if } J/4 > V_{max}, \\ \dfrac{J}{4} & \text{if } J/4 < V_{max}, \end{cases} \tag{A.8}$$

$$\kappa := \frac{1}{D_{CO_2}} \times \tau_{as}^2 \left(\frac{a_{chl}}{a_{as}}\right)\left(\frac{a_{as}}{v_{as}}\right)\frac{1-n_{as}}{n_{as}} \times \begin{cases} \dfrac{-J g_{liq} p_o}{(8 g_{liq} p_o + 2\tau J)} & \begin{cases} \text{if } q_s \leqslant 0 \quad \text{and } J/4 < V_{max}, \\ \text{if } q_s > 0 \quad \text{and } J/4 > V_{max}, \end{cases} \\ \dfrac{-g_{liq} V_{max} K_o p_o}{2\tau[g_{liq} K_c (K_o + p_o) + K_o V_{max}]} & \begin{cases} \text{if } q_s \leqslant 0 \quad \text{and } J/4 > V_{max}, \\ \text{if } q_s > 0 \quad \text{and } J/4 < V_{max}, \end{cases} \end{cases} \tag{A.9}$$

$$k^2 := \frac{1}{D_{CO_2}} \times \tau_{as}^2 \left(\frac{a_{chl}}{a_{as}}\right)\left(\frac{a_{as}}{v_{as}}\right)\frac{1-n_{as}}{n_{as}} \times \begin{cases} \dfrac{-J\tau g_{liq} R_{gas} T}{(4 g_{liq} p_o + \tau J)} & \begin{cases} \text{if } q_s \leqslant 0 \quad \text{and } J/4 < V_{max}, \\ \text{if } q_s > 0 \quad \text{and } J/4 > V_{max}, \end{cases} \\ \dfrac{-g_{liq} V_{max} K_o R_{gas} T}{g_{liq} K_c (K_o + p_o) + K_o V_{max}} & \begin{cases} \text{if } q_s \leqslant 0 \quad \text{and } J/4 > V_{max}, \\ \text{if } q_s > 0 \quad \text{and } J/4 < V_{max}. \end{cases} \end{cases} \tag{A.10}$$

The parameter r_c, which has been introduced in eqn (A.7), is defined by the equation $C(r_c) = C_{q_c}$, where C_{q_c} is the equivalent of the pressure q_c in terms of concentration. It is obtained by equating eqn (A.2) with eqn (A.5), setting $q = q_c$ via eqn (A.3) and solving for C. r_c divides the assimilation area into two layers defined by $r_0 \leqslant r \leqslant r_c$ and $r_c \leqslant r \leqslant r_1$, respectively. In the outer part of the assimilation layer, photosynthesis then works in the "saturated mode" [i.e. the case $q_c \leqslant q$ in eqn (A.2)], and in the inner part of the layer in the "linear mode" [i.e. $0 \leqslant q \leqslant q_c$ in eqn (A.2)]. As $A_{lin}^{chl}(q)$ is a positive constant in the first case and can become negative (if $q < p_o/2\tau$) only in the second case, CO_2 production (due to a drop of the partial pressure q of carbon dioxide in the chloroplasts below the carbon dioxide compensation point) is allowed by the model only in the inner part of the assimilation layer. This is no real restriction, because the extreme cases $r_c = r_0$ or $r_c = r_1$ are allowed by the mathematics of the model, meaning that the complete layer assimilates either in the saturated or in the linear mode, respectively.

We note that the information contained in the right-hand side (r.h.s.) of eqn (A.7) divides into the three categories of assumptions (and reliability) [according to eqns (A.8)–(A.10)] discussed in former sections: the first factor, $1/D_{CO_2}$, is a time-independent constant of nature, the second factor contains—apart from (a_{chl}/a_{as})—measurable quantities obtained from the fossil record, and the third factor reflects photosynthetic considerations for extant C_3-plants. In contrast, the water vapour flux depends only on the first two categories and is therefore less prone to the imponderabilities of evolution.

5.5 Roth-Nebelsick, A., Konrad, W.: *Assimilation and transpiration capabilities of rhyniophytic plants from the Lower Devonian and their implications for palaeoatmospheric CO_2 concentration*, Palaeogeography, Palaeoclimatology, Palaeoecology 202 (2003), p. 153–178.

ELSEVIER

PALAEO

Palaeogeography, Palaeoclimatology, Palaeoecology 202 (2003) 153–178

www.elsevier.com/locate/palaeo

Assimilation and transpiration capabilities of rhyniophytic plants from the Lower Devonian and their implications for paleoatmospheric CO_2 concentration

Anita Roth-Nebelsick *, Wilfried Konrad

Institut für Geowissenschaften der Universität Tübingen, Sigwartstr. 10, D-72076 Tübingen, Germany

Received 23 April 2002; received in revised form 13 August 2003; accepted 5 September 2003

Abstract

The characteristic basic construction of early land plants with an upright posture is represented by a simple leaf- and rootless axis system with a central conducting bundle ('rhyniophytic habit'). Variations of this simple architectural principle in different early land plant taxa probably reflect different ecophysiological requirements. In this contribution, the assimilation and transpiration of three different Rhynie Chert taxa (Pragian, Lower Devonian) which show this fundamental construction are analyzed in detail: *Aglaophyton major*, *Rhynia gwynne-vaughanii* and *Nothia aphylla*. The analysis was conducted by applying a simulation method based on diffusion through a porous material. The results demonstrate that the capability of gaseous exchange increases from *A. major* to *R. gwynne-vaughanii* to *N. aphylla*. *A. major* shows the most strict water-conserving strategy of the three taxa. The results are consistent with data from the fossil record concerning ecophysiological strategies and life styles. Furthermore, the results indicate clearly that the structural properties of early land plants reflect an optimization strategy with a fine-tuning of gaseous exchange. The rhyniophytic habit is strongly adapted to and dependent on high atmospheric CO_2 concentrations. The results provide evidence that the atmospheric CO_2 concentration of the Lower Devonian amounted to roughly 120 mmol/m^3.

Keywords: Lower Devonian; Plantae; Photosynthesis; Paleoecology; Paleoclimatology

1. Introduction

The earliest land plants which possessed an upright posture showed a rather uniform body structure. They consisted of a system of dichotomously branching leaf- and rootless axes with terminal sporangia and a central conducting bundle (see, for example, Stewart and Rothwell, 1993). This 'telomic' system represents very probable the constructional basis leading to modern cormophytes (extant plants composed of roots, stem and leaves) after several morphological transformations. It is widely accepted that all land plants including mosses, lycophytes and horsetails represent descendants of early land plants with such a rhyniophytic habit (Zimmermann, 1959; Kenrick and Crane, 1997; Bateman et al., 1998). The sys-

* Corresponding author. Tel.: +49-7071-2973561; Fax: +49-7071-295217.
E-mail address: anita.roth@uni-tuebingen.de (A. Roth-Nebelsick).

0031-0182/03/$ – see front matter © 2003 Elsevier B.V. All rights reserved.
doi:10.1016/S0031-0182(03)00634-5

tematic affinities of early land plants are complex and there is clear evidence that plants with a rhyniophytic habit belonged to different systematic groups. A rhyniophytic organization was expressed, for example, by the Rhyniopsida and several basal members of the Lycophytina (see thorough discussion in Kenrick and Crane, 1997). The term 'rhyniophytic' will thus be used here not in a systematic sense but in order to denote the telomic organization.

Despite fundamental differences between rhyniophytic plants and extant cormophytes, certain tissues of rhyniophytic plants are similar to tissues of modern land plants (Edwards, 1993; Remy and Hass, 1996; Edwards et al., 1998). Rhyniophytic plants show parenchyma with intercellular air spaces, stomata, cuticle and water transport tissue which is arranged within the central protostele. Rhyniophytic plants were thus equipped with all devices necessary for maintaining a homoiohydric state (Raven, 1984, 1993; Edwards et al., 1998). At first glance, the typical and uniform structure of 'characteristic' rhyniophytic plants appears to suggest correspondingly uniform ecophysiological properties. Recent findings of macrofossils of early land plants document, however, that early land plants were able to colonize various habitats with numerous survival strategies and functional adaptations (for example, Edwards, 1998; Edwards et al., 2001; Gerrienne et al., 2001). It was, for example, suggested by Gerrienne et al., 2001, that unusual spines on the axes of Lower Devonian plants existing in higher paleolatitudes were involved in freezing avoidance.

Well preserved plants of the Rhynie Chert also document numerous differences in tissue fine structure and morphology as well as in the habitats which were settled by different taxa (Edwards et al., 1998; Kerp et al., 2001). *Aglaophyton*, for example, produced more massive axes than *Rhynia*. The aerial axes of the systematically problematic *Nothia aphylla*, which was originally placed within the Rhyniopsida and is now classified as a plesiomorphic member of the Lycophytina, shows a rough surface strewn with protuberances (Kerp et al., 2001). The stomata are located on the summit of these protuberances. Furthermore, *Nothia* shows a much more intense underground rhizome system than *Aglaophyton* and *Rhynia*. An important question which will be addressed in this paper is whether or not these differences indicate significantly different ecophysiological requirements which reflect different ecological niches settled by Rhynie Chert taxa.

Any attempt to approach early land plant ecophysiology has to take paleoenvironmental conditions into account. One of the outstanding aspects of the early and lower middle Paleozoic climate is represented by the high atmospheric CO_2 concentrations, compared to the Recent conditions. During the Lower Devonian, for example, the atmosphere contained about 10 times more CO_2 than today, although the error range concerning this value is considerably high (Berner and Kothvala, 2001). Since the rhyniophytic habit represents the starting point of modern plants and because it evolved under – compared to Recent conditions – extremely high atmospheric CO_2 concentrations, an improvement of our knowledge about possible ecophysiological profiles of these archaic plants is valuable. One aspect of this consideration is the fact that stomatal densities of early land plants including rhyniophytic plants were utilized as proxy data of past atmospheric CO_2 concentrations (McElwain, 1998).

In this contribution, a detailed study of gaseous exchange of rhyniophytic plants is presented. Since experimental studies on fossil plants are impossible, theoretical methods are necessary. Calculations or simulations of assimilation and transpiration of early land plants were undertaken in some earlier studies. Raven (1984, 1993), for example, carried out calculations of gaseous exchange of early land plants. Beerling and Woodward (1997) applied an approach which couples photosynthesis and CO_2 influx. Description of molecular fluxes in analogy to electrical networks is a widely used concept. This method, however, produces correct results only if the pathways of the molecules can be described as straight lines (as is the case with flat leaves) and if no molecules are extracted from the diffusional gas flow. Rhyniophytic plants are however axisymmetric and CO_2 is removed from the gas flux along the cortex tissue due to the process of assimilation.

An alternate approach using a porous model approximation based on an approach of Parkhurst and Mott (1990) and Parkhurst (1994) was thus formulated and applied in the present study. It allows for detailed considerations of differences in tissue organization and systematic parameter variations. The following taxa are considered in this paper: *Aglaophyton major*, *Rhynia gwynne-vaughanii* and *Nothia aphylla*. The limits and ranges of their gaseous exchange are explored and compared. Implications for the atmospheric CO_2 concentrations of the Lower Devonian are also regarded.

2. The model system

2.1. The mathematical approach

A thorough presentation and discussion of the theoretical approach is provided in Konrad et al. (2000) and only a short explanation will thus be given here. The system of equations is based on Fick's first law of diffusion:

$$\vec{j} = -D \operatorname{grad} C \tag{1}$$

where $\vec{j}$ (in mol/m^2/s) denotes the diffusional flux, D (in m^2/s) the constant of diffusion, C (in mol/m^3) the concentration and grad the differential operator grad $f := (\partial f/\partial x, \partial f/\partial y, \partial f/\partial z)$.

If a gas diffuses through a tissue, then the diffusional pathways represent a complex network, because molecules can only diffuse through the void spaces between cells. This effect can be included into Eq. 1 by substituting D by the parameter S, the conductance:

$$S := D\,\frac{n}{\tau^2} \tag{2}$$

with porosity $n = V_p/V$ (V_p = pore volume of tissue, V = total volume of tissue). The tortuosity τ represents the 'averaged' increase of the molecular pathway due to the existence of hindrances (i.e. cells) which cannot be crossed by the molecules and have to be by-passed.

The desired mathematical solution of the present problem is given by insertion of Eq. 1 into the principle of mass conservation. A partial differential equation results which cannot be solved analytically in its most general form. Therefore, some approximations were introduced: (1) the system is supposed to be axially symmetric, (2) only the stationary state is considered, and (3) the tissue is treated as a porous medium. Approximation (1) is reasonable, because a telome of a rhyniophytic plant shows axial symmetry. Approximation (2) has the consequence that rapid temporal changes in gaseous exchange cannot be calculated exactly. Due to the typical dimensions of rhyniophytic plants, however, any 'diffusional state' remaining constant for at least $\approx 10^{-2}$ s can be treated as stationary with high accuracy. Approximation (3) averages the discontinuous system of single cells and voids of a certain tissue into a fictitious continuous tissue with uniform porosity and tortuosity.

After application of all approximations, the following ordinary differential equation results:

$$\frac{1}{r}\frac{\mathrm{d}}{\mathrm{d}r}\left(r\frac{\mathrm{d}C}{\mathrm{d}r}\right) = -\frac{Q}{S} \quad S = \text{const.} \quad C = C(r)$$

$$Q = Q(r, C(r)) \tag{3}$$

and

$$j(r) = -S\frac{\mathrm{d}C(r)}{\mathrm{d}r} \tag{4}$$

In order to solve Eq. 3 we have to specify the sink term $Q = Q(r,C(r))$, which represents in the case of CO_2 the photosynthesis model. A widely used photosynthesis model introduced by Farquhar et al. (1980) will be used for this purpose. It is shortly presented in the Appendix. A detailed discussion of the mathematical aspects of the model (including the solution procedure) is provided in Konrad et al. (2000).

A model of stomatal closure is not included in the system. A stomatal regulation mechanism which optimizes transpirational water loss and CO_2 influx appears to be realized in many angiosperms (Cowan and Farquhar, 1977). Several models of stomatal behavior exist (Ball et al., 1987; Jones, 1992; Aphalo and Jarvis, 1993; Beerling and Woodward, 1995). These models are, however, only applicable to angiosperms. In more ancient plant groups, such as ferns or coni-

fers, stomatal behavior is different from typical angiosperm characteristics (see Robinson, 1994 and citations therein). The fern *Pteridium aquilinum*, for example, shows a very slow stomatal movement with a strong endogeneous rhythm (Jarvis and Penny, unpublished results, discussed in Robinson, 1994). *P. aquilinum* and *Osmunda regalis* do not react instantaneously by rapid stomatal closure on variations in leaf-to-air vapor pressure deficit as is the case with many angiosperms (Franks and Farquhar, 1999). Edwards et al. (1996) suggested that rhyniophytic plants probably did not show control mechanisms of stomatal closure which are identical to control systems in extant angiosperms. No data are available about the mechanism of stomatal closure in rhyniophytic plants (Edwards et al., 1998). Regarding these considerations, the formulation of a reasonable model concerning stomatal closure in early land plants is currently not feasible. The model simulations include, however, a study on the effect of stomatal closure on gaseous exchange of the rhyniophytic axis.

Gaseous exchange was assumed to occur only by diffusion through the stomatal pores. Diffusion through the cuticle was not considered. The possibility cannot be excluded that the cuticle of rhyniophytic plants permitted a certain amount of gaseous exchange. Although *Aglaophyton*, for example, shows a distinct cuticle of several μm, this does not necessarily imply impermeability with respect to H_2O diffusion, because the permeance of a cuticle is more dependent on content and distribution of waxes and thus on its biochemical composition than on its thickness (Becker et al., 1986; Edwards et al., 1996). In extant plants, it was shown that low rates of gaseous exchange can occur via the cuticle (Kerstiens, 1996). It was, however, suggested that in many of these experiments a significant portion of gas flow occurred through incompletely closed stomata (Kerstiens, 1996). The actual permeance of extant cuticles thus appears to be very low in general. In rhyniophytic plants, the extremely low stomatal density together with the occurrence of a hypodermal channel (in the case of *Rhynia* and *Aglaophyton*) suggest a constructional principle of severely controlled gaseous exchange and thus low cuticular transpiration, which was therefore neglected in the model.

The entire system of Eqs. 3–9 is applied to concentrically arranged layers representing the cross-sectional model of a rhyniophytic axis and includes the boundary layer, stomatal layer, hypodermal layer (if present) and outer cortex layer (see Fig. 1) (for Eqs. 5–9 see the Appendix). The final layer specific versions of Eqs. 3 and 4 are solved for each layer in such a way that the overall solution becomes a continuously differentiable function of r. The calculations were performed with the commercial computer code MAPLE. A detailed representation and discussion of the solution procedure is provided by Konrad et al. (2000).

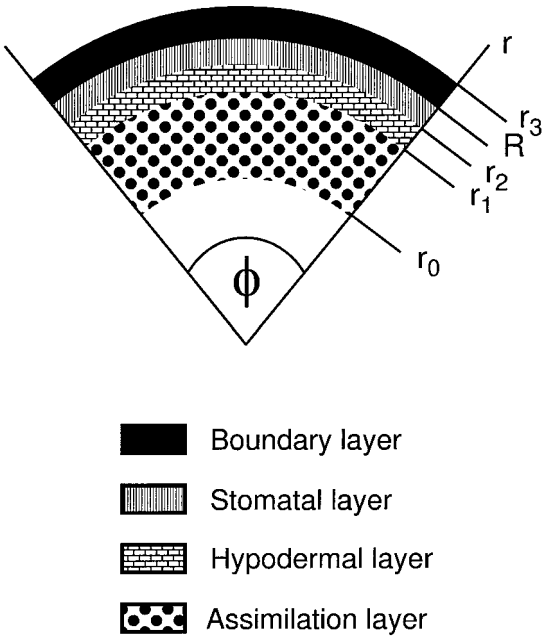

Fig. 1. Schematic representation of the tissue layer structure of the plant models. Only the tissue layers which are considered by the mathematical model are shown. Note that the radial dimensions of the layers in this illustration do not indicate real layer thickness. The z-axis (longitudinal axis) is orientated perpendicularly to the illustration. Black: boundary layer (R–r_3, R: plant radius); hatched: stomatal layer (r_2–R); ruled: hypodermal layer (r_1–r_2); dotted: assimilation layer (r_0–r_1). After Konrad et al., 2000.

2.2. Determination of parameters and sensitivity analyses

The simulations require several parameters of different classes: environmental, anatomical and biochemical. All parameters are listed in Tables 1–3 together with their sources. The values summarized in Tables 1–3 are termed 'initial data set' throughout the rest of the paper. The values of several parameters have to be derived from other parameters. These parameters are specially marked in the tables and the calculation methods are provided in the Appendix. For several parameters, the chosen values will be shortly discussed in the following section. All other parameter values will be discussed in Section 4.1.

The atmospheric CO_2 content is derived from model simulations which indicate R_{CO_2} values (R_{CO_2} = fossil CO_2 concentration/Recent CO_2 concentration) of the Lower Devonian between 10 and 15 (Berner and Kothvala, 2001). For the Pragian (age of Rhynie Chert) a value of $R_{CO_2} = 12$ is suggested by Berner and Kothvala (2001). For the initial data set, a CO_2 concentration 12 times higher than the Recent value was thus chosen. The best fit curve of past CO_2 concentrations is, however, enveloped by an error range of considerable size (Berner and Kothvala, 2001). Possible implications of the present results for estimations of Lower Devonian CO_2 concentrations are discussed in Section 4.4.

The irradiance value is based on the Recent solar constant and the various processes of scattering and reflection of electromagnetic radiation back into space (see, for example, Gates, 1980 or Nobel, 1999). The amount of visible light which is then absorbed by the plant axis is calculated according to the elevation of the sun and by taking the cylindric shape into account (see method in the Appendix) (Niklas and Kerchner, 1984).

Most of the anatomical parameters are obtained from the literature dealing with excellently preserved specimen from the Rhynie Chert, Scotland or from our own measurements. These permineralized specimen allow for reliable reconstructions of axis diameter, geometric properties or thickness of tissue layers, such as width of stomatal pore or thickness of epidermis, as well as the determination of tissue porosity. Since chloroplasts are, however, not preserved by fossilization processes, the surface factor of the chloroplasts has to be estimated on the basis of data from extant plants (see description in the Appendix).

All biochemical parameters have to be taken from corresponding literature data obtained for extant plants. V_{max} and J_{max}, for example, were taken from the range of values found for extant conifers and then fine-tuned in such a way that the ratio between internal and external CO_2 concentration amounts to $C_i/C_a = 0.7$. It is generally assumed that this ratio represents – at least on an averaging long-term scale – a common value realized in land plants (Kürschner, 1996; Beerling and Woodward, 1997). The values of V_{max} and J_{max} are in this case at the lower range of values found in extant conifers (see Appendix). The reliability of the biochemical parameters is discussed in Section 4.

The present contribution contains several sensi-

Table 1
The environmental parameters of the simulation model

Parameter	Value	Source
Wind velocity u_{atm} (m/s)	0.8	arbitrary
Boundary layer thickness d_{bl} (10^{-3} m)		derived
Atmospheric CO_2 content C_a (mmol/m^3)	168	Berner and Kothvala, 2001
Atmospheric H_2O content $C_{atm}^{H_2O}$ (mmol/m^3)[a]	843	arbitrary
Air temperature T (°C)	30	Beerling et al., 2001
Irradiance $I_{\Theta=45^\circ}$ (μmol/m^2/s)	620	arbitrary

In the case of the derived parameters, the method of calculation is provided in the Appendix.
[a] Parameter is varied, see text.

Table 2
The anatomical parameters of the simulation model

Parameter	*Aglaophyton*	*Rhynia*	*Nothia*
Radius of plant R (10^{-3} m)[a]	2.25	1.0	1.050[b]
Depth of stomatal pore d_{st} (10^{-3} m)[c,d,e]	0.03	0.015	0.03
Long axis of stoma h_{st} (10^{-3} m)[c,d]	0.039	0.029	0.021
Short axis of stoma w_{st} (10^{-3} m)[c,d]	0.0105	0.01	0.0025
Area of stomatal pore a_{st} (10^{-10} m^2)[c,d,e]	3.216	2.278	0.412
Stomatal density v_{st} (10^6/m^2)[d,f]	1.0	1.75	3.35
Porosity of stomatal layer n_{st} (10^{-3})[f,g]	0.32	0.399	0.357
Tortuosity of stomatal layer τ_{st} (10^{-3})[f,g]	1.34	1.57	1.12
'Conductivity'[h] of stomatal layer n_{st}/τ_{st}^2 (10^{-3})[g,h]	0.18	0.16	0.28
Thickness of hypodermal layer d_{hc} (10^{-3} m)[c,d,f]	0.075	0.105	–
Long axis of hypodermal channel h_{hc} (10^{-3} m)[c,d,e]	0.04	0.03	–
Short axis of hypodermal channel w_{hc} (10^{-3} m)[c,d,e]	0.03	0.02	–
Area of hypodermal channel a_{hc} (10^{-10} m^2)[c,d,e]	9.42	4.71	–
Porosity of hypodermal layer n_{hc} (10^{-3})[f,g]	0.96	0.87	–
Tortuosity of hypodermal layer τ_{hc} (10^{-3})[f,g]	1.0	1.0	–
'Conductivity'[h] of hypodermal layer n_{hc}/τ_{hc}^2 (10^{-3})[f,g]	0.96	0.87	–
Thickness of assimilation layer d_{as} (10^{-3} m)[c,d]	0.25	0.1	0.42[i]
Cortex cell radius σ (10^{-6} m)[c,d]	55	50	45
Specific surface of cortex cell (a_{as}/v_{as}) (1/m)[g]	36 364	40 000	44 444
Surface factor of chloroplasts (a_{chl}/a_{as}) (–)[g]	2.345	2.345	2.345
Porosity of assimilation layer n_{as} (10^{-3})[j]	0.35	0.35	0.35
Tortuosity of assimilation layer τ_{as} (10^{-3})[g]	1.571	1.571	1.571
'Conductivity'[h] of assimilation layer n_{as}/τ_{as}^2 (10^{-3})[f,g]	0.142	0.142	0.142

In the case of the derived parameters, the method of calculation is provided in the Appendix.

[a] Various sources.

[b] In the case of *Nothia* this indicates the 'outer' radius of the plant (i.e. including *Nothia*'s emergences). The 'inner' radius (measured at the bases of the emergences) amounts to 0.72 10^{-3} m.

[c] Edwards et al., 1998.

[d] Kerp et al., 2001.

[e] Kerp and Hass, personal communication.

[f] Parameter is varied, see text.

[g] Parameter is derived.

[h] The conductance $S = Dn/\tau^2$ splits up into a factor D containing properties of the diffusing substance and a factor n/τ^2 describing the morphology of the medium. The term 'conductivity' stands for the second factor.

[i] In the case of *Nothia* the emergences are supposed to contain assimilating tissue.

[j] Parameter was obtained by own measurements.

tivity analyses. During a sensitivity analysis, one or two parameters are varied systematically, while the others are kept constant. Sensitivity analyses are valuable in order to, (1) analyze system behavior, and (2) check the reliability and limitations of the model approach. If a sensitivity analysis is carried out, then the varied parameters are explicitly described in the corresponding sections, while the other parameters show the values provided in the initial data set listed in Tables 1–3.

3. Results

3.1. Local fluxes of H_2O and CO_2 with initial data set

The flux of H_2O is caused only by the water potential gradient between plant tissue and atmosphere whereas for CO_2 the flux is generated by the assimilation process. Fig. 2 shows the local fluxes of CO_2 and H_2O for *Aglaophyton*, *Rhynia* and *Nothia* for the initial data set, plotted against

Table 3
The biochemical parameters of the simulation model

Parameter	*Picea*	*Aglaophyton*	*Rhynia*	*Nothia*
Effective conductance through a cortex cell g_{liq} (10^{-3} mmol/m^2/s/Pa)	0.5	0.5	0.5	0.5
Light-saturated rate of electron transport J_{max} (10^{-3} mmol/m^2/s)[a]	2.048	1.047	2.884	0.792
Michaelis–Menten constant for carboxylation K_c (Pa)	189	189	189	189
Michaelis–Menten constant for oxygenation K_o (Pa)	42 382	42 382	42 382	42 382
Local maximum carboxylation rate V_{max} (10^{-3} mmol/m^2/s)[a]	0.842	0.430	1.185	0.325
Partial pressure of oxygen at chloroplasts p_o (Pa)	20 260	20 260	20 260	20 260
Efficiency of light conversion α (–)	0.2	0.2	0.2	0.2
Specificity factor for Rubisco θ (–)	1 906	1 906	1 906	1 906

The values of the local maximum carboxylation rate V_{max} and of the light-saturated rate of electron transport J_{max} labeled *Aglaophyton*, *Rhynia* and *Nothia*, respectively, are calculated in such a way that the condition $C_i/C_a = 0.7$ is fulfilled.
The data are compiled from the following sources: Harley and Sharkey, 1991; Harley et al., 1992; Kirschbaum and Farquhar, 1984; Parkhurst and Mott, 1990; Wullschleger, 1993.
[a] Parameter is varied, see text.

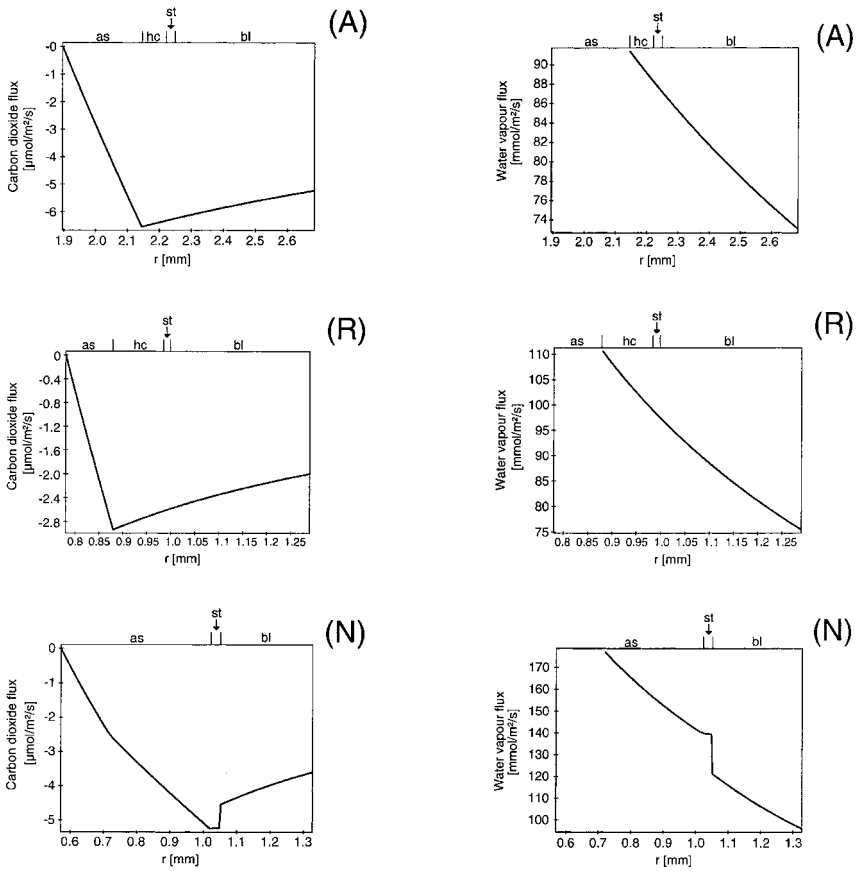

Fig. 2. Local fluxes of H_2O and CO_2 plotted against radial coordinate for *Aglaophyton major* (A), *Rhynia gwynne-vaughanii* (R) and *Nothia aphylla* (N). as, hc, st and bl are abbreviations for assimilation layer, hypodermal channel, stomatal layer and boundary layer, respectively.

the distance r from the symmetry axis (listed in Tables 1–3). For *Aglaophyton* and *Rhynia*, the fluxes of H_2O and CO_2 (outside the assimilation layer) are smooth functions of r. This is due to, (1) the axial symmetry of the plant, and (2) the principle of conservation of mass which forces the fluxes to increase or decrease inversely proportional to r if sources or sinks are absent. In the case of *Nothia*, the fluxes behave somewhat less smoothly, because *Nothia*'s emergences destroy the complete axial symmetry of the plant axes. Inside the assimilation layer, the CO_2 flux changes for all three species from an increase to a strong decrease due to the consumption of CO_2 during the assimilation process. Fig. 3 shows the local concentrations of H_2O and CO_2. Strong gradients are visible along: (1) the stomatal pore and (2) the hypodermal channel (in the cases of *Aglaophyton* and *Rhynia*). In the case of CO_2, a gradient along the assimilation layer has established. It is, however, weak if compared to the stomatal and hypodermal gradient. The initial values of V_{max} and J_{max} lead to values of intercellular CO_2 concentration of about $C_i/C_a = 0.7$ (see Section 2.2). Assimilation is saturated under these conditions.

3.2. Transpiration and assimilation rates with initial data set

The transpiration rate (i.e. the efflux of H_2O

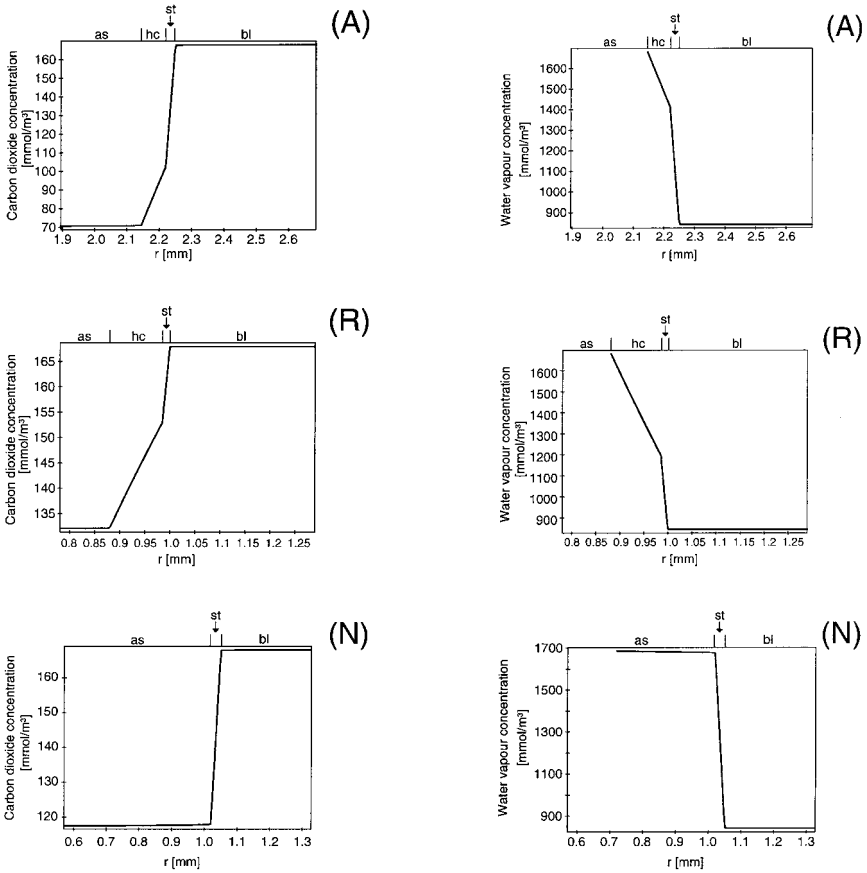

Fig. 3. Local concentrations of H_2O and CO_2 plotted against radial coordinate for *Aglaophyton major* (A), *Rhynia gwynne-vaughanii* (R) and *Nothia aphylla* (N). as, hc, st and bl are abbreviations for assimilation layer, hypodermal channel, stomatal layer and boundary layer, respectively.

out of the axis surface per unit surface area) for *Aglaophyton*, *Rhynia* and *Nothia* is plotted as a histogram in Fig. 4. *Aglaophyton* and *Rhynia* show similar transpiration rates. *Nothia* shows the highest transpiration rate. The transpiration is low for all three taxa compared to common values of extant plants. *Aglaophyton*, for example, transpires 0.087 mmol/m^2/s whereas for leaves of mesophytic trees values of 3 mmol/m^2/s are common (see, for example, Larcher, 1997). It is, however, more reasonable in the case of rhyniophytic plants to relate their water loss to their volume (see underlying ideas in Section 4.2). This is accomplished by calculating $\mathcal{T} = j^{H_2O}(R) \times 2\pi RL/(\pi R^2 L) = 2/R \times j^{H_2O}(R)$ where L denotes the axis length. The results are included in Fig. 4. In this case, *Aglaophyton* shows the lowest transpiration rate, *Nothia* develops again the highest rate, while *Rhynia* lies in between these two values.

Fig. 5 shows the values of CO_2 influx per unit surface area into the plant axes for *Aglaophyton*, *Rhynia* and *Nothia*. The CO_2 influx values represent the assimilation rates. Assimilation is highest for *Nothia* and lowest for *Aglaophyton* with *Aglaophyton* and *Rhynia* showing similar values. Note that the CO_2 influx is not related to projected surface area as is usual for assimilation rates of extant plants. Converting assimilation rates per projected surface area to allow for the direct comparison with literature data of extant plants requires the multiplication of the presented values with the factor 4.44 (because of $2\pi RL/(2RL \cos \Theta) = \pi/\cos \Theta = 4.44$, if the sun is elevated $\Theta = 45°$ above the horizon and with an axis of length L). If the assimilation is, however, related to volume by the same procedure as was applied in the case of the water efflux (see above and underlying ideas in Section 4.2), then *Aglaophyton* shows a distinctly lower value than *Rhynia* while *Nothia* develops again the highest value (see Fig. 5). The formal definition of the assimilation rate per volume is given by $\mathcal{A} = j^{CO_2}(R) \times 2\pi RL/(\pi R^2 L) = 2/R \times j^{CO_2}(R)$).

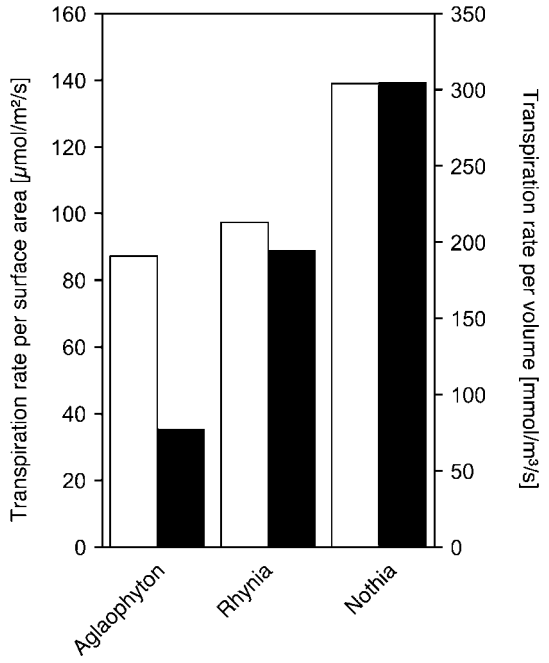

Fig. 4. Transpiration rates of *Aglaophyton major*, *Rhynia gwynne-vaughanii* and *Nothia aphylla*. White columns: transpiration rate per surface area (µmol/m^2/s). Black columns: transpiration rate per volume (mmol/m^3/s).

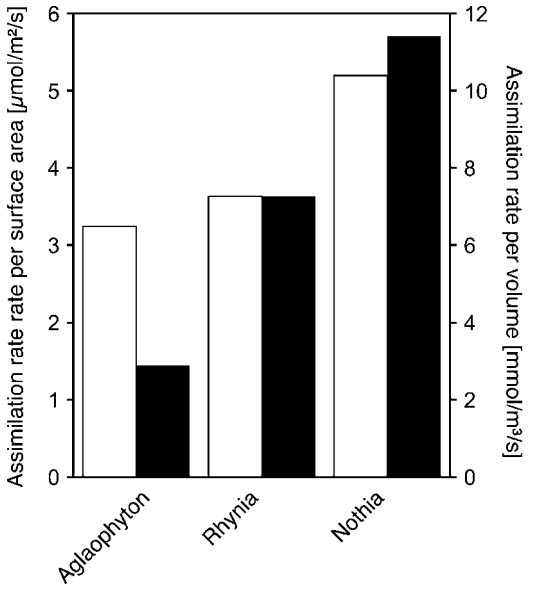

Fig. 5. Assimilation rates of *Aglaophyton major*, *Rhynia gwynne-vaughanii* and *Nothia aphylla*, obtained with V_{max} and J_{max} from the initial data set. White columns: assimilation rate per surface area (µmol/m^2/s). Black columns: assimilation rate per volume (mmol/m^3/s).

The parameter of WUE ('water use efficiency') gives the ratio between the numbers of assimilated CO_2 molecules and transpired H_2O molecules. It is usually expressed as µmol CO_2 fixed per mmol H_2O lost. The value of WUE represents the instantaneous water loss during photosynthesis and is therefore strongly dependent on various parameters, such as the degree of stomatal closure, temperature or relative humidity. In a real plant, the WUE thus represents a strongly fluctuating parameter whose instantaneous value changes with various factors. In order to obtain a long-term value of net carbon gain, long-term parameters, such as the seasonal amount of water transpired per dry matter produced, are often used especially in agricultural studies (Kramer, 1983). It is, however, possible to obtain 'characteristic' WUE values of extant and unstressed C_3 plants with their stomata fully opened (Nobel, 1999). With the initial data set, the calculated assimilation and transpiration rates of *Aglaophyton*, *Rhynia* and *Nothia* yield values around WUE ≈ 37, which is about 18 times higher than the 'typical' extant value. Similar WUE values for all three plants under the conditions of the initial data set are to be expected as the WUE depends – at least approximately – not on the morphology of a plant but rather on the ratio of the (free air) diffusional constants with respect to CO_2 and H_2O times the ratio of the concentration gradients of CO_2 and H_2O, i.e. $\mathrm{WUE} = D^{CO_2}/D^{H_2O} \times \Delta C^{H_2O}/\Delta C^{H_2O}$ (Farquhar et al., 1989).

3.3. Sensitivity analyses

3.3.1. Variation of V_{max} and J_{max}

With the present V_{max} and J_{max} values, small variations of these two parameters lead to strong changes of the assimilation rate. In order to perform a sensitivity analysis with respect to V_{max} and J_{max}, different values of these two parameters were inserted. By doing this, the concept of $C_i/C_a = 0.7$ is dismissed. For this sensitivity analysis, V_{max} and J_{max} values of a certain extant conifer (*Picea abies*, Wullschleger, 1993) are applied ($V_{max} = 0.842$ µmol/m²/s and $J_{max} = 2.05$ µmol/m²/s) instead of the values of the initial data set (see Table 3, note that the original literature data have been transformed according to rhyniophytic anatomical structure, see Appendix). These values were chosen, because V_{max} and J_{max} of conifers are rather low and it is reasonable to assume that V_{max} and J_{max} of rhyniophytic plants were located at the lower range of the extant spectrum of assimilation parameters (see Section 4.1.2).

With these values, *Aglaophyton* exhibits distinctly higher assimilation rates per surface area than *Rhynia* (see Fig. 6). If related to axis volume, however, *Aglaophyton* and *Rhynia* show almost identical values (see Fig. 6). The assimilation rate of *Nothia* approximately doubles on replacing the V_{max} and J_{max} values of the initial data set by the *Picea abies* values and attains again the highest value of all three taxa, both with respect to surface area and to volume (see Fig. 6). The WUE values change in accordance with the assimilation rates, because the transpiration rate is not influenced by the values of V_{max} and J_{max} (see Fig. 7). The ratios of internal CO_2 concentration to external CO_2 concentration now amount to

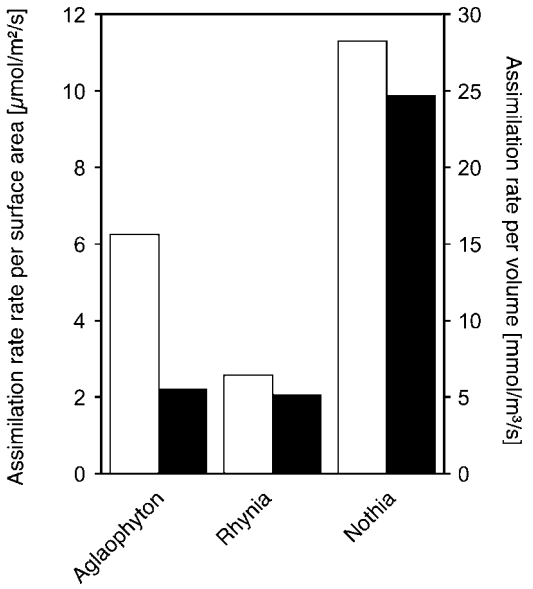

Fig. 6. Assimilation rates of *Aglaophyton major*, *Rhynia gwynne-vaughanii* and *Nothia aphylla*, obtained with V_{max} and J_{max} from *Picea abies*. White columns: assimilation rate per surface area (µmol/m²/s). Black columns: assimilation rate per volume (mmol/m³/s).

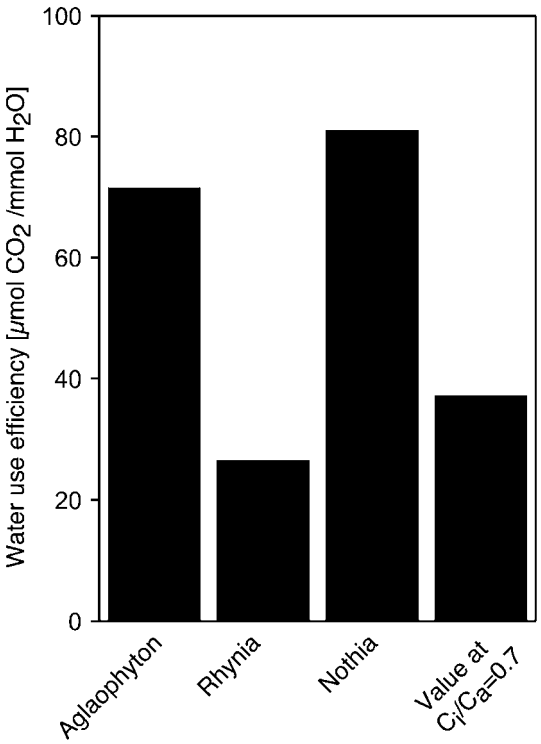

Fig. 7. Values of WUE of *Aglaophyton major*, *Rhynia gwynne-vaughanii* and *Nothia aphylla*. Values of V_{max} and J_{max} from *Picea abies* lead to different values of WUE for each species (left three columns). Values of V_{max} and J_{max} from the initial data set (derived via the condition $C_i/C_a = 0.7$) result in a common WUE value for all three species (right column).

$C_i/C_a = 0.42$ for *Aglaophyton*, $C_i/C_a = 0.79$ for *Rhynia* and $C_i/C_a = 0.35$ for *Nothia*. The reason for the strong effect of this moderate variation of V_{max} and J_{max} is illustrated by Fig. 8 which shows the CO_2 influx as depending on V_{max} and J_{max}. The initial values of V_{max} and J_{max} are located at the critical 'flank' and small variations of these two values thus result in strong changes of the CO_2 influx.

3.3.2. Variation of stomatal density, thickness of hypodermal channel and stomatal opening

The assimilation rate plotted against length of the hypodermal channel d_{hc} and stomatal density ν_{st} for *Aglaophyton* is shown in Fig. 9a. The ranges are $d_{hc} = 0...1.05$ mm and $\nu_{st} = 0...20/m^2$. All other values correspond to the initial data set. The graph illustrates the threshold behavior of the assimilation rate with respect to the parameter ν_{st}. Below the threshold value of ν_{st}, the assimilation rate decreases strongly with decreasing ν_{st} and changes with d_{hc} in a non-linear manner. Above the threshold value, an increase in ν_{st} has

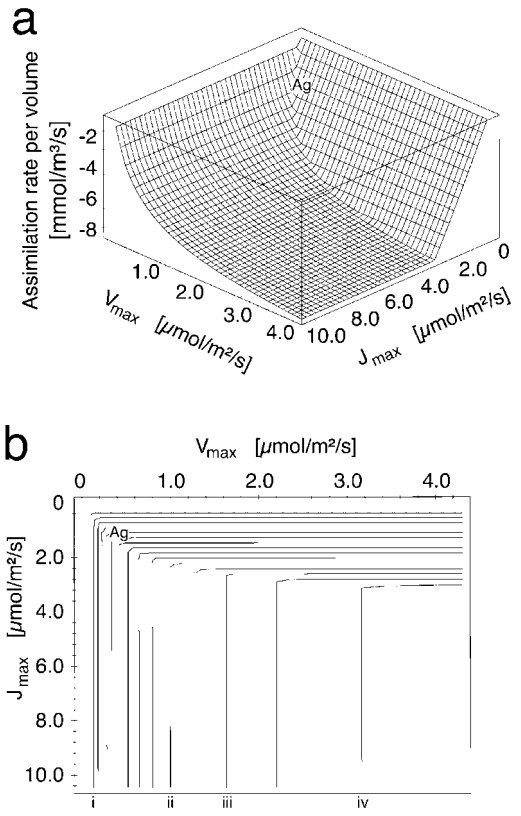

Fig. 8. a: Sensitivity analysis: dependence of assimilation rate per volume on V_{max} and J_{max} for *Aglaophyton major* plotted in a three-dimensional representation. The position of the result obtained with the initial data set is indicated in the graph by the mark 'Ag'. b: Sensitivity analysis: dependence of assimilation rate per volume on V_{max} and J_{max} for *A. major* plotted in a two-dimensional representation (contour plot). The graph can be described as top view of Fig. 8a. The lines are lines of constant assimilation rate per volume. The lines marked i to iv represent the following assimilation rates per volume: -1.5 mmol/m^3/s, -6 mmol/m^3/s, -7 mmol/m^3/s and -8 mmol/m^3/s, respectively. Values of adjacent lines differ by 0.5 mmol/m^3/s. The position of the result obtained with the initial data set is indicated in the graph by the mark 'Ag'.

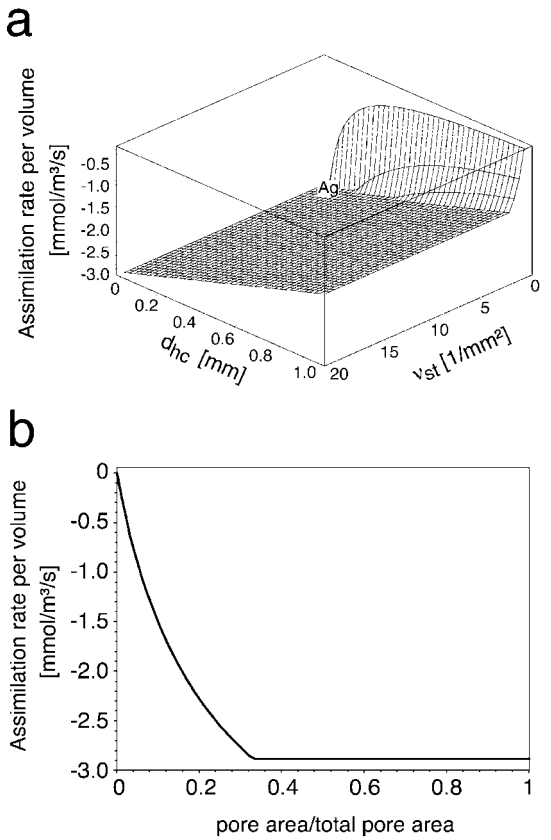

Fig. 9. a: Sensitivity analysis: assimilation rate per volume plotted against length of hypodermal channel d_{hc} and stomatal density v_{st} for *Aglaophyton major*. The position of the result obtained with the initial data set is indicated in the graph by the mark 'Ag'. b: Sensitivity analysis: assimilation rate per volume plotted against degree of stomatal closure, expressed as ratio between pore area and total pore area. This ratio can take values between 0 (= fully closed stomata) and 1 (= fully opened stomata).

no significant effect on assimilation, whereas the assimilation rate increases approximately linearly with decreasing d_{hc}. The same behavior can be observed for *Rhynia* and *Nothia* (data not shown). For all three plants, the (calculated) threshold values of v_{st} are close to the (measured) values which were used in the initial data set.

Fig. 9b shows the change of assimilation rate during stomatal closure which is provided in the figure as ratio between the pore area and the area of the completely opened pore (the value of 1 represents thus fully opened stomata). Fig. 9b demonstrates that the assimilation rate increases strongly when the pore begins to open and reaches a plateau at a degree of stomatal opening of about 0.3 (= 30%). Further increase in stomatal opening does not result in increasing assimilation rates.

Fig. 10a depicts how the transpiration rate of *Aglaophyton* depends on d_{hc} and v_{st}. d_{hc} and v_{st} are varied across the same ranges as in the sensitivity analysis of the assimilation rate. For $d_{hc} \lessapprox 0.2$ mm and for $v_{st} \lessapprox 1.5/mm^2$, the transpira-

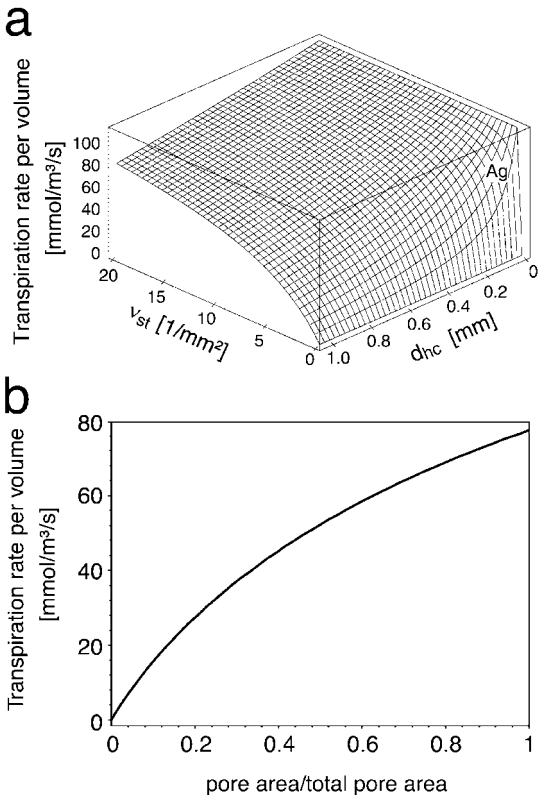

Fig. 10. a: Sensitivity analysis: transpiration rate per volume plotted against length of hypodermal channel d_{hc} and stomatal density v_{st} for *Aglaophyton major*. The position of the result obtained with the initial data set is indicated in the graph by the mark 'Ag'. b: Sensitivity analysis: transpiration rate per volume plotted against degree of stomatal closure, expressed as ratio between pore area and total pore area. This ratio can take values between 0 (= fully closed stomata) and 1 (= fully opened stomata).

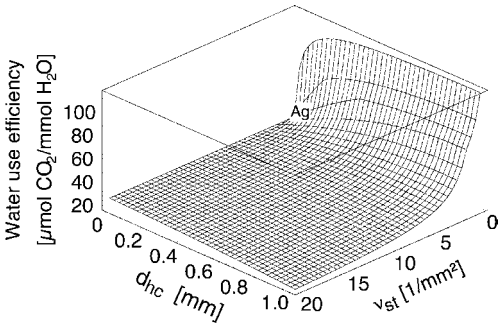

Fig. 11. Sensitivity analysis: WUE plotted against length of hypodermal channel d_{hc} and stomatal density ν_{st} for *Aglaophyton major*. The position of the result obtained with the initial data set is indicated in the graph by the mark 'Ag'.

tion rate varies strongly and in a non-linear manner on both ν_{st} and d_{hc}. With higher values of the stomatal density, the transpiration reacts more moderately on changes in ν_{st} and d_{hc}. Inspection of Fig. 10a reveals that the 'actual' transpiration rate of *Aglaophyton* is located at the upper end of the steep flank. The same behavior can be observed for *Rhynia* and *Nothia* (data not shown). In Fig. 10b the change of transpiration rate during stomatal closure is represented. It can be seen that – contrary to the change in assimilation rate, shown in Fig. 9b – the transpiration rate increases smoothly with increasing stomatal opening. At a degree of stomatal opening of roughly 0.3 – which suffices for achieving maximum assimilation rate – the transpiration rate amounts to about half the value of transpiration with fully open pores.

The WUE (which can, by definition, be viewed as combining effects of assimilation rate and transpiration rate) is shown as a function of d_{hc} and ν_{st} in Fig. 11. A steep flank develops for $\nu_{st} \lessapprox 1.5/\text{mm}^2$ and $d_{hc} \lessapprox 0.2$ mm. The WUE value obtained with the initial data set is seated at the bottom of this flank.

3.3.3. Variation of atmospheric CO_2 concentration

The assimilation rates are plotted against the atmospheric CO_2 concentration C_a for the range $C_a = 10...250$ mmol/m^3 in Fig. 12a,b. V_{max} and J_{max} values correspond to the initial data set (Fig. 12a) or are taken from extant *Picea abies* (Fig. 12b) (see Section 3.3.1). In the horizontal segments (i.e. parallel to the abscissae) of the curves photosynthesis is saturated, in the inclined parts it is undersaturated. Under the conditions of the initial data set, saturation of photosynthesis starts at $C_a \approx 120$ mmol/m^3 (Fig. 12a). For V_{max} and J_{max} of *Picea*, starting points of saturated photosynthesis are located at $C_a \approx 106$ mmol/m^3 (*Rhynia*), $C_a \approx 166$ mmol/m^3 (*Aglaophyton*), and $C_a \approx 193$ mmol/m^3 (*Nothia*) (Fig. 12b).

In another sensitivity analysis, C_a and ν_{st} are varied simultaneously. With the other values corresponding to the initial data set, Fig. 13a,b shows the result for *Aglaophyton*. A large, plain 'floor' represents combinations of C_a and ν_{st} which lead to saturation of photosynthesis, while

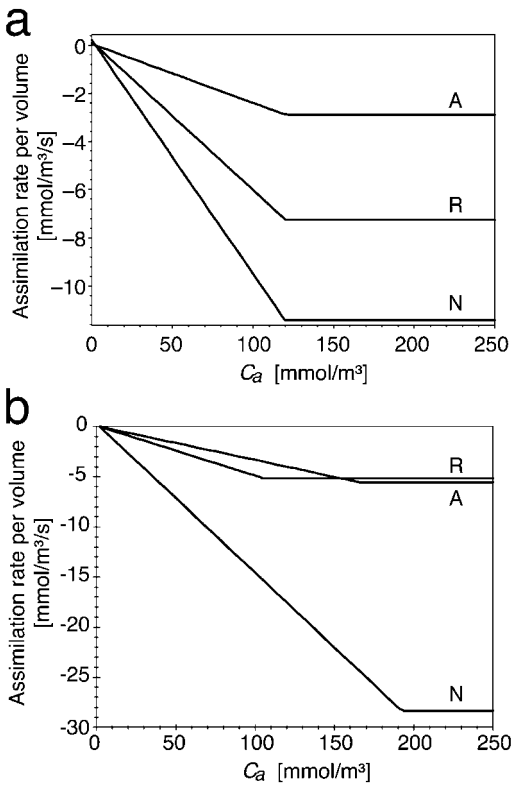

Fig. 12. Sensitivity analysis: assimilation rate per volume plotted against atmospheric CO_2 concentration C_a for *Aglaophyton major* (A), *Rhynia gwynne-vaughanii* (R) and *Nothia aphylla* (N). a: J_{max} and V_{max} of the initial data set (leading to $C_i/C_a = 0.7$). b: J_{max} and V_{max} of an extant plant (*Picea abies*).

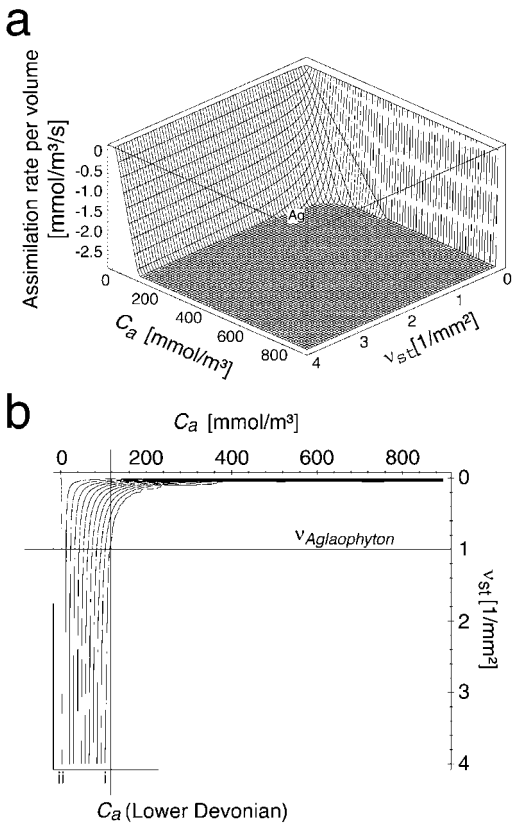

Fig. 13. a: Sensitivity analysis: assimilation rate per volume plotted against atmospheric CO_2 concentration C_a and stomatal density ν_{st} for *Aglaophyton major*. The position of the result obtained with the initial data set is indicated in the graph by the mark 'Ag'. b: Sensitivity analysis: assimilation rate per volume plotted against atmospheric CO_2 concentration C_a and stomatal density ν_{st} for *A. major* in a two-dimensional representation (contour plot). The graph can be described as top view of Fig. 13a. The lines are lines of constant assimilation rate per volume. The lines marked i and ii represent values of assimilation rate per volume of -2.75 mmol/m^3/s and 0 mmol/m^3/s, respectively. Values of adjacent lines differ by 0.25 mmol/m^3/s.

the two 'walls' result from strong variations of the assimilation rate for (C_a,ν_{st})-pairs which are too low to allow for saturation of photosynthesis. For $\nu_{st} \gtrapprox 1.4/mm^2$, saturation is nearly independent of ν_{st} and is given as long as $C_a \gtrapprox 120$ mmol/m^3 is fulfilled. $\nu_{st} \lessapprox 1.4/mm^2$, however, requires increasingly high values of C_a in order to keep photosynthesis saturated. For $C_a \gtrapprox 400$ mmol/m^2, the value of C_a has little influence on saturation, provided $\nu_{st} \gtrapprox 0.1/mm^2$ is satisfied. Variation of the photosynthesis parameters V_{max} and J_{max} changes the positions, where the 'undersaturated' walls raise from the 'saturated' floor, but not the qualitative features of the graph. If, for example, V_{max} and J_{max} of *Picea abies* are used, then $\nu_{st} \gtrapprox 1.5/mm^2$ requires $C_a \approx 160$ mmol/m^3 to saturate photosynthesis, and C_a loses its influence on saturation only for values of $C_a \gtrapprox 650$ mmol/m^2 (again under the premises $\nu_{st} \gtrapprox 0.1/mm^2$). *Rhynia* and *Nothia* show similar behavior.

3.3.4. *Variation of other photosynthesis parameters and chloroplast density*

There are some other parameters, which influence assimilation: the effective conductance through the interior structures of the cortex cells g_{liq}, the specificity factor for Rubisco θ, the irradiance I, the efficiency of light conversion α and the chloroplast surface factor a_{chl}/a_{as}.

In order to find out whether any of these parameters are critical (in the sense, that small deviations from their exact values result in high changes of the results) we performed sensitivity analyses by plotting the assimilation rate as a function of each of these variables while keeping the other variables constant. These graphs (not shown) have several features in common: (1) when the independent variable approaches zero, the assimilation rate disappears as well, (2) the assimilation rate increases continuously with increasing independent variable, and (3) all curves behave asymptotically, i.e. the assimilation rate is saturated for sufficiently high values of the independent variable. According to the positions, which are occupied by the parameter values of the initial data set, we draw the following conclusions: (1) g_{liq} and θ are uncritical, because their initial data set values are positioned on the asymptotic segment of the curves, (2) I and α are 'semi-critical' in the following sense: their initial data set values lie at the 'beginning' of the asymptotic segment, i.e. if their 'true' values would be higher than the values assigned to them in the initial data set, then this error would not influence the assimilation rate, but if the 'true' values would be lower, the initial data set would produce mis-

leadingly high results, (3) the chloroplast surface factor a_{chl}/a_{as} is critical: its initial data set value lies on the segment of the curve which exhibits the steepest gradient.

4. Discussion

4.1. Reliability of input parameters

4.1.1. Humidity, wind speed and temperature

Humidity and wind speed were arbitrarily chosen, because it is very probable that these parameters showed a similar wide range of values during the Lower Devonian as they do today. Humidity (i.e. atmospheric H_2O concentration) influences the results via the transpiration rate, because the evaporative water loss is proportional to the gradient of the water vapor concentration between the intercellular spaces of the plant and the atmosphere (see, for example, Jones, 1992 or Nobel, 1999). More precisely, transpiration rate is a linear function of the atmospheric H_2O concentration C^{H_2O}. In a plot, the two quantities are related by a straight line. The slope of this line depends on the details of the plant morphology. That is, at a given humidity, the studied species lose water at different rates.

The wind speed influences the results via the boundary layer thickness, which decreases with decreasing characteristic dimension (for a cylindrical structure its radius) and increasing wind speed. The boundary layer thickness governs the boundary layer conductance both for gaseous exchange and heat transfer (see review by Schuepp, 1993). The main resistance to gaseous exchange, however, is contributed not by the boundary layer, but by the low stomatal density of rhyniophytic plants, and variation of wind speed has thus a low or even no effect on the gas fluxes through the stomata (see Section 4.2). Convective heat transfer (heat is carried away by air movements), however, does not depend on stomatal conductance and is therefore strongly influenced by wind speed.

The process of heat transfer was not included in the present simulations. We assumed instead from the outset that the temperature of the axis is similar to air temperature. The justification for this assumption is as follows. Heat transfer via convection (sensible heat) and evaporative cooling due to transpiration (latent heat) represent important mechanisms for heat transfer in plants (see, for example, Gates, 1980; Monteith and Unsworth, 1990). Evaporative cooling is, however, of little importance for rhyniopyhtic plants due to the high stomatal resistance leading to low transpiration rates and it is therefore to be expected that convective cooling dominates heat transfer in rhyniophytic plants (Roth-Nebelsick, 2001). During low wind speed or calm air, the temperature of the plant axis, if exposed to direct sunlight, can reach values which are several degrees higher than air temperature (Roth-Nebelsick, 2001). Higher wind speeds ($u_{atm} \gtrapprox 0.5...1$ m/s) lead to effective convective cooling of the cylindrical plant axis, because the intensity of this exchange process varies inversely to the boundary layer thickness, which is small for a body with a low characteristic dimension (Beerling et al., 2001; Roth-Nebelsick, 2001). Thus, under the conditions of the initial data set, the temperature of the rhyniophytic plant axis should approach the air temperature.

4.1.2. Biochemical parameters

All biochemical parameters have to be taken from extant plants. These parameters, together with the chloroplast surface factor (see Section 2.2 and Appendix), represent an outstanding factor of uncertainty. The extent of uncertainty to be faced depends on whether a parameter is 'critical', that is, whether small changes of the parameter have significant influence on the results or not. In the latter case, an accurate knowledge of the value of this parameter is less crucial. Such sensitivity analyses show that the chloroplast surface factor $\{a_{chl}/a_{as}\}$ as well as V_{max} and J_{max} represent critical parameters whereas the other parameters are far less crucial (see Sections 3.3.1, 3.3.4 and Fig. 8).

The values for V_{max} and J_{max} of the initial data set are chosen according to two criteria: they are typical for plants belonging to phylogenetic older groups, such as conifers or cycads. In order to narrow this range, we fine-tuned V_{max} and J_{max}

in such a way, that the ratio between the internal and the external CO_2 concentrations amounts to $C_i/C_a = 0.7$. How reliable this choice is, if applied to rhyniophytic plants, will be discussed in the following.

(1) It is generally assumed that rhyniophytic plants were C_3 plants (Raven, 1993). Furthermore, the properties of photosynthetic enzymes appear to be rather similar among extant plants (Badger and Andrews, 1987; Bowes, 1993). It is therefore to be expected that the kinetic properties of Rubisco in early land plants were similar to those being measured in extant C_3 plants. It appears thus justified to use values of the extant spectrum.

(2) The question arises which values of V_{max} and J_{max} of the extant spectrum should be used. Rhyniophytic plants evolved in an atmosphere with outstandingly higher atmospheric CO_2 concentrations compared to Recent conditions. Under extant atmospheric conditions, the Rubisco of those plants utilizing mechanisms which result in higher CO_2 concentrations at the carboxylation site (such as C_4 and CAM plants or aquatic plants with CO_2 concentrating mechanisms) shows a lower affinity to CO_2 than the Rubisco of C_3 plants with lower CO_2 concentrations at the carboxylation site. It is thus not to be expected that early land plants which evolved under high CO_2 showed assimilation parameters of high performance C_3 plants which evolved under much lower atmospheric CO_2 concentrations. Using values located at the lower range of the extant spectrum thus appears to be justified.

(3) $C_i/C_a = 0.7$ is generally considered as representing a common value among vascular plants (Robinson, 1994; Beerling and Woodward, 1997; Larcher, 1997). Numerous species do actually show this value during photosynthesis (von Caemmerer and Evans, 1991; Franks and Farquhar, 1999). It is, however, not strictly obeyed by plants and in many cases the C_i/C_a ratio can deviate significantly from 0.7 (Farquhar et al., 1989; Franks and Farquhar, 1999). It is not clear whether $C_i/C_a = 0.7$ was also obeyed by early land plants which evolved and existed under completely different external CO_2 concentrations if compared to Recent conditions. Robinson (1994) suggested that steeper gradients of CO_2 from the outside to the intercellular air spaces may have been maintained by plants living under higher atmospheric CO_2 concentrations than today. Nonetheless, applying the $C_i/C_a = 0.7$ criterion to early land plants results in reasonable assimilation rates (see Section 4.3). According to these considerations, we choose the values of V_{max} and J_{max} in the initial data set such that a ratio $C_i/C_a = 0.7$ is maintained. Substituting instead values from *Picea abies* for V_{max} and J_{max} leads in the case of *Rhynia* to a ratio which hardly deviates from $C_i/C_a = 0.7$. For *Aglaophyton* and *Nothia*, however, the *P. abies* values lead to steep CO_2 gradients: the ratios C_i/C_a amount to $C_i/C_a = 0.42$ (*Aglaophyton*) and $C_i/C_a = 0.35$ (*Nothia*), and the assimilation rates are twice as high as is the case for $C_i/C_a = 0.7$ (see Fig. 6). The rather constant values of $\delta^{13}C$ of terrestrial organic matter since the Devonian, however, indicate that the ratio of C_i/C_a was more or less constant through time (Edwards et al., 1998).

4.2. Transpiration of the rhyniophytic axes

Significant differences in transpiration rate exist between the considered taxa (Fig. 4). These differences are only due to anatomical and morphological properties. *Nothia* shows the highest water loss rate due to the high stomatal density and the lack of narrow hypodermal channel underneath the stomata. Relating transpiration rate to surface area, however, does not provide any information about the differences in the degree of water loss in cylindrical plant axes with different radii. With the same transpiration rate per surface area, the parenchyma of a thicker axis loses a smaller fraction of water than the parenchyma of a thinner axis. This is because the volume of a plant axis increases with the radius squared while the transpiring surface area increases proportional to the radius. If the transpiration rate is related to volume, then the transpiration rate of *Aglaophyton* is significantly lower than that for *Rhynia* and much lower than that for *Nothia*. *Aglaophyton* thus shows a significantly more strict water conservation strategy than *Rhynia* and *Nothia*.

The position of the stomata in *Nothia*, on the summits of the emergences, and the surface roughening due to these emergences were interpreted as increasing transpiration rate, because: (1) the exposed position of the stomata would cause the pore to be positioned outside the low velocity region of the boundary layer, and (2) a rough surface promotes a turbulent boundary layer (Kerp et al., 2001). The boundary layer does, however, not represent the main diffusive resistance for gaseous exchange. The following ratios of resistances res (inverse of conductance *S*) are valid for diffusion of both CO_2 and H_2O: (bl = boundary layer, st = stomatal layer, hy = hypodermal layer, if present, as = assimilation layer) $res_{bl}:res_{st}:res_{hy}:res_{as} = 1:5560:1037:7$ for *Aglaophyton*, 1:6166:1144:7 for *Rhynia* and $res_{bl}:res_{st}:res_{as} = 1:73\,682:5$ for *Nothia*. Reducing the boundary layer resistance (i.e. increasing the boundary layer conductance) thus does not influence gaseous exchange significantly, neither in *Aglaophyton* and *Rhynia* nor in *Nothia*. It is therefore improbable that the rough surface of *Nothia* increased gaseous exchange. An unequivocal interpretation of possible functional features of the emergences of *Nothia* is difficult at present. It could be speculated that these structures possibly played a role in heat transfer because heat transfer is (1) mainly independent of stomata and the gas fluxes through them, and (2) sensitive to boundary layer thickness and turbulence.

The strict water-conserving strategy of *Aglaophyton* and – to a lower extent – in *Rhynia* is in accordance with information available about the growth form of these plants. *Aglaophyton* and *Rhynia* do not show massive underground rhizom systems and the ability of *Aglaophyton* and *Rhynia* with respect to water absorption was probably severely restricted despite the fact that both taxa occurred in more humid habitats (there is, for example, evidence that *Aglaophyton* was able to survive flooding events, see Remy and Hass, 1996). Transpiration rate could additionally be decreased by stomatal closure during, for example, periods of high plant-to-air vapor pressure deficits, as shown in Fig. 10b.

The effects of mycorrhizal fungi which are present in many rhyniophytic taxa cannot yet be fully assessed. Mycorrhizal fungi are usually interpreted as improving the nutrient supply as is the case in extant mycorrhizas (Harley and Smith, 1983; Taylor et al., 1992; Taylor and Taylor, 1997). There is evidence that in some cases extant mycorrhizae may contribute also to the water supply of the host plant (Ruiz-Lozano and Azcon, 1995). It is, however, unclear whether this also occurred in rhyniophytic plants to a significant amount.

The role of mycorrhizae on gaseous exchange in rhyniophytic plants – except of decreasing the size of intercellular voids by settlement of fungal hyphae – is difficult to estimate until more studies are made. At any rate, water conservation was very probably of utmost importance for rhyniophytic plants (Edwards et al., 1998).

The higher transpiration rate of *Nothia* (which is still low compared to common transpiration rates of extant plants) is also supported by fossil data. *Nothia* showed an extensive underground rhizom system. This massive rhizomatous system of *Nothia* shows clusters of rhizoids being directly connected to the stele of the aerial axes (Kerp et al., 2001). This indicates that *Nothia* probably had a better water-absorbing capacity than *Aglaophyton* and *Rhynia* and could thus sustain the comparatively high transpiration rate of the aerial system. Additionally, the aboveground axes probably had a short life span and were shedded during unfavorable (dry?) periods whereas *Aglaophyton* and *Rhynia* possessed more long-living axes. This is indicated by the poorer preservation potential of the aerial axes of *Nothia* compared to *Aglaophyton* and *Rhynia*.

4.3. Assimilation of the rhyniophytic axes

With the initial data set, the assimilation rates of *Aglaophyton*, *Rhynia* and *Nothia* (related to projected surface area) are 14.4 μmol/m^2/s (*Aglaophyton*), 16.1 μmol/m^2/s (*Rhynia*) and 23.1 μmol/m^2/s (*Nothia*), respectively. That is, they lie in the lower to middle range of values of net photosynthesis usually found in extant plants (see, for example, Long et al., 1993; Larcher, 1997). Extant plants with very low assimilation rates, such as the ferns *Osmunda regalis* and *Pteridium aquili-*

num, show values in the range 10...12 μmol/m^2/s under optimal conditions (Franks and Farquhar, 1999). Typical values of conifers lie in the range of 6...10 μmol/m^2/s and the morphological and anatomically similar extant species *Psilotum nudum* shows characteristic assimilation rates of 2.5 μmol/m^2/s (Long et al., 1993; Larcher, 1997). The rhyniophytic values are caused by the high external CO_2 concentration leading to saturation of photosynthesis. Calculations carried out by Raven (1993) who also demonstrated that saturated photosynthesis occurred in rhyniophytic plants, arrived at even higher values of about 94 μmol/m^2/s and he described this value as representing a possible maximum. This value is based, however, on maximum photosynthesis rate per exposed internal cell area of extant leaves and is thus not fully comparable to the present approach. Beerling et al. (2001) presented values of about 10 μmol/m^2/s. It is, however, not clear whether these are expressed on a projected surface area basis. The high WUE values of the three taxa which are about 20 times higher than typical WUE values of extant mesophytic plants are due to the low transpiration rates.

More germane to rhyniophytic plants than assimilation per surface area, however, is the CO_2 influx per plant volume. The energetic demand of the plant is not proportional to its surface but to the amount of living tissue and thus to the volume of the plant. The assimilation process has to take place at the peripheral region of the cylinder, because light and gas cannot penetrate further than to a certain depth of the tissue (Niklas, 1997). For the cylindric shape, the volume (proportional to the amount of energy consuming tissue) increases with the radius squared while the surface (proportional to the amount of energy producing assimilation tissue) increases proportional to the radius (see also Section 4.2). The energy-consuming volume thus increases stronger with radius than the energy producing surface. If assimilation rates obtained with the initial data set are represented as rates per volume then *Aglaophyton* shows the lowest and *Nothia* the highest value (see Fig. 5).

In the case of *Aglaophyton* and *Rhynia*, the assimilation rates obtained during the calculations appear to be more than sufficient for maintaining the plants since both taxa show neither an extensive rhizome system which has to be supported by the aerial axes nor costly support tissues, because rhyniophytic plants were turgor-stabilized (Speck and Vogellehner, 1988). In perennial plants, half of the carbohydrate products are consumed by the root system and by building tissues for structural support (Givnish, 1979; Raich and Nadelhoffer, 1989). *Nothia* shows a massive rhizom system representing a carbohydrate sink which indicates a demand for higher assimilation rate in *Nothia*. Moreover, the apparently seasonal occurrence of the aerial axes of *Nothia* can be interpreted as intensifying a demand for their high productivity. That *Nothia* exhibits in all cases the highest assimilation rate is therefore corroborated by information provided by the fossil record.

For all three taxa, saturation of photosynthesis was probably important in order to obtain sufficient carbohydrate gain. Saturation of photosynthesis is dependent on: (1) the external CO_2 concentration, and (2) anatomical parameters, mainly stomatal density ν_{st}. It is obvious from Fig. 9a (assimilation rate per volume plotted against d_{hc} and ν_{st}) that with the initial data set (and also with the *Picea abies* set of J_{max} and V_{max}) the (calculated) threshold values of ν_{st} leading to saturated photosynthesis in *Aglaophyton* are close to their actual stomatal densities which are obtained from fossilized specimen. Decreasing ν_{st} significantly would strongly decrease the assimilation rate, because photosynthesis would no longer be saturated. Fig. 11 shows that the WUE value of the initial data set is seated at the beginning of the steep flank leading to maximum WUE. In the light of Fig. 10a (showing transpiration rate plotted against d_{hc} and ν_{st}), the 'actual' stomatal density of *Aglaophyton* appears to represent a compromise between transpiration and assimilation, leading to an optimized gaseous exchange. Simulation of stomatal closure for *Aglaophyton* demonstrated that – with the initial data set – transpiration can be strongly reduced by closing the stomatal pore while assimilation remains largely unaffected (Figs. 9b and 10b). Actual WUE values could thus be even larger in rhyniophytic plants, with photosynthesis being saturated.

Fig. 13a,b shows that saturation can be achieved over a wide range of combinations of C_a and v_{st} values. Higher C_a values than in the initial data set allow lower values of v_{st} while assimilation stays saturated. It is usually difficult to detect stomata on fossilized axes of early land plants dating further back than to the Lower Devonian (Edwards, 1998). Since the atmospheric CO_2 content during the Silurian was even higher than during the Lower Devonian (Berner and Kothvala, 2001), the results summarized in Fig. 13a,b suggest that plant axes of this ancient age could survive with a very low stomatal density, drastically reducing the probability of their detection. Fig. 13a,b also shows that decreasing C_a leads eventually to a regime in which a strong increase in v_{st} is necessary in order to allow for saturated photosynthesis. The strong decrease of atmospheric CO_2 content during the Middle Devonian may thus be involved in the disappearance of rhyniophytic plants during this time period, because they were probably not able to adapt their stomatal densities to these new conditions.

The results summarized so far indicate that the actual values of stomatal density (together with the depth of the hypodermal channels, if present) represent a fine-tuning of gaseous exchange which integrates maximum carbon gain and minimum transpiration rate to a compromise solution of optimized gas fluxes. This optimum also reflects the limited capacity of water absorption in rhyniophytic plants. Rhyniophytic plants represent an ancient construction originating in the colonization process of terrestrial environments by green plants (Edwards, 1998). The low and optimized values of gaseous exchange are very probably a consequence of the restricted water-absorbing capacity, and it is therefore possible that the high atmospheric CO_2 concentrations were required in order to 'permit' the evolution of upright terrestrial plants (Edwards et al., 1998). On the one hand, rhyniophytic plants were, as indicated by the results, excellently adapted to early Paleozoic conditions. On the other hand, the high atmospheric CO_2 conditions were probably the fundamental precondition for the evolution of the rhyniophytic habit.

4.4. Implications of the results for atmospheric CO_2 concentration of the Lower Devonian

The structure of Fig. 13a – an extended plain lowland representing saturated photosynthesis framed on two sides by the continuously ascending slopes of undersaturated photosynthesis – contributes additional information for determining the CO_2 concentration of the Lower Devonian atmosphere.

Consider a hypothetical plant X with stomatal density v_X living in an atmosphere with CO_2 concentration C_X. If the values of v_X and C_X give X a position somewhere within the 'lowland of saturation', X has reached its optimum conditions with respect to assimilation. Its performance with respect to transpiration, however, would obviously be better at smaller values of v_X, as can be seen from Fig. 11. Therefore, we may expect that X exhibits a tendency to occupy a position with as low v_X values as possible without impairing photosynthesis saturation. This evolutionary optimum is obviously realized by a v_X value on the borderline between the 'lowland of saturation' and the 'slopes of undersaturated photosynthesis'.

In order to determine the CO_2 concentration of the Lower Devonian atmosphere from the known stomatal density $v_{rhyniophyte}$ of the rhyniophytes, we can turn this argument around (see Fig. 13b): on the premises that the rhyniophytes were well adapted to their environment the Lower Devonian CO_2 concentration can be found from the position where a straight line at $v_{st} = v_{rhyniophyte}$ parallel to the abscissa intersects the borderline separating saturated and undersaturated photosynthesis. This 'cut' through Fig. 13b is represented by Fig. 12a. The shape and extent of the area of saturated photosynthesis in Fig. 13a,b depend, however, on the choice of the assimilation parameters, especially of J_{max} and V_{max}. The sensitivity analysis described in Section 3.3.1 demonstrates the effects of changing J_{max} and V_{max}. In this sensitivity study, values of J_{max} and V_{max} of an extant plant (*Picea abies*) were inserted (effect on assimilation shown by Figs. 6 and 12b); then the construction just given leads to three different optimum values for the atmospheric CO_2 concentration: $C_a \approx 166$ mmol/

m^3 (*Aglaophyton*), $C_a \approx 193$ mmol/m^3 (*Nothia*) and $C_a \approx 106$ mmol/m^3 (*Rhynia*, see Fig. 12b). In this case, the range of plausible atmospheric CO_2 concentrations is thus $C_a \approx 106...193$ mmol/m^3. The assimilation parameters of *Picea* result, however, in extremely low values of C_i/C_a: 0.42 for *Aglaophyton* and 0.35 for *Nothia*. It is therefore reasonable to assume that the values of the initial data set which result in $C_i/C_a = 0.7$ represent a good approximation. If we thus impose – in view of the discussion in Section 4.1.2 – the initial data set in order to fine tune the values of J_{max} and V_{max}, then we obtain $C_a \approx 120$ mmol/m^3 which is about 8.5 times the Recent value. It is lower than the value provided by the standard curve of R_{CO_2} returned by GEOCARBIII, which is about 12 times the Recent value (Berner and Kothvala, 2001). McElwain (1998) provided two estimations of atmospheric CO_2 of the Lower Devonian based on stomatal densities of the Lower Devonian plants *Sawdonia ornata* and *Aglaophyton major*: the first one amounts to a range $R_{CO_2} = 7...10$ (by using a 'Recent standard') and the second one gives a range $R_{CO_2} = 9.5...12.5$ (by using a 'Carboniferous standard'). The estimation obtained by the present contribution is thus seated within the first range. It should, however, be noted that the method applied by McElwain (1998) is based on producing ratios between the stomatal densities of the fossil taxon and an extant plant species termed 'NLE' (nearest living equivalent) whose ecological and structural properties are claimed to be similar to those of the fossil taxon. Additionally, the value of stomatal density of *Aglaophyton* which were used by McElwain (1998) ($\nu_{st} = 4.5/mm^2$) is much higher than the stomatal density which was applied in this contribution (McElwain and Chaloner, 1995; McElwain, 1998, see also Edwards et al., 1998). The data of stomatal density available so far show some variation. As indicated in Table 2, the anatomical parameters provided by Edwards et al. (1998) and Kerp et al. (2001) as well as their data on stomatal density were used in order to create a consistent data set. A direct comparison of the present results and the results of McElwain (1998) thus appears to be problematic.

5. Conclusions

(1) The three considered taxa differ in transpiration and assimilation rate and show the following order of increasing gaseous exchange provided the condition $C_i/C_a = 0.7$ is applied: *Aglaophyton major* < *Rhynia gwynne-vaughanii* < *Nothia aphylla*. The transpiration rates of all three taxa are markedly lower than the rates which are usually attained by extant plants. The assimilation rates are seated at the lower to middle range of the extant spectrum due to photosynthesis saturation under Lower Devonian CO_2 concentrations.

(2) The fact that *Nothia aphylla* shows the highest rates of gaseous exchange is consistent with the fact that this species developed a massive rhizom system which represented very probably a carbon sink on one hand while providing a much better source of water supply than was present in *Aglaophyton major* and *Rhynia gwynne-vaughanii* on the other hand. The fossil evidence of seasonally shedding of the aerial axes of *N. aphylla* additionally indicates a demand for higher productivity of these axes during their lifetime.

(3) The protuberances at the axis surface of *Nothia aphylla* did not increase gaseous exchange.

(4) The differences in gaseous exchange of the three taxa thus probably reflect differences in their lifestyles and ecophysiological properties.

(5) The results indicate on one hand that the construction of rhyniophytic plants is strongly adapted to a high atmospheric CO_2 concentration by producing optimized gaseous exchange. This means, however, on the other hand that the evolution and existence of rhyniophytic plants – and therefore the prototype of land plants with an upright posture – was dependent on such high CO_2 concentrations.

(6) The results concerning interrelationship between fine-tuning of gaseous exchange, assimilation rate, anatomical properties and external CO_2 concentration suggest that the Lower Devonian CO_2 concentration amounted roughly to about $C_a \approx 120$ mmol/m^3.

6. Glossary

see also Tables 1–3.

Environmental and physical parameters and constants

A	assimilation rate per volume
C	gas concentration
C_i	intercellular CO_2 concentration
C_a	atmospheric CO_2 concentration
C^{CO_2}	atmospheric CO_2 concentration
C^{H_2O}	atmospheric H_2O concentration, humidity
D	free air diffusional constant
D^{CO_2}	free air diffusional constant for CO_2
D^{H_2O}	free air diffusional constant for H_2O
d_{bl}	thickness of boundary layer
grad	gradient operator
$\vec{j}$	diffusional gas flux
j^{CO_2}	assimilation rate per area
j^{H_2O}	transpiration rate per area
I	irradiance
l	path length
l_e	path length around hindrance
n	porosity
Q	gas sink
r	radial coordinate
R_{CO_2}	fossil CO_2 concentration/Recent CO_2 concentration
R_{gas}	universal gas constant
S	effective conductance
$S_\odot$	solar constant
τ	tortuosity
T	absolute temperature
$\mathcal{T}$	transpiration rate per volume
u_{atm}	wind velocity

Anatomical and morphological parameters

A	total leaf surface
A^{chl}	total area of all chloroplasts
A^{mes}	total area of all mesophyll cells
a_{as}	surface of cortex cell
a_{chl}	surface of all chloroplasts in a cell
A_η	surface of a chloroplast
a_{st}	area of stomatal pore
d_{st}	depth of stomatal pore
d_{hc}	length of hypodermal channel
h_{hc}	long axis of hypodermal channel
L	axis length
n_{as}	porosity of assimilation layer
n_{st}	porosity of stomatal layer
R	radius of plant axis
R_c	length of longer axis of chloroplast
V	tissue volume
V_p	tissue pore volume
η	ratio of chloroplast thickness and chloroplast length
v_{as}	volume of cortex cell
w_{hc}	short axis of hypodermal channel
v_{st}	stomatal density
ρ	effective pore radius
σ	radius of cortex cell
τ_{st}	tortuosity of stomatal layer

Photosynthesis parameters

g_{liq}	effective conductance through a cortex cell
J	current of molecules
j	flux into plant surface
j_{as}	flux into assimilating tissue
j_{chl}	flux into chloroplast
$J(I)$	potential rate of electron transport
J_{max}	light-saturated rate of electron transport
K_c	Michaelis–Menten constant of carboxylation
K_o	Michaelis–Menten constant of oxygenation
p_o	Partial pressure of oxygen at assimilating site
q	partial pressure of CO_2 at assimilating site
V_{max}	local maximum carboxylation rate
W_c	carboxylation rate limited by Rubisco activity
W_j	carboxylation rate limited by Rubisco regeneration
α	efficiency of light conversion
θ	specificity factor of Rubisco

Acknowledgements

This work was supported by the German Science Foundation (DFG: Mo 412/13;c-1). We want to thank H. Kerp and H. Hass for many helpful discussions and J.H. Nebelsick for critically reading the English manuscript.

Appendix A

A.1. Photosynthesis model

The CO_2 flux into chloroplasts, j_{chl}, is given by

$$j_{chl}(q,I) = \left(1-\frac{p_o}{2\theta q}\right)\min\{W_c(q), W_j(q,I)\} \quad (5)$$

with

$$W_c(q) := V_{max}\frac{q}{q+K_c\left(1+\frac{p_o}{K_o}\right)}$$

$$W_j(q,I) := J(I)\frac{q}{4\left(q+\frac{p_o}{\theta}\right)} \quad (6)$$

and

$$J(I) := = \frac{\alpha I}{\sqrt{1+\left(\frac{\alpha I}{J_{max}}\right)^2}} \quad (7)$$

where q stands for the partial pressure of CO_2 and p_o for the local O_2 concentration (the various other parameters are listed in Table 3 and in the glossary).

The expression $\min\{W_c(q), W_j(q,I)\}$ denotes the smaller of $W_c(q)$ (carboxylation rate limited by the activity of Rubisco) and $W_j(q,I)$ (carboxylation rate limited by regeneration of Rubisco via electron transport).

j_{chl} is connected to Q by the following equation:

$$Q = -\left(\frac{a_{chl}}{a_{as}}\right)\left(\frac{a_{as}}{v_{as}}\right)(1-n_{as})j_{chl}(q,I) \quad (8)$$

with the ratio a_{chl}/a_{as} between the sum of the surfaces of all chloroplasts within one cortex cell to the surface a_{as} of this cell (termed 'chloroplast surface factor' throughout the text), the porosity n_{as} of the assimilation layer and a_{as}/v_{as} as the surface-to-volume ratio of a typical cortex cell. Eq. 8 thus states that the sink is produced by the chloroplast layer located at the periphery of a cortex cell. A final step is required which converts the partial pressure q of CO_2 inside the chloroplasts in Eq. 7 into the CO_2 concentration $C(r)$ in the intercellular air spaces (Parkhurst and Mott, 1990):

$$j_{chl} = g_{liq}(C(r)R_{gas}T - q) \quad (9)$$

where R_{gas} represents the universal gas constant, T the absolute temperature and g_{liq} the effective conductance through the interior structures of the cortex cells (see Fig. 14 for a schematic overview of the model).

A.2. Boundary layer

The thickness of the boundary layer (air layer with reduced wind velocity) adjacent to the axis surface is determined according to an approximation provided by Nobel, 1999:

$$d_{bl} = 5.8\ mm\sqrt{\frac{2R}{u_{atm}}\frac{1}{s}} \quad (10)$$

with d_{bl} the thickness of boundary layer, R the radius of the plant axis, and u_{atm} the wind velocity.

A.3. Stomatal layer

Permineralized specimen of *Aglaophyton*, *Nothia* and *Rhynia* provide the necessary anatomical data: average area of stomatal pore a_{st}, depth of stomatal pore d_{st} and number of stomata per unit surface v_{st}. These parameters are used in order to calculate porosity n_{st} and tortuosity τ_{st} of the stomatal layer:

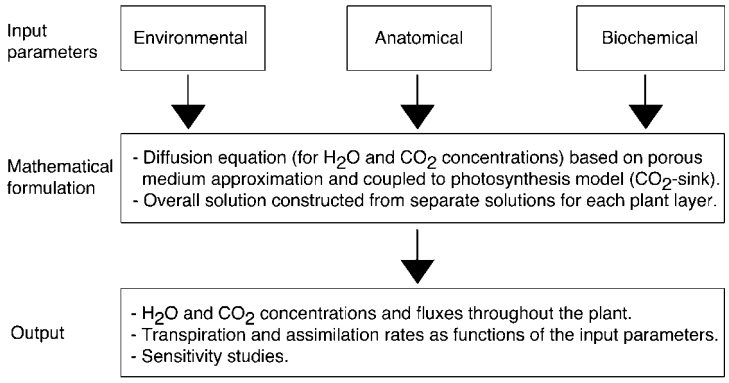

Fig. 14. Schematic overview of the model.

$$n_{st} = a_{st} v_{st} \tag{11}$$

$$\tau_{st} = 1 + \frac{\rho_{st}}{d_{st}} \tag{12}$$

with ρ_{st} the effective pore radius (see Nobel, 1999). The tortuosity stems from the fact that lines of equal concentration within the boundary layer bulge out over the stomata so that molecules diffusing out of the stomata still experience stomatal conditions although they have already left the stomatal layer (Nobel, 1999).

A.4. Hypodermal layer

A hypodermal layer is included in the system, if hypodermal channels are present. These structures are narrow channels beneath the stomata and can be found in *Aglaophyton* and *Rhynia*. *Nothia* has substomatal chambers. Hypodermal channels are elliptical in cross-section with a longer axis h_{hc} and a shorter axis w_{hc}. Their number equals the number of stomata. The porosity of the hypodermal layer reads as:

$$n_{hy} = \frac{\pi}{4} h_{hc} w_{hc} v_{st} \frac{2R - d_{st}}{2R - (2d_{st} + d_{hy})} \tag{13}$$

A.5. Assimilation layer

It is generally assumed that assimilation took place mainly in the outer cortex (see, for example, Edwards et al., 1998). The assimilation layer is therefore represented by the outer cortex layer. Measurements carried out by using methods of image processing on thin slices of fossil material yield an average value for porosity of $n_{as} = 0.35$ for all three taxa. For measured thickness values of the outer cortex layer of the three taxa see Table 2. In order to calculate the tortuosity τ_{as}, a rough approximation is applied: a molecule diffusing around a cell has to move along a half circular path with a distance r to the cell center. The pathlength l_e amounts to $l_e = r$ and the direct travel distance is $l = 2r$. The tortuosity is therefore given by:

$$\tau_{as} = \frac{l_e}{l} = \frac{\pi}{2} \approx 1.57 \tag{14}$$

The specific surface (a_{as}/v_{as}) of a long cylindrical cortex cell with radius σ reads as:

$$\left(\frac{a_{as}}{v_{as}}\right) = \frac{2}{\sigma} \tag{15}$$

The ratio (a_{chl}/a_{as}) represents the sum of the surfaces of all chloroplasts a_{chl} within one cortex cell to the surface a_{as} of this cell. In a sense this value thus describes how much space of a cell is occupied by chloroplasts. The value is determined by two factors: (1) the orientation of the chloroplasts in the cell, and (2) the degree of (inner) surface occupation of the cell by chloroplasts. Typical chloroplasts of land plants are similar to oblate spheroids. The surface of a chloroplast is then provided by

$$A_\eta = 2\pi R_c^2 + \pi R_c^2 \frac{\eta^2}{\sqrt{1-\eta^2}} \ln\left(\frac{1+\sqrt{1-\eta^2}}{1-\sqrt{1-\eta^2}}\right) \quad (0 \le \eta \le 1) \tag{16}$$

with R_c the length of the spheroid's longer axis and η the ratio of chloroplast thickness to chloroplast length. The shorter axes of typical chloroplasts of land plants are about half as long as their two longer axes. If the inner surface of a cortex cell would be completely occupied by these chloroplasts, CO_2 diffusing into one chloroplast would have to diffuse through a cortex cell area of πR_c^2. The ratio (a_{chl}/a_{as}) would then be given by (a_{chl}/a_{as}) = 2.760. Chloroplasts in land plants differ in size. Typical values are, according to Moore et al., 1998, 4...8 μm for the chloroplast diameter and 2...3 μm for the chloroplast thickness (see also Raven, 1993). We adopt the mean values of these two intervals and arrive at (a_{chl}/a_{as}) = 2.606 for $\eta = 0.429$. The inner cell surfaces of cells containing chloroplasts are, however, not completely occupied by these cell organelles. According to Parkhurst and Mott, 1990, a value of 90% which is typical for mesophyll cells of extant leaves is adopted. A value of

$$(a_{chl}/a_{as}) = 2.3454 \tag{17}$$

thus results which was used in the calculations.

A.6. V_{max} and J_{max}

Values of V_{max} and J_{max} provided in the literature cannot be applied directly, because the fluxes usually given are related to a fictitious external leaf area far away from the chloroplasts. In order to be used within the framework of our calculations, values from the literature have to be corrected for the actual A^{mes}/A values of the rhyniophytic plant. V_{max} and J_{max} are thus redefined according to the following considerations. Consider a current of molecules J diffusing into or out of the chloroplasts under stationary conditions. A^{chl}, A^{mes} and A represent the total areas of chloroplasts, of all mesophyll cells and of the total leaf surface. If the corresponding fluxes – the symbol j stands for either V_{max} or J_{max} – are defined by

$$j_{chl} := \frac{J}{A^{chl}} \quad j_{mes} := \frac{J}{A^{mes}} \quad j := \frac{J}{A} \tag{18}$$

then elimination of J results in

$$j_{chl} A^{chl} = j_{mes} A^{mes} = jA \tag{19}$$

and thus

$$j_{chl} = j\left(\frac{A}{A^{chl}}\right) = j\left(\frac{A}{A^{mes}}\right)\left(\frac{A^{mes}}{A^{chl}}\right) \tag{20}$$

Since $(A^{chl}/A^{mes}) = (a_{chl}/a_{as})$, we conclude

$$j_{chl} = j\left(\frac{A}{A^{mes}}\right)\left(\frac{a_{as}}{a_{chl}}\right) \tag{21}$$

Own measurements of (A^{mes}/A) provided a value of $(A^{mes}/A) = 10$ and $(a_{chl}/a_{as}) = 2.3454$ has been calculated above. The local values of V_{max} and J_{max} can now be obtained by substituting the appropriate literature data of V_{max} or J_{max} for j on the right hand side of Eq. 21.

A.7. Irradiance

The value of the Recent solar constant $S_\odot$ amounts to $S_\odot = 1360$ W/m^2 (see, for example, Nobel, 1999). About 45% of this amount is absorbed in the upper atmospheric layers or reflected back into space. On a global average, 55% thus reaches the earth's surface. About 45% of this amount of radiation is within the range of photosynthetically valuable wavelengths.

If the sun is elevated above the horizon by an angle Θ, the projective absorption area of an upright plant axis with a radius of R and a height of L is given by $2RL \cos \Theta$. On distributing the impinging light evenly onto the telome surface $2\pi RL$, the factors R and L drop out and the number I_Θ of photons reaching the axis per unit time and unit axis area is given by:

$$I_\Theta = \cos \Theta \times 877 \frac{\mu\text{mol}}{\text{m}^2\ \text{s}} \tag{22}$$

Assuming $\Theta = 45°$ and taking into account differences in the inner structures of *Aglaophyton*, *Rhynia* and *Nothia*, we arrive at an expression between I_Θ and the number I of photons at the assimilating sites per unit time and unit area, which is similar to the one obtained above for the relation between j and j_{chl}:

$$I = I_\Theta \left(\frac{A}{A^{mes}}\right)\left(\frac{a_{as}}{a_{chl}}\right) \tag{23}$$

References

Aphalo, P.J., Jarvis, P.G., 1993. An analysis of Ball's empirical model of stomatal conductance. Ann. Bot. 72, 321–327.

Badger, M.R., Andrews, T.J., 1987. Co-evolution of Rubisco and CO_2 concentrating mechanisms. In: Biggins, J. (Ed.), Progress in Photosynthesis Research. Martinus Nijhoff, Dordrecht, pp. 501–609.

Ball, J.T., Woodrow, I.E., Berry, J.A., 1987. A model predicting stomatal conductance and its contribution to the control of photosynthesis under different environmental conditions. Biggins, J. (Ed.), Progress in Photosynthesis Research. Martinus Nijhoff, Dordrecht, pp. 221–224.

Bateman, R.M., Crane, P.R., DiMichele, W.A., Kenrick, P., Rowe, N.P., Speck, T., Stein, W., 1998. Early evolution of land plants: phylogeny, physiology, and ecology of the primary terrestrial radiation. Annu. Rev. Ecol. Syst. 29, 263–292.

Becker, M., Kerstiens, G., Schönherr, J., 1986. Water permeability of plant cuticles: permeance, diffusion and partition coefficients. Trends Ecol. Evol. 1, 54–60.

Beerling, D.J., Woodward, F.I., 1995. Leaf stable carbon isotope composition records increased water-use efficiency of C_3 plants in response to atmospheric enrichment. Funct. Ecol. 9, 394–401.

Beerling, D.J., Woodward, F.I., 1997. Changes in land plant function over the Phanerozoic: reconstructions based on the fossil record. Bot. J. Linn. Soc. 124, 137–153.

Beerling, D.J., Osborne, C.P., Chaloner, W.G., 2001. Evolution of leaf from in land plants linked to atmospheric CO_2 decline in the late Palaeozoic era. Nature 419, 352–354.

Berner, R.A., Kothvala, Z., 2001. GEOCARBIII: A revised model of atmospheric CO_2 over Phanerozoic time. Am. J. Sci. 301, 182–204.

Bowes, G., 1993. Facing the inevitable: Plants and increasing atmospheric CO_2. Annu. Rev. Plant Physiol. Plant Mol. Biol. 44, 309–332.

Cowan, I.R., Farquhar, G.D., 1977. Stomatal function in relation to leaf metabolism and environment. Symp. Soc. Exp. Biol. 31, 471–505.

Edwards, D., 1993. Tansley Review No. 53. Cells and tissues in the vegetative sporophytes of early land plants. New Phytol. 125, 225–247.

Edwards, D., 1998. Climate signals in Palaeozoic land plants. Philos. Trans. R. Soc. London Ser. B 353, 141–157.

Edwards, D., Abbott, G.D., Raven, J.A., 1996. Cuticles of early land plants: a palaeoecophysiological evaluation. In: Kerstiens, G. (Ed.), Plant Cuticles, an Integrated Functional Approach. ios Scientific Publishers, Oxford, pp. 1–31.

Edwards, D., Kerp, H., Hass, H., 1998. Stomata in early land plants: an anatomical and ecophysiological approach. J. Exp. Bot. 49, 255–278.

Edwards, D., Morel, E., Poiré, D.G., Cingolani, C.A., 2001. Land plants in the Devonian Villaricencio Formation, Mendoza Province, Argentina. Rev. Palaeobot. Palynol. 116, 1–18.

Farquhar, G.D., von Caemmerer, S., Berry, J.A., 1980. A biochemical model of photosynthetic CO_2 assimilation in leaves of C_3 species. Planta 149, 78–90.

Farquhar, G.D., Ehleringer, J.R., Hubick, K.T., 1989. Carbon isotope discrimination and photosynthesis. Annu. Rev. Plant Physiol. Plant Mol. Biol. 40, 503–537.

Franks, P.J., Farquhar, G.D., 1999. A relationship between humidity response, growth form and photosynthetic operating point in C_3 plants. Plant Cell Environ. 22, 1337–1349.

Gates, D.M., 1980. Biophysical Ecology. Springer Verlag, New York.

Gerrienne, P., Bergamaschi, S., Pereira, E., Rodrigues, M.-A.C., Steemans, P., 2001. An Early Devonian flora, including *Cooksonia*, from the Parana' Basin (Brazil). Rev. Palaeobot. Palynol. 116, 19–38.

Givnish, T.J., 1979. On the adaptive significance of leaf form. In: Solbrig, O.T., Jain, S., Johnson, G.B., Raven, P.H. (Eds.), Topics in Plant Population Biology. Columbia University Press, New York, pp. 375–473.

Harley, P.C., Sharkey, T.D., 1991. An improved model of C_3 photosynthesis at high CO_2: Reversed O_2 sensitivity explained the lack of glycerate re-entry into the chloroplast. Photosynth. Res. 27, 169–178.

Harley, J.L., Smith, S.S., 1983. Mycorrhizal Symbiosis. Academic Press, New York.

Harley, P.C., Thomas, R.B., Reynolds, J.F., Strain, B.R., 1992. Modelling the photosynthesis of cotton grown in elevated CO_2. Plant Cell Environ. 15, 271–282.

Jones, H.G., 1992. Plants and Microclimate. Cambridge University Press, Cambridge.

Kenrick, P., Crane, P.R., 1997. The origin and early diversification of land plants: a cladistic study. Smithsonian Series in Comparative Evolutionary Biology. Smithsonian Institution Press, Washington, DC.

Kerp, H., Hass, H., Mosbrugger, V., 2001. New data on Nothia aphylla Lyon, 1964 ex El Saadawy et Lacey, 1979: a poorly known plant from the Lower Devonian Rhynie Chert. In: Gensel, P.G., Edwards, D. (Eds.), Plants Invade the Land: Evolutionary and Environmental Perspectives. Columbia University Press, Columbia, pp. 52–82.

Kerstiens, G., 1996. Cuticular water permeability and its physiological significance. J. Exp. Bot. 47, 1813–1832.

Kirschbaum, M.U.F., Farquhar, G.D., 1984. Temperature dependence of whole leaf photosynthesis in *Eucalyptus pauciflora* Sieb. ex Spreng. Aust. J. Plant Physiol. 11, 519–538.

Konrad, W., Roth-Nebelsick, A., Kerp, H., Hass, H., 2000. Transpiration and assimilation of Early Devonian land plants with axially symmetric telomes – simulations on the tissue level. J. Theor. Biol. 206, 91–107.

Kramer, P.J., 1983. Water Relations of Plants. Academic Press, New York.

Kürschner, W.M., 1996. Leaf stomata as biosensors of palaeoatmospheric CO_2 levels. Ph.D. thesis, Utrecht.

Larcher, W., 1997. Physiological Plant Ecology, 3rd edn. Springer Verlag, New York.

Long, S.P., Postl, W.F., Bolhár-Nordenkampf, H.R., 1993. Quantum yields for uptake of carbon dioxide in C_3 vascular plants of contrasting habitats and taxonomic groups. Planta 189, 226–234.

McElwain, J.C., 1998. Do fossil plants signal palaeoatmospheric CO_2 concentration in the geological past? Philos. Trans. R. Soc. London Ser. B 353, 83–96.

McElwain, J.C., Chaloner, W.G., 1995. Stomatal density and index of fossil plants track atmospheric carbon dioxide in the Palaeozoic. Ann. Bot. 76, 389–395.

Monteith, J.L., Unsworth, M.H., 1990. Principles of Environmental Physics. Edward Arnold, London.

Moore, R., Clark, W.D., Vodopich, D.S., 1998. Botany. McGraw-Hill, Boston.

Niklas, K.J., 1997. The Evolutionary Biology of Plants. University of Chicago Press, Chicago, IL.

Niklas, K.J., Kerchner, V., 1984. Mechanical and photosynthetical constraints on the evolution of plant shape. Paleobiology 10, 79–101.

Nobel, P.S., 1999. Physicochemical and Environmental Plant Physiology, 2nd edn. Academic Press, New York.

Parkhurst, D.F., 1994. Tansley Review No. 65. Diffusion of CO_2 and other gases inside leaves. New Phytol. 126, 449–479.

Parkhurst, D.F., Mott, K.A., 1990. Intercellular diffusion limits to CO_2 uptake in leaves. Plant Physiol. 94, 1024–1032.

Raich, J.W., Nadelhoffer, K.J., 1989. Belowground carbon allocation in forest ecosystems: Global trends. Ecology 70, 1254–1346.

Raven, J.A., 1984. Physiological correlates of the morphology of early vascular plants. Bot. J. Linn. Soc. 88, 105–126.

Raven, J.A., 1993. The evolution of vascular plants in relation to quantitative functioning of dead water-conducting cells and stomata. Biol. Rev. 68, 337–363.

Remy, W., Hass, H., 1996. New information on gametophytes and sporophytes of Aglaophyton major and inferences about possible environmental adaptations. Rev. Palaeobot. Palynol. 90, 175–193.

Robinson, J.M., 1994. Speculations on carbon dioxide starvation, Late Tertiary evolution of stomatal regulation and floristic modernization. Plant Cell Environ. 17, 345–354.

Roth-Nebelsick, A., 2001. Heat transfer of rhyniophytic plant axes. Rev. Palaeobot. Palynol. 116, 109–122.

Ruiz-Lozano, J.M., Azcon, R., 1995. Hyphal contribution to water uptake in mycorrhizal plants as affected by the fungal species and water status. Physiol. Plant. 95, 472–478.

Schuepp, P.H., 1993. Tansley Review No. 59. Leaf boundary layers. New Phytol. 125, 477–507.

Speck, T., Vogellehner, D., 1988. Biophysical examinations of the bending stability of various stele types and the upright axes of early 'vascular' plants. Bot. Acta 101, 262–268.

Stewart, W.N., Rothwell, G.W., 1993. Palaeobotany and the Evolution of Plants, 2nd edn. Cambridge University Press, Cambridge.

Taylor, T.N., Remy, W., Hass, H., 1992. Fungi from the Lower Devonian Rhynie Chert: Chytridiomycetes. Am. J. Bot. 79, 1233–1241.

Taylor, T.N., Taylor, E.L., 1997. The distribution and interactions of some Paleozoic fungi. Rev. Palaeobot. Palynol. 95, 83–94.

von Caemmerer, S., Evans, J.R., 1991. Determination of the average partial pressure of CO_2 in chloroplasts from leaves of several C_3 plants. Aust. J. Plant Physiol. 18, 287–306.

Wullschleger, S.D., 1993. Biochemical limitations to carbon assimilation in C_3 plants – a retrospective analysis of the A/C_i curves from 109 species. J. Exp. Bot. 44, 907–920.

Zimmermann, W., 1959. Die Phylogenie der Pflanzen. Fischer, Stuttgart.

5.6 Konrad, W., Roth-Nebelsick, A.: *Stomatal density response to atmospheric CO_2 derived from an optimisation principle: Implications for reconstructing palaeoatmospheric CO_2*, to be submitted to Journal of Theoretical Biology.

The manuscript of this article is *in statu nascendi*. It contains the material of sections 3.4 through 3.7 in condensed form.

6 Epilogue

6.1 Please reconsider, I think you will find that reality is much overrated.

Mit dieser Bemerkung quittiert Commander Bradshaw (der im übrigen glücklich mit einer Berggorilladame verheiratet ist) die Aufforderung, der Realität hinkünftig größeres Gewicht zuzugestehen (siehe [29]).

Wissenschaftliche Theorien changieren zwischen Realität und Imagination: Manche stellen eine glatte, klare Trennfläche zwischen beiden Bereichen dar. Bei anderen Theorien präsentiert sich diese Trennfläche als schwer überschaubares, in sich verschlungenes und gefälteltes Gebilde, das eher den Charakter eines fließenden Überganges zwischen Realität und Imagination hat. Diese Uneindeutigkeit hat ihren Reiz und ist wissenschaftlich auch nicht weiter bedenklich, so lange die mathematisch-quantitative Version einer Theorie Vorhersagen liefert, welche sich experimentell überprüfen lassen.

Nach Kindheit und Schulzeit wußte ich zunächst nicht, womit ich mich beschäftigen sollte. Da das Leben trotzdem weitergeht, fand ich mich nach einiger Zeit zunächst im Physikstudium und schliesslich im extraterrestrischen Teil des frühen Universums wieder, ohne daß ich recht erklären konnte, wie ich dorthin gekommen war. Jedenfalls versuchte ich dort, mit Hilfe unendlich dünner Hohlkugeln allgemein-relativistische Sternmodelle zu bauen, was auch leidlich gelang. Da Raumzeit und Hilbertraum — bei aller Schönheit der ihnen innewohnenden Mathematik — auf die Dauer doch etwas karge, unwirtliche Orte sind, begann ich, mich dem ästhetisch zwar weniger vollkommenen, letztlich aber doch lebensfroheren Hier und Jetzt zu nähern.

Bei meinem Ausgangspunkt (und angesichts der während meiner wissenschaftlichen Tätigkeit erworbenen *déformation professionelle*) lag es nahe, den Weg durch die jüngere Vergangenheit des Universums, also über Erdgeschichte, Geologie und Paläontologie einzuschlagen. Die Reise gestaltete sich interessanter als erhofft. Nach vielen realen Reisen im Zuge von Exkursionen und Kartierkursen in zumeist mediterrane Gefilde, schloß sich ein eher imaginär geprägter Aufenthalt im Unterdevon an, und die Beschäftigung mit den damals entstandenen Gefäßpflanzen.

Weiter fortschreitend bin ich mittlerweile fast in der Gegenwart angekommen: Die in dieser Arbeit entwickelten physiologischen Modelle beschreiben ebenso gut rezente wie fossile Pflanzen. Der wesentliche Unterschied besteht nur darin, daß man die Physiologie rezenter Pflanzen in der Regel im Gewächshaus untersuchen kann. Bei fossilen (oder schlimmer noch: ausgestorbenen) Pflanzen ist man dagegen zwingend auf mathematische Modelle angewiesen.

Und da mir Theoretische Physik und Mathematik sehr ans Herz gewachsen sind, empfinde ich es als großes Glück, daß ich Paläontologie und Biologie genauer kennenlernen kann, ohne allzu viel Altes aufgeben zu müssen.

6.2 Danksagungen

Viele Leute haben Anteil am Werden dieser Arbeit, auch wenn dies manchen von ihnen vielleicht nicht bewusst ist.

Explizit möchte ich zunächst meiner Kollegin Anita Roth-Nebelsick danken. Auch dafür, dass sie diese Arbeit betreut hat. Vor allem aber für unsere schon einige Jahre währende Zusammenarbeit, die sich als sehr ertragreiches Aufeinandertreffen von Biologie und Physik erwiesen hat. Bedankt sei in diesem Zusammenhang auch Jimmy Nebelsick: Ursprünglich war es nämlich seine Idee gewesen, dass unsere unterschiedlichen Ansätze sich gut ergänzen könnten.

Sehr gedeihlich empfand ich auch die Atmosphäre in der — bis auf eine kleine Konkursmasse — dahingegangenen AG Mosbrugger, während deren hiesiger Existenz ein grosser Teil dieser Arbeit entstanden ist. Ähnlich Nostalgisches gilt für Luci Schlemmer, die sich leider in den Vorruhestand begeben hat. Immerhin hat sie statt einer Lücke Anne Schulze hinterlassen.

Ob der ganzen Mathematik und Modellbilderei gerät die Geländegeologie immer wieder ins Hintertreffen, obwohl es mir eines der schönsten Vergnügen ist, eine Landschaft zu erlaufen und zu erhämmern. Die Exkursionen in die Wutachschlucht und den Nordschwarzwald mit Christopher Traiser und Lolek stellen einen gewissen Ausgleich dar. Ich hoffe, dass uns diese (und eventuell neu dazukommende) Exkursionen noch lange erhalten bleiben.

Gefreut habe ich mich, daß Dieter Korn und Birgit Binder Illustrationen beigesteuert haben und Wolfgang Gerber einige von ihnen photographiert hat. Laci Müller danke ich recht herzlich fürs Übersetzen.

Erstaunlicherweise gibt es auch noch ein Leben außerhalb der Wissenschaft: Zum einen die Blaskapellen *Trotzblech* und *Compressso Musicale*, welche die undogmatische Blasmusik pflegen. Zum andern das äußerst erfreuliche Zusammenleben mit Birgit Binder und den Tieren.

Zum Schluß bitte ich alle zu Unrecht ungenannt Gebliebenen, mir dies nachzusehen.

Tübingen, den 13. April 2007

Die Illustration auf der vorletzten Seite stammt von Friedrich Karl Waechter ([69]).

6.3 Miscellaneous

Sitting On A Fence

Since I was young I've been very hard to please
And I don't know wrong from right
But there is one thing I could never understand
Some of the sick things that a girl does to a man, so

I'm just sittin' on a fence
You can say I got no sense
Trying to make up my mind
Really is too horrifying
So I'm sittin on a fence

All of my friends at school grew up and settled down
And they mortgaged up their lives
One things not said too much, but I think it's true
They just get married cause there's nothing else to do, so

I'm just sittin' on a fence
You can say i got no sense
Trying to make up my mind
Really is too horrifying
So I'm sittin on a fence

The day can come when you get old and sick and tired of life
You just never realize
Maybe the choice you made wasn't really right
But you go out and you don't come back at night, so

I'm just sittin' on a fence
You can say I got no sense
Trying to make up my mind
Really is too horrifying
So I'm sittin on a fence

Mick Jagger and Keith Richards ([35])

Legende von der Entstehung des Buches Taoteking auf dem Weg des Laotse in die Emigration

1
Als er Siebzig war und war gebrechlich
Drängte es den Lehrer doch nach Ruh
Denn die Güte war im Lande wieder einmal schwächlich
Und die Bosheit nahm an Kräften wieder einmal zu.
Und er gürtete die Schuh.

2
Und er packte ein, was er so brauchte:
Wenig. Doch es wurde dies und das.
So die Pfeife, die er abends immer rauchte
Und das Büchlein, das er immer las.
Weißbrot nach dem Augenmaß.

3
Freute sich des Tals noch einmal und vergaß es
Als er ins Gebirg den Weg einschlug
Und sein Ochse freute sich des frischen Grases
Kauend, während er den Alten trug.
Denn dem ging es schnell genug.

4
Doch am vierten Tag im Felsgesteine
Hat ein Zöllner ihm den Weg verwehrt:
„Kostbarkeiten zu verzollen?“ - „Keine.“
Und der Knabe, der den Ochsen führte, sprach: „Er hat gelehrt.“
Und so war auch das erklärt.

5
Doch der Mann in einer heitren Regung
Fragte noch: „Hat er was rausgekriegt?“
Sprach der Knabe: „Daß das weiche Wasser in Bewegung
Mit der Zeit den harten Stein besiegt.
Du verstehst, das Harte unterliegt.“

6
Daß er nicht das letzte Tageslicht verlöre
Trieb der Knabe nun den Ochsen an
Und die drei verschwanden schon um eine schwarze Föhre
Da kam plötzlich Fahrt in unsern Mann
Und er schrie: „He, du! Halt an!

7
Was ist das mit diesem Wasser, Alter?“
Hielt der Alte: „Intressiert es dich?
Sprach der Mann: „Ich bin nur Zollverwalter

Doch wer wen besiegt, das interessiert auch mich.
Wenn du's weißt, dann sprich!

8
Schreib mir's auf! Diktier es diesem Kinde!
So was nimmt man doch nicht mit sich fort.
Da gibt's doch Papier bei uns und Tinte
Und ein Nachtmahl gibt es auch: ich wohne dort.
Nun, ist das ein Wort?"

9
Über seine Schulter sah der Alte
Auf den Mann: Flickjoppe. Keine Schuh.
Und die Stirne eine einzige Falte.
Ach, kein Sieger trat da auf ihn zu.
Und er murmelte: „Auch du?"

10
Eine höfliche Bitte abzuschlagen
War der Alte, wie es schien, zu alt.
Denn er sagte laut: „Die etwas fragen
Die verdienen Antwort." Sprach der Knabe: „Es wird auch schon kalt."
„Gut, ein kleiner Aufenthalt."

11
Und von seinem Ochsen stieg der Weise
Sieben Tage schrieben sie zu zweit
Und der Zöllner brachte Essen (und er fluchte nur noch leise
Mit den Schmugglern in der ganzen Zeit).
Und dann war's soweit.

12
Und dem Zöllner händigte der Knabe
Eines Morgens einundachtzig Sprüche ein.
Und mit Dank für eine kleine Reisegabe
Bogen sie um jene Föhre ins Gestein.
Sagt jetzt: kann man höflicher sein?

13
Aber rühmen wir nicht nur den Weisen
Dessen Name auf dem Buche prangt!
Denn man muß dem Weisen seine Weisheit erst entreißen.
Darum sei der Zöllner auch bedankt:
Er hat sie ihm abverlangt.

Bertolt Brecht ([12])

Bildungsgang

8. März 1955	geboren in Karlsruhe
1962 – 1974	Volksschule in Zaisenhausen (Baden) und Melanchthon-Gymnasium in Bretten
	Physik:
1974 – 1984	Physikstudium an der Eberhard-Karls-Universität Tübingen mit Abschluss Diplom Diplomarbeit: *Ein Modell zur nichtlinearen Abschirmung der Schwerkraft* betreut von Herbert Pfister vom Institut für Theoretische Physik der Universität Tübingen
1984 – 1990	Dissertation zum Thema *Exakte Lösungen der Einsteinschen Feldgleichungen für rotierende Massenschalen* am Institut für Theoretische Physik der Universität Tübingen bei Herbert Pfister
	Geologie und Paläontologie:
1996 – 2002	Studium der Geologie und Paläontologie an der Eberhard-Karls-Universität Tübingen mit Abschluss Diplom Diplomarbeit: *A Mathematical Model for the Transpiration and Assimilation of Early Devonian Land Plants with Axially Symmetric Telomes*, betreut von Anita Roth-Nebelsick und Volker Mosbrugger Diplomkartierung: *Das Becken von Prosilio (nahe Kozani, Griechenland)*, betreut von James Nebelsick und Volker Mosbrugger
2004 – 2007	Dissertation zum Thema *Functional Anatomy and Biophysical Mechanisms of Fluid Transport in Vascular Plants: Implications for Structural Optimisation in Fossil and Extant Plants* am Institut für Geowissenschaften der Universität Tübingen bei Anita Roth-Nebelsick